Thiolated metallic nanoparticles and their interactions with lipid membranes

BUNGA, YOUSILLYA

Thiolated metallic nanoparticles and their interactions with lipid membranes

Yousillya Bunga

A thesis submitted in partial-fulfillment of the degree of Doctor of Philosophy

Department of Chemistry

Durham University

2019

Abstract

The thesis investigates the interactions between thiolated metal nanoparticles (electroactive and non-electroactive ligands), and complex thiolated polymeric gold nanoparticles with lipid membranes (artificial lipid models and biological bacterial cells) as a potential tool for drug carriers.

Nanoparticle (NP)-electrode collision behaviours of thiol-capped metal NPs on gold electrodes were investigated using Resonance Enhanced Surface Impedance (RESI) and Chronoamperometry (CA) in microfluidic cells setup with integrated electrodes. Factors such as flow rates and ligand electroactivity were found to have a significant impact on the NP-electrode collision events. The NP-electrode collision events of non-electroactive dodecanethiol (DDT) NPs were detected either as agglomerates or individual particles depending on their nano-impact sizing characteristics. While the introduction of electroactive ligands, *ω*-ferrocenylhexanethiolate (FcHT), generated NP-electrode collision events under potentiated electrode conditions (oxidising potential for ferrocene).

The investigation of the penetration behaviour of thiol-capped AuNPs (electroactive and non-electroactive) through artificial lipid membranes were undertaken using AFM, RESI and electrochemical techniques. The tBLM models were incubated in NPs solutions at different time intervals and the results revealed that NPs adsorption was the first stage of NPs-membrane interactions which was followed by lipid defects formation for the penetration of NPs through the lipid membrane, then lipid collapse and/or membrane displacement by NPs monolayer. The other investigation on the effect of NPs size (FcHT-AuNPs) on NPs-membrane interactions revealed that small NPs (5 nm) have non-destructive penetration behaviours, whereas larger NPs (10 and 20 nm) caused irreversible changes to the lipid membrane.

The investigation on the effect of NPs surface charge on NPs-membrane interactions with complex thiolated polymeric AuNPs revealed that the AuNPs containing bulky aromatic cationic ligands were not able to penetrate through tBLM models whilst aliphatic cationic ligands altered the membrane's architecture as they penetrated through. MIC assay investigation using biological bacterial cells (*E. coli*) concluded that the presence of bulky aromatic substituents play a role in inhibiting bacterial growth.

Declaration

The work described in this thesis was carried out predominantly in the Department of Chemistry at Durham University from October 2013 to July 2018. All the work is my own, unless stated otherwise.

No part of this work has been previously submitted for a degree at this or any other university.

Statement of Copyright

Acknowledgments

In the course of this PhD journey, I have to thank the following people;

To my supervisor Prof. Ritu Kataky, for the guidance, support and constant encouragements throughout every step of the challenging years of my PhD journey. Sincere gratitude.

To Durham University and ESPRC for financial support, to the GJ Russel Group Microscopy Facility, Dr Buddhika Mendis and Mr Leon Bowen.

To the electrosparklers, Drs. Bongie and Nyasha, Rodrigo and Angie, I finally made it! You were more than colleagues. You were my friends, and my family. Thanks for the laughter, the kind words, the advice and the admonitions. The PhD journey was memorable because of you all.

To Janet, Gillian and the Beta group, for the mental and spiritual support and guidance especially when things looked bleak. Thank you for always being there for me, with a listening ear, a helping hand and a praying heart.

To my inimitable Nigerian friends especially Weni, Dr. David, Arinze, Udoka, Alex, Lucius, Uchenna, Chimaobi, Otto, Vincent, Mexzi and Collins. Your diligence was inspirational, and your friendships were second to none.

And last but not least, to my very loving family, Papa, Maman, Y'Aurélien, Aurore and Jenny, words can hardly express how grateful I am for having you all as my family. Thank you for your love, encouragement and prayers. And not forgetting the meal runs from Oldbury to Durham at the expense of your time and resources. Botondi Mingi!!

Above all, I thank God for His grace and mercy that got me through the tears, struggles and joy of this chapter of my life.

Publications

One part of this thesis is based on the following publication:

Y. Bunga and R. Kataky

Silver nanoparticle impacts on gold electrode surfaces in flow-injection configuration

*Sensors Actuators B Chem., 2019, **290**, 140–146*

Table of Contents

List of Abbreviations

AC	alternating electric current
AFM	atomic force microscopy
Ag	silver
Au	gold
CA	chronoamperometry
CV	cyclic voltammetry/voltammogram
DDT	1-dodecanethiol
DLS	dynamic light scattering
DNA	deoxyribonucleic acid
DPPTE	1,2-dipalmitoyl-sn-glycero-3-phosphothioethanol
DPV	differential pulse voltammetry
EIS	electrochemical impedance spectroscopy
(E)QCM	(electrochemical) quartz crystal microbalance
FIA	flow injection analysis
Fc	ferrocene
FcHT	6- or *ω*-(ferrocenyl)hexanethiol
FTIR	Fourier transform infrared spectroscopy
FU	fluorouracil
HCl	hydrochloric acid
ICP	inductively coupled plasma
IR	infrared
LB	Langmuir-Blodgett
MIC	minimum inhibitory concentration
MPC(s)	monolayer-protected cluster(s)
MS	mass spectrometry
NP(s)	nanoparticle(s)
OD	optical density
PAMAN	polycationic polymer
PBS	phosphate buffer solution
PEG	poly(ethylene glycol)

POPC	2-oleoyl-1-palmityol-sn-glycero-3-phosphocholine
Pt	platinum
QD	quantum dot
QDL	quantised double layer
RESI	resonance enhanced surface impedance
ROS	reactive oxygen species
SAM	self-assembled monolayer
SLB	supported lipid bilayer
SPR	surface plasmon resonance
(S/T)EM	(scanning/transmission) electron microscope
(t)BLM	black lipid membrane or (tethered) bilayer lipid membrane
TEG	triethylene glycol
TOAB	tetraoctylammonium bromide
UME	ultramicroelectrode

1. Introduction

Nanotechnology has allowed researchers to reduce materials to their nanoscale and, with the newly found characteristics of these nanomaterials, these can then be used to improve, develop and design new products ideas in a wide range of applications.[1,2] Nanomaterials such as metallic nanoparticles (NPs) have been reported as promising platform for better targeting, more selective and more effective drug delivery systems.[3] This is achieved by modifying the surface of the NPs with active agents at high concentrations or encapsulating the drug within a protective sheath that can be manipulated to release its content for more targeted tissue-specific delivery.[3–5] Even with the extensive research work undertaken to present about the clinical applications of NPs as therapeutics, there is still more work to be done in overcoming the problems associated with NPs more so in their toxicity in terms of long term health risks that they pose once administered into the human body.[6] Though metallic NPs has seen a boom in their use in many applications from cancer therapy treatments to their use in chemical and biological sensing.[7] There seems to be limited publication on the interaction of metallic NPs stabilised with thiolated ligands with lipid membranes. In view of the desirability of NPs because of their unique properties; when coupled with stable thiol ligands, we hope to gain a better understanding on such NPs and their penetration behaviour through lipid membranes, via the use of study of their electrochemical activities at electrode-lipid membrane interfaces. The purpose of this thesis is to outline the appropriateness of thiol-protected NPs in this expanding field of sensing as potential tools for drug carriers.

This thesis looks to highlight the interactions between thiolated metal NPs (electroactive and non-electroactive ligands), and complex thiolated polymeric AuNPs with lipid membranes (artificial lipid models and biological bacterial cells). The thesis considers how the thiolated metal NPs and complex thiolated AuNPs interact with artificial lipid models (lipid membranes immobilised on gold eletrodes) and, how those complex thiolated AuNPs interact with biological bacteria cells.

My thesis is divided as follows:

Chapter two (2) provides background information on lipid membrane; including an introduction on the cell membrane as well as the different models that mimic the bilayer lipid membrane. An overview of NPs, with an introduction to NPs setting the scene on what they are and the most common synthetic routes. Eventually concluding the chapter on the types of NPs and their effects on the NP-cell membrane interactions.

Chapter three (3) outlines the different methodologies, techniques and instrumentations used in the research. Also, this chapter gives an introduction on each technique as well as all experimental parameters inclusive of the experimental materials.

Prior to investigating the effect and interactions of NPs with cell membrane models, we first examined the effect of metallic NPs on electrode surfaces. **Chapter four** (4) reports on the effect of flow rates on the fate of nanoparticles impacting an electrode surface. Comparison studies were carried out between silver (Ag) and gold (Au) NPs for both non- and electroactive functionalised metal cores in the monitoring of NPs collision behaviours using two techniques; a well-known technique called particle Chronoamperometry and a more novel method called Resonance Enhanced Surface Impedance (RESI).

In **chapter five** (5), the research focused on determining the penetration behaviours of AuNPs (both non- and electroactive functionalised) through artificial lipid membrane models (tethered lipid bilayer immobilised on gold electrodes). The focus was on AuNPs due to their low heterogeneity as well as their commercial availability in different sizes. The techniques that enabled the studies to be undertaken included atomic force microscopy (AFM), electrochemical techniques, such as cyclic voltammetry and differential potential voltammetry and RESI.

The next logical step was to investigate the surface functionality of NPs and how these affect cell membranes. **Chapter six** (6) reports on how differently functionalised (charged, aromatic and non-aromatic) AuNPs interacted with both artificial cell membranes and real bacterial

cells, Gram-negative Escherichia coli (*E. coli*) bacterial cells using different techniques; Quartz crystal microbalance (QCM), RESI and electrochemical impedance spectroscopy (EIS) for the studies on artificial membrane models i.e. tethered lipid membrane (tBLM) on gold electrodes. And the biological cell studies were carried out with the minimum inhibitory concentration (MIC) technique is used to investigate of potency of these NPs against *E. coli* cells.

The final chapter of this thesis, **chapter seven** (7), includes a general conclusion to the research work carried out as well as potential future research work that can be developed from this work.

1.1. References

1 M. Benelmekki, in *Designing Hybrid Nanoparticles*, Morgan & Claypool Publishers, 2015, pp. 1–14.

2 A. Trafton, *MIT News Off.*, 2018.

3 M. Singh, S. Manikandan and A. K. Kumaraguru, *Res. J. Nanosci. Nanotechnol.*, 2011, **1**, 1–11.

4 D. Kumar, N. Saini, N. Jain, R. Sareen and V. Pandit, *Expert Opin. Drug Deliv.*, 2013, **10**, 397–409.

5 S. Jain, D. G. Hirst and J. M. O'Sullivan, *Br. J. Radiol.*, 2012, **85**, 101–113.

6 M. Fakruddin, Z. Hossain and H. Afroz, *J. Nanobiotechnology*, 2012, **10**, 31.

7 N. Elahi, M. Kamali and M. H. Baghersad, *Talanta*, 2018, **184**, 537–556.

2. Background Information

Colloids are systems that cannot be observe by a naked eye due to their small particle sizes ranging in dimensions between few nanometres and few tens of nanometres; generally when referring to the size of these systems, the particle diameter not the radius is referred to.[1] Colloids are found in nature as natural macromolecules: starch, nucleic acids, proteins and they can be synthesised using different routes tailoring for their dimensions and geometries.[2] Colloidal nanoparticles, or nanoparticles (NPs), have been reported to have a wide range of application in health, cosmetics, electronics etc[3] because of the many desired properties that they hold, as a result there has been a growing interest in the field of research.

For the successful NPs-based applications, it is imperative that properties such as size, morphology, surface functionality and purity of the NPs are well-defined during the synthetic route as these will have a great influence over reactivities. Thanks to nanotechnology, it has been possible to precisely engineer nanomaterials exhibiting fundamental properties such as “solubility, diffusivity, blood circulation half-life, drug release characteristics, and immunogenicity[4] that are required within the field of medicine, therapeutic and diagnostic applications. As a result, it is imperative that a better and more complete understanding of the NPs biological interactions is developed through research, thus enabling improved, more specific and successful treatment pathways that yield minimal side effects.

2.1. An introduction on lipid membrane

Lipid membrane or lipid bilayer also known as phospholipid bilayer is a crucial component of the cell membrane. It is made up of phospholipid molecules arranged in bilayer formation, providing the barrier separating the interior of the cell from its external environment. The structure of the phospholipids is key to the permeability of the cell membrane; with hydrophilic region exposed to the aqueous environment and the hydrophobic region forming the interior

of the bilayer (Figure 2.1-1). This bilayer formation impedes large and small polar molecules from passing through.

The fluidity of the cell membrane is due to the arrangement of individual phospholipid molecules allowing free movement of molecules within the lipid bilayer, hence its name as fluid phospholipid bilayer.[5] The first and accepted model of the lipid membrane is called the fluid Mosaic model (Figure 2.1-1), which is made up of components other than the phospholipid membrane including: transmembrane proteins (responsible for transporting molecules across the membrane); cholesterol (provides cell support and stability as well as decreases membrane fluidity and permeability); and other proteins (providing cell support, acting as cell receptors etc.).[6] The presence of all these components makes for the complexity of the cell membrane structure; hydrophilic polar head group consists of phosphate group (PO_4^{3-}) and glycerol molecule ($C_3H_8O_3$).[5] In most mammalian cells, phosphatidylcholine (PC) is the most common headgroup. It has been reported that the electrolyte ions interact with the charged lipid head groups; some recorded interactions have been of weak influence, allowing the free movement of ions along the membrane and other interactions are far stronger causing the membrane to become rigid.[7]

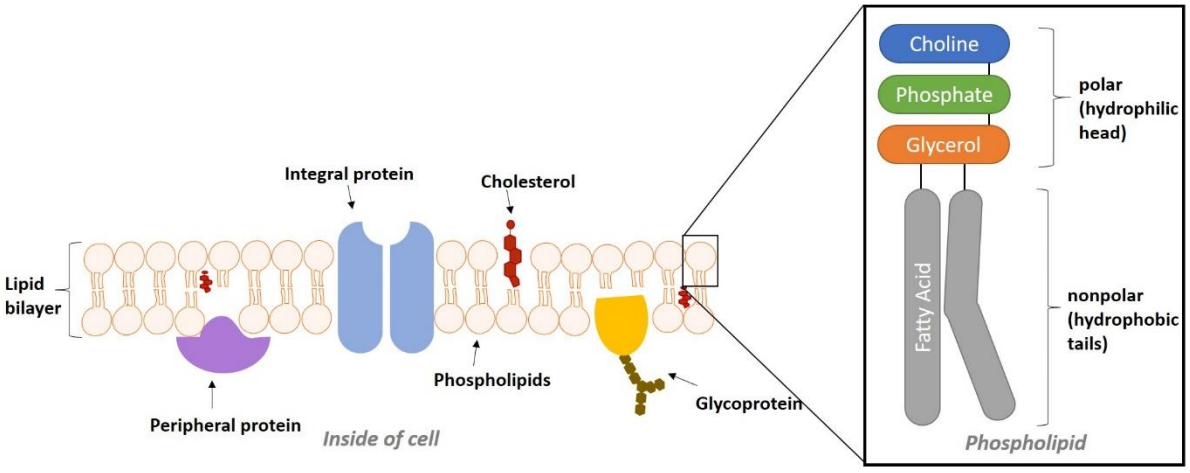

Figure 2.1-1: Schematic representation of mosaic model of a fluid lipid bilayer and its constituents; choline ($C_5H_{14}NO^+$), hydrophobic tails (saturated and unsaturated fatty acids).

Owing to the structural complexity of the cell membrane composition, it has become necessary to synthetically fabricate lipid bilayers in the laboratories; these are called model

lipid bilayers, divided into two main models: black lipid membranes and lipid membranes on solid substrates (Figure 2.1-2).[8,9]

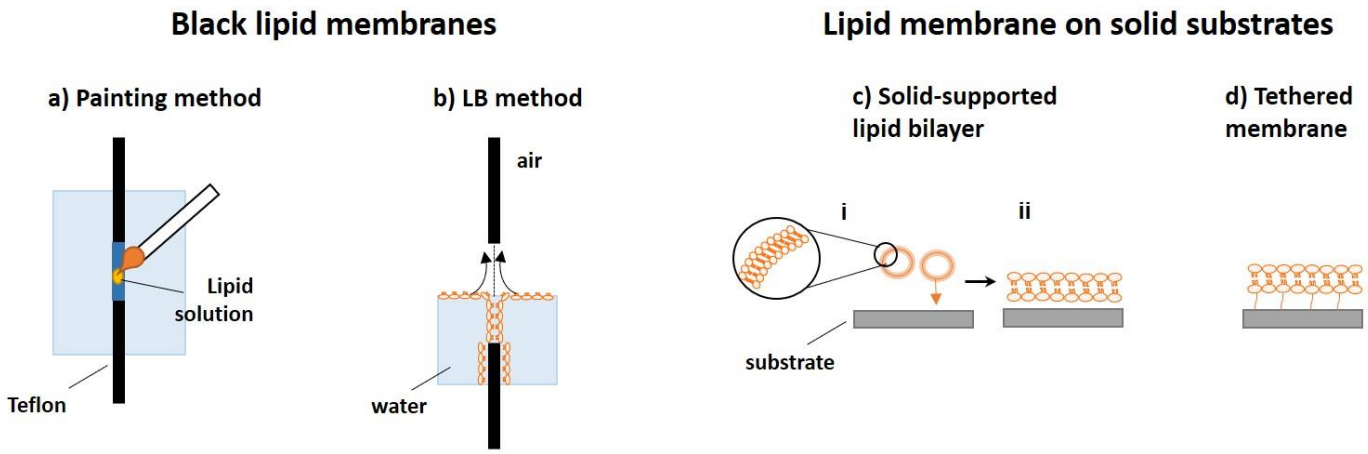

Figure 2.1-2: Conventional methods for the formation of black lipid membranes; a) painting and b) Langmuir-Blodgett (LB) methods and, the formation of lipid bilayer on solid substrates; c) solid-supported lipid bilayer and d) tethered membrane.

2.1.1. Black lipid membranes

Black lipid membranes (BLMs) are generally referred to as 'painted' bilayer owing to the method used to form them. There are two main methods for forming BLMs. One of which is the Painting Technique which is carried out by manually painting the lipids dissolved in an organic solvent such as n-dodecane across a small aperture (< 1 nm) on the surface of a hydrophobic polyethylene or Teflon film (Figure 2.1-2a).[8,10] The other lipid formation method is the use of a Langmuir-Blodgett (LB) trough, by raising and lowering the Teflon film with an aperture across a reservoir filled with dissolved lipids spread over the aqueous surface, forming a lipid bilayer membrane at air-water interface (Figure 2.1-2b).[9] Although the painting technique is a simple method to carry out without the need of complex or cumbersome apparatus compared to the LB technique, however, the use of volatile organic solvent (to dissolve the lipid) hinders the normal function of protein molecules within the lipid bilayer.[8]

Both 'painting' and LB techniques are commonly used methods for the formation of free-standing bilayer membranes as the main advantage is the lack of unwanted interferences in the bilayer formed. The ability to access the membrane on both sides, i.e. top and bottom sides, makes this artificial bilayer model the most consistent model with a living system.[11,12]

However, the major limitations to the LB technique include short lifetime (only a few hours) of the membranes due the membranes' poor stability, its fragile state, as well as the incompatibility of the solvent used for lipid spreading with proteins such as: G-protein-coupled receptors and their analogues.[13,14]

2.1.2. Different models of lipid membranes on solid substrates

In recognition of the fragility and instability of the BLM methods as highlighted above, and to overcome these limitations, von Tscharner and McConnell[15] developed the Lipid Membrane on Solid Substrates method which involves transferring lipid monolayers onto solid substrates. This planar membrane model system is considered as more robust and stable than the BLM model.[8,12] Within the model system for lipid membranes on solid substrates, there are three main types; (solid)-supported lipid bilayers (Figure 2.1-2c), self-assembled lipid monolayers and tethered lipid-bilayers (Figure 2.1-2d).

2.1.2.1. Supported lipid bilayers

The (solid)-**supported lipid bilayers** (SLBs) model has become the most popular model of cell membrane mimic. There are three main methods of forming SLBs on solid substrates: one method uses the (LB) trough, the other two methods use lipid vesicles fusion to form lipid bilayer on the substrate.[8]

In the LB trough technique mentioned above when discussing BLMs, the same protocol can be used however, in this case, solid substrate is deployed instead of a Teflon film. The mechanism consists of a dip and pull of the solid substrate into a lipid solution thus enabling the transfer of the lipid monolayer onto the solid substrate.[12]

The other method for bilayer formation is by lipid vesicles adsorption and rupture over a solid substrate (glass[16], oxidised silicon[17] to name a few).[14,18,19] Figure 2.1-2c shows the suggested mechanisms of SLB formation; 1st stage is the adsorption of lipid vesicles on the substrate surface, 2nd stage is either the rupture of lipid vesicles or fusion of vesicles followed by vesicles

rupture and final stage is the formation of a single bilayer on the surface as the vesicles rupture.[18,20]

The SLB models have many advantages over BLMs; they are highly robust, and form more stable membranes compared to BLMs model, the issue of solvent-protein compatibility is no longer applicable. Moreover, surface sensitive techniques[21] can be used (atomic force microscopy, quartz crystal microbalance etc.), thus making it a far more favourable model to use for bio-sensing applications. Some of the limitations to this method of lipid formation include the non-uniform formation of lipid bilayer on the substrate, the high probability of defects and holes at the lipid surface, and the inability to use both sides of the substrate once the bilayer is formed compared to the painted system where both sides of the bilayer are accessible.[18,19]

Another approach to lipid bilayer on solid substrate is by creating a cushion layer separating the lipid bilayer and the substrate. This approach is referred to as the tethered lipid membrane (tBLM).[22] More details about this approach is discussed later in the chapter.

2.1.2.2. Self-assembled monolayers

A monolayer is defined as a thin film (1-3 nm in thickness) made up of particles, atoms or molecules closely packed together in a single layer. In this process, these particles are said to arrange themselves to form an organised and structured assembly on the surface of a solid, a process referred to as **self-assembled monolayer** (SAM) due to the spontaneous adsorption of the molecules to form the monolayer.[23]

SAMs are formed by a chemisorption, adsorption due a chemical reaction between the surface of the substrate and the adsorbate molecules. There are three parts that constitute SAM adsorbed layer; the surface group, the alkyl chain and the anchor group (Figure 2.1-3).[24] The **surface group** or the functional group defines the surface properties; this is the outer surface of the film thus the group that interacts directly with the bulk solution. The **alkyl chain** or spacer group defines the arrangement of the final layer by connecting the surface group and the

anchoring group. This part of the molecule affects the intermolecular interaction and orientation. The **anchor group** binds to the surface of the substrate via covalent bonding.

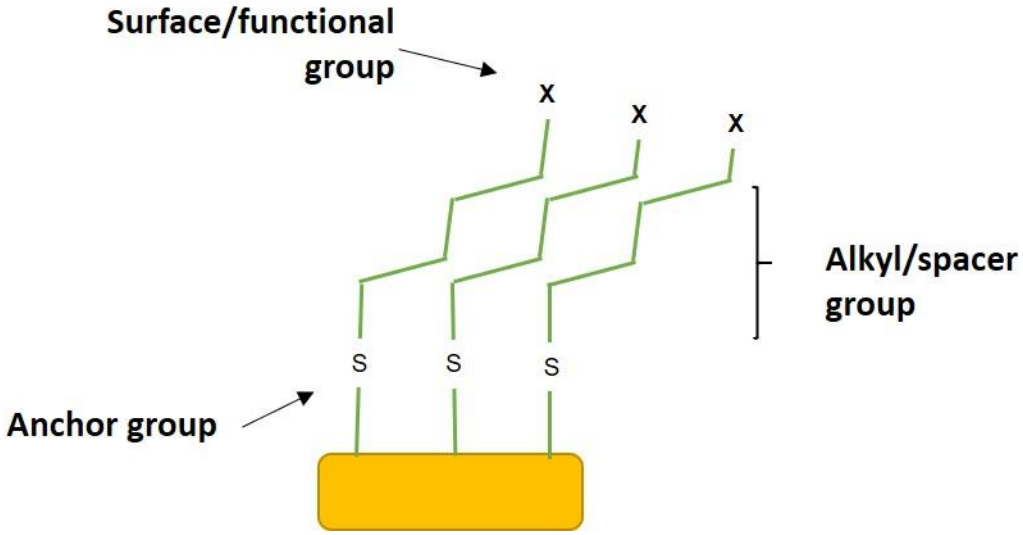

Figure 2.1-3: Schematic view of constituents of a self-assembled monolayer molecule.

Earlier literature using SAM in their studies included different types of organosulphur compounds such as: alkanethiols (HS-R-X), dialkyl disulphides (X-R_1-S-S-R_2-X) with different functional (end groups i.e. X) including methyl, alcohol and carboxylic acids.[25] These experiments were the foundation for the characterisation of these systems in terms of their surface structure, the orientation and organisation of their chains. Selecting the head group will depend on the type of the applications of the SAM molecule.[24] Alkanethiol SAM has become the most common SAM to be used, due to its desirable characteristics such as its strong thiolate bond and stable resulting monolayer.

Alkanethiol SAM

Thiol is a compound with hydrogen-sulphur (-SH) group. These compounds are widely used for SAM on gold as the binding of alkanethiols ($CH_3(CH_2)_nSH$) to a metal surface occurs via metal-sulphur bond formation. The most studied alkanethiol SAM is with gold because of the metal's inertness, its weak tendency to form oxides and its strong interaction with sulphur resulting in a very stable monolayer.[26] S-Au bond formed is around 50 kcal mol^{-1}, enabling

the alkanethiol molecules to occupy every available site on the metal surface to optimise its organisation.

The formation of S-Au bond is not well understood, but it is assumed that starts with the loss of hydrogen from the –SH group to form thiolate (R-S- group) which is then covalently bonded to the metal surface thus generating strong thiolate bonding (Eq.2-1).

$$R - SH + Au_n^0 \rightarrow R - S^- Au^+ + {}^1/_2\, H_2 \qquad \textbf{(2-1)}$$

The **kinetics** of this formation is understood to be as follows; the first stage of SAM formation is when the molecules become adsorbed onto the surface of the substrate; this is a very fast process. The second stage lasts several hours where the surface of the substrate is saturated with alkenethiol molecules and, these can organise themselves in order to reach equilibrium and form an ordered film.[26,27]

Electron diffraction studies of the monolayer on gold surfaces have revealed a hexagonal lattice packing arrangement with S--S spacing at approximately 5 Å.[28] The van der Waals interaction (the interactions between the neighbouring molecules) is maximised by tilting the alkyl tail by ca. 30°, determined by FTIR measurements, this also balances the headgroup-substrate interaction in order to minimise the surface energy.

The **formation** of alkanethiol SAM on solid surfaces is done by immersing the substrate in an ethanoic solution of organic thiols (Figure 2.1-4a). The immersion time is dependent on the nature and concentration of thiols.[29,30] Moreover, the quality of the monolayer depends on many factors such as roughness and cleanliness of the solid substrates to minimise the formation of defects.[25]

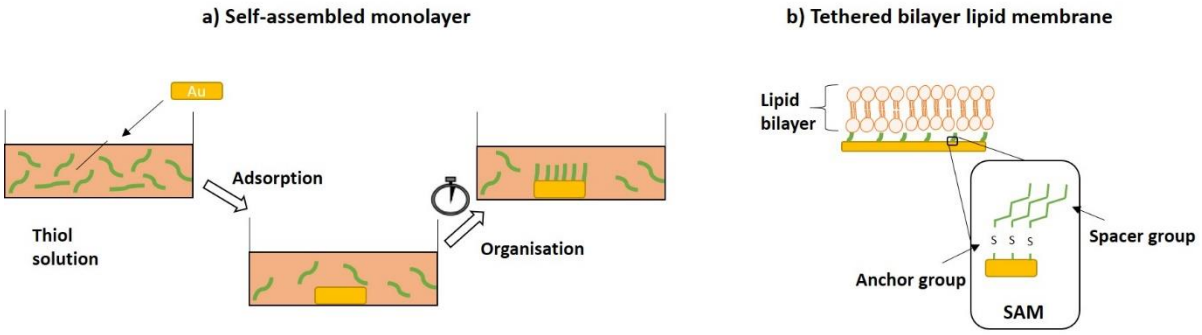

Figure 2.1-4: a) adsorption of alkanethiol on gold substrate for the formation of self-assembled monolayer (SAM); b) schematic illustration depicting tethered bilayer lipid membrane (tBLM) after its formation on gold substrate.

The simplest and most common lipid membrane form is of a solid substrate consisting of a monolayer of alkanethiol to be used as lower leaflet, and forming a stable and rigid hydrophobic monolayer, followed by a monolayer of phospholipid[8] Despite the mentioned benefits of SAM lipid bilayer membrane for their rigid properties, the use of alkanethiol SAM as lower leaflet hinders fluidic movement of a normal lipid membrane due to the crystalline nature of the alkanethiol SAM.[16]

2.1.2.3. Tethered bilayer lipid membranes

The **tethered bilayer lipid membranes** (tBLMs) encapsulate the advantage of SAMs as stable and durable systems that can mimic the cell environment i.e. the cytoplasmic membrane as well as enable the system to have an aqueous layer/reservoir in between the surface of the substrate and the lipid bilayer thus enabling membrane fluidity.[17,31,32]

tBLM models are comprised of the lipid group attached to the surface of the substrate; a lower end of the spacer molecule shown in Figure 2.1-4b has an anchor group that covalently bonds to the substrate (disulphide and thiol are used with gold and silane is used for silicon and aluminium surfaces)[22]; while the other end of the spacer contains alkyl chain, creating a hydrophobic layer which promotes the fusion with lipid liposomes/vesicles to form tethered lipid bilayer.[33]

Since the first report using this system by Lang *et al.*[34,35] their publications presented a new technique of attaching lipid bilayers on gold surfaces via covalent bonding of the sulphur and

di-sulphur groups on the thiol molecule to the gold surface. These thiolipid bound models have been reported to yield stable lipid membranes on gold surfaces which has been found to be much more robust than BLM models and, they were found to have highly insulating membrane properties.[17,36,37] The discovery of such chemisorbed lipid bilayer on gold surfaces enabled the incorporation of toxins/proteins[38] within the membrane model due to the water layer that reduces the hydrophobicity of the metal surface, the inclusion of ion channels.[32] In this later study, a new biosensor for the detection of influenza virus was created with gramicidin ion channels that enabled the detection of target analytes, influenza nucleocapsid protein,[39] via cross-linking of the analytes with the gramicidin detectors incorporated within the lipid membrane. As a result, this membrane model allows for surface sensitive techniques to be carried out.[40]

Moreover, this permits the investigations on the interactions between nanoparticles and cell membrane which will be discussed in detail in this chapter, and in the general course of this thesis.

2.2. An introduction to nanoparticles

Metals like gold (Au) and silver (Ag) in their bulk or dispersed state have very desirable properties such as chemical stability; and thermal and electrical conductivities. However, these metals (i.e. gold and silver) as nanoparticles (NPs) have quite different properties from their bulk or dispersed state which include lower melting point and specific optical properties.[41]

NPs are defined as clusters of atoms with crystalline structure (metallic nanocrystals) surrounded by a protective monolayer of organic molecules also known as monolayer-protected clusters (MPCs); ranging in size from 1-100 nm.[42–44]

The use of NPs can be traced back to the Middle Ages by craft workers who made use of NPs to decorate/glaze their potteries and ceramics.[45] Other uses include application to stained glass windows for their vivid colours after it was discovered that by controlling certain

properties (size and shape of NPs) during their synthesis, it was possible to obtain a spectrum of colours.[42]

Optical properties are not the only desirable advantage of NPs over other particles. The uses of NPs have blossomed over the last few decades and are seen in different fields (such as cosmetics, fabrics, electronic circuits). Furthermore, another desirable advantage of NPs is its enhancement of surface reactivity by its ability to yield large surface to volume ratio because of its small size.[46] A way to enhance and harness such physiochemical properties is by surface modification or functionalisation. Over time, the synthesis of these nanomaterials have become more reliable and high yielding with the alteration of the particles' surface functionality i.e. by changing ligands or capping agents via ligand place- exchange reactions[47,48] hence enabling the particles to have increased affinities and selectivity for specific uses in the biomedical field with applications positively favoured in imaging, diagnosis and drug delivery.[49,50]

Finally, there is no shortage of disputes between the proponents of the use of NPs in nano-medicine for their biological activities and critics of its toxic effects, as the physiochemical characterisations/properties (size, surface charge, shape) of NPs are directed by their nature.[49] The consensus lies in the extensive toxicological studies via the use of experimental models, both *in vivo* and *in vitro* models, of which all nanoproducts must undergo before they can be considered safe for human applications and the environment.[51]

2.2.1. An introduction to metallic nanoparticles

Gold (Au) is a precious metal that has held varied interest throughout history. Initially, it was because of its visual appearance and malleability thus it was used in the production of artefacts, jewellery etc.[50] Like Au, silver (Ag), also a precious metal has had many uses over centuries as coins, utensils, electrical conductors and many more.

In 1659, the alchemist, Johann Rudolf Glauber synthesised the first recorded gold colloidal solution with the reduction of gold salts by tin chloride.[52] Since its discovery, colloidal solutions

have been extensively used over the centuries in various applications.[52] This laid the foundation for the discovery, introduction and study of nanomaterials within the scientific field. With this new area of research came the understanding and development of new materials and devices by controlling their dimensions at nanoscale. This has opened up a wide range of applications for metal nanoparticles.[41,46] Over the years, there have been many applications of metal NPs owing to their desirable optical-electronic properties; electronic conductors, drug delivery devices for medical applications and sensory probes.

Consequently, metal NPs such as Au and Ag possess attractive physical properties because of their range in sizes and their chemical stability. This has opened an area of interest for scientists in synthesising such chemically stable compounds that will enable the adjustment of their surface properties.[53]

2.2.2. The different synthetic routes for preparing metallic nanoparticles

A way to enhance the properties of metal NPs is by surface modification or functionalisation. The properties of NPs can be engineered specifically to suit various applications by optimising the active sites of the NPs surface.[54] Such methods can generate novel and interesting opportunities. Over the years, different methodologies have been developed and used to synthesise NPs and they are the top-down approaches, and the bottom-up approaches (Figure 2.2-1).[42,55–58]

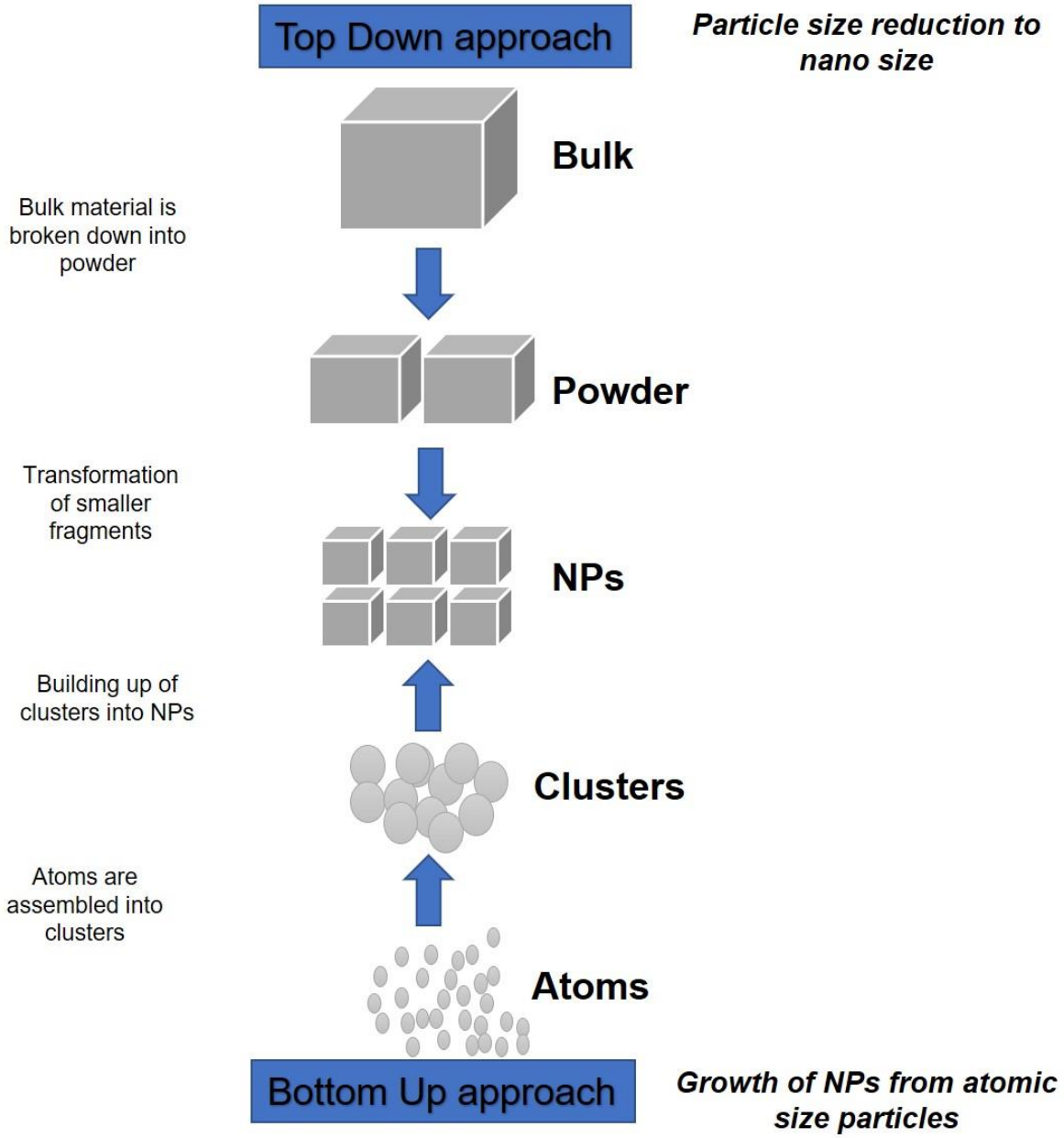

Figure 2.2-1: Schematic representation of the top-down and bottom-up approaches for the synthesis of nanomaterials.

Top-down approaches refer to the application of an external force to a bulk material or solid, leading to its breakdown into smaller particles i.e. nanomaterials. This approach was first developed and is widely used in the microelectronics industry.[55] The main advantage of this method is the ease at which large quantity of nanomaterials can be manufactured, thus making more favourable for nanomaterials fabrication in industries.[56] However, the disadvantages of this approach are in the inability to control sizes of the NPs during synthesis as well the imperfections that can arise in the surface structure of the nanomaterials.[59]

Bottom-up approaches on the other hand, refer to the synthesis of nanomaterials starting from atoms, gas or liquids that are 'built-up', clusters by clusters resulting in nanostructures yielding uniform shapes and monodispersed sizes.[55] The advantage of this approach over top-down is the likelihood of the nanomaterials being more homogeneous in their chemical composition and having fewer defects due to the precise control of the molecular structure at molecular level.[55]

Focusing specifically on chemical reduction method as is the simplest and most commonly used of the bottom up approaches for synthesis of metallic nanoparticles.

The Turkevich method[60] being popular for synthesis of citrate-stabilised metal NPs in solutions and Brust-Schiffrin method[61] for the synthesis of thiol-stabilised metal NPs in organic solvents.

2.2.2.1. The Turkevich method for the synthesis of gold and silver nanoparticles

Gold nanoparticles preparation using the Turkevich method

In 1951, Turkevich *et al.*[60] synthesised AuNPs using what is now called the citrate reduction method or the one phase method. This method is one of the most used protocols in the production of aqueous AuNPs suspension in water; the monodisperse nanoparticles produced are spherical in shape, with size dimensions of approx. 20 nm in diameter. In this method, the synthesis is carried out at high temperatures whereby a small amount of hydrogen tetrachloroaurate also known as choloroautic acid ($HAuCl_4$), reacts with aqueous solutions of sodium citrate and ascorbic acid which act as reducing agents. The sodium citrate also acts as the ligand stabiliser in ensuring the production of monodispersed AuNPs. As Au(III) is reduced to Au(0), the citrate ions stabilise the AuNPs by binding onto their surface by electrostatic repulsion.

In 1973, Frens[62] used the Turkevich method as a template to base his research on expanding the wide range in size of the produced AuNPs; which was previously between 10-50 nm. The results from Frens' research showed that by changing the citrate:gold ratio, this influenced the size of the produced AuNPs (ranging from 16-147 nm). Further revision of the Turkevich

method was carried out by Kimling *et al.*[63] in 2006 in achieving AuNPs with size ranging in dimensions between 9-120 nm.

Silver nanoparticles preparation using the Turkevich method

AgNPs have been prepared using the Turkevich method in the reduction of silver nitrate ($AgNO_3$) by sodium citrate, yielding aggregates of different shapes with sizes ranging from 60-200 nm.[64,65] in this synthetic route, the sodium citrate acts as both reducing agent and stabiliser, resulting in such a wide range of clusters being formed and making the method unreliable in terms of size control. Tali Dadosh improved the method by adding tannic acid with the reducing agent to prevent the agglomeration of AgNPs, which decreased the average NP sizes with sizes ranging from 18-27 nm.[66]

The major drawback of the Turkevich method were the inability to control the sizes and shapes of the NPs during synthesis; smaller particle sizes were difficult to obtain, and the production of larger NPs was to the detriment of monodispersity and shape of the colloidal solution.[67]

2.2.2.2. The Brust-Schiffrin method for the synthesis of gold and silver nanoparticles

Gold nanoparticles preparation using the Brust-Schiffrin method

The synthesis of was developed by in 1997, Brust and Schiffrin synthesised AuNPs and the two-phase method or Brust-Schiffrin method[61] was developed. The advantage of the new method enabled the synthesis of AuNPs which were thermal and air stable with core size ranging from 1–3 nm in diameter (thiol:gold mole ratio of 1:1). Moreover, these could be isolated, dried, and re-dissolved in organic solvent without particles aggregating or decomposing.

This method was carried by reacting a solution of tetraoctylammonium bromide (TOAB), made up in toluene, with $HAuCl_4$ then adding sodium borohydride and a strong binding agent such as 1-dodecanethiol. TOAB is used as a phase-transfer catalyst, a reagent used in a heterogeneous reaction to facilitate the change in phase of the reactants by forming micelles that contain water in the toluene thus enabling NPs to grow; $HAuCl_4$ is transformed from

aqueous phase to organic phase. Alkanethiol is used as capping agent or stabiliser in stabilising the NPs being formed as well as preventing their aggregation. Polymers such as alkanethiol are good capping agent as they cover a large surface area of the NPs. Au(III) is reduced to Au(I) by the addition of alkanethiol (1-dodecanethiol), this is further reduced to Au(0) with the addition of by sodium borohydride.

Another method was developed by the team using bi-functional organic thiol compound called *p*-mercaptophenol for the one-phase method which eliminated the step in the synthesis for the extraction of the compound into alkaline aqueous solution, thus allowing the direct functionalisation of the metal core.[68] This method yielded stable thiol-stabalised Au clusters ranging in sizes from 2.4-7.6 nm.

Silver nanoparticles preparation using the Brust-Schiffrin method

Although, thiolated ligands are not the most common stabilisers for AgNPs, citrate, with the most used being 'polyvinyl alcohol, poly(vinylpyrrolidone), bovine serum albumin, citrate, and cellulose'[41]. The drawback of these colloidal solutions was of the inability of the synthetic routes to yield NPs of narrow size distribution, many of the NPs prepared were agglomerates or clusters with sizes >10 nm. Seen that thiol stabilised AuNPs produced via Brust-Schiffrin method yielded stable and monodispersed NPs of smaller sizes, Murthy *et al.*[69] proved that AgNPs stabilised by dodecanethiol ligands can be obtained; adding an ethanoic solution of silver perchlorate with the stabiliser and sodium borohydride ($NaBH_4$, reducing agent), the synthesis was carried out under argon atmosphere. The NPs yielded average sizes ranging from 1.5 to 4.5 nm. Kang and Kim[70] modified the method further an compared the synthesis of dodecanethiol stabilised AgNPs using one-phase and two-phase systems. The difference in their synthesis was in the one-phase system, ethanoic solutions of silver nitrate and sodium borohydride (reducing agent) were added with the thiol agent (dodecanethiol) as stabiliser to produce AgNPs with average size of 7.9 nm. However, the two-phase system was carried out by the vigorous shaking of aqueous silver nitrate and hexadecanesulfonic acid in toluene (acts as a phase transfer agent/catalyst), followed by the reducing and stabilising agents (sodium

borohydride and dodecanethiol respectively) after the aqueous phase was decanted which yielded NPs with average size of 7.7 nm. Their findings predominantly yielded NPs that are stable and, with comparable sizes. Although Kang and Kim's methods did not yield NPs <5 nm compared to Murphy and co-workers, however, the modified method from the duo (one-phase system) negated the use of a phase transfer agent as a result, simplifying the synthetic route. Following the one-phase system, Farrell *et al.*[71] synthesised dodecathiol stabilised AgNPs ranging in average size from 3-30 nm; silver nitrate as precursor, sodium borohydride as reducing agent and dodecanethiol as stabilising agent. As their study investigated the effect that varying reducing agent and stabilising agent concentrations at constant silver salt concentration have on the formation of AgNPs. They concluded that the lower the ratio of $[NaBH_4]/[AgNO_3]$ or $[DDT]/[AgNO_3]$, the bigger the NPs as the more prone the synthetic route is to produce clusters or aggregates with average sizes between 10-30 nm.

2.2.2.3. Other synthetic routes for the preparation of alkanethiol stabilised metallic nanoparticles

Using the thiosulfate protocol for the synthesis of metal nanoparticles

In this method, silver nitrate is reduced by sodium borohydride; this reaction generates borate ions which temporarily stabilising the surface of the NPs by providing an electrostatic layer on the surface thus preventing the newly formed colloidal particles from aggregating. Sodium S-dodecylthiosulfate is added to the solution where the S-dodecylthiosulfate ligands undergo bond cleavage ($S\text{-}SO_3^-$) as they react with metal core, to become dodecanethiolate ligands, to form stable alkanethiol stabilised AgNPs with average size of 3.3 nm.[72,73] The alkanethiol stabilised AuNPs (with average core size 3.6 nm) were synthesised via the reduction of $HAuCl_4$ by $NaBH_4$, with the stabilising agent being sodium S-dodecylthiosulfate, as a one-phase system without the need for the phase transfer reagent.[72,74]

The synthesis of platinum, palladium and iridium NPs stabilised by alkanethiol following the thiosulphate protocol were carried out using two-phase systems. Potassium

tetrachloropalladate was used as the precursor for the synthesis of palladium NPs (ranging in average core size between 2-3 nm), was reduced by $NaBH_4$ in toluene/water with sodium S-dodecylthiosulfate as stabilising reagent and TOAB as phase transfer reagent.[72,75] For the synthesis of thiol-stabilised platinum NPs, dihydrogen hexachloroplatinate (IV) was the precursor and the solvent was dichloromethane instead of toluene; the synthesis yielded NPs of average sizes between 1.5-2.0 nm.[72,76] The synthesis of dodecanethiolate stabilised iridium NPs was carried out following the reduction of potassium hexachloroiridate(IV) with $NaBH_4$ in toluene, stabilised with thiosulfate ligands. The preparation of the NPs was done in a 60 °C water bath and the newly synthesised NPs were characterised by TEM with 1.2 nm as the average core size.[72,77]

San and Shon[72] investigated the catalytic activities of alkanethiol stabilised platinum and palladium NPs for the hydrogenation of alkynes (alkenes, dienes, trienes, and allylic alcohols). They concluded that the NPs had good catalytic activities and high selectivity even after 14 reaction cycles.

Using high temperatures to prepare alkanethiol metal nanoparticles

A mixture of bismuth neodecanoate in organic solvent (octadecene), 1-dodecanethiol as the stabilising reagent and oleylamine as the reducing agent were mixed together in a hot oil bath at 80 °C; yielding dodecanethiolate bismuth NPs with an average diameter of ca. 40 nm.[78] These NPs were further modified with poly(ethylene glycol), PEG, to increase the NPs stability and biocompatibility for the investigation of their potency against tumour cells via thermoradiotherapy. The authors concluded that the modified NPs exhibited high photothermal therapeutic potency against breast cancer cells.

The synthesis of thiol stabilised copper NPs was carried out with the reduction of copper(II) chloride dihydrate by *tert*-butylamine–borane complex in dodecane under oxygen free conditions (constant N_2 purge) at temperatures >145 °C. The NPs were stabilised by dodecanethiol ligands and had average sizing in the 3-10 nm range; the authors investigated

the decomposition path of alkanethiol stabilised copper NPs, they concluded of the instability of the thiol NPs due to the inevitable cleavage of the Cu-S bonds as copper sulphide clusters are formed.

Zheng *et al*[79] reported the synthesis of stable dodecanethiol stabilised AuNPs using one-phase system (with average NPs size ranging from 5-10 nm). Triphenylphosphinegold(I) chloride was reduced by *tert*-butylamine–borane complex in benzene and, the synthesis was kept at 55 °C. The same synthetic route was utilised for the successful synthesis of dodecanethiol stabilised silver and palladium NPs, using different metal precursors (silver acetate and palladium(II) acetylacetonate) yielding average sizes of 5.5 nm and 6.3 nm for silver and palladium NPs respectively.

2.2.3. The different characterisation techniques for nanoparticles

It is important to have information about the particles' size and structural make-up of NPs, thus the need for NP characterisation.[59] There are many techniques for NP characterisation which may be either morphological or structural characterisation.

In terms of morphological characterisation techniques, scanning electron microscope (SEM) and TEM are the most common techniques.[80] These microscopic techniques not only enable the determination of the physical form of the NPs i.e. the homogeneity of the sample under analysis, but also the particle size distribution.

Structural characterisation is also important as it enables the structure composition of the NPs under investigation to be known. Infrared (IR) spectroscopy and mass spectrometry (MS) are examples of such characterisation techniques for giving information about the nature of bonding.[81] In IR spectroscopy, it is possible to identify functional groups from matching spectrum with their reference spectrum i.e. fingerprint region as a way to identify the structure of the sample under analysis. Fourier transform infrared spectroscopy (FTIR) has been used to determine the spectral bands of proteins bound to NPs surfaces.[81] On the other hand in MS, the ionised sample is fragmented into multiple ions that are detected according to their

mass-to-charge ratio, ensuring accurate molecular weight determination of the sample under study. MS coupled with inductively coupled plasma (ICP), this technique enables the determination not only of the sample's mass, but also the size distribution, NPs concentration as well as its composition.[82]

By using thiosulfate ligands, which have weaker interactions with nanoparticle surfaces and slower passivation kinetics due to the polar head group, the resulting nanoparticles could be grown into larger particles during the nucleation-growth-passivation process.

2.2.4. The unique and desired properties of nanoparticles

As NPs have unique properties compared to their bulk material, their physical as well as chemical properties will determine their reactivities and toxicities towards biological systems.[83] Take gold for instance; when bulk gold interacts with visible light, it appears vibrant in colour (shiny yellow). However, gold as NPs appear blue and as the sizes decrease down to approximately 3 nm, the colour changes from blue to orange then dark red under visible light. This dramatic change in colour is due to the surface plasmon resonance (SPR).[84] This is when a frequency from the visible region of the electromagnetic wavelength, is applied on the surface of the metal causing the conduction electrons to oscillate resulting in the intensity of the colours observed.[83]

As mentioned in the previous sections, NPs can be engineered to have required functionalisation for the study under investigation. Surface characteristics play an important role in the colloidal behaviour of the NPs especially regarding their interactions with biological systems. For instance, a study by Kohli and Alpar[85] report the ability of negatively charged NPs to penetrate the surface of the skin for potential use in vaccine delivery. Thus, it is essential to know and understand the interaction of NPs with biological systems especially in view of their use in various applications including regulating metabolic pathways in plants and targeted delivery of therapeutic agents in medical treatments.

2.2.5. The uses of nanoparticles in biomedical applications

Within medicine, the use of nanomaterials has given rise to early detection and prevention of diseases as well as improved diagnosis leading to specific and targeted treatments.[49,86] There are many advantages to using nanomaterials in medicine, this spans from their use in cancer treatments to the fabrication of biological sensors; thanks to their physiochemical properties (size, shape, chemical composition, optical, magnetic, thermal, catalytic and electrical properties).[87]

Most conventional anticancer treatments such as chemotherapy are non-specific, targeting and killing in the process both healthy and cancerous cells, they generate side effects on the patients such as bone marrow and gastrointestinal toxicity.[88] A cocktail of anticancer drugs is given to the patient during the treatments; their overuse can contribute to multiple drug resistance, decreasing its potency as anticancer treatments, adding to that, these drugs generally have poor solubility and bioavailability, thus further reducing its use as anticancer agents.[87] Following the NPs desirable and unique properties, these NPs can overcome many of the disadvantages that conventional anticancer treatments possess, the synthesis of NPs can ensure biocompatibility and solubility via surface modification; it is possible to engineer NPs with functional groups that have complementary binding activities to that of targeted cancerous cells.[89,90] thus making NPs more efficient, by increasing the selectivity of the NPs to the targeted cells and reducing their toxicity to the healthy cells whilst being delivered at lower doses.[91,92]

2.2.5.1. NPs used in cancer therapy

NPs can be used on their own or conjugated with the anticancer drug to target cancerous cells. Focusing on NPs as cancer treatments; in their own right, platinum NPs were investigated as inhibitor of the growth in lung cancer cells, the authors found that the efficacy of the NPs as therapeutic agents was dependent on their concentrations.[93]

NPs have been used in photothermal therapy; a form of therapy that uses electromagnetic radiation to "generate heat for thermal destruction of cancer cells"[94]. The advantages of this technique over conventional therapy include its high selectivity and minimal invasiveness.[95] Hirsch *et al.*[96] were the first group to investigate the potency of silica-gold nanoshells modified with PEG ligands against human breast carcinoma cells. Comparing untreated cells with those incubated with nanomaterials, the latter showed an enhanced loss of cell viability under low exposure of near-infrared irradiation. Iron oxide NPs have been used in this form of therapy has been employed to reduced malignant growth on lymph nodes, under irradiation of near infrared (non-toxic radiation), these NPs were found to generate reactive oxygen species (free radicals) which are toxic to tumour cells.[87,95]

Another way that NPs are used in cancer therapy is radiotherapy; in this technique, high-energy radiation (x-ray) is used to kill cancer cells in the targeted area of the treatment, by damaging the DNA replication mechanism of the cells thus causing their eventual cell lysis.[97]

2.2.5.2. NPs conjugated with drugs and their use in drug delivery

The careful design and synthesis of drug-NPs complexes will inherit the unique physiochemical properties of the NPs of one being NPs' nanosize which would enable the complex to readily pass through the membrane boundaries and be taken into the tumorous cells.[98] Once inside the cells, the drugs can be released and take effect; the complexes have enhanced activities due to the increased drug molecules added onto the surface of NPs leading to an increased drug loading capability, benefitting a patient with the decrease in drug consumption thus treatment expenses.[86]

Drug delivery systems with metal nanoparticles

AuNPs have been recorded to act as drug carriers for the drug delivery system; AuNPs attached to anticancer drugs have been reported to high potency compared to drug free when tested.[99] Folate-modified PEG-AuNPs conjugated with doxorubicin (anticancer drug) were tested for their potency against cancerous cells; the study revealed that compared to free

doxorubicin, the drug modified NPs had a higher level of cell cytotoxicity.[100] In a study on the effect of drug modified NPs against bacterial cells, a study by Nirmala Grace and Pandian[101] coated AuNPs with the following drugs: streptomycin, gentamycin and neomycin, for the investigation of their antibacterial efficacy against Gram-positive and Gram-negative bacteria. The findings showed that the antibacterial activities of the drugs-AuNPs were higher compared to the drug only, for both Gram-positive and negative bacteria. Polyethylene glycol (PEG) stabilised AuNPs were conjugated with BTZ (proteasome inhibitor) was tested for its potency in human prostate cancer cells.

In view of the usefulness of AuNPs within the biomedical industry, the research outlined in the thesis with AuNPs stabilised with thiol ligands of various surface chemistries and their penetration behaviour through lipid membranes, for potential sensing applications.

2.3. NPs-lipid membrane interactions

Having considered the NPs and their properties and how these can affect their colloidal behaviours, it is important to examine NPs and their interaction with biological membranes, especially because of the increasing development in nanotechnology and their use in medicine as therapeutic agents. The importance lies with the issue that arises in the toxicity of these particles to the human health, although, understanding and controlling such interactions can lead to the development of more effective and efficient drugs.[102] The knowledge of factors and mechanisms by which NPs interact with the cell membrane leading to their uptake into the cells, bringing desirable effects to the target cells without endangering other living organisms is vital; thus their use as intracellular delivery of therapeutics.[103] However, the scope in this thesis does not focus on the health impacts of the NPs but, on the effects of NPs size, surface charge, hydrophobicity and composition leading to their uptake and how they interact with biological membranes.

According to previous investigations, NPs size and shape, surface charge and hydrophobicity are the main factors determining the NPs mode of interaction with the lipid bilayer, coupled

with the properties of the lipid membrane which consequently affect the cellular membrane integrity.[104–107]

2.3.1. Investigating the effect of NPs size and shape

NPs size and shape have been reported to influence cellular uptake greatly.[103] Furthermore, controlling both size and shape of NPs during the synthesis can be used for more efficient targeting of desired cells.[107,108]

2.3.1.1. Size

One other advantage of NPs is its use as drug carriers due to the particles' large surface area-to-volume ratio that facilitate their cellular uptake compared to larger molecules which are unable to overcome the membrane-associated barriers.[108] Even with the increase in research on NPs interactions with cell membrane and their uptake into cells, relating NPs sizes with lipid membrane disruption and the change in membrane morphologies are still not well understood.

Despite this, the decrease of NPs size has a big impact on their cellular uptake as smaller NPs readily diffused into the cells compared to bigger NPs with the possibility of having an optimum NPs size for efficient uptake into the cells.[107] Roiter *et al.*[109] investigated the effect of silica NP sizes on lipid bilayer. Their studies have revealed two distinct behaviours (Figure 2.3-1); one where the lipid bilayer envelopes the polar NPs (> 22 nm) and where polar NPs formed pores in the lipid bilayer (< 22 nm). In their study, the NPs were deposited on planar substrates and the lipid bilayer membrane were added on top, covering the NPs. Their findings concluded that there is a relationship between NPs size distribution and lipid stability upon interactions; the different sizes of NPs can cause different levels of destabilisation of the lipid bilayer upon interaction due to the formation of defects such as pores within the lipid bilayer or/and by affecting the membrane fluidity.[110] This effect was said to be because of the curvature of the lipid membrane upon contact with the NPs expressed as wrapping of the membrane around the NPs (fully or partially).

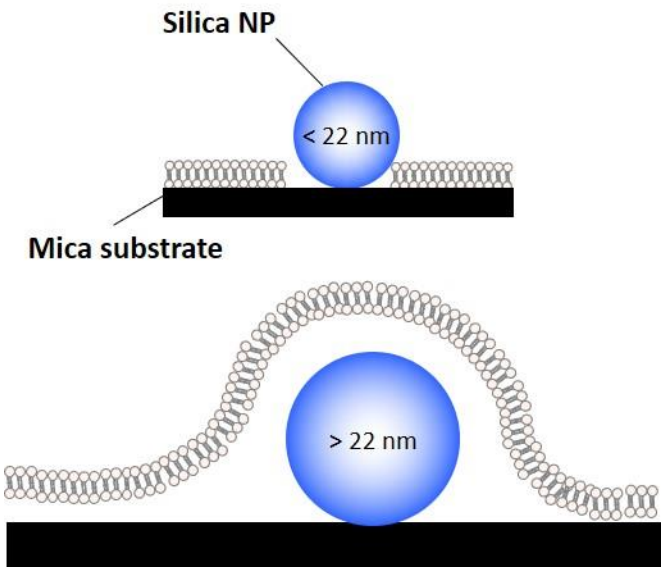

Figure 2.3-1: Lipid bilayer formation in the presence of particles larger than lipid bilayer thickness; formation of lipid pore around the NPs for particles < 22 nm compared to the envelopment of NPs by the lipid bilayer for particles > 22 nm. Adapted from Ref. 109.

Membrane stability can be affected by NPs sizes, this was investigated with citric-acid stabilised AuNPs of various sizes; 2, 5, 10 and 40 nm, their interactions with lipid membrane revealed small losses of lipid mass (up to 6 ng) resulting in the removal of lipid molecules from the lipid bilayer.[111] Smaller NPs (<10 nm) exhibited no significant changes to the lipid bilayer following their exposure, however the larger NPs (40 nm), the exposure of NPs to the bilayer caused defects to develop on the membrane and subsequent lipid molecules to be lost.

Adding to that AgNPs have been investigated against bacteria for their viability as antibacterial agents[112] Lu *et al.*[113] investigated the toxicity of AgNPs of different sizes (5, 15 and 55 nm) against oral anaerobic and aerobic pathogenic bacteria, they concluded that smaller NPs were more toxic against the bacteria than bigger NPs also that aerobic bacteria were more susceptible to the NPs compared to anaerobic bacteria; the minimum inhibitory concentration (MIC) value for 5 nm was 6 µg/mL for *E. coli*, compared to 25 µg/mL for *F. nuceatum* and *A. actinomycetemcomitans*. These were the values of the NPs concentrations for the complete inhibition of bacteria growth. Smaller NPs were more advantageous in their bactericidal effect because their large surface area enabled them to have a higher percentage of interaction with the bacteria, the mechanism of this effect was explained as the release of Ag+ ions inside the cell which “inactivate respiratory chain dehydrogenases” of the cell, viewing that aerobic

bacteria such as *E. coli*, have ample supply of oxygen and the anaerobic bacteria such as *F. nuceatum* do not hence the latter have a higher MIC values.

2.3.1.2. Shape

The shape of the NPs also plays a crucial role in the cellular uptake of NPs, it has been found to affect the amount of time the NPs reside inside the cell and how long it takes the NPs to get to the target cells.[108,114] Nowadays nanoparticles can be engineered into a variety of shapes; spheres, cube or rod-like, both regular and irregular shapes (Figure 2.3-2).

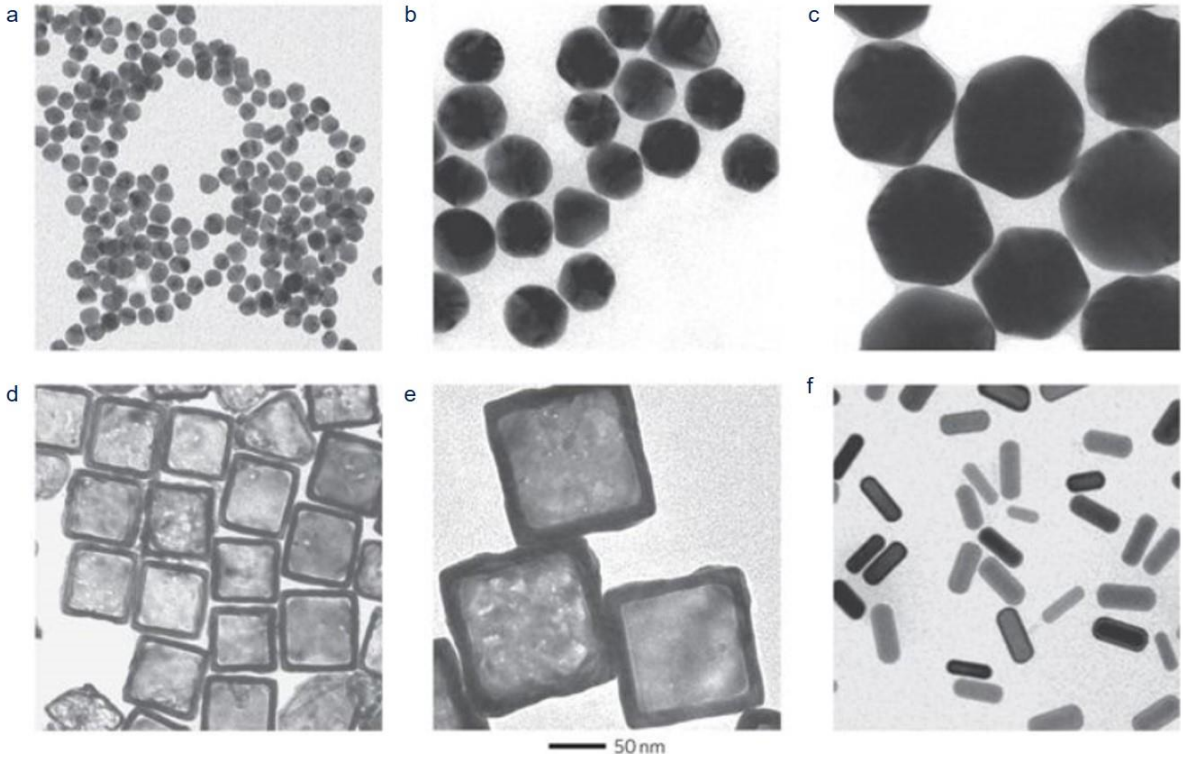

Figure 2.3-2: TEM images of NPs with different shapes; a) 15 nm (diameter) nanospheres, b) 54 nm nanospheres, c) 100 nm nanospheres, d) 62 nm (outer edge length) nanocages, e) 118 nm nanocages, f) nanorods (16 nm × 40 nm, diameter by length). The length of the scale bar corresponds to 50 nm. Reprinted from Ref. 109 with permission from Springer Nature (Nature Technology).

Using similar particle sizes but different shapes, it was reported that spherical NPs (14 or 74 nm) can easily penetrate the cells compared to rod-shaped NPs (74 x 14 nm).[115] Elongated spherical NPs have higher cellular uptakes than spherical or prism-shaped particles.[107,108] This phenomenon can be explained in terms of membrane curvature. NPs-membrane interaction induces membrane indentation; as a result, the membrane becomes wrapped around the particle. Particles with sharp edges cause unstable and unfavourable packing of the

phospholipid bilayer around the particles, as opposed to 'flat' particles.[116] In a study by Dasgupta *et al.*[117] into the correlation between NPs shape and orientation following cellular uptake, they reported two main membrane wrapping modes; submarine and rocket modes. The first (submarine) mode is predominantly seen in spherical NPs with its orientation being parallel to that of the membrane which enabled fast wrapping (lower wrapping fraction) of the membrane, thus higher NPs uptake. In the rocket mode, the long axis of the particle is perpendicular to the membrane thus enabling higher wrapping fraction yielding unfavourable or lower NPs uptake.

Differently shaped AgNPs (spherical, disk-like and triangular plate-shaped) were investigated for their antimicrobial activity against bacteria (gram-positive and negative); the authors concluded that spherical NPs had the highest antimicrobial effect on the bacteria compared to disk and triangular plate-shaped NPs.[118] They attributed the shape and surface area of the NPs to their antibacterial activity; spherical NPs were found to release more Ag^+ ions compared to the other shapes which in turn enhanced their cytotoxicity as antibacterial agents.

2.3.2. Investigating the effect of NPs surface charge

Functional groups on NPs determine the solubility of the NPs as well as their interactions with macromolecules and cell membranes, thus depending on the charge on the NPs, these particles can follow different pathways into the cells (Figure 2.3-3); cationic NPs can cause permanent destabilisation of the cell membrane via formation of pores in the membrane structure or membrane thinning whereas anionic and neutral NPs can penetrate the lipid membrane without causing major membrane disruption.[119,120]

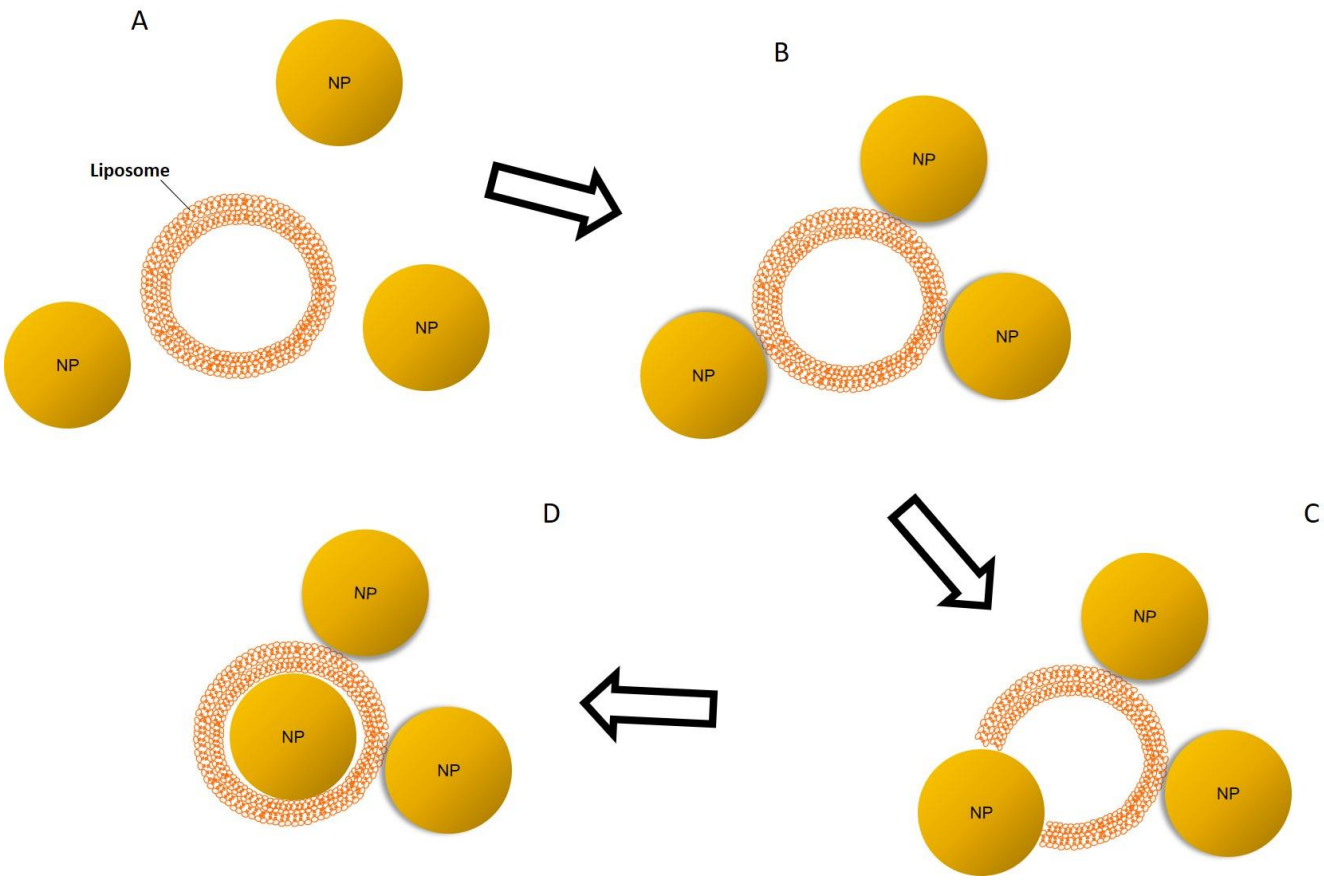

Figure 2.3-3: Schematic illustration of the various types of NPs-membrane interactions; A) charged NPs approaching liposome (surface of lipid bilayer membrane), B) adhesion of NPs onto membrane surface, C) defect (pore) formation caused by NPs and D) NP encapsulation inside liposome. Adapted from Ref. 121.

2.3.2.1. Neutral NPs

The synthesis of NPs preventing their interactions with biological macromolecules and cell membrane has been documented using neutral ligands such as PEG or zwitterionic (Zw) ligands. As a result, coating the NPs with such ligands can be used to avoid and minimise non-specific or unwanted NPs-membrane interactions thus, such interactions can diminish the effectivity of the target-specified drugs.[107,122]

PEG, an uncharged, hydrophilic polymer is found to be non-immunogenic (not able to provoke a response from the immune system). PEGylated nanomaterials tagged with a drug such as Methotrexate, was reported to yield higher level of cytoxicity as the NP-drug conjugate compared to the NP-free drug, thus making the case of their use in cancer therapy treatments as effective and efficient drug carriers.[123] Alternatively, zwitterionic ligands as capping agents

for NPs are favoured due to their ability to enhance solubility of NPs. Moreover, they are shown to yield stable NPs compared to citrate capped AuNPs in the presence of polyelectrolytes and proteins with the latter NPs showing signs of NPs aggregation.[124] Agasti *et al.*[125] have shown Zw-functionalised AuNPs as a nontoxic drug carrier, thanks to a successful photocontrolled release of anticancer drug (5-fluorouracil, 5-FU). Other examples of neutral NPs include polysaccharides[126], polymeric NPs,[127] peptides and proteins[128]; these ligands have been reported to facilitate the penetration of NPs as drug carriers into the cell without signs of membrane disruption.

PEG-functionalised AuNPs were found to have no effect on *E. coli* bacteria using the MIC test due to the non-specific interaction between the PEGylated NPs and the bacteria.[129,130] Thus, these neutral ligands aids biocompatibility and stability of the NPs as well as enabling further addition of functional groups onto the NPs.[131]

2.3.2.2. Positively charged (cationic) NPs

The interaction of positively charged (cationic) NPs with negatively charged cell membrane occurs via electrostatic attraction, facilitating the cellular uptake of the NPs over neutral or negatively charged NPs.[132] Previous findings using coarse-grained molecular dynamics simulations have shown that positively charged AuNPs interact with the phosphate head group (negatively charged part of the phospholipid molecule) of the membrane made up of Zw lipids and this type of interaction caused the altering of the tilt angle of the lipid molecules resulting to the change in the lipid's architecture. Such interactions have been reported to perturb membrane architecture, without necessarily affecting the membrane fluidity.[116,133,134]

Another way that cationic NPs interact with lipid membrane is by the NPs becoming wrapped around by the lipid membrane, forming NPs-lipid vesicles (Figure 2.3-3D). This is an interaction driven by enhanced electrostatic attraction with the hydrophobic portion of the lipid bilayer due to the high coverage of cationic charges on NPs, which results in different types of internalisation mechanisms i.e. membrane thinning, membrane rupture, defects formation in the membrane (Figure 2.3-3C) etc.[105,135] A study by Lerouile *et al.*[136] has shown that NPs

with: different shapes, sizes and flexibility; polycationic polymer (PAMAN) and amine-terminated gold and silica particles, can disrupt the lipid bilayer's architecture thus ensuring such internalisation mechanisms and altering the cell membrane permeability to enable NPs penetration into the cell. AgNPs functionalised with cationic polymers were investigated for their antibacterial effect against gram-positive and negative bacteria, the results showed that the binding of these cationic NPs was much favourable with negatively charged bacterial membrane thus far more effective at killing gram-negative bacteria.[132]

Positively charged NPs carrying cationic polymer chitosan-HCl was found to penetrate the gastrointestinal mucous barrier more easily than negatively charged NPs due to electrostatic interactions with the negatively charged cell membrane. Once inside the cell, the reduced form of the polymer, cyclosporin-A, a poorly absorbable drug on its own due to its lipophilic nature, is readily available inside the cell. This finding resulted in a recommendation of the possibility of lowering the drug dosage and consequently its side effects.[137]

2.3.2.3. Negatively charged (anionic) NPs

As we have seen, differently charged NPs do influence the NPs-membrane interactions but in different ways. Negatively charged (anionic) NPs are shown to have non-specific cellular uptake pathways as reported by Ayala *et al.*[138] after using carboxymethyl dextran-coated iron oxide NPs. Cationic NPs were reported to become engulfed within the lipid bilayer. Anionic particles on the other hand, become adsorbed at the surface of the membrane (as illustrated in Figure 2.3-3B); the subsequent absorbed NPs can form clusters at cationic sites of the plasma membrane.[107,119,139] NPs-membrane interactions with the adsorption of anionic NPs onto the membrane surface causes membrane gelation (phase transition from liquid to gel), leading to the lipid liposome (an assembly of phospholipid in a spherical manner) to shrink as seen in Figure 2.3-4.[140]

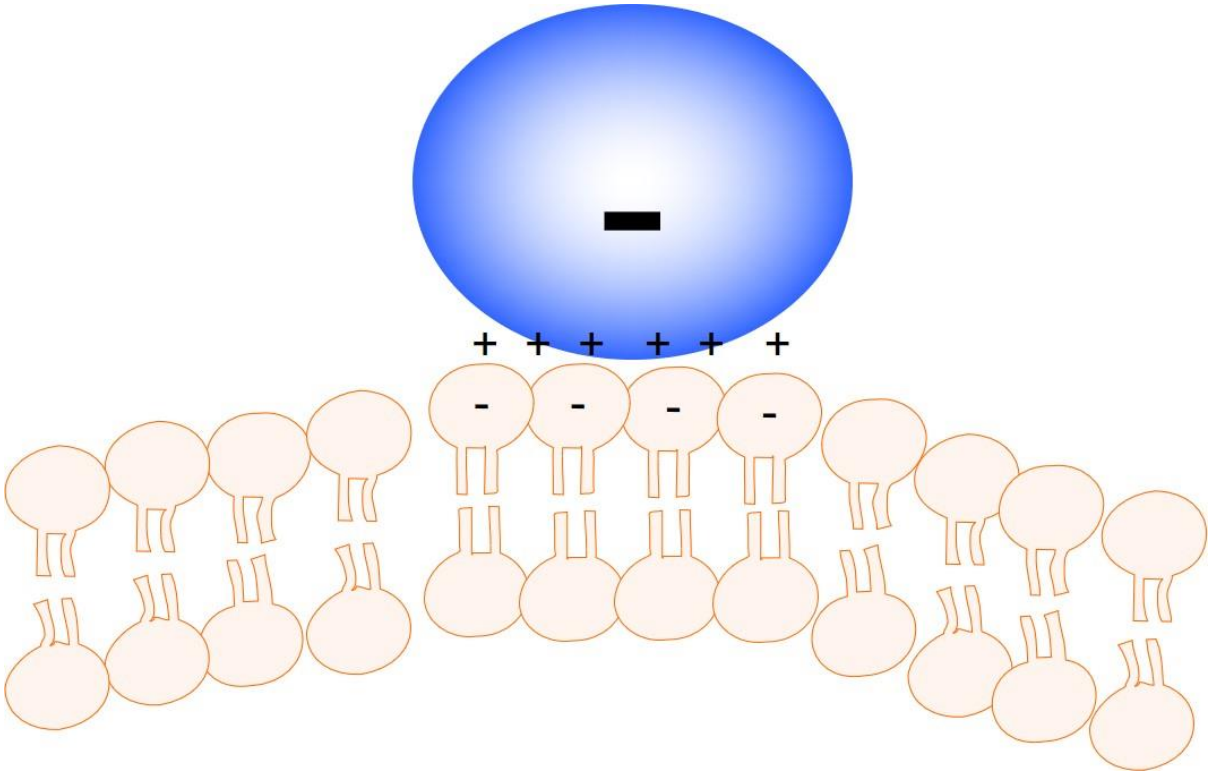

Figure 2.3-4: Membrane gelation caused by anionic NPs-membrane interactions. Adapted from Ref. 140.

However, the interaction between gram-negative bacteria and anionic NPs were found to unfavourable due to the repulsion of like charges.[141]

2.4. Focus of the thesis

The purpose of the research presented in this thesis focuses on the electrochemical characterisation of thiolated metal nanoparticles with their interaction with lipid membranes; both non-electroactive and electroative thiol-protected metal NPs. Each of the experimental chapters (chapters four, five and six) includes detailed analysis and discussion of the interactions of NPs with mimics of the cell lipid membrane. The novelty of this work lies in the interaction of ferrocenyl-thiolated metal NPs as electroactive NPs and cationic ammonium thiolated polymer metal NPs as non-electroactive NPs with cell membrane mimics, via the use of electrochemical techniques including relatively new impedance derived technique, Resonance Enhanced Surface Impedance (RESI). This novel technique allowed the monitoring in real-time the changes in RESI capacitance with the interactions of NPs with lipid membranes to be studied.

2.5. Conclusion

In conclusion, this chapter focused on providing background information on nanoparticles, lipid membranes and the type of interactions that occur when they react together; inclusive of literature reports on applications and benefits of these systems.

Following the different lipid membrane models outlined in the previous section, lipid membranes on solid substrates was chosen to be the most suitable method that would enable the execution of the research outlined in the coming chapters of the thesis. SAM and tBLM models were chosen as these permitted the use of electrochemical techniques to be carried out, being the main analytical technique of the thesis. These models were already outlined to contain advantages such as the ability to mimic part of the biological lipid bilayer membrane thus enabling the investigation of specific metallic NPs with artificial cell membranes.

In terms of metallic NPs, Au and Ag were the focus in the thesis as these metallic NPs have a wide range application within the nanomedical field. The synthetic route for AuNPs was based on the Brust-Schiffrin method to produce alkanethiol stabilised AuNPs with well-reported reliability in size, morphology and stability as colloid solutions. Alkanethiol stabilised AgNPs were synthesised using the latter method by Farrell and co-workers for the one-step synthesis of stable NPs. Following the evaluation of NPs sizes and their interactions with lipid membrane, we chose the synthetic routes that would yield small NPs with sizes <10 nm and with spherical morphology as small NPs were reported to be less destabilising to the membrane's architecture and, the uptake behaviour of spherical NPs by cells are more favourable than non-spherical NPs.

In terms of surface functionalities of the NPs, these will be at the centre of the investigations in this thesis for the interactions of alkanethiol stabilised metal NPs with both artificial and biological lipid membranes; electroactive functionalised ligands with ferrocenyl moieties, non-electroactive groups such as dodecanethiol ligands and positively charged functionalised ligands such as cationic ammonium moieties. The investigations on the interactions of these

NPs with lipid membranes would support the publications within the expanding field thiolated metallic NPs for sensing applications.

2.6. References

1 T. Cosgrove, *Colloid Science: Principles, Methods and Applications*, Wiley, 2nd edn., 2010.

2 F. T. C. Moreira, J. R. L. Guerreiro, L. Brandão and M. G. F. Sales, in *Biomimetic Technologies*, ed. T. D. Ngo, Woodhead Publishing, 2015, pp. 18–23.

3 S. E. Lohse and C. J. Murphy, *J. Am. Chem. Soc.*, 2012, **134**, 15607–15620.

4 L. Zhang, F. X. Gu, J. M. Chan, A. Z. Wang, R. S. Langer and O. C. Farokhzad, *Clin. Pharmacol. Ther.*, 2008, **83**, 761–769.

5 B. Alberts, A. Johnson, J. Lewis, M. Raff, K. Roberts and P. Walter, *Ann Bot*, 2002, **91**, 401.

6 W. Stillwell, *An Introduction to Biological Membranes: From Bilayers to Rafts*, Elsevier Science, 2013.

7 M. Pekker and M. N. Shneider, *J. Phys. Chem. Biophys.*, 2015, **5**, 1.

8 E. T. Castellana and P. S. Cremer, *Surf. Sci. Rep.*, 2006, **61**, 429–444.

9 M. Zagnoni, *Lab Chip*, 2012, **12**, 1026–1039.

10 M. Winterhalter, *Curr. Opin. Colloid Interface Sci.*, 2000, **5**, 250–255.

11 M. S. Khan, N. S. Dosoky, B. K. Berdiev and J. D. Williams, *Eur. Biophys. J.*, 2016, **45**, 843–852.

12 M. S. Khan, N. S. Dosoky and J. D. Williams, *Int. J. Mol. Sci.*, 2013, **14**, 21561–21597.

13 E. Reimhult and K. Kumar, *Trends Biotechnol.*, 2008, **26**, 82–89.

14 Y.-H. M. Chan and S. G. Boxer, *Curr. Opin. Chem. Biol.*, 2007, **11**, 581–587.

15 V. von Tscharner and H. M. McConnell, *Biophys. J.*, 1981, **36**, 409–419.

16 I. Möller and S. Seeger, *J. Mater. Chem. B*, 2015, **3**, 6046–6056.

17 R. Naumann, S. M. Schiller, F. Giess, B. Grohe, K. B. Hartman, I. Kärcher, I. Köper, J. Lübben, K. Vasilev and W. Knoll, *Langmuir*, 2003, **19**, 5435–5443.

18 R. P. Richter, R. Bérat and A. R. Brisson, *Langmuir*, 2006, **22**, 3497–3505.

19 R. P. Richter and A. R. Brisson, *Biophys. J.*, 2005, **88**, 3422–3433.

20 I. Reviakine and A. Brisson, *Langmuir*, 2000, **16**, 1806–1815.

21 I. Gözen and A. Jesorka, *Anal. Chem.*, 2012, **84**, 822–838.

22 J. Andersson and I. Köper, *Membranes (Basel).*, 2016, **6**, 30.

23 A. Hasan and L. M. Pandey, in *Nanobiomaterials*, ed. R. Narayan, Woodhead Publishing, 2018, pp. 137–178.

24 M. Boeckl and D. Graham, *Mater. matters*, 2006, **1**, 3–5.

25 J. C. Love, L. A. Estroff, J. K. Kriebel, R. G. Nuzzo and G. M. Whitesides, *Chem. Rev.*, 2005, **105**, 1103–1170.

26 C. D. Bain, E. B. Troughton, Y. T. Tao, J. Evall, G. M. Whitesides and R. G. Nuzzo, *J. Am. Chem. Soc.*, 1989, **111**, 321–335.

27 G. Haehner, C. Woell, M. Buck and M. Grunze, *Langmuir*, 1993, **9**, 1955–1958.

28 A. Ulman, J. E. Eilers and N. Tillman, *Langmuir*, 1989, **5**, 1147–1152.

29 X. Han, K. Critchley, L. Zhang, S. N. D. Pradeep, R. J. Bushby and S. D. Evans, *Langmuir*, 2007, **23**, 1354–1358.

30 A. L. Plant, M. Brighamburke, E. C. Petrella and D. J. Oshannessy, *Anal. Biochem.*, 1995, **226**, 342–348.

31 A. Kilic and F. N. Kok, *Surf. Innov.*, 2016, **4**, 141–157.

32 J. Jackman, W. Knoll and N.-J. Cho, *Materials (Basel).*, 2012, **5**, 2637–2657.

33 S. M. Schiller, R. Naumann, K. Lovejoy, H. Kunz and W. Knoll, *Angew. Chemie Int. Ed.*, 2003, **42**, 208–211.

34 H. Lang, C. Duschl, M. Grätzel and H. Vogel, *Thin Solid Films*, 1992, **210**–**211**, 818–821.

35 H. Lang, C. Duschl and H. Vogel, *Langmuir*, 1994, **10**, 197–210.

36 L. Santesson, T. M. H. Wong, M. Taborelli, P. Descouts, M. Liley, C. Duschl and H. Vogel, *J. Phys. Chem.*, 1995, **99**, 1038–1045.

37 S. Lingler, I. Rubinstein, W. Knoll and A. Offenhäusser, *Langmuir*, 1997, **13**, 7085–7091.

38 W. Knoll, I. Köper, R. Naumann and E.-K. Sinner, *Electrochim. Acta*, 2008, **53**, 6680–6689.

39 S.-K. Lee, L. G. Cascão-Pereira, R. F. Sala, S. P. Holmes, K. J. Ryan and T. Becker, *Ind. Biotechnol.*, 2005, **1**, 26–31.

40 A. Kılıç, M. Fazeli Jadidi, H. Ö. Özer and F. N. Kök, *Colloids Surfaces B Biointerfaces*, 2017, **160**, 117–125.

41 E. Roduner, *Chem. Soc. Rev.*, 2006, **35**, 583–592.

42 S. Horikoshi and N. Serpone, in *Microwaves in Nanoparticle Synthesis*, Wiley-VCH Verlag GmbH & Co. KGaA, 2013, pp. 1–24.

43 V. V Mody, R. Siwale, A. Singh and H. R. Mody, *J. Pharm. Bioallied Sci.*, 2010, **2**, 282–289.

44 T. M. Carducci, R. E. Blackwell and R. W. Murray, *J. Am. Chem. Soc.*, 2014, **136**, 11182–11187.

45 V. Amendola, R. Pilot, M. Frasconi, O. M. Maragò and M. A. Iatì, *J. Phys. Condens. Matter*, 2017, **29**, 203002.

46 D. Pissuwan, T. Niidome and M. B. Cortie, *J. Control. Release*, 2011, **149**, 65–71.

47 A. C. Templeton, W. P. Wuelfing and R. W. Murray, *Acc. Chem. Res.*, 2000, **33**, 27–36.

48 G. H. Woehrle, L. O. Brown and J. E. Hutchison, *J. Am. Chem. Soc.*, 2005, **127**, 2172–2183.

49 T. L. Doane and C. Burda, *Chem. Soc. Rev.*, 2012, **41**, 2885–2911.

50 D. A. Giljohann, D. S. Seferos, W. L. Daniel, M. D. Massich, P. C. Patel and C. A. Mirkin, *Angew. Chem. Int. Ed*, 2010, **49**, 3280–3294.

51 H. Bahadar, F. Maqbool, K. Niaz and M. Abdollahi, *Iran. Biomed. J.*, 2016, **20**, 1–11.

52 L. B. Hunt, *Gold Bull.*, 1976, **9**, 134–139.

53 L. Wei, J. Lu, H. Xu, A. Patel, Z.-S. Chen and G. Chen, *Drug Discov. Today*, 2015, **20**, 595–601.

54 R. A. Sperling and W. J. Parak, *Philos. Trans. R. Soc. A Math. Phys. Eng. Sci.*, 2010, **368**, 1333–1383.

55 A. Biswas, I. S. Bayer, A. S. Biris, T. Wang, E. Dervishi and F. Faupel, *Adv. Colloid Interface Sci.*, 2012, **170**, 2–27.

56 V. M. Arole and S. V Munde, *J. Mater. Sci.*, 2014, **1**, 89–93.

57 Z. Guo and L. Tan, *Fundamentals and applications of nanomaterials*, Artech House, 2009.

58 P. G. Jamkhande, N. W. Ghule, A. H. Bamer and M. G. Kalaskar, *J. Drug Deliv. Sci. Technol.*, 2019, **53**, 101174.

59 I. Khan, K. Saeed and I. Khan, *Arab. J. Chem.*, , DOI:https://doi.org/10.1016/j.arabjc.2017.05.011.

60 J. Turkevich, P. C. Stevenson and J. Hillier, *Discuss. Faraday Soc.*, 1951, **11**, 55–75.

61 M. Brust, M. Walker, D. Bethell, D. J. Schiffrin and R. Whyman, *J. Chem. Soc. Chem. Commun.*, 1994, 801–802.

62 G. Frens, *Nat. Phys. Sci.*, 1973, **241**, 20.

63 J. Kimling, M. Maier, B. Okenve, V. Kotaidis, H. Ballot and A. Plech, *J. Phys. Chem. B*, 2006, **110**, 15700–15707.

64 P. C. Lee and D. Meisel, *J. Phys. Chem.*, 1982, **86**, 3391–3395.

65 P. Hildebrandt and M. Stockburger, *J. Phys. Chem.*, 1984, **88**, 5935–5944.

66 T. Dadosh, *Mater. Lett.*, 2009, **63**, 2236–2238.

67 Y. A. Krutyakov, A. A. Kudrinskiy, A. Y. Olenin and G. V Lisichkin, *Russ. Chem. Rev.*, 2008, **77**, 233–257.

68 M. Brust, J. Fink, D. Bethell, D. J. Schiffrin and C. Kiely, *J. Chem. Soc. Chem. Commun.*, 1995, 1655–1656.

69 S. Murthy, T. P. Bigioni, Z. L. Wang, J. T. Khoury and R. L. Whetten, *Mater. Lett.*, 1997, **30**, 321–325.

70 S. Y. Kang and K. Kim, *Langmuir*, 1998, **14**, 226–230.

71 Z. Farrell, C. Shelton, C. Dunn and D. Green, *Langmuir*, 2013, **29**, 9291–9300.

72 A. K. San and Y.-S. Shon, *Nanomaterials*, 2018, **8**, 346.

73 Y.-S. Shon and E. Cutler, *Langmuir*, 2004, **20**, 6626–6630.

74 Y.-S. Shon, S. M. Gross, B. Dawson, M. Porter and R. W. Murray, *Langmuir*, 2000, **16**, 6555–6561.

75 E. Sadeghmoghaddam, C. Lam, D. Choi and Y.-S. Shon, *J. Mater. Chem.*, 2011, **21**, 307–312.

76 K. A. San, V. Chen and Y.-S. Shon, *ACS Appl. Mater. Interfaces*, 2017, **9**, 9823–9832.

77 D. J. Gavia, Y. Do, J. Gu and Y.-S. Shon, *J. Phys. Chem. C*, 2014, **118**, 14548–14554.

78 N. Yu, Z. Wang, J. Zhang, Z. Liu, B. Zhu, J. Yu, M. Zhu, C. Peng and Z. Chen, *Biomaterials*, 2018, **161**, 279–291.

79 N. Zheng, J. Fan and G. D. Stucky, *J. Am. Chem. Soc.*, 2006, **128**, 6550–6551.

80 E. J. Cho, H. Holback, K. C. Liu, S. A. Abouelmagd, J. Park and Y. Yeo, *Mol. Pharm.*, 2013, **10**, 2093–2110.

81 P.-C. Lin, S. Lin, P. C. Wang and R. Sridhar, *Biotechnol. Adv.*, 2014, **32**, 711–726.

82 J. M. Costa-Fernández, M. Menéndez-Miranda, D. Bouzas-Ramos, J. R. Encinar and A. Sanz-Medel, *TrAC Trends Anal. Chem.*, 2016, **84**, 139–148.

83 M. A. Gatoo, S. Naseem, M. Y. Arfat, A. Mahmood Dar, K. Qasim and S. Zubair, *Biomed Res. Int.*

84 N. N. Long, L. Van Vu, C. D. Kiem, S. C. Doanh, C. T. Nguyet, P. T. Hang, N. D. Thien and L. M. Quynh, *J. Phys. Conf. Ser.*, 2009, **187**, 012026.

85 A. K. Kohli and H. O. Alpar, *Int. J. Pharm.*, 2004, **275**, 13–17.

86 A. P. Nikalje, *Med chem*, 2015, **5**, 81–89.

87 A. Sharma, A. K. Goyal and G. Rath, *J. Drug Target.*, 2018, **26**, 617–632.

88 D. S. Shewach and R. D. Kuchta, *Chem. Rev.*, 2009, **109**, 2859–2861.

89 M. Singh, S. Manikandan and A. K. Kumaraguru, *Res. J. Nanosci. Nanotechnol.*, 2011, **1**, 1–11.

90 A. M. Ealias and M. P. Saravanakumar, in *14th ICSET-2017*, IOP Conf. Ser. Mater. Sci.

Eng., 2017, vol. 263.

91 J. K. Patra, G. Das, L. F. Fraceto, E. V. R. Campos, M. del P. Rodriguez-Torres, L. S. Acosta-Torres, L. A. Diaz-Torres, R. Grillo, M. K. Swamy, S. Sharma, S. Habtemariam and H.-S. Shin, *J. Nanobiotechnology*, 2018, **16**, 71.

92 I. Brigger, C. Dubernet and P. Couvreur, *Adv. Drug Deliv. Rev.*, 2012, **64**, 24–36.

93 B. Yogesh, B. Vineeta, N. Rammesh and P. Saili, *J. pharmacopuncture*, 2016, **19**, 114.

94 K. Sztandera, M. Gorzkiewicz and B. Klajnert-Maculewicz, *Mol. Pharm.*, 2019, **16**, 1–23.

95 L. Zou, H. Wang, B. He, L. Zeng, T. Tan, H. Cao, X. He, Z. Zhang, S. Guo and Y. Li, *Theranostics*, 2016, **6**, 762–772.

96 L. R. Hirsch, R. J. Stafford, J. A. Bankson, S. R. Sershen, B. Rivera, R. E. Price, J. D. Hazle, N. J. Halas and J. L. West, *Proc. Natl. Acad. Sci.*, 2003, **100**, 13549.

97 N. P. Praetorius and T. K. Mandal, *Recent Pat. Drug Deliv. Formul.*, 2007, **1**, 37–51.

98 G. Liu and Y. Lin, *Talanta*, 2007, **74**, 308–17.

99 M. Aioub, L. A. Austin and M. A. El-Sayed, in *Inorganic Frameworks as Smart Nanomedicines*, ed. A. M. Grumezescu, William Andrew Publishing, 2018, pp. 41–91.

100 B. Asadishad, M. Vossoughi and I. Alemzadeh, *Ind. Eng. Chem. Res.*, 2010, **49**, 1958–1963.

101 A. Nirmala Grace and K. Pandian, *Colloids Surfaces A Physicochem. Eng. Asp.*, 2007, **297**, 63–70.

102 L. Zhang, M. Becton and X. Wang, *J. Phys. Chem. B*, 2015, **119**, 3786–3794.

103 B. Duncan, C. Kim and V. M. Rotello, *J. Control. Release*, 2010, **148**, 122–7.

104 M. Schulz, A. Olubummo and W. H. Binder, *Soft Matter*, 2012, **8**, 4849.

105 V. V. Ginzburg and S. Balijepalli, *Nano Lett.*, 2007, **7**, 3716–3722.

106 P. R. Leroueil, S. Hong, A. Mecke, J. R. Baker, B. G. Orr and M. M. B. Holl, *Acc. Chem. Res.*, 2007, **40**, 335–342.

107 A. Verma and F. Stellacci, *Small*, 2010, 6, 12–21.

108 S. Salatin, S. Maleki Dizaj and A. Yari Khosroushahi, *Cell Biol. Int.*, 2015, **39**, 881–890.

109 Y. Roiter, M. Ornatska, A. R. Rammohan, J. Balakrishnan, D. R. Heine and S. Minko, *Nano Lett.*, 2008, **8**, 941–944.

110 S.-H. Park, S.-G. Oh, J.-Y. Mun and S.-S. Han, *Colloids Surfaces B Biointerfaces*, 2006, **48**, 112–118.

111 C. M. Bailey, E. Kamaloo, K. L. Waterman, K. F. Wang, R. Nagarajan and T. a. Camesano, *Biophys. Chem.*, 2015, **203**–**204**, 51–61.

112 A. Ivask, I. Kurvet, K. Kasemets, I. Blinova, V. Aruoja, S. Suppi, H. Vija, A. Käkinen, T. Titma, M. Heinlaan, M. Visnapuu, D. Koller, V. Kisand and A. Kahru, *PLoS One*, 2014, **9**, e102108.

113 Z. Lu, K. Rong, J. Li, H. Yang and R. Chen, *J. Mater. Sci. Mater. Med.*, 2013, **24**, 1465–1471.

114 D. H. Kim, J. C. Park, G. E. Jeon, C. S. Kim and J. H. Seo, *Biotechnol. Bioprocess Eng.*, 2017, **22**, 210–217.

115 B. D. Chithrani, A. A. Ghazani and W. C. W. Chan, *Nano Lett.*, 2006, **6**, 662–668.

116 T. Tree-Udom, J. Seemork, K. Shigyou, T. Hamada, N. Sangphech, T. Palaga, N. Insin, P. Pan-In and S. Wanichwecharungruang, *ACS Appl. Mater. Interfaces*, 2015, **7**, 23993–24000.

117 S. Dasgupta, T. Auth and G. Gompper, *Nano Lett.*, 2014, **14**, 687–693.

118 J. Y. Cheon, S. J. Kim, Y. H. Rhee, O. H. Kwon and W. H. Park, *Int. J. Nanomedicine*, 2019, **14**, 2773–2780.

119 J. Lin, H. Zhang, Z. Chen and Y. Zheng, *ACS Nano*, 2010, **4**, 5421–5429.

120 C. M. Goodman, C. D. McCusker, T. Yilmaz and V. M. Rotello, *Bioconjug. Chem.*, 2004, **15**, 897–900.

121 P. B. Santhosh, A. Velikonja, Š. Perutkova, E. Gongadze, M. Kulkarni, J. Genova, K. Eleršič, A. Iglič, V. Kralj-Iglič and N. P. Ulrih, *Chem. Phys. Lipids*, , DOI:10.1016/j.chemphyslip.2013.11.009.

122 G. Rossi and L. Monticelli, *Adv. Phys. X*, 2016, **1**, 276–296.

123 N. Kohler, C. Sun, A. Fichtenholtz, J. Gunn, C. Fang and M. Zhang, *Small*, 2006, **2**, 785–792.

124 L. L. Rouhana, J. A. Jaber and J. B. Schlenoff, *Langmuir*, 2007, **23**, 12799–12801.

125 S. S. Agasti, A. Chompoosor, C. C. You, P. Ghosh, C. K. Kim and V. M. Rotello, *J. Am. Chem. Soc.*, 2009, **131**, 5728–5729.

126 C. Lemarchand, R. Gref and P. Couvreur, *Eur. J. Pharm. Biopharm.*, 2004, 58, 327–341.

127 K. Yin Win and S.-S. Feng, *Biomaterials*, 2005, **26**, 2713–2722.

128 M. Morishita and N. A. Peppas, *Drug Discov. Today*, 2006, **11**, 905–910.

129 R. P. Allaker and Z. Yuan, in *Nanobiomaterials in Clinical Dentistry (Second Edition)*, eds. K. Subramani and W. Ahmed, Elsevier, 2019, pp. 243–275.

130 D. N. Williams, S. H. Ehrman and T. R. Pulliam Holoman, *J. Nanobiotechnology*, 2006, **4**, 3.

131 N. N. Mahmoud, A. A. Alhusban, J. I. Ali, A. G. Al-Bakri, R. Hamed and E. A. Khalil, *Sci.*

Rep., 2019, **9**, 5796.

132 A. Gupta, S. Mumtaz, C.-H. Li, I. Hussain and V. M. Rotello, *Chem. Soc. Rev.*, 2019, **48**, 415–427.

133 A. Velikonja, P. B. Santhosh, E. Gongadze, M. Kulkarni, K. Eleršič, Š. Perutkova, V. Kralj-Iglič, N. P. Ulrih and A. Iglič, *Int. J. Mol. Sci.*, 2013, **14**, 15312–15329.

134 Y. Li and N. Gu, *J. Phys. Chem. B*, 2010, **114**, 2749–2754.

135 P. B. Santhosh, S. Peni?, J. Genova, A. Igli?, V. Kralj-Igli? and N. P. Ulrih, *J. Phys. Conf. Ser.*, , DOI:10.1088/1742-6596/398/1/012034.

136 P. R. Leroueil, S. A. Berry, K. Duthie, G. Han, V. M. Rotello, D. Q. McNerny, Baker James R., B. G. Orr and M. M. Banaszak Holl, *Nano Lett.*, 2008, **8**, 420–424.

137 M. . El-Shabouri, *Int. J. Pharm.*, 2002, **249**, 101–108.

138 V. Ayala, A. P. Herrera, M. Latorre-Esteves, M. Torres-Lugo and C. Rinaldi, *J. Nanoparticle Res.*, 2013, **15**, 1874.

139 C. Wilhelm, F. Gazeau, J. Roger, J. N. Pons and J. C. Bacri, *Langmuir*, 2002, **18**, 8148–8155.

140 B. Wang, L. Zhang, S. C. Bae and S. Granick, *Proc. Natl. Acad. Sci. U. S. A.*, 2008, **105**, 18171–18175.

141 Z. Li, J. Ma, J. Ruan and X. Zhuang, *Nanoscale Res. Lett.*, 2019, **14**, 195.

3. Experimental Methods & Techniques

Sections 3.1 and 3.2 of this chapter give details of the experimental materials and methodology used in the research; including a list of materials, chemicals and outlined procedures employed in the preparations of the nanoparticles, lipid solutions and substrate materials used. The theoretical background of each technique used is outlined in Section 3.3., including an overview of each technique and instrumentation as well as details of the experimental parameters.

3.1. Materials

3.1.1. Chemicals and Reagents

2-oleoyl-1-palmityol-sn-glycero-3-phosphocholine (POPC), 1-dodecanethiol (DDT), 6-(Ferrocenyl)hexanethiol (FcHT), hydrogen tetrachloroaute ($HAuCl_4$), sodium borohydride ($NaBH_4$), tetraoctylammonium bromide (TOAB), silver nitrate ($AgNO_3$), hydrogen peroxide (H_2O_2), sulfuric acid (H_2SO_4), potassium ferrocyanide ($K_4[Fe(CN)_6]$), potassium ferricyanide ($K_3[Fe(CN)_6]$), potassium phosphate monobasic (KH_2PO_4), potassium phosphate dibasic (K_2HPO_4), hydrochloric acid (HCl), potassium nitrate (KNO_3), Lysogeny broth (LB), hexane, ethanol (EtOH), toluene were purchased from Sigma-Aldrich, Oxoid Iso-Sensitest Broth purchased from Thermo Scientific and 1,2-dipalmitoyl-sn-glycero-3-phosphothioethanol (DPPTE, INstruchemie, the Netherlands).

All solvents used were without purification and all solutions were made with purified (resistivity > 18.2 MΩ cm) water from a Sartorius Atrium Comfort I water purifying system.

3.2. Methodology

3.2.1. Preparations of the nanoparticles

3.2.1.1. Synthesis of DDT stabilised silver nanoparticles

DDT-capped AgNPs were synthesised using a modified method reported by Farrell *et al.*[1] An ethanoic solution of $NaBH_4$ (0.4 M, 50 mL) was mixed with DDT (1013 µl), $AgNO_3$ (30 mM, 30 mL) was added in drops to the stirred mixture, turning the solution from misty white to dark orange then dark brown as all $AgNO_3$ was added. The mixture was stirred vigorously for one hour at room temperature. The crude product was obtained by centrifuging at 90 000 rpm for 50 min, then the supernatant was decanted and replaced with fresh ethanol (EtOH). The centrifugation and EtOH wash steps were repeated three times. The NPs were re-dispersed in 10 mL EtOH for storage at 4 °C.

3.2.1.2. Synthesis of DDT stabilised gold nanoparticles

DDT-protected AuNPs were synthesised using the Brust–Schiffrin method[2]. $HAuCl_4$ (30 mM, 30 ml) was mixed with TOAB solution (made up in toluene, 50 mM, 80 ml) and stirred vigorously for 30 min; the colour change observed was from yellow ($HAuCl_4$) to red as TOAB was added. The organic layer was separated from the mixture and 0.17g DDT was added to the organic phase to make up the mole ratio 1(Au):2(thiol). A fresh solution of $NaBH_4$ (0.4 M, 25 ml) was added slowly in drops to the mixture with vigorous stirring for 3 hrs, changing the mixture colour to dark red. The organic was separated from the mixture, the solvent was removed using the rotary evaporator and 400 ml of ethanol was added to the flask and kept at -18˚C overnight. The crude product was obtained by centrifugation at 9000 rpm for 50 min as very little precipitate was formed during the overnight process then the solvent was decanted, the final product was then dissolved in 10 ml toluene for storage at 4 °C.

3.2.2. Modification of the nanoparticles by ligand-place exchange reaction

Ligand-capped AuNPs can be used as template to introduce other functionalities to the metal surface in order to obtain the desired applications whether it is as a catalyst or for biomedical

purposes. The functionalisation of ligand-capped AuNPs such as thiolate ligands on AuNPs can be achieved by changing the functional groups of the AuNPs in order to give rise to different properties; ligand place-exchange[3], polymerisation and coupling reactions[4] are some of the methods used to functionalise AuNPs.

During ligand place-exchange, the alkanetholiate stabilised AuNP in solution is mixed with the new ligand causing it to be incorporated onto the surface of the metal core and the displaced thiolate becomes their own thiol molecules in the solution. The exchange of thiol ligands during the reaction can be affected by the bulkiness of the functional group as well as the chain length of both the protecting and the incoming ligands[5]; short chain of thiolated AuNPs are readily displaced by long chain thiolated AuNPs, this is due to the tight packing of long chain thiols on AuNPs resulting in more stable coating of the thiol ligands on the metal surface thus improving the protection of the AuNPs[3].

In our case, DDT ligands (long chain, non-electroactive thiol) were replaced by FcHT ligands (short chain, electroactive thiol). The DDT-capped metal NPs were modified with 10 mM FcHT in EtOH or toluene to make FcHT-metal NPs.[5] In order to modify the DDT-capped metal NPs with FcHT, equal volumes of metal NPs colloid and 10 mM FcHT in EtOH or toluene were shaken on a vortex stirrer for 48 hours, centrifuged for 20 min and removing the supernatant and the crude product was re-dissolved in 5 mL EtOH or toluene.

3.2.3. Preparations of the organic lipid solutions

DPPTE received in powder form, was dissolved in chloroform (25 mg/mL) and stored at -20 °C for further use, this procedure prevented the oxidation of the lipid stock solution.[6] For each preparation of the lipid solution (1 mM), the solution was dried in a clean glass vial under N_2 stream, and re-dissolved in ethanol (1 ml) and stored in the fridge until use.[7]

POPC received as a lipid solution in chloroform, was dried in a clean glass vial under N_2 stream then the vial was left in a desiccator overnight to remove any remaining solvent. The dry lipid was rehydrated using phosphate buffer solution (PBS, 0.1 M) making lipid

concentration of 1 mg/ml. For POPC lipid vesicles to form, the solution was sonicated for 45 min. All lipid solutions were stored at 4 °C until use.

3.2.4. Preparations of the substrates

3.2.4.1. Preparing glass substrates using electron-beam evaporation

Glass microscope slides were used as substrates in AFM experiments. These were chemically cleaned by immersion in different solutions then sonicated for 15 min at each step; acetone, propanol, a mixture of decon90 and deionised water (1:3 ratio) and deionised water. The substrates were then blow dried with pure N_2. Gold substrates were prepared by evaporating 100 nm of gold thin film on a glass slide with 10 nm chromium layer for adhesion using an electron-beam (e-beam) evaporator.

3.2.4.2. Cleaning of commercial electrodes

Macroelectrodes

Commercially bought gold electrodes (BASi) were polished with diamond polish slurries in a figure-eight pattern, and then sonicated with ethanol and water for 10 min, soaked in piranha solution (mixture of H_2SO_4 and H_2O_2 at 3:1 volume ratio) for 5 min followed by another sonication in water for 10 min then drying with N_2 gas. Further cleaning was carried out in an electrochemical cell with cyclic voltammetry (CV) in 1.0 M H_2SO_4 between 0 and 1.4 V (vs. Ag/AgCl reference electrode) at a scan rate of 0.1 V/s until a stable voltammogram was obtained.

Micrux and RESI sensors

Micrux sensors were cleaned according to the manufacturer's guidelines; 10 Cyclic Voltammetry cycles in a solution of 0.5 M H_2SO_4 between 0 and 0.8 V at scan rate of 0.1 V/s, these sensors were of single use.[8]

RESI sensors were cleaned by UV-ozone exposure on for 10 min followed by Milli-Q water rinse.

QCM electrodes

Commercially available EQCM sensors; 6 MHz gold-coated crystals (Metrohm, UK) were cleaned according to the manufacturer's guidelines; immersion of sensors in piranha solution (30% H_2O_2 and 70% concentration H_2SO_4) for 1 min followed by a rinse with deionised water, N_2 air drying.[9] Further cleaning was done with CV cycles in a solution of 0.5 M H_2SO_4 between 0 and 0.8 V at scan rate of 0.1 V/s, these sensors were of single use.

3.2.5. Modification of the substrates with lipid thiolated SAM on electrode surface

3.2.5.1. Spontaneous assembly of lipid SAM on electrode surfaces

Clean sensor chips (for RESI experiments), gold substrates (for AFM experiments) and gold macroelectrodes were firstly modified with the SAM lipid solution by self-assembly for 48 hours at 4 °C.[7] Any loose thiols on the electrode surface were removed by rinsing with ethanol and water and, dried under a stream of argon.

3.2.5.2. Electrochemical deposition of lipid thiolated SAM on electrode surfaces

A thiol solution was deposited on gold electrode surfaces following the procedure outlined by Brett *et al.*[10]; clean QCM electrodes were fitted into the cell filled with a mixture solution of thiol lipids dissolved in EtOH (1 mM, DPPTE) and 0.1 M KNO_3. For the adsorption of thiol molecules on gold electrodes to take place, a potential of 0.6 V was held at the working electrode for 45 min using chronoamperometry technique.[10] the electrochemical set up was that of a 3-electrode set up with a Pt flag as counter electrode and Pt wire as pseudo-reference electrode and the QCM crystal as the working electrode. At the end of the run, the electrodes were rinsed with ethanol to get rid of any loose thiols, then with deionised water and air dried with N_2 gas.

3.2.5.3. Overnight immersion of SAMs into POPC lipid solutions

The hydrophobic SAM (DPPTE) layer on gold electrodes was prepared as mentioned in section 3.2.3. The SAM modified electrodes were immersed in a prepared solution of POPC lipid vesicles (see section 3.2.3) and the tBLM layer was left to form overnight by vesicles

fusion process.[11] All macroelectrodes (BASi electrodes) were modified in the same way as described above.

3.2.6. Minimum Inhibitory Concentration (MIC) assay

The MIC assay was adapted from Andrews[12] work, to determine bacterial resistance or to test the efficacy of various antimicrobials on microorganisms.

3.2.6.1. Overnight preparation of the bacterial culture

Cultures were prepared by streaking *E. coli* from frozen stocks onto Lysogeny broth (LB) agar plates with an inoculation loop and incubated overnight with shaking at 37 °C. A single, isolated colony was selected and transferred to a 15 mL Falcon tube containing 5 mL if Iso-Sensitest broth and incubated at 37 °C with shaking overnight.

3.2.6.2. MIC procedure by serial dilutions

50 mL of the overnight culture of *E. coli* was added to 2 mL of Iso-Sensitest broth in a sterile semi-micro cuvette and covered with parafilm. The culture was grown at 35-37 °C with shaking until an absorbance of 0.07 at 650 nm was reached, then the cuvette was placed in ice. The culture was diluted ten-fold in fresh broth then mixed, by inverting the tube and kept on ice. Serial dilutions of the NPs were made; where the concentration reduced by half down the series for each antimicrobial solution with the bacteria media. Figure 3.2-1 shows an illustration of a typical plate layout for the determination of MIC. Plates were incubated for approximately 16 hours with shaking at 120 – 130 rpm in a 37 °C incubator.

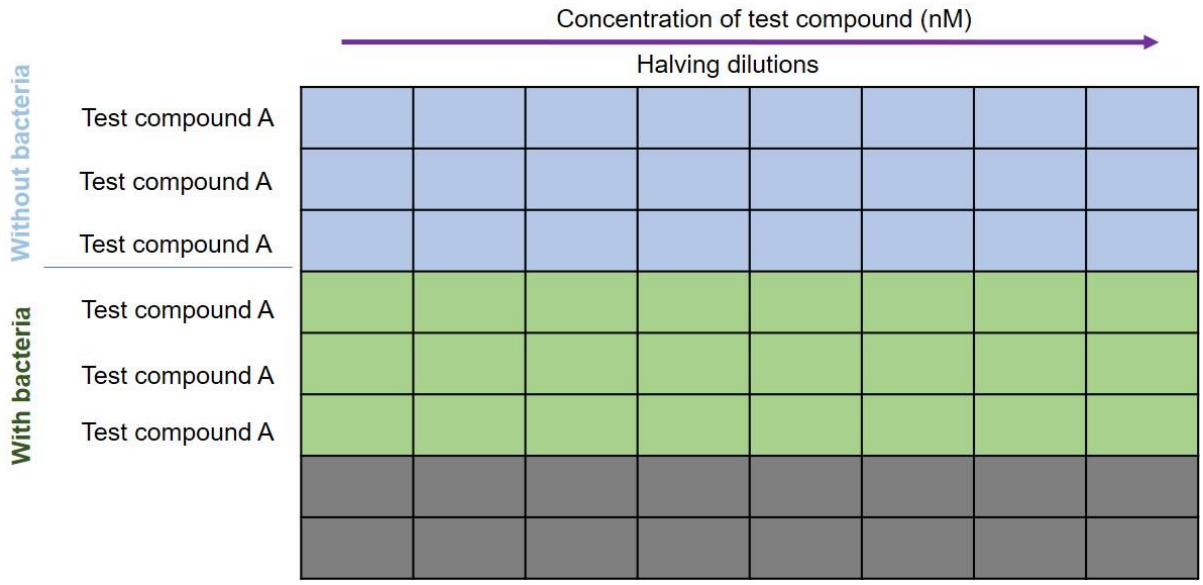

Figure 3.2-1: A typical plate layout for MIC determination.

3.3. Instrumentation and Techniques

3.3.1. Transmission Electron Microscopy

Transmission Electron Microscopy (TEM) works in similar concept as light microscope but it uses electron beam as 'light source' instead of light resulting in higher degrees of magnification (due to a higher voltage applied to the electromagnetic lenses) and resolution (due to shorter wavelength of electron beam than visible light) compared to light microscope.[13]

In this technique, electron beam in a vacuum (necessary for electrons not to be deflected by gas molecules) passes through the sample which seats on a copper grid. In order to produce an image, the electron beam from the electron gun is focused by the condenser lens onto a thin foil specimen.[14] As the electron beam hits the specimen, depending on its thickness and electron transparency, the electron beam can be either transmitted, absorbed or backscattered.[15] The transmitted beam is then focused by the electromagnetic objective lens, which collects the scattered electrons onto a single point, then the projector lens magnifies the image that can be seen onto a screen.[16] The image is formed either as an electron micrograph or it is seen in a screen using charge coupled device (CCD) camera.

Some limitations of this technique include the inability to observe live organisms as the whole system needs to be in a vacuum, the lack of colour with the image created and for nanoparticles characterisation, these can become unstable under electron beam.[17]

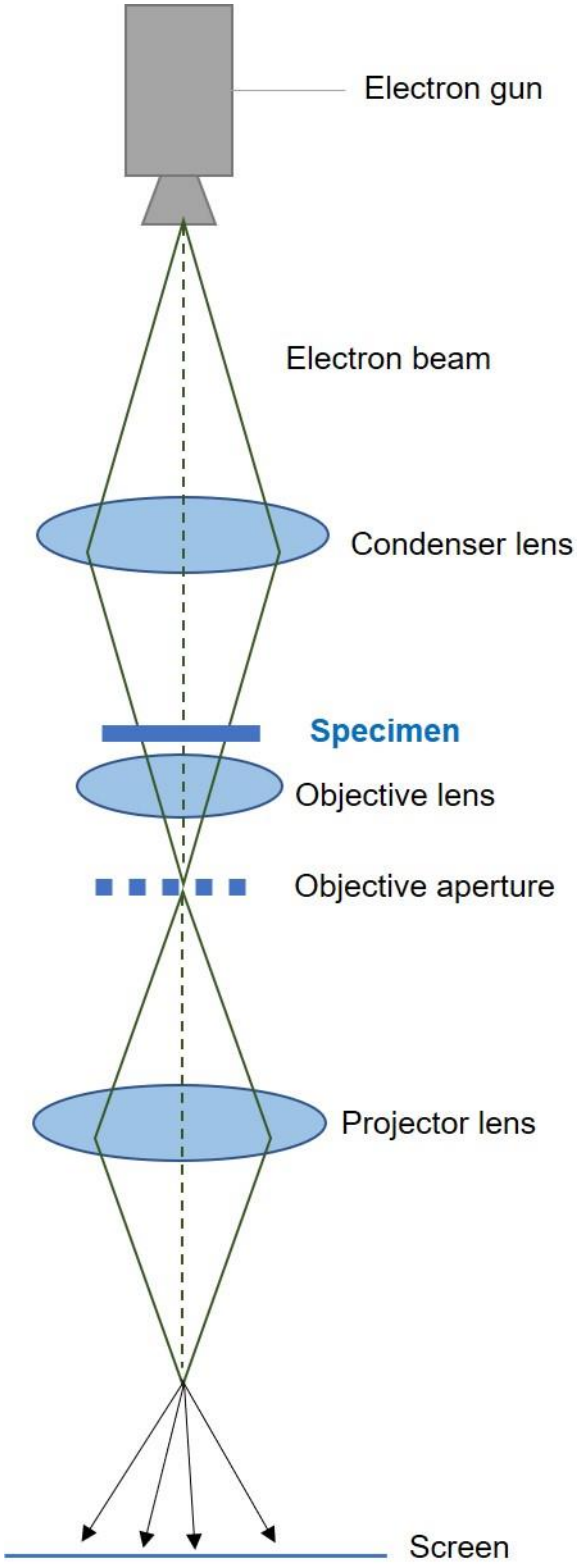

Figure 3.3-1: An illustration for the basic set up of TEM.

Transmission electron microscopy (TEM; JEOL 2100F FEG TEM) was used to determine the particle size, uniformity and morphology of the NPs. TEM samples were prepared by air drying TEM grids made from copper mesh pipetted with droplets of the colloid solutions. ImageJ

software was used to do particle size determination measure with a minimum of 150 particles.

3.3.2. Atomic Force Microscopy

Atomic Force Microscopy (AFM) is part of the family of scanning probe microscopy, in this technique the topography of the specimen is measured providing 3D imaging as well as physical properties of the sample (height, friction etc.).[18] Unlike other microscopy techniques which uses light beam to generate images, AFM uses force between the very sharp tip on the cantilever and the surface of the sample to give high resolution images.

This technique is carried out by measuring the interactions between the tip and the sample by monitoring the movement of the tip. The sample is placed on a piezoelectric scanner, and a feedback loop controls the height of the tip above the sample's surface. Coupling with the use of an optical method, laser beam is focused on the tip and any deflections at the cantilever (towards or away from the sample) are detected by a photodiode; different features (bumps or flat areas) on the sample will influence the deflections of the cantilever thus generating an accurate topographic map of the sample.[19]

Some advantages of AFM include accurate height information of the sample with 3D topographical images, the ability to study living organisms and the simple sample preparation required (sample attached/deposited on a solid substrate). Some limitations include cell detachment with the use of sample adsorption method for living cells, damaging of tip and sample and the limited range for scanning area 150x150 microns.

Atomic Force Microscopy was used to determine the morphological changes to the lipid membranes. The equipment used for all AFM measurements was Nanoscope V MultiMode 8 and NCR-50, AFM tapping mode was used throughout the experiments. The height images were analysed NanoScope Analysis 1.5.

3.3.3. Quartz Crystal Microbalance

Quartz crystal microbalance (QCM) is a technique used to measure the mass change of analytes on the surface of an electrode when the material is deposited on or removed from

the electrode.[20] This technique is very a useful analytical tool because of the linear relationship between the measured signal being the frequency of the crystal resonance and the mass deposited on the crystal.[21] One of the advantages of using this technique is its detection to nanogram of masses per unit area thus, making the technique highly sensitive to the change in mass at the electrode surfaces. QCM consists of a thin quartz crystal, a piezoelectric quartz resonator with metal electrodes on either side. These electrodes are attached to an oscillator circuit, and once an alternative current (AC) is applied to the top and bottom part of the metal electrodes; this triggers a mechanical oscillation at frequency *f* at the crystal. The change in frequency can be quantified using the Sauerbrey's equation (Eq. 3-1),

$$\Delta \boldsymbol{f} = \frac{-2\Delta \boldsymbol{m} \boldsymbol{f}_0^2}{\boldsymbol{A}(\boldsymbol{\rho}_q \boldsymbol{\mu}_q)^{1/2}} = -\boldsymbol{C}_f \Delta \boldsymbol{m} \qquad \textbf{(3-1)}$$

where Δf = frequency change of the quartz crystal (Hz), Δm = elastic mass change (g), f_o = intrinsic crystal frequency, A = electrode area (cm^2), μ_q = shear modulus of quartz (AT-cut quartz crystal = 2.947 x 10^{11} dyn cm^{-2}), ρ_q = density of quartz = 2.65 g cm^{-3}, C_f = integrated QCM sensitivity (56.6 Hz cm^2 μg^{-1}).

3.3.4. Electrochemical Techniques

In an electrochemical process there is a flow of electrons between two substances, this drive of electron flow is due to reduction-oxidation (redox) reactions. In redox reaction, electrons are transferred from the substance that is being oxidised (substance losing electrons) to the substance being reduced (gaining the electrons). There are two types of electrochemical cells; galvanic and electrolytic cells. In the galvanic cell, spontaneous reaction releases energy that can be used as electricity however, and in an electrolytic cell, the electrical energy is used to drive a non-spontaneous reaction.[20] In an electrochemical reaction, an electrical current is passed between a solid electrode and an electrolyte solution and, this involves the transfer of charges or electrons from one species to another.[22] At the electrode-solution interface; there is depletion of reactants to the surface of the electrode. The concentration of reactants and products will differ from the region near the surface of the electrode and from the bulk solution.

At the application of a positive potential at an electrode immersed in an electrolyte solution, there would be a surge of current which will then decay to near zero rapidly with no electroactive species at the electrode surface. This generated current will create an excess or deficiency of negative charge at the surface of the electrode, the layer of solution adjacent to the electrode surface would acquire an opposite charge due to ionic mobility. The assembly of charge at the electrode surface and the solution adjacent to the surface is known as an electrical double layer.[20]

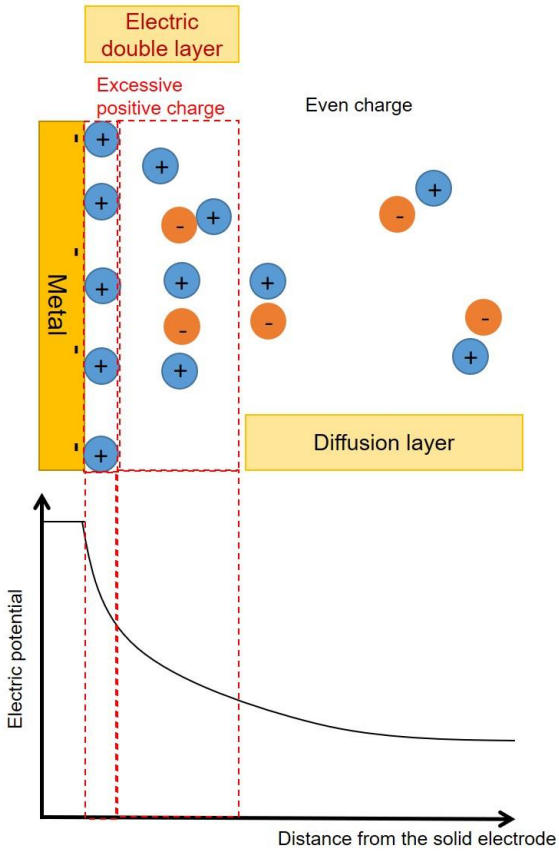

Figure 3.3-2: An illustration of the assembly of charges at the electrode's surface and a graph showing the charge and electric potential distribution in the electric double layer at electrode surface.

3.3.4.1. Cyclic Voltammetry

Cyclic voltammetry (CV) belongs to the group of the sweep voltammetry techniques where the current is measured whilst the potential applied at the working electrode is swept linearly in time.[22] In this technique, the potential is scanned between two values at a fixed rate; from E_1 (potential at which no redox activities takes place) to E_2 (potential that induces redox activities i.e. electron transfer), this is the forward scan. This scanning of the potential to more positive

values induces oxidation reaction to take place at the electrode's surface. The reverse scan is when the potential is reversed back from E_2 to E_1, this scan reduces the species. The switching of potentials produces a triangular potential waveform.

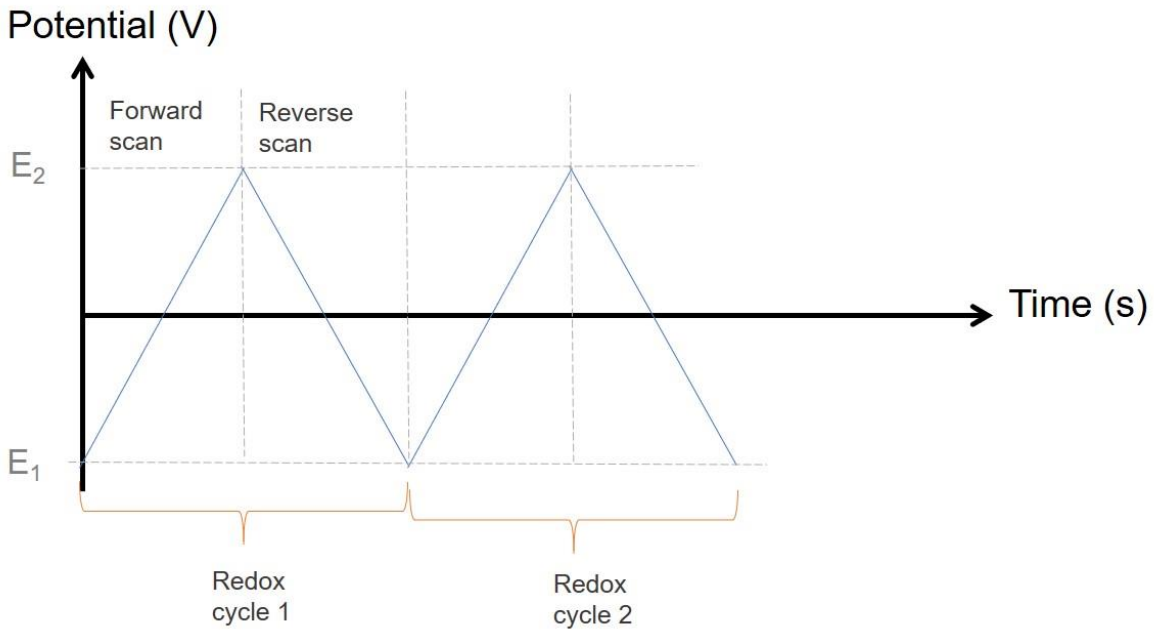

Figure 3.3-3: An illustration of CV triangular wavefunction; the voltage is scanned between 2 potential values (E_1 and E_2) at a fixed rate.

As the potential at the working electrode is increased, initiating an increase in the current from E_1 to E_2 passing the potential at which the redox species in the electrolyte solution is oxidised, to reach the maximum point (peak current, I_p), at which there is no more excess of redox materials at the electrode's surface. The peak current in a CV experiment is given by the Randles-Sevick equation (Eq. 3-2) at 298 K;

$$\boldsymbol{I_p = \left(2.69\, x\, 10^5\right) n^{3/2}\, ACD^{1/2} v^{1/2}} \qquad \textbf{(3-2)}$$

where n = number of electrons in the redox reaction, A = electrode area (cm^2), C = bulk concentration (mol/cm^3), D = diffusion coefficient (cm^2/s) and υ = potential scan rate (V/s).

3.3.4.2. Differential Pulse Voltammetry

Unlike CV where the potential applied produce a triangular potential waveform, with differential pulse voltammetry (DPV), the potential applied generates a combined or superimposed staircase and pulse forms (Figure 3.3-4). In this technique, the potential pulse is applied in

small intervals and, the current is measured just before the pulse is applied and at the end of the pulse. In this manner, the effect of the non-faradaic (charging) current is minimised i.e. the current difference is zero, it is only at the redox potential that the current difference reaches its maximum.[22] The plot that is generated is the difference in the currents.

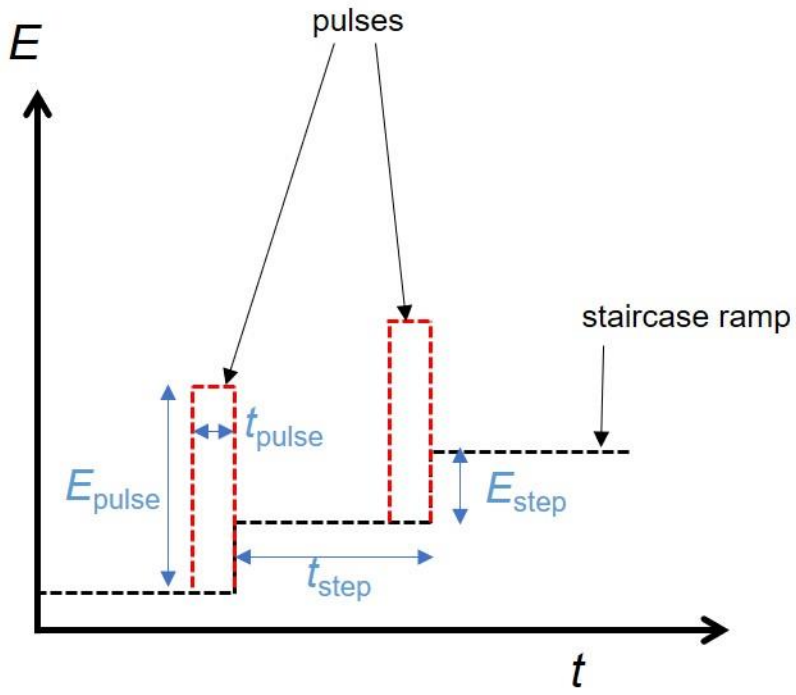

Figure 3.3-4: An illustration of the superposition of a staircase ramp with potential pulses. Adapted from Ref. 23.

3.3.4.3. Chronoamperometry

Chronoamperometry (CA) also called 'controlled-potential voltammetry, or the potential step technique, in this technique the current is measured as a function of time and, it is said to be diffusion-controlled.[24,25] In CA, the potential is applied in steps instead of applying the current linearly like in CV; the potential can be applied from a potential value that does not induce redox process (E_1) to a potential value where the analyte can be oxidised or reduced (E_2). In this way the potential is applied to the electrodes, allowing the redox reaction to occur to completion. At planar electrode, the current decays with time and is described using the Cottrell equation;

$$\boldsymbol{I(t) = \frac{nFACD^{1/2}}{\sqrt{\pi t}}} \qquad \textbf{(3-3)}$$

where i = current (A), n = number of electrons, F = Faraday constant (C mol^{-1}), A = area of the planar electrode (cm^2), C = concentration of the analyte (mol cm^{-3}), D = diffusion coefficient (cm^2 s^{-1}) and t = time (s).

Some of the limitations of this technique includes the inability to discriminate compounds that are oxidised at different potentials.[26]

3.3.4.4. Electrochemical Impedance Spectroscopy

Ohm's Law ($V = iR$) relates to the relationship between voltage (V) and current (i), which is applicable in DC techniques. Considering the complex behaviour of circuit elements found in the real world, the simple concept of resistance can no longer be adopted. So, the impedance (Z) is then substituted into the Ohm's Law equation instead of the resistance to overcome the limitations of Ohm's Law; this impedance becomes valid for both AC and DC techniques ($V = iZ$).[27]

In electrochemical impedance spectroscopy (EIS), a small sinusoidal potential of changing frequency is applied to an electrochemical system and the impendence at each frequency is measured. EIS allows the study of a system at a range of frequencies to enable the capture of information when a small perturbation/stimulus is applied; electrode kinetic information is captured at high frequencies and diffusion or mass transport at low frequencies.

An electrochemical cell is not a linear system i.e. doubling the voltage does not double the current, however applying a small perturbation (AC signal, 1-10 mV), the electrochemical cell becomes a pseudo-linear system and this results in a phase shift.

The input signal (excitation signal or wave) can be expressed as a function of time;

$$\boldsymbol{E_t = E_0 \sin(\omega t)} \quad \textbf{(3-4)}$$

where E_t = the potential at time t, E_0 = the amplitude of the excitation signal, ω = radial frequency ($2\pi f$) and t = time. The responding current signal (I_t) will be expressed as:

$$\boldsymbol{I_t = I_0 \sin(\omega t + \phi)} \quad \textbf{(3-5)}$$

where I_0 = current amplitude and ϕ = phase shift (phase being the difference between the 2 waves).

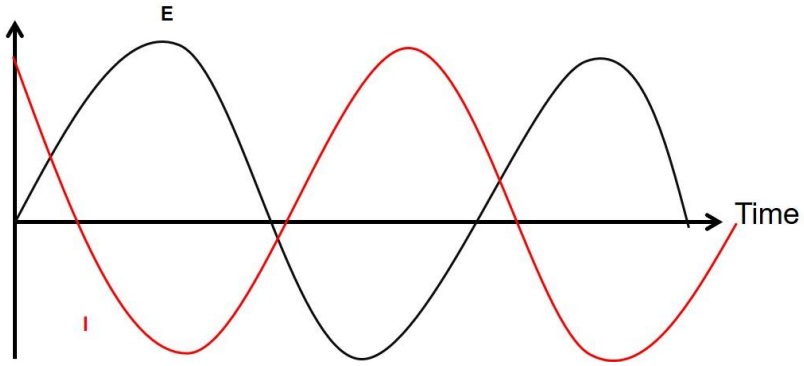

Figure 3.3-5: AC waveforms for an applied potential and its current response; AC stimulus is applied as the voltage (red line) and AC current (black line) is measured as the response.

Applying Ohm's law to the impedance (Z), to relate the voltage to the current.

$$\boldsymbol{Z = \frac{E_t}{I_t} = \frac{E_0 \sin(\omega t)}{I_0 \sin(\omega t + \phi)} = Z_o \frac{\sin(\omega t)}{\sin(\omega t + \phi)}} \qquad \textbf{(3-6)}$$

Using Euler principle, the above expression can be expressed as a complex function, using $\exp(j\phi) = \cos\phi + j\sin\phi$

$$\boldsymbol{Z(\omega) = \frac{E}{I} = Z_0 \exp(j \sin \phi) = Z_0(\cos \phi + j \sin \phi) = Z_r + jZ_j} \qquad \textbf{(3-7)}$$

where Z_r = real part of the impedance and Z_j = imaginary part of the impedance. The most common way of representing EIS data is by Nyquist plot; $-Z_r$ vs Z_j plot where each point on the plot represents the impedance at a frequency. Another way to represent EIS data is by Bode plot, this plot shows frequency information; log frequency (Log *f*) on the X-axis and the absolute values of the impedance ($|Z|=Z_0$) and the phase-shift (Φ) on the Y-axis.

Figure 3.3-6 shows 2 plots representing the same electrochemical impedance data for a Randles circuit, one for Nyquist representation and the other for the Bode representation.[28] The Randle's circuit is the simplest circuit model and is used as a building block for more complex models. This circuit is represented by a resistor in series with resistor capacitor (RC) system in parallel; the first resistor (R_1) in series referred to the solution resistance and the second resistor (R_2) in parallel with the capacitor represents the resistance to the Faradaic

reaction or charge transfer resistance and, the capacitor (C) represents the electrochemical double layer at the electrode's surface. When electrons flow through the circuit and the frequency set is at higher values, the impedance of the capacitor is low due to its reverse relationship as a result, the response seen is that of the values of the series resistance i.e. R_1. At lower frequencies, the impedance of the capacitor is very high, so the measured impedance is that of the combined resistance values i.e. $R_1 + R_2$.

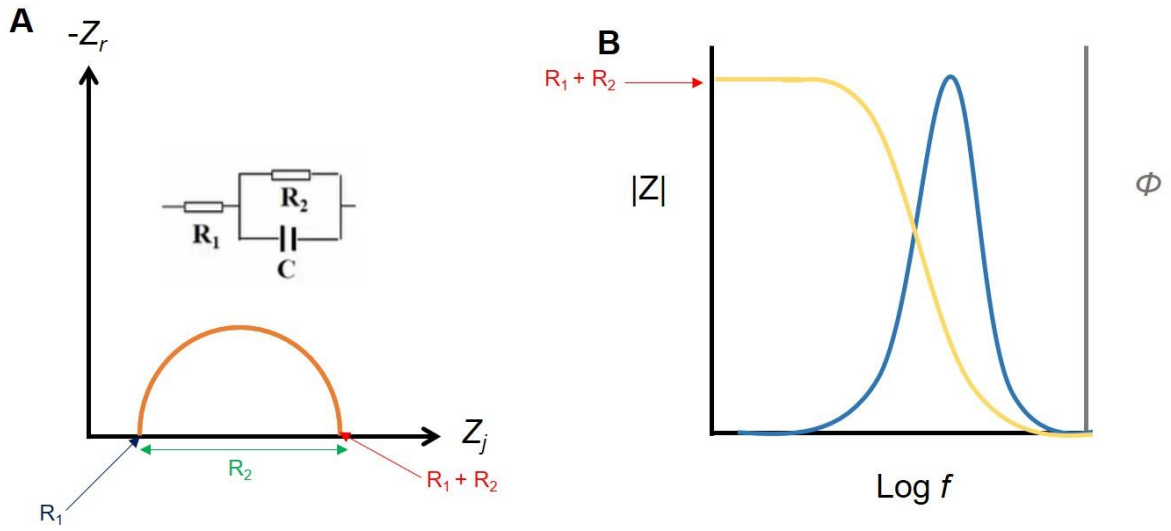

Figure 3.3-6: Electrochemical impedance data representing R(RC) Randles circuit for A) Nyquist and B) Bode plots.

3.3.4.5. Resonance Enhanced Surface Impedance

Resonance enhanced surface impedance (RESI) is an electrochemical method that involves the use of the Layerlab AB z-LAB instrument in conjunction with the z-Measure control software to effectively calculate real-time changes in capacitance and electrical resistance at surface interfaces. The instrument can perform measurements at a user-defined temperature within the range of 20 and 40 °C (± 0.1 °C).

The measurements involve the use of a resonance circuit where an external inductive element is connected in parallel to a pair of microelectrodes (surface area = 0.002 cm^2 with 30 µm gap between the integrated electrodes) which is then immersed in an electrolyte solution together with a Ag/AgCl reference electrode (RE) and platinum counter electrode (CE), seen as the blue shaded area Figure 3.3-7B. The reason for the pair of microelectrons is to "become part

of a resonator with a resonance frequency essentially determined by the interface capacitance".[29] The reference and counter electrodes can be used together with the integrated potentiostat to bias the sensor electrodes.

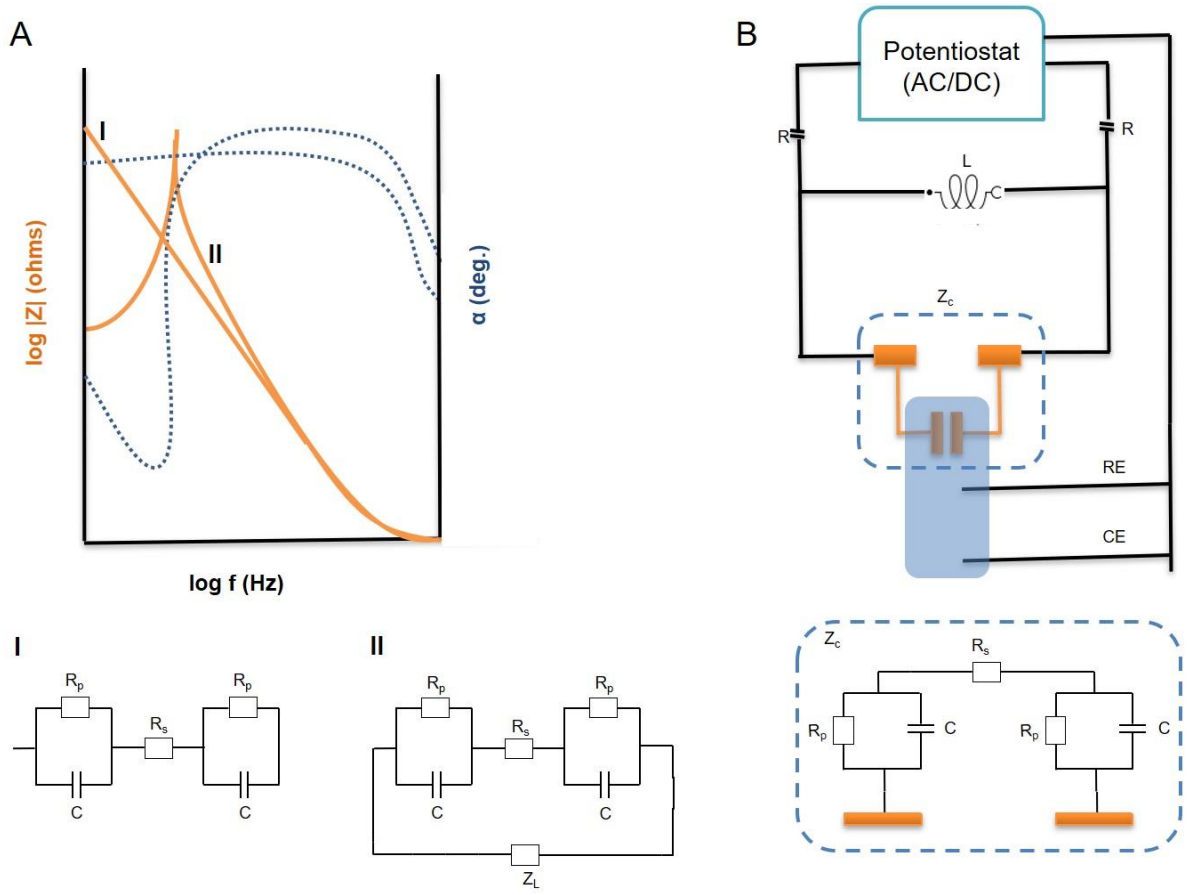

Figure 3.3-7: A) Bode plot to illustrate the effect of the inductive impedance (Z_L) connected in parallel with the sensor (circuit diagram II) and without it (circuit diagram I). B) An illustration of the z-LAB circuitry for the integrated sensor chip.

The integrated sensor chip is represented by an internal impedance, Z_c, (WE1 and WE2 consisting of Z_c) which is connected in parallel with an inductive impedance (L). The principal components of the sensor comprised resistors (R) and capacitors (C). The insets are circuit representations of the dual electrodes, where each electrode interface is represented by a capacitance (C) and a resistance (R_p). The resistance of the electrolyte between the electrodes is denoted by R_s. Adapted from Ref. 29.

A 40 mV sinusoidal voltage is applied to the circuit. This experimental setup causes the microelectrodes to form part of the resonator and the corresponding impedance spectrum comprises a sharp maximum resonance peak. The maximum resonance frequency is a function of the capacitance at the sensor-solution interface; the frequency range for each impedance spectrum is measured between 0.1 Hz to 1 MHz. Changes in the resonance frequency in real time can be detected by mapping the resonance peak and consequently,

RESI provides an efficient method for resolving small capacitance changes of less than 0.2 pF with a time resolution of 0.25 Hz. A surface process will prompt a change in interfacial capacitance and resistance, leading to a resonance peak shift.

RESI, data acquisition can be performed in real time, which enables time-resolved measurements with enhanced sensitivity and improved signal resolution. When a nanoparticle passes through the cell, it can form reversible agglomeration or pass through the flow cell. The effective capacitance and resistance in the region between the electrodes will change, accordingly, resulting in a shift in the actual resonance frequency.

The RESI capacitance can be calculated from the maximum resonance frequency, at f_0, when the current is minimum, and the total impedance is at the maximum. Below f_0, the circuit is inductive and above f_0, the circuit is capacitive and dominated by the electrode impedance. For most ordinary electrolytes, the solution resistance R_s matches the inner resistance of the inductor R_L (R_s~R_L).[29] From the circuitry (Figure 3.3-7), the electrode pair becomes the resonator and its resonance frequency is related, relatively accurately, to the RESI capacitance (C) according to Eq. 3-8, valid for an ideal RCL-resonator.

$$\boldsymbol{f_0 = \frac{1}{2\pi\sqrt{LC_R}}} \qquad \textbf{(}3\text{-}8\textbf{)}$$

Where f_0 = resonance frequency, L = inductance and C_R = RESI capacitance.

RESI, data acquisition can be performed in real time, which enables time-resolved measurements with enhanced sensitivity and improved signal resolution. When a nanoparticle passes through the cell, it can form reversible agglomeration or pass through the flow cell. The effective capacitance and resistance in the region between the electrodes will change, accordingly, resulting in a shift in the actual resonance frequency. An interpretation of the RESI capacitance (C_R) is complex in a flow cell and needs further exploration. In a qualitative explanation, the RESI capacitance (C_R) can be viewed as influenced by the interface at an electrode-electrolyte interface comprised of the compact layer (C_L) with the inner and outer

Helmholtz planes and the diffusion layer (D_L). The capacitance increases with decreasing separation between the electrode surface and plane of closest approach of ionic charges. When an adsorbed layer comprised of NPs is deposited on the electrode surface, the electrolyte will be partially shielded from the electrode, if the adsorbed layer is insulating or result in a rougher and larger surface area, if it's conducting. This can be described as a serial connection between a Helmholtz-type capacitor (C_{CL}) and the diffuse layer capacitance (C_{DL}) with the total capacitance (C_R) given by:

$$\frac{1}{C_R} = \frac{1}{C_{CL}} + \frac{1}{C_{DL}} \qquad \textbf{(3-9)}$$

where C_R = RESI capacitance, C_{CL} = compact layer capacitance and C_{DL} = diffuse layer capacitance.

At planar surfaces and high electrolyte concentrations, the compact layer capacitances (C_{CL}) tend to be significantly smaller than diffuse layer capacitances (C_{DL}) and dominate values C_R (C_{CL}~C_R). C_{CL} is nominally determined by $\varepsilon\varepsilon_0 A d^{-1}$, where ε is the dielectric constant of the medium, ε_0, the permittivity of free space, A the electrode area and d the distance that separates the electrolyte from the electrode. In microfluidic systems, C_{DL} can vary empirically with bulk properties such as electrolyte charge, concentration, dielectric constants of solvents, physical structure of microfluidic channels and flow rates.[30,31]

3.3.5. Nano-impact events on bare electrode surfaces

NP collision also known as nano-impact, is a process by which NPs dispersed in a colloidal solution interacts by coming into electrical contact with the surface of an electrode generating a current response that can be detected electrochemically.[32,33] The significance of this technique is that all the electrochemical activity detected at the electrode surface is from the NP collisions. However, the drawback is that the technique gives limited information on the electrochemical reaction derived from the current-time responses.

Over the years, different experimental systems have been published using the electrocatalytic current amplification technique such as: indirect particle voltammetry with different NP metal cores (including IrOx, Au, C)[34]; electrode materials (including C, Au, Pt)[34]; and electroactive reactant molecules (including N_2H_4, $NaBH_4$ oxidations, H_2O_2 reduction) etc.[35–37]

A new strategy for the quantitative detecting and characterising NPs upon collision with a potentiated electrode was published by Compton *et al.*[38], based on the Faradaic charge transfer as AgNPs collide with the electrode. This new approach was referred to as direct particle voltammetry. Unlike the indirect particle voltammetry that uses electrocatalytic amplification technique, direct particle voltammetry does not require electroactive reagents to generate nano-impact events. In this technique, the NPs are directly oxidised/reduced once in contact with the potentiated electrode surface. While employing the direct particle voltammetry technique, Haddou *et al.*[39] demonstrated the possibility of deriving reversible and irreversible kinetic data from the oxidation of copper NPs. Metallic NPs were not the only particles under investigation in their study, other nanomaterials were reported including organic NPs such as indigo[40,41]; and soft NPs such as emulsion droplets[42] and liposomes[43].

In the course of nanoparticle-electrode interactions, two main collision responses have been identified, current spikes and current staircases, arising from the transient times i.e. the time taken for the NPs to come into contact with the electrode surface (see Figure 3.3-8).[44]

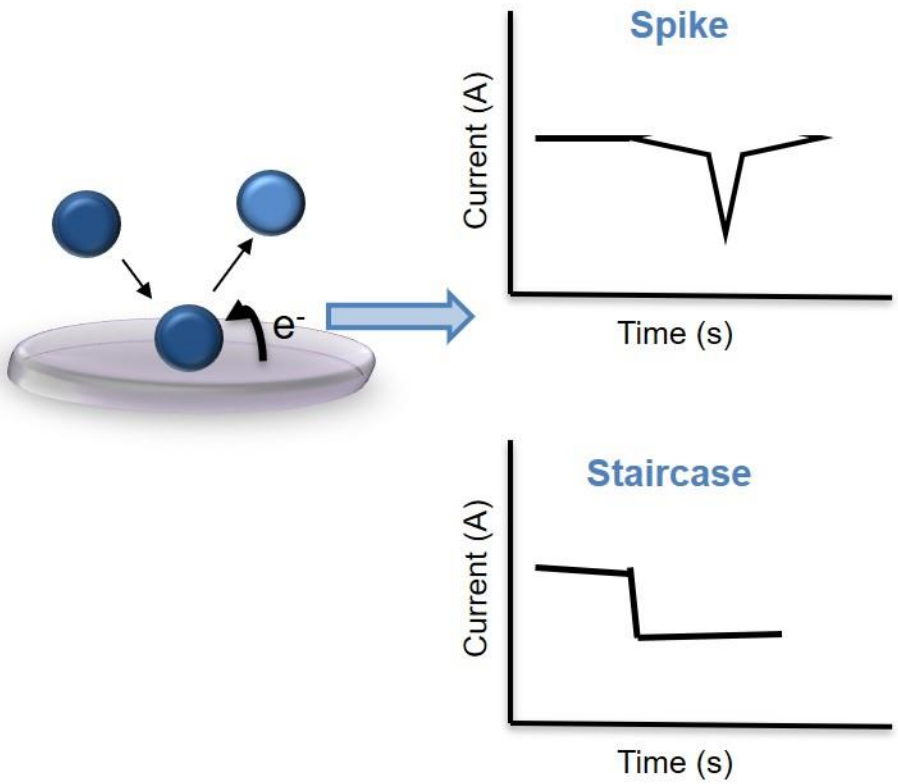

Figure 3.3-8: Schematic of NPs impact at inert electrode surface. Chronoamperometric curves showing the collision responses of individual Pt NPs (diameter ca. 4 nm) at Ni UME E = 0.12 V (spike) and E = 0 V (staircase) in 50 mM PBS (pH 7) containing 8.7 mM hydrazine. Adapted from Ref. 45.

The current spikes are caused by a brief interaction of the NPs with the electrode surface while the current staircase responses are caused by more permanent changes at the electrode surface.[36] It has been reported that these changes were caused by agglomeration or aggregation of NPs at impacts, depending on the type of collision responses.

3.3.5.1. Spike responses caused by nano-impact collisions

Faradaic and non-Faradaic currents can generate spikes on electrochemical profiles (Figure 3.3-8), and such responses are facilitated by short contact time of nanoparticles at electrode surface causing their temporary adsorption.[46] Furthermore, Scholz studies observed that non-Faradaic spikes were caused by charge transfer on current-time transients. Interestingly, the Compton group have shown that Faradaic charge transfer can also give rise to current time transients via the direct oxidation of AgNPs during collisions at electrode surface.[38] In their findings, they were able to distinguish agglomerates from individual NPs, and these estimates

were in sensible agreement with the microscopic characterisation of the NPs via transmission electron microscope (TEM) and scanning electron microscope (SEM).[47,48]

As previously mentioned, nano-impact has been used as a tool to determine NP size using oxidising current spikes. Particle size[49,50] is not the only quantitative information that can be deduced from NP collision, other publications include the use of landing frequency to determine NP concentration[51,52] and solution viscosity[49].

3.3.5.2. Staircase responses caused by nano-impact collisions

Having considered the response from temporary collision of NPs on electrode surface i.e. spikes response, it is important to comment on the other type of collision response (Figure 3.3-8). Staircase or stepwise current response denotes more permanent changes at the electrode surface due to the cumulative adsorption of NPs at the electrode surface.[46] As the NPs approach the electrode surface, they irreversibly collide with and stick to the electrode surface, whereby the permanent adsorption of NPs at electrode surface causes discreet current increments. The first observation of such a response was published by the Bard group[51]. From their publication, using the indirect particle voltammetry technique, dilute solutions of Pt NPs were added in electrolyte solution with low concentration of hydrazine, the hydrazine oxidation was found to occur only at NP surface generating a staircase response. Similar to the finding by the Compton group on particle size determination with nano-impact experiment, the Bard group[51] have also shown that their method is useful in the determination of particle size as their results were found to be in agreement with TEM images.[51]

Nano-impact collision events were carried out using electrochemical technique called chronoamperometry with the Autolab potentiostat and the zLAB was used to carry out the RESI experiments.

3.3.5.3. Chronoamperometry experiments

All chronoamperometry experiments were carried out using a microfluidic flow cell; a thin-film integrated sensor (MicruX Technologies, Spain) was mounted onto PEEK flow-cell. The PEEK

flow cell was composed of AIO-cell fitted with PEEK Add-on (MicruX Technolgies, Spain) which was connected to an Aladdin pump (World Precision Instruments, UK) with a syringe and 0.056 I.D. AutoAnalyser pump tubes (Technicon Corporation, USA) attached to the flow cell. The 'inflow' tubing brought the electrolyte and NPs solution to the flow cell from the attached Aladdin pump and syringe and, the 'outflow' tubing removed the cell content to the waste beaker. The cell's internal volume is between 60-500 nL with an inlet channel of 0.5 mm.[53] The flow cell was connected to a universal cable then to the potentiostat with banana plugs to attach the reference, working and counter electrode connections from the instrument.

The Chronoamperometry measurements were performed on Autolab PGSTAT 12 potentiostat (Metrohm Autolab B. V., The Netherlands) using the latest NOVA software. The Chronoamperometry setting were adapted according to the experiment being carried out; potential hold and time duration of the experiment.

3.3.5.4. RESI experiments

The RESI experiments (RESI capacitance measurements) were carried out using z-LAB-210-S2 (Layerlab, Sweden. Clean gold sensor chips provided by Layerlab AB were mounted onto the sample holder, all measurements were carried out using z-Measure software from the same company. The apparatus has a cell volume of up to 1 µL. Once the flow rate was set to the appropriate flow set on the z-Measure software, the 'wash' sensor chip was mounted to enable the wash of the electrolyte or solvent, depending on the study undertaken, to run through the system prior the start of the measurement. Once the system was ready, the 'wash' sensor chip was removed and the clean sensor chip (bare of immobilised with lipid molecules) was mounted, the software would then be set to start recoding the measurements. This initial run of electrolyte solution would be set for 15 min to allow the system to stabilise before injections of NPs or solvent can be carried out. A syringe was used to inject the appropriate liquid (electrolyte, lipid vesicles solution or NPs solutions, 200 µL) into the integrated injection valve containing a loop system of 200 µL volume, this enabled the solution/sample to be injected into the microfluidic system. For every injection, the start and end of injection would

be recorded and so would its duration. The overall duration of the measurement was dependent on the study under investigation and this would also determine the different stages of solutions injections and electrolyte runs.

3.4. References

1 Z. Farrell, C. Shelton, C. Dunn and D. Green, *Langmuir*, 2013, **29**, 9291–9300.

2 M. Brust, M. Walker, D. Bethell, D. J. Schiffrin and R. Whyman, *J. Chem. Soc. Chem. Commun.*, 1994, 801–802.

3 M. J. Hostetler, A. C. Templeton and R. W. Murray, *Langmuir*, 1999, **15**, 3782–3789.

4 J. Pillay, K. I. Ozoemena, R. T. Tshikhudo and R. M. Moutloali, *Langmuir*, 2010, **26**, 9061–9068.

5 G. H. Woehrle, L. O. Brown and J. E. Hutchison, *J. Am. Chem. Soc.*, 2005, **127**, 2172–2183.

6 M. Naumowicz and Z. Figaszewski, *Bioelectrochemistry*, 2003, **61**, 21–27.

7 R. Campos and R. Kataky, *J. Phys. Chem. B*, 2012, **116**, 3909–3917.

8 M. Technologies, Thin-film double metal single-electrodes, https://www.micruxfluidic.com/en/shop/electrochemical-solutions/thin-film-electrochemical-sensors/?p=all.

9 A. Tlili, A. Abdelghani, S. Hleli and M. A. Maaref, *Sensors (Basel).*, 2004, **4**, 105–114.

10 C. Brett, S. Kresak, T. Hianik and A. M. Oliveira Brett, *Electroanalysis*, 2003, **15**, 557–565.

11 B. R. Dorvel, H. M. Keizer, D. Fine, J. Vuorinen, A. Dodabalapur and R. S. Duran, *Langmuir*, 2007, **23**, 7344–7355.

12 J. M. Andrews, *J. Antimicrob. Chemother.*, 2001, **48**, 5–16.

13 D. B. Williams and C. B. Carter, *Transm. Electron Microsc.*, , DOI:10.1007/978-1-4757-2519-3_1.

14 A. Tlili, A. Abdelghani, S. Hleli, M. A. Maaref, V. C. Yang, T. T. Ngo, C. G. Zoski, P. Zanello, R. S. of C. (Great Britain), R. S. of C. (Great Britain)., R. S. of C. Staff, N. G. Connelly, L. Reimer, D. B. Williams and C. B. Carter, *Transmission Electron Microscopy: Physics of Image Formation and Microanalysis*, Springer US, 2003, vol. 4.

15 D. B. Williams and C. B. Carter, *Transmission Electron Microscopy: A Textbook for Materials Science*, Springer, 2009.

16 Z. L. Wang, *J. Phys. Chem. B*, 2000, **104**, 1153–1175.

17 W. D. Pyrz and D. J. Buttrey, *Langmuir*, , DOI:10.1021/la801367j.

18 Y. F. Dufrêne, *J. Bacteriol.*, 2002.

19 G. Binnig, C. F. Quate and C. Gerber, *Phys. Rev. Lett.*, 1986, **56**, 930.

20 A. J. Bard and L. R. Faulkner, *Electrochemical methods: Fundamentals and applications*, New york, 2001.

21 C. Köβlinger, E. Uttenthaler, S. Drost, F. Aberl, H. Wolf, G. Brink, A. Stanglmaier and E. Sackmann, *Sensors Actuators B Chem.*, 1995, **24**, 107–112.

22 R. G. Compton and C. E. Banks, *Understanding voltammetry*, World Scientific, 2011.

23 F. Scholz, *ChemTexts*, 2015, **1**, 17.

24 P. Zanello, R. S. of C. (Great Britain), R. S. of C. (Great Britain)., R. S. of C. Staff and N. G. Connelly, *Inorganic Electrochemistry: Theory, Practice and Applications*, Royal Society of Chemistry, 2003.

25 C. G. Zoski, *Handbook of Electrochemistry*, Elsevier Science, 2007.

26 V. C. Yang and T. T. Ngo, *Biosensors and Their Applications*, Springer US, 2000.

27 G. Instruments, Basics of Electrochemical Impedance Spectroscopy, https://www.gamry.com/application-notes/EIS/basics-of-electrochemical-impedance-spectroscopy/.

28 A. Lasia, in *Modern Aspects of Electrochemistry*, eds. B. E. Conway, J. O. Bockris and R. E. White, Springer US, Boston, MA, 2002, pp. 143–248.

29 A. Lundgren, J. Hedlund, O. Andersson, M. Brändén, A. Kunze, H. Elwing and F. Höök, *Anal. Chem.*, 2011, **83**, 7800–7806.

30 G. Zhang, in *COMSOL Conference*, 2010.

31 N. C. Hoyt, J. S. Wainright and R. F. Savinell, *J. Electrochem. Soc.*, 2015, **162**, A1102–A1110.

32 K. Tschulik, C. Batchelor-McAuley, H.-S. Toh, E. J. E. Stuart and R. G. Compton, *Phys. Chem. Chem. Phys.*, 2014, **16**, 616–623.

33 X. Xiao and A. J. Bard, *J. Am. Chem. Soc.*, 2007, **129**, 9610–9612.

34 E. Katelhon and R. G. Compton, *Chem. Sci.*, 2014, **5**, 4592–4598.

35 S. V. Sokolov, K. Tschulik, C. Batchelor-McAuley, K. Jurkschat and R. G. Compton, *Anal. Chem.*, 2015, **87**, 10033–10039.

36 S. M. Oja, M. Wood and B. Zhang, *Anal. Chem.*, 2013, **85**, 473–486.

37 K. McKelvey, M. A. Edwards and H. S. White, *J. Phys. Chem. Lett.*, 2016, **7**, 3920–3924.

38 Y.-G. Zhou, N. V Rees and R. G. Compton, *ChemPhysChem*, 2011, **12**, 2085–2087.

39 B. Haddou, N. V Rees and R. G. Compton, *Phys. Chem. Chem. Phys.*, 2012, **14**, 13612–13617.

40 W. Cheng, X.-F. Zhou and R. G. Compton, *Angew. Chemie Int. Ed.*, 2013, **52**, 12980–12982.

41 W. Cheng and R. G. Compton, *TrAC Trends Anal. Chem.*, 2014, **58**, 79–89.

42 B. K. Kim, J. Kim and A. J. Bard, *J. Am. Chem. Soc.*, 2015, **137**, 2343–2349.

43 W. Cheng and R. G. Compton, *Angew. Chemie Int. Ed.*, 2014, **53**, 13928–13930.

44 W. Wang and N. Tao, *Anal. Chem.*, 2013, **86**, 2–14.

45 A. R. Jung, S. Lee, J. W. Joo, C. Shin, H. Bae, S. G. Moon and S. J. Kwon, *J. Am. Chem. Soc.*, 2015, **137**, 1762–1765.

46 S. M. Oja, Y. Fan, C. M. Armstrong, P. Defnet and B. Zhang, *Anal. Chem.*, 2015, **88**, 414–430.

47 C. Batchelor-McAuley, J. Ellison, K. Tschulik, P. L. Hurst, R. Boldt and R. G. Compton, *Analyst*, 2015, **140**, 5048–5054.

48 Y. Zhou, N. V Rees and R. G. Compton, *Angew. Chemie Int. Ed.*, 2011, **50**, 4219–4221.

49 S. J. Kwon, H. Zhou, F.-R. F. Fan, V. Vorobyev, B. Zhang and A. J. Bard, *Phys. Chem. Chem. Phys.*, 2011, **13**, 5394–5402.

50 S. J. Kwon, F.-R. F. Fan and A. J. Bard, *J. Am. Chem. Soc.*, 2010, **132**, 13165–13167.

51 X. Xiao, F.-R. F. Fan, J. Zhou and A. J. Bard, *J. Am. Chem. Soc.*, 2008, **130**, 16669–16677.

52 S. E. F. Kleijn, B. Serrano-Bou, A. I. Yanson and M. T. M. Koper, *Langmuir*, 2013, **29**, 2054–2064.

53 M. Technologies, All-In-One Platform for thin-film electrodes, https://www.micruxfluidic.com/en/electrochemical-solutions/electrochemical-platforms/all-in-one-platform/.

4. Nanoparticle impacts on gold electrode surfaces in Flow-Injection configuration

This chapter reports on the effect of flow rates on the fate of nanoparticles impacting an electrode surface, in real, commercially available flow systems. Resonance Enhanced Surface Impedance (RESI) and particle Chronoamperometry (CA) were used for monitoring dodecanethiolate (DDT-) and (ω-ferrocenylhexanethiolate) NPs (FcHT-) stabilised silver (Ag) and gold nanoparticles (AuNPs) as they collide at bare gold working electrode surfaces in a Flow Injection Analysis (FIA) format.

4.1. Introduction

Stochastic NP electrochemistry has boosted the interest in the study of random events of NP collisions at electrode surface. To carry out a nano-impact experiment, an inert electrode in a colloidal suspension is immersed in an electrolyte solution, and a potential is applied to the electrode which aides NP-electrode collisions that would otherwise occur due to Brownian motion of NPs.[1]

4.1.1. General aspects of NP collisions

NP electrochemistry has become a good platform for the electrochemical detection of individual and multiple NP collisions with electrode surface. A fast, simple and easy method of employing electrocatalytic current amplification technique was first developed and published by Xiao and Bard.[2] In this technique, the redox reactions only take place at the surface of the electrocatalytically active NPs as these come into contact with the surface of the electrode; such interactions result in the amplification of the current response.[3] Prior to this method, it was challenging to detect individual NP collision process due to noise and background level being far greater than the current signals arising from few electrons transfer

between NPs and electrode surface. According to Xiao and Bard[2], a carbon fibre ultramicroelectrode (UME) was immersed in an aqueous solution containing dispersed Pt NPs and electroactive species, the UME was held at constant potential to promote redox reaction on the Pt NP and not on the electrode. The signal produced in current-time profile is indicative of the collision behaviour of NP at electrode surface.

4.1.2. Formation of nanoclusters by either agglomeration or aggregation

NPs tend to form clusters either by aggregation or agglomeration; aggregates refer to strongly bonded colloidal particles and agglomerates to weakly bonded particles, which can lead to reversible phase separation.[4] However, under conventional particles characterisation such as TEM or SEM or even Dynamic Light Scattering (DLS), it is difficult to distinguish one clustering process from another. A study published by the Compton's group[5] have demonstrated the ability of the electrochemical nano-impact technique in identifying the modes of NPs clustering, in high ionic strength solutions. Their results revealed that the particles detected by nano-impact experiments were agglomerates not aggregates, as smaller sizes were determined after mechanical agitation; they referred to this process as reversible agglomeration. The Unwin group[6] published a study that contradicts the use of nano-impact events as 'not appropriate', for a general method as size characterisation technique for NPs. They argued that though the technique enables the acquisition of useful information on the physicochemical interactions between impacting NPs and potentiated electrode surfaces, however partial or incomplete oxidation of impacting NPs resulted in wrong size estimations thus inaccurate size distribution was analysed for large particles (>20 nm). Their article raises a valid conclusion; however, we hope that the use of the nano-impact technique coupled with flow injection system would shed a light into mode of clustering of thiol stabilised NPs at potentiated electrodes.

Though nano-impact in a Flow Injection Analysis (FIA) configuration is complicated by near wall hindered diffusion in addition to Brownian motion. Compton *et al.*[7] reported the concept of reversible 'hydrodynamic adsorption' resulting from near-wall hindered diffusion which

increased the residence time within the tunnelling region of the electrode where the particles are influenced by the electrode potential.

The purpose, in this chapter, is to study the effects of flow rates and redox activity on the (semi)quantitative, transient collision behaviour of thiol-capped silver and gold NPs on bare gold electrodes, in analytical systems with time scales that are representative of real analytical applications. Experimental results, using two different techniques, are reported. The well-known direct particle chronoamperometry is used together with a lesser known technique, Resonance Enhanced Surface Impedance (RESI)[8] to give complementary information on the effect of NP collisions on an electrode surface.

Two types of nanoparticles were used in these studies. Dodecanethiol (DDT) modified NPs were used while investigating the effect of changing the flow rate of NP injection. Redox active, ω-ferrocenylhexanethiolate (FcHT) NPs were used to investigate the effect of oxidation of the ferrocene moieties at the electrode surface poised at an oxidizing potential.

In this research, we have chosen to use direct particle voltammetry to eliminate the use of extra redox species needed in catalytic reactions as well as simplify the signal interpretations arising with NPs interacting at electrode's surface. The RESI technique which is a new platform in the study of nanoparticle-electrode collisions will also be used in this research to enable the investigation of AgNPs interactions while monitoring in real-time the change in RESI capacitance.

4.2. Results & Discussion

Stochastic collisions of NPs occur at bare electrode surface and these can cause the adsorption of NPs at electrode surface. Depending on the collision behaviour, the adsorption can either be permanent or semi-permanent thus generating discrete current-time traces.[9,10] The different studies in this chapter investigate the interactions between thiol-capped silver and gold NPs on bare gold electrode surfaces, to determine the effects of particle flow rates and NP electroactivity. In both RESI and the Micrux microfluidic cells, laminar flow was used; ensuring that the mixing between miscible fluids in contact with each other occurs only through diffusion.

The NPs were synthesised using chemical reduction methods and the ligands modification was carried out according to published works to yield electroactive FcHT-Ag and AuNPs.[11,12]

Particle size distribution from TEM analyses has demonstrated mono- and polydisperse metallic NPs nanoparticles (Figure 4.2-1), the mean particle sizes for all NPs were determined in Table 4.2-1.

Table 4.2-1: Particle size distribution of metallic NPs by TEM technique.

	AuNPs	**AgNPs**
DDT	2.8 ± 1.04 nm	4.9 ± 1.2 nm
FcHT	5.5 ± 2.91 nm	8.0 ± 2.4 nm

The aryl, ferrocenated thiol ligands, adds steric crowding around the metal core.[13,14] When compared to the alkyl, dodecane thiol ligand stabilising the metal core, the later would exhibit smaller sizing of the NP due to its straight chain alkane thiol whilst FcHT NPs would yield larger core diameter sizes.

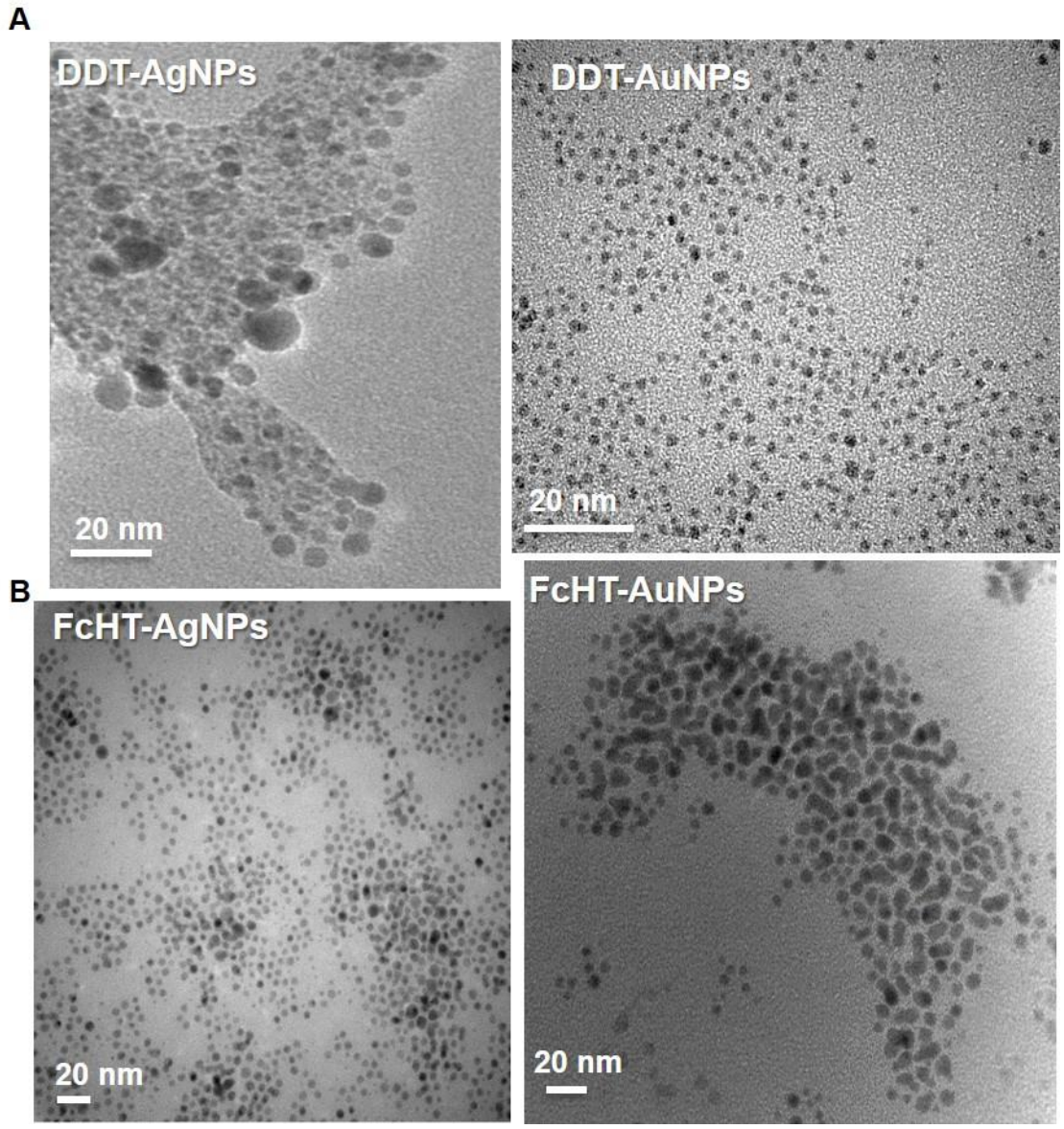

Figure 4.2-1: Transmission electron microscopy (TEM) images of thiolated silver and gold nanoparticles; A) DDT-AgNPs and DDT-AuNPs, B) FcHT-AgNPs and FcHT-AuNPs.

In this chapter we will discuss the different collision behaviours of both NPs (silver and gold) at gold electrode surfaces; we expect the nanoparticle-electrode collision processes of both NPs to yield different nano-impact characteristics due to their varied stability and homogeneity.

Every experiment at each study, for both Ag and AuNPs, was carried out in the same way unless stated otherwise. All the Chronoamperometry experiments were performed using thin-film integrated sensors (MicruX Technologies, Spain) incorporating three-electrode configuration; 150 nm thin-film gold electrode (A = 0.8 mm^2), 150 nm thin-film platinum counter and reference electrodes (Figure 4.2-2). To set the flow rate for the measurements, an Aladdin

pump (World Precision Instruments, UK) was used with a syringe and appropriate tubing attached to a PEEK flow-cell (MicruX Technolgies, Spain) and, the flow settings were as indicated in the studies. The cell was placed in a Faraday cage to minimise interferences and all measurements were carried out at room temperature. Baseline corrections and any other additional data analysis were carried out using OriginPro 2017 (Origin Lab Corporation).

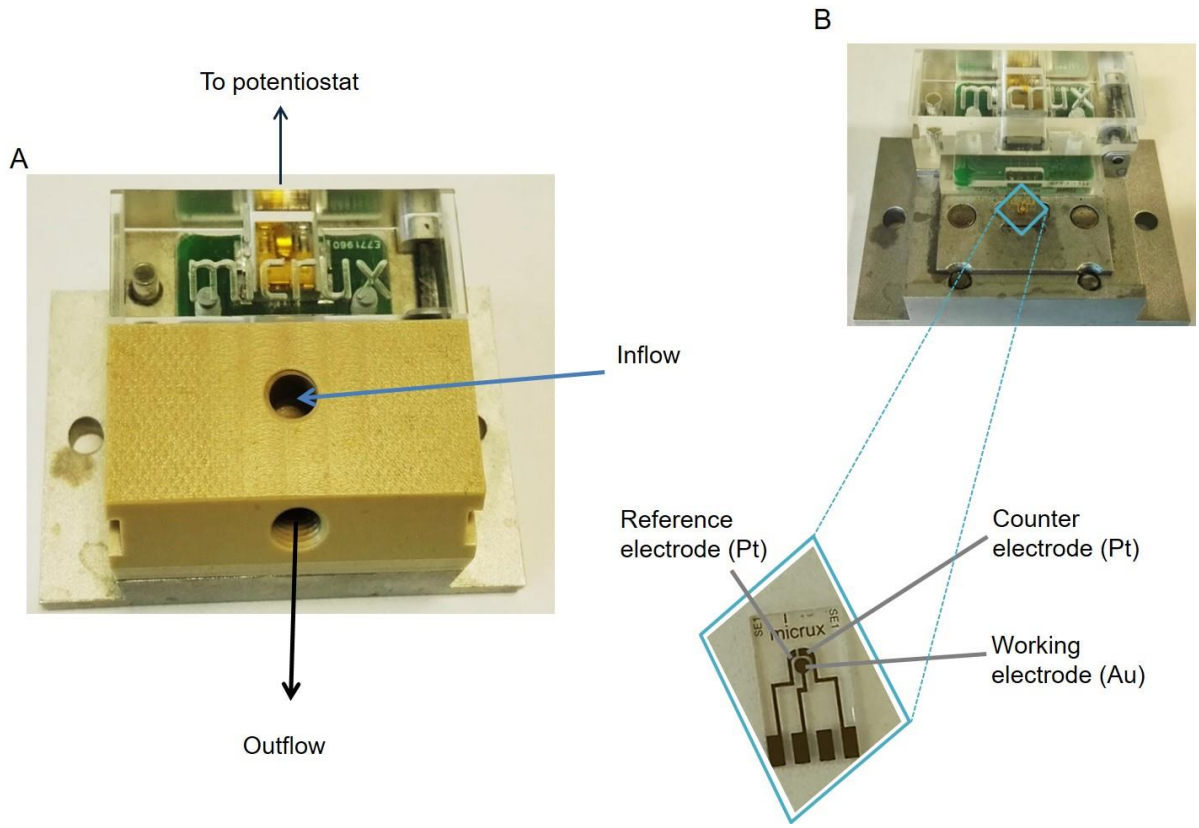

Figure 4.2-2: A PEEK flow-cell showing its connections: A) to the potentiostat and connectors (inflow – connecting to the Aladdin pump and outflow connected to the dispenser), B) the cell being fitted with the electrode with the inset of the thin film electrode (Au/Pt) incorporating the three-electrode system, made from glass substrate.

4.2.1. Preliminary results of nano-impact collisions

Initially three different concentrations of DDT-AgNPs and DDT-AuNPs were used to monitor the effects of concentration at a flow rate of 5 µL/min (Figure 4.2-3 and Figure 4.2-4). Three concentrations are compared, ~1 µmol dm^{-3}, ~5 µmol dm^{-3} and ~25 µmol dm^{-3}. The 1 µmol dm^{-3} plots showed that the NPs remained at the surface of the electrode with the longest dwell time which would allow chronoamperometric studies to be performed. The 5 µmol dm^{-3} showed very low dwell times on the electrode surface especially for DDT-AgNPs,

whereas the 25 μmol dm^{-3} showed the smallest change in RESI capacitance. These differences are likely to be due to changes in agglomerate formation. Subsequent, detailed studies were carried out with the 1 μmol dm^{-3} AgNP solution. RESI results revealed that the concentration of NPs influenced the nano-impact collision events at electrode's surface. Whereby at lower NP concentrations, U-shaped valleys were detected (synonymous of long stay of the adsorbed NPs at electrode's surface before NPs adsorption took place) and at higher concentrations, spikes were detected (synonymous of "Hit-n-Run" collisions). Results from the Chronoamperometric measurements revealed that the more concentrated the NP solution, the more agglomerated NPs were detected at nano-impact collision events (Figure 4.2-3 and Figure 4.2-4).

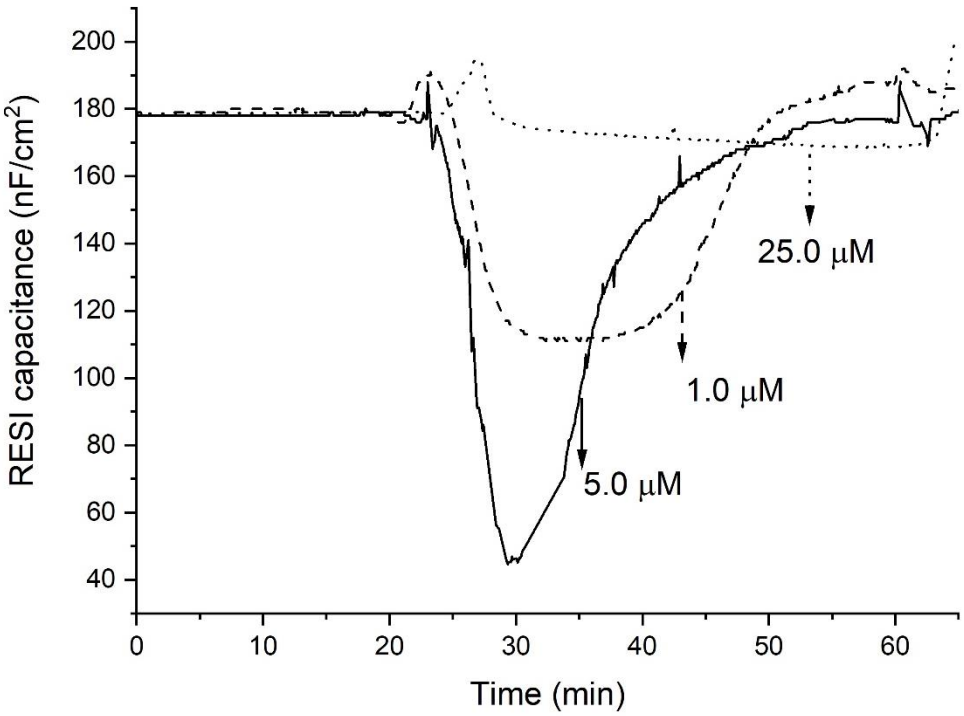

Figure 4.2-3: Change in RESI capacitance vs time observed upon injection of 3 different concentrations of DDT-AgNPs on gold electrode surfaces in a running electrolyte solution of 0.1 M KNO_3; at 5 μL/min flow rate.

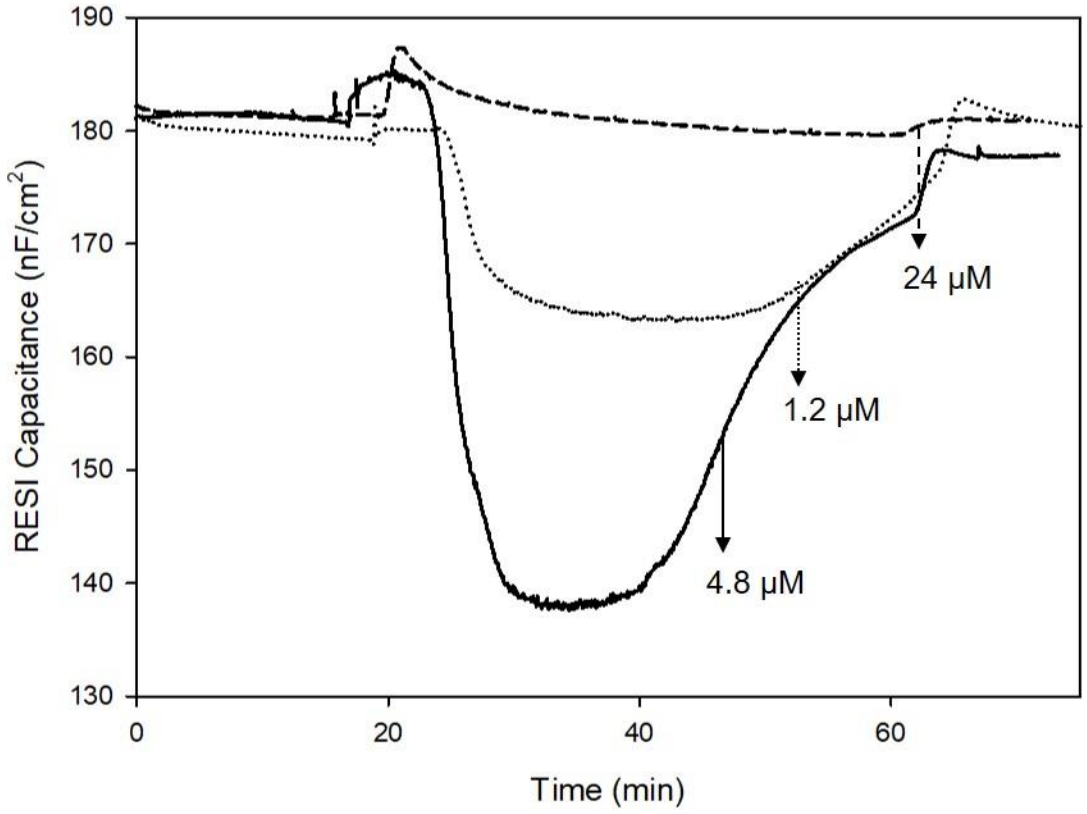

Figure 4.2-4: Change in RESI capacitance vs time observed upon injection of three different concentrations of DDT-AuNPs on gold electrode surfaces in a running electrolyte solution of 0.1 M KNO_3; at 5 µL/min flow rate.

Table 4.2-2: Quantitative determination of nanoparticle-electrode collisions of DDT-AgNPs on gold electrodes for systems at different concentration ratios.

[a] results for DDT-AgNPs and [b] results for DDT-AuNPs.

NP concentrations (µM)	**Number of metal atoms**	**Nano-impact sizing (nm)**
~1.0	1.89×10^{9} [a] 1.49×10^{9} [b]	6.71 ± 2.05 [a] 3.99 ± 0.90 [b]
~5.0	6.86×10^{9} [a] 2.56×10^{9} [b]	12.8 ± 3.96 [a] 5.86 ± 2.16 [b]
~25	7.18×10^{9} [a] 6.12×10^{9} [b]	13.8 ± 4.70 [a] 7.84 ± 2.12 [b]

4.2.2. Nano-impact collisions of DDT-capped metal nanoparticles

The effect of changing the flow rates on DDT-AgNPs and the nanoparticle-electrode collision behaviour at bare gold electrode surfaces was studied using RESI and Chronoamperometry. Flow rate of 5 µL/min with the residence time for 40 min compared to the flow rate of 100 µL/min at 5 min residence time were compared. Furthermore, this study will compare the nano-impact events of DDT-AgNPs with that of DDT-AuNPs using both RESI and particle chronoamperometry technique i.e. Chronoamperometry.

For more detailed information on the set up of the nano-impact collision experiments and the physical meaning of RESI capacitance responses were outlined in Chapter 3.

4.2.2.1. Nano-impact collision experiments of DDT-AgNPs

RESI analysis

The collision and adsorption behaviour of DDT-AgNPs (1.1 µM) was investigated using z-LAB for real-time measurements by following changes in RESI capacitance in a background solution of 0.1 M KNO_3, upon injection of NP dispersed in EtOH. 200 µL of the dispersed solution (DDT-AgNPs dispersed in EtOH solvent) was injected into the system after 15 min stabilisation and the changes in RESI capacitance responses were recorded (Figure 4.2-5).

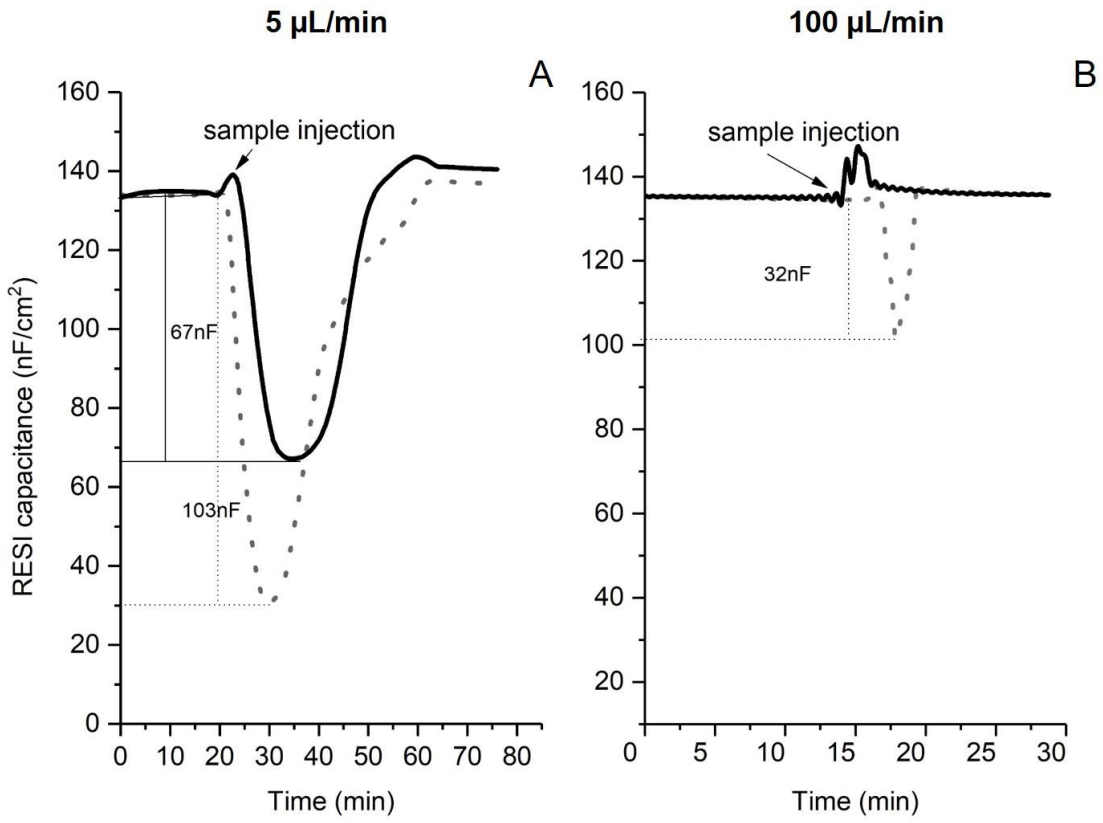

Figure 4.2-5: Change in RESI capacitance vs time at different flow rates for the collision behaviour of DDT-AgNPs (**black solid line**) on gold electrode surfaces in a running electrolyte solution of 0.1 M KNO_3; A) 5 µL/min and B) 100 µL/min. DDT-AgNPs compared to solvent (EtOH - **dotted grey line**). [DDT-AgNPs] = 1.1 µM.

Two flow rates were compared to assess the effects of flow rate by collision behaviour of DDT-AgNPs on the electrode surface. At a low flow rate (5 µL/min, Figure 4.2-5A), the injection of EtOH to the aqueous KNO_3 background electrolyte resulted in a decrease in RESI capacitance of 103 ± 6.3 nF (Figure 4.2-5A dotted line). It has been reported that the Electrical Double Layer (EDL) capacitance varies with the physical properties of the solvent in the electrolyte.[15,16] A study by Hou *et al.*[17] using Electrochemical Impedance Spectroscopy, a two-electrode system with platinum electrodes was carried out to identify the key properties of solvent that has a greater influence on the EDL capacitance. They reported that the EDL capacitance changes were not related directly to dielectric constants or dipole moments of the solvent but were proportional to the length of the molecule along the dipole moment.[17] A range of solvents were tested (acetonitrile, ethanol, water etc.) and the EDL capacitance value for

water was 35 μF cm^{-2} compared to 11 μF cm^{-2} for EtOH. It is likely that a similar trend is manifested in the changes in RESI capacitances observed.

The injection of DDT-AgNPs loaded EtOH showed an instantaneous U-shaped decrease in RESI capacitance of 67 ± 2.9 nF (Figure 4.2-5A **solid line**), which is approximately 36 nF less decrease in RESI capacitance compared to EtOH without the AgNPs. Although we have attributed the U-shaped dip to the adsorption/agglomeration followed by desorption/disintegration of any AgNPs clusters formed at the gold electrode's surface. An alternative interpretation could be that the U-shaped response be due to the solvent in which the NPs were suspended in, and the shoulder peak increase seen on Figure 4.2-5A **solid line** between t = 50 and 60 min, referring to the reversible agglomeration of NPs at electrode surface followed by desorption and disintegration of NPs clusters. This process (reversible NPs clustering and consequence disintegration) can cause an increase in surface roughness and consequently the surface area of the electrode, resulting in higher RESI capacitance compared to the injection of EtOH.

At a higher flow rates (100 μL/min, Figure 4.2-5B) injection of EtOH displayed less decrease in RESI capacitance of the order of 32 nF ± 2.4 nF (relative to the background electrolyte). The DDT-AgNPs loaded EtOH did not show any decrease in RESI capacitance (C_R) at this given flow rate, a blip was observed with a slight increase in RESI capacitance of about 10 nF, suggestive of NPs clustering and disintegration at electrode's surface.

These preliminary experiments indicate that at the slow flow rate of 5 μL/min, dwell time in the microfluidic chamber is sufficiently slow to enable the particles to form reversible agglomerates on the Au electrode surface. These qualitative, first experiments clearly indicated the major effect of flow rate on the capacitance on an electrode in a microfluidic chamber.

Chronoamperometric analysis

The redox behaviour of the DDT-AgNPs was first identified by modifying the surface of the gold electrode with DDT-AgNPs; the electrodes were held at a potential of 0.6 V and the cell was filled with a solution of NPs in EtOH dispersion and 0.1 M KNO_3 for 45 min. This technique enabled the immobilisation with thiolated NPs to form SAM layer *in situ* on gold electrode surface by electrochemical deposition method (method outlined in Chapter 3).[18] Following the modification of the working electrode surfaces, electrochemical experiments were performed in a solution of 0.1 M KNO_3 which yielded an anodic peak at 0.05 V and a small cathodic peak at -0.28 V (vs Pt reference electrode), at a scan rate of 50 mV/s. The background solution (before) did not show any peaks (Figure 4.2-6). The Cyclic Voltammograms (CVs) observed were not dissimilar to those reported previously[11,17,19]. There are few reports of size related physical properties of silver nanoparticles less than 15 nm which differ from those of bulk metal. Chaki *et al.*[20] performed CVs on DDT-AgNPs of different sizes dropcast on Pt disc electrode from toluene dispersions. They reported small peak currents with CVs showing sharper anodic than cathodic peaks, they suggested that this was due to “more facile oxidation process”.

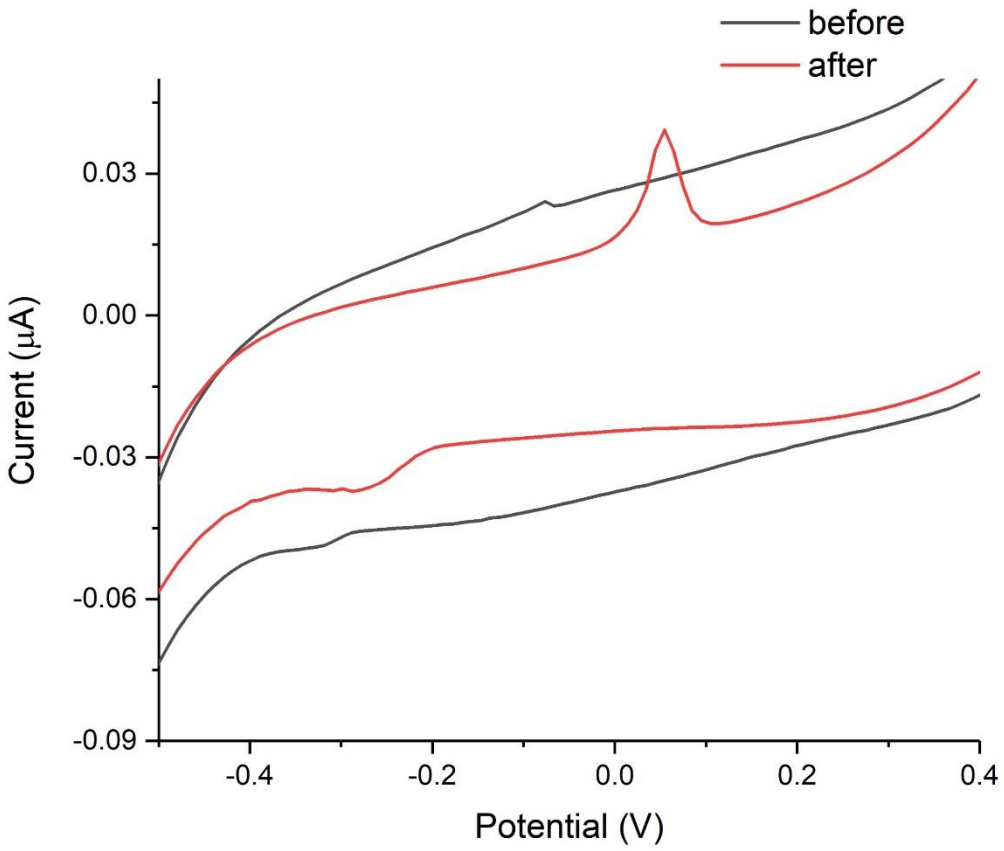

Figure 4.2-6: Cyclic Voltammetry responses of DDT-AgNPs modified gold electrode in 0.1 M KNO_3 at 50 mV/s scan rate; 'before' refers to the measurements carried out using unmodified electrode and 'after' refers to the measurements carried out using the DDT-AgNPs modified electrode.

Chronoamperometric measurements were performed using a flow cell system set at the appropriate flow rates with the working electrode held at 0.1 V vs a Pt pseudo reference electrode (Figure 4.2-7); a potential that promotes the oxidation of DDT-AgNPs. Results obtained at a flow rate of 5 µL/min indicate that following the injection of DDT-AgNPs dispersed in EtOH (1.1 µM) into the running electrolyte solution (Figure 4.2-7A), a sharp increase in current by approximately 132 nA, followed by subsequent current transients, were observed. However, the injection of blank EtOH into the background electrolyte was featureless (inset on right hand side in Figure 4.2-7). The large increase in current at the slow scan rate must be caused by agglomerated DDT-AgNPs on the Au electrode surface. The insets in Figure 4.2-7A show the shape of the two peaks obtained in approximately 80 s after injection. These spikes observed likely correspond to the partial oxidation of agglomerated DDT-AgNPs.

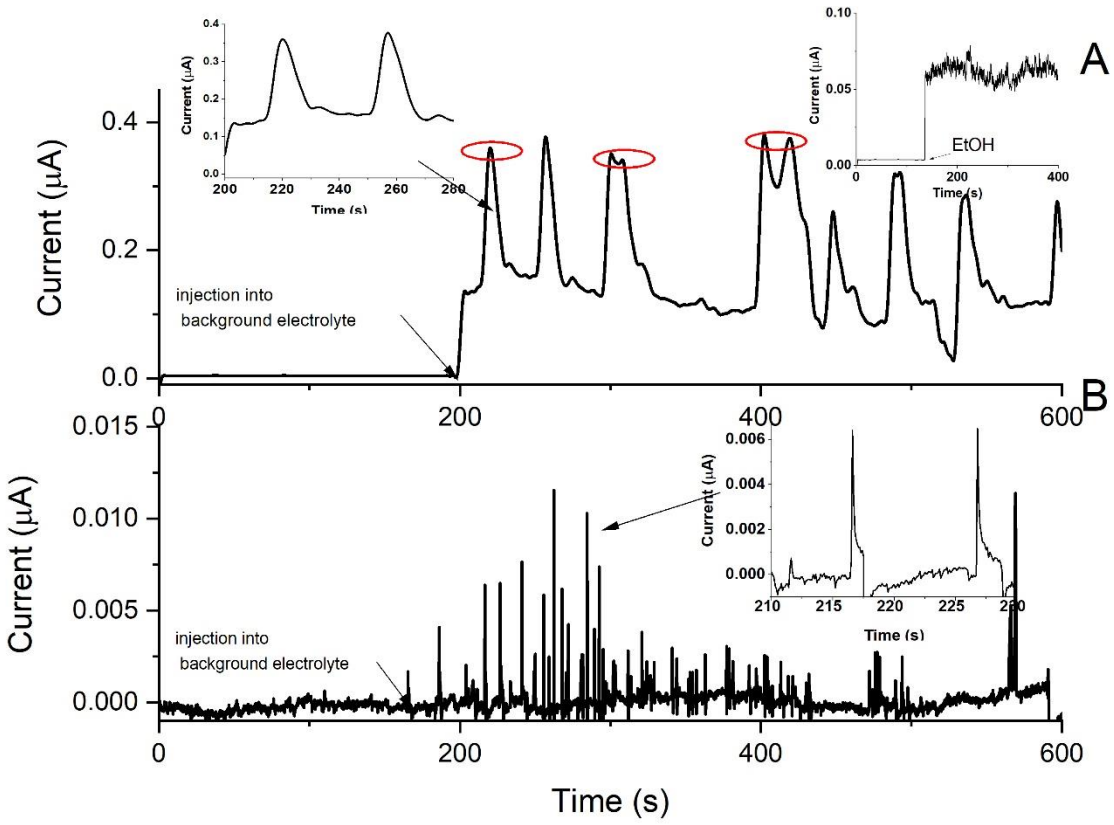

Figure 4.2-7: Current-time signals representing DDT-AgNPs (1.1 μM) oxidation at bare gold electrodes by applying E = 0.1 V at **(A)** 5 μL/min and **(B)** 100 μL/min as the set flow rate in a running electrolyte solution of 0.1 M KNO_3. The 1st 200 s in both runs is the stabilisation period with only electrolyte solution running. After 200 s, the DDT-AgNPs dispersed in EtOH was injected. Injection points are depicted by an arrow. [DDT-AgNPs] = 1.1 μM.

The insets on the left, show the first 2 oxidation peaks following the insertion of NPs. The inset on the top right shows the effect of the solvent EtOH without NPs.

From the information extracted from Figure 4.2-7A, spike charge (*Q*, charged passed under an individual spike) at impact was determined by the integration of spike area under current-time signal, ($Q = \int Idt$).[21] From this value, assuming full oxidation of Ag (this assumption is not strictly accurate but gives an indication of the minimum number of AgNPs in an agglomerate), the number of Ag atoms oxidised per NP impact was determined as it is related to the anodic charge by Faraday's Law where *n* is the number of moles of Ag and *z* the number of electrons exchanged during the oxidation of Ag atoms ($Q = nzF$), *z* which corresponds to 1 and the Faraday constant (*F*, 9.65 x 10^4 C mol^{-1}).[21]

A study by Ellison *et al.*[21] on the use of nano-impact events to determine the sizes of AgNPs as well as the state at which these NPs aggregate or agglomerate. In their study, they

assumed that NPs were spherical in size and that the direct oxidation of AgNPs were responsible for the spike current, although their results detected both aggregates and agglomerates at nano-impact events, they used Eq. 4-1 to enable them to carry out the distinction of states. The same method was utilised in our study to quantify the nano-impact events; for each current spike generated, the impacting NPs at the working electrode generated anodic spikes which were associated with the charge passed during the oxidation of the NPs at impact on the electrode's surface. Eq. 4-1, taken from ref. [22], was used to determine the NPs diameter size (d_{NP}) from charge Q, atomic molar mass of silver (M_w, 107.9 g mol^{-1}), the Faraday constant (F, 9.65 x 10^4 C mol^{-1}) and density of silver (ρ, 1.05 x 10^6 g m^{-3}).[23]

$$d_{NP} = 2^3 \sqrt{\frac{3M_w Q}{4F\pi\rho}} \qquad \textbf{(4-1)}$$

From the results of the direct oxidation of DDT-AgNPs at 5 and 100 µL/min, after the injection of the NPs into the background electrolyte was analysed using the equation stated below to determine d_{NP} (Eq. 4-1) and N ($Q = eN$ with e = electron charge, 1.60 x 10^{-19} C) at nano-impact events.

Table 4.2-3: The determination of the NP diameter (d_{NP}) and the number of Ag atoms (N) for each peak taken from Figure 4.2-7 inserts following the insertion of NPs for the oxidation of DDT-AgNPs at 5 and 100 µL/min.

Flow rate		**NP or aggregate diameter (d_{NP}) /nm**	**Number of Ag atoms (N) for each peak**
5 µL/min	Peak 1	9.0 x 10^2	3.1 x 10^{13}
	Peak 2	9.1 x 10^2	3.2 x 10^{13}
100 µL/min	Peak 1	5.0 x 10^1	9.4 x 10^{10}
	Peak 2	3.5 x 10^1	4.8 x 10^{10}

Analysis of each of the first two peaks gives approximately a diameter of 9.1 x 10^2 nm (5 µL/min, Table 4.2-3), corresponding to large aggregates of at least 100-150 Ag NPs. Subsequently, split spikes (circled in Figure 4.2-7A) were observed. We believe these spikes

were caused by a perturbation and breakdown of the large agglomerates of DDT-AgNPs on the Au electrode surface accompanied by multi-electron tunnelling of electrons.

At a higher flow rates (100 µL/min, Figure 4.2-7B), the injection of DDT-AgNPs loaded EtOH did not show an increase in baseline capacitance compared to the background solution. Sharp spikes were observed with peak currents of about 6 nA. The inset in Figure 4.2-7B, showing an expanded view of the first 40 s after injection of the NP; indicate an exponential decay of current. The current spikes died down after approximately 700 s, indicating any adsorbed NPs were washed out by the background electrolyte in this time frame. We are confident the spikes are caused by NP impact as EtOH without the NPs under similar conditions, did not display the spiking behaviour. Chronoamperometric analysis of the first two peaks gave an agglomerate diameter of 50 nm for the first peak and 35 nm for the second peak, corresponding to much smaller sizes of 4-5 NPs per agglomerate, compared to the sizes determined at slower flow rate. This phenomenon must have been due to the reduced dwell time of the AgNPs containing solution in the microfluidic chamber at higher flow rate, identified in the RESI results.

Conventionally, nanoparticle collision experiments are carried out in static systems whereby the Brownian motion transports the NPs to the electrode's surface. Jiang *et al.*[24] investigated the role of magnetic stirrers in such experiments while Robinson *et al.*[25] used a magnetic field to help guide magnetic NPs through microfluidic devices for their detection via impact events. Both findings, from Jiang and that of Robinson and their co-workers, have demonstrated the use of hydrodynamic systems for an increase in current intensities during collision events; using forced convection dramatically increased the collision frequencies showing up to 6-fold current signal increase. In our experiments, we observed an expected increase in collision frequencies with increased flow rate. The related observation was of the shape and size of the current spikes. Broader spikes as detected at lower flow rate (5 µL/min) were found to be synonymous to the detection of large agglomerated particles at impact events. The narrower

spikes detected at higher flow rates (100 µL/min), may be evidence of multiple individual collisions yielding smaller agglomerated particles. The responses at higher flow rates are likely to be to more "Hit-n-Run" type collisions with multiple individual collisions seen with the presence of Faradaic spikes and short transient time. At slower flow rates; the response was likely to be a combination of "Hit-n-Stand" and "Hit-n-Run "collision, with more "Hit-n-Stand" characteristics consistent with the detection of semi-permanent adsorbed NPs agglomerates at electrode's surface.[26] We would expect that if large agglomerates hit the surface of the electrode without fully being desorbed, this would lead to partial detachment of adsorbed NPs at electrode's surface followed by the generation of stepwise current increases with subsequent NPs collisions however, this was not detected during our experiments.

4.2.2.2. Nano-impact collision experiments of DDT-AuNPs

RESI analysis

Similar procedures were used in the study with DDT-AgNPs was carried out for the collision and adsorption behaviour of DDT-AuNPs, the changes in RESI capacitance responses to the nano-impacts events at electrode's surface were recorded (Figure 4.2-8).

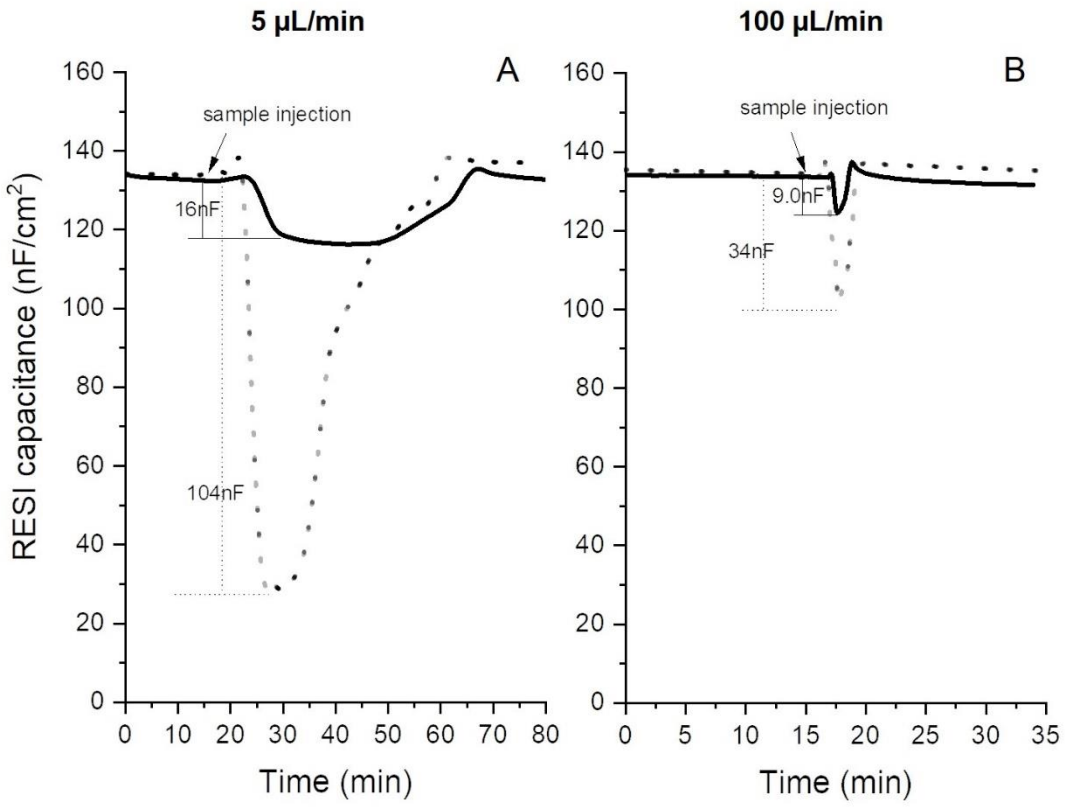

Figure 4.2-8: Change in RESI capacitance vs time at different flow rates for the collision behaviour of DDT-AuNPs (**black solid line**) on gold electrode surfaces in a running electrolyte solution of 0.1 M KNO_3; A) 5 µL/min and B) 100 µL/min. [DDT-AuNPs] = 1.2 µM.

The collision behaviour study of DDT-AuNPs was investigated by comparing the two flow rates; 5 and 100 µL/min (Figure 4.2-8), in assessing the effects of flow rate on the electrode surface.

Following the interpretation of the RESI results that the shoulder peak on the NPs curve be that of reversible NPs agglomeration at electrode's surface seen in Figure 4.2-8A and B between t = 60-70 min at 5 µL/min and between t = 17-20 min at 100 µL/min, these results can be said to support such conclusion. With the presence of U-shaped RESI capacitance showing solvent effect instead of the reversible AgNPs clustering process formed at the gold electrode's surface. Alternatively, the reduced RESI capacitance for DDT-AuNPs; 16 nF ± 5.3 nF compared to 67 ± 2.9 nF of DDT-AgNPs, could be said to be evidence of minimal agglomeration of absorbed NPs at electrode surface at lower flow rate compared to high flow rate showing reduced agglomeration and adsorption events.

What we need to understand from these metallic NPs is that, AgNPs are known to have a higher heterogeneity thus they have an increased instability as colloidal solution, their NPs instability lies in the 'failure of the protective coating to prevent agglomeration'[27] as the compatibility of dodecanethiol ligands depend on the nature of the solvent.[28] A study by Stevenson *et al*.[29] investigating different strategies to maintain homogeneity of AgNPs in aqueous solutions have found that making alloys of the compound i.e. bi-metallic core shells such as Ag-Au, are more stable than simple AgNPs. On the other hand, Au has higher electron affinity than Ag, hence as metallic core, they form stronger interactions with their capping ligands to make stable NPs compared to AgNPs. As a result, Au containing NPs have improved size, long term stability and homogeneity.

Chronoamperometric analysis

The redox behaviour of the DDT-AuNPs was first identified by modifying the surface of the gold electrode with DDT-AuNPs in the same way with that of the DDT-AgNPs, then performing electrochemical experiments in a solution of 0.1 M KNO_3 which yielded a strong anodic peak at 0.05 V (vs Pt reference electrode), at a scan rate of 50 mV/s. From Figure 4.2-9, two anodic peaks are seen, it has been reported that alkanethiolate-protected AuNPs generate multiple peaks.[30]

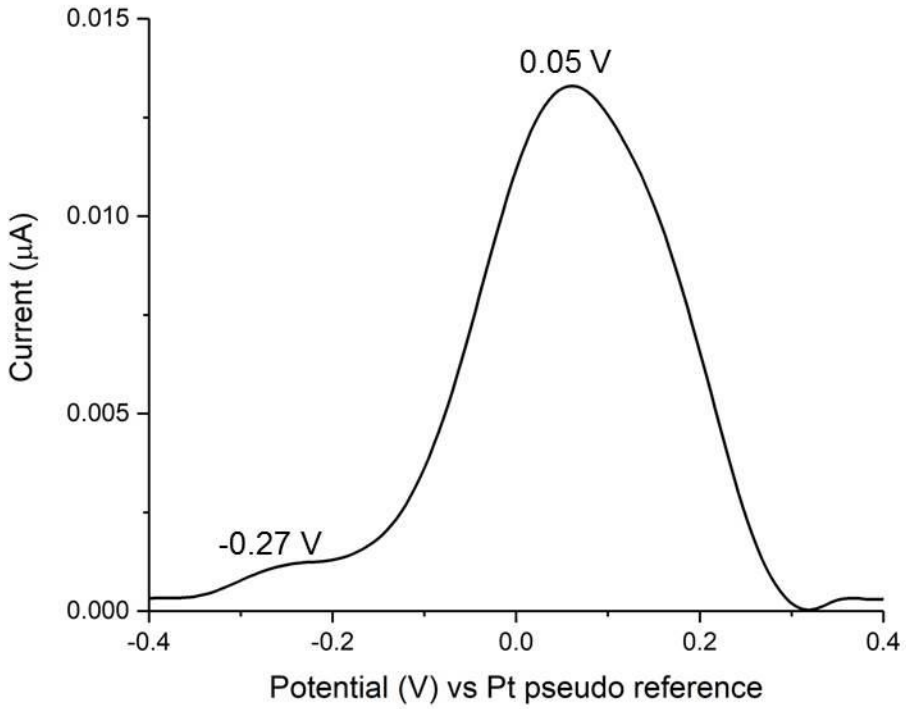

Figure 4.2-9: DPV responses of DDT-AuNPs modified gold electrode in 0.1 M KNO_3 at 50 mV/s scan rate.

Chronoamperometric measurements were performed using a flow cell system set by poising the electrode potential of the working electrode at 0.1 V vs a Pt pseudo reference electrode (Figure 4.2-11), applying the appropriate flow rates and measuring the current response from the oxidation of DDT-AuNPs at potentiated electrode surface.

Following the injection of DDT-AuNPs dispersed in EtOH (1.5 µM) into the running electrolyte solution (Figure 4.2-11), a similar sharp increase in current by approximately 0.33 pA was recorded, followed by subsequent current transients, were observed. Although we observed a slight increase in mean diameter sizes for DDT-AuNPs, from 4.2 ± 1.6 nm to 5.2 ± 1.7 nm with increasing flow rates, 5 µL/min and 100 µL/min respectively. However, further analysis of the number of Au atoms detected per nano-impact events revealed that larger aggregates of NPs were determined at slower flow rate (5 µL/min), synonymous to the large number of Au atoms (Figure 4.2-10).

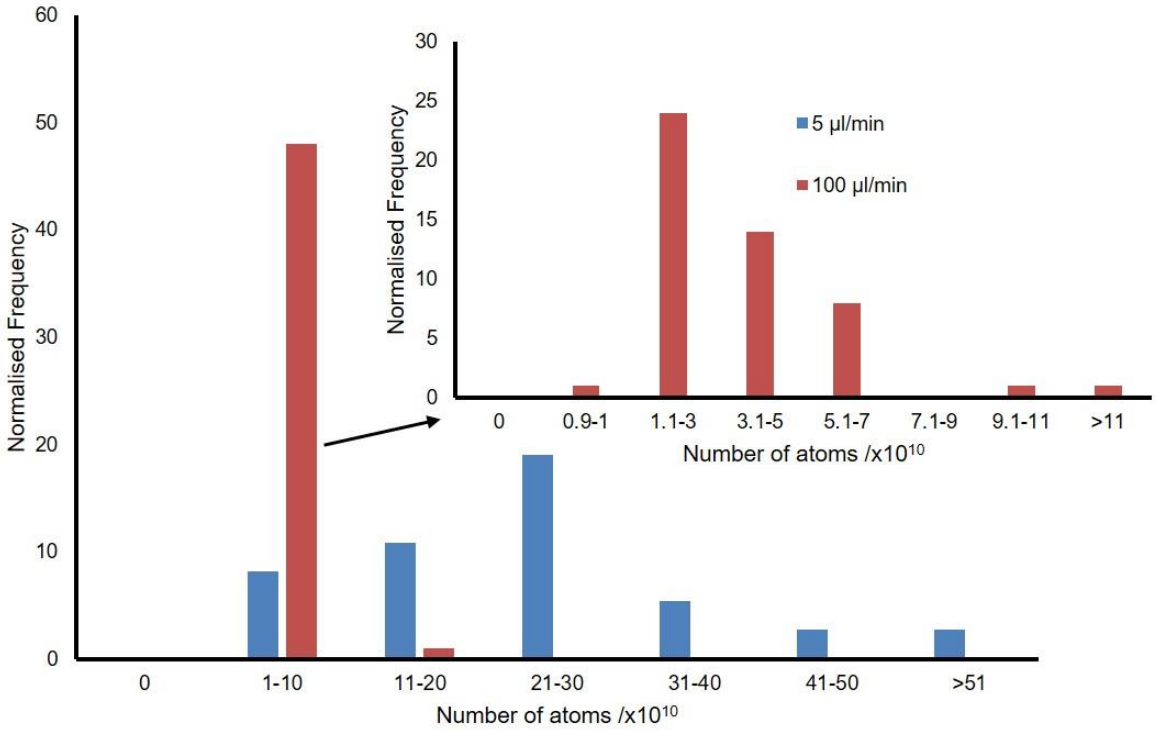

Figure 4.2-10: Distribution of NP size obtained from $Q = eN$ to determine the number of Au atoms per nano-impact event, based on the nano-impact results from Figure 4.2-11 of DDT-AuNPs dispersed in EtOH in a running electrolyte solution of 0.1M KNO_3.

On the other hand, the analysis of DDT-AgNPs registered a decrease in mean NP sizes from 527 ± 575 nm to 33 ± 8.5 nm with increasing flow rates (Table 4.2-4). Consequently, we can differentiate the findings from both metallic NPs, with agglomerated AgNPs forming clusters and increasing in sizes as the flow rates are lowered, while no such evidence of cluster formation was detected for DDT-AuNPs. Thus, supporting the conclusion of the instability of AgNPs in aqueous solvents, and its higher affinity to aggregate especially at lower flow rate.

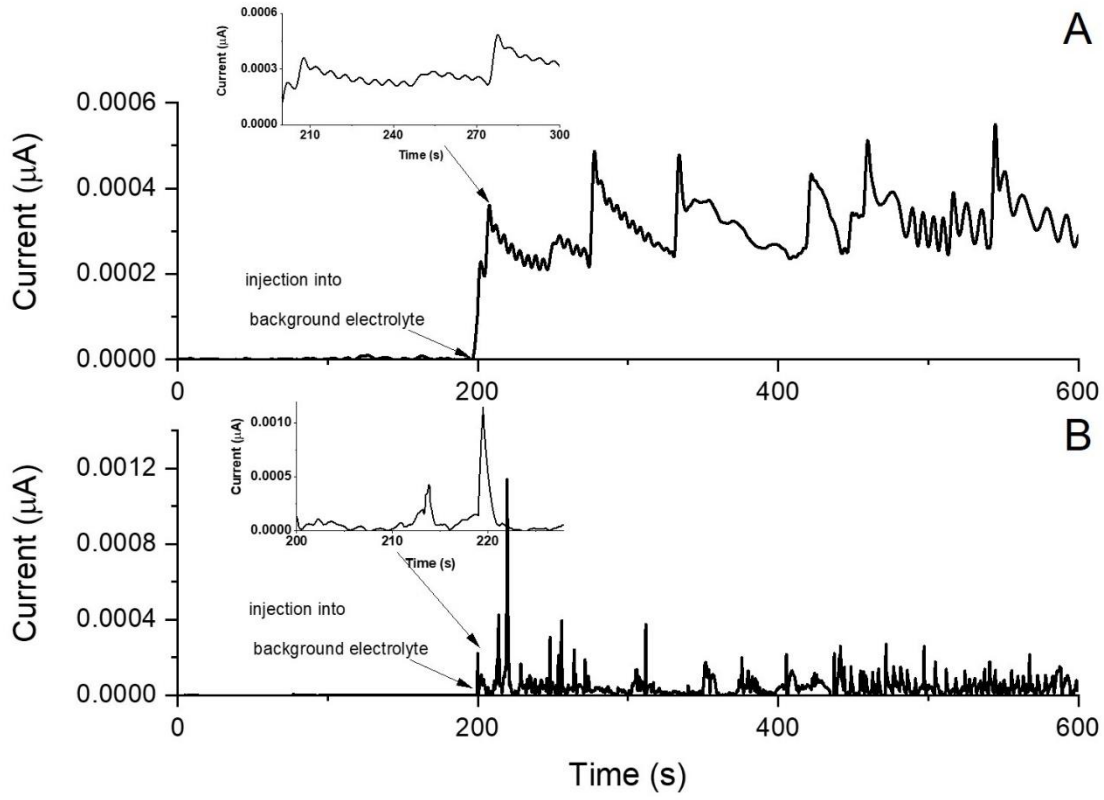

Figure 4.2-11: Current-time signals representing DDT-AuNPs (2.3 μM) oxidation at bare gold electrodes by applying E = 0.1 V at (A) 5 μL/min and (B) 100 μL/min as the set flow rate in a running electrolyte solution of 0.1 M KNO_3. The 1st 200 s in both runs is the stabilisation period with only electrolyte solution running. After 200 s, the DDT-AuNPs dispersed in EtOH was injected. Injection points are depicted by an arrow. [DDT-AuNPs] = 1.2 μM.

The insets on the left, show the first 2 oxidation peaks following the insertion of NPs. The inset on the top right shows the effect of the solvent EtOH without NPs.

Table 4.2-4: Quantitative determination of nanoparticle-electrode collisions comparing nano-impact sizing of DDT-AgNPs with DDT-AuNPs on gold electrodes at different flow rates: [a] d_{NP} was determined from Eq.4-1. Spike analysis and fitting were carried using OriginPro.

Flow rates (μL/min)	Mean NP or aggregate diameter of 1st peaks (d_{NP}) /nm [a]		Mean nano-impact sizing /nm [a]		Mean number of metal atoms (*N*)	
	AgNPs	***AuNPs***	***AgNPs***	***AuNPs***	***AgNPs***	***AuNPs***
5	583 ± 316	4.58 ± 1.75	527 ± 575	4.18 ± 1.57	$8.30 \pm 5.10 \times 10^{12}$	$2.46 \pm 1.93 \times 10^{11}$
100	29.4 ± 9.20	4.85 ± 0.78	33 ± 8.50	5.16 ± 1.68	$1.08 \pm 0.57 \times 10^{11}$	$3.64 \pm 2.92 \times 10^{10}$

When comparing the collision behaviour of DDT-AuNPs with DDT-AgNPs at different flow rates in a background solution of 0.1 M KNO_3 (DDT-AuNPs - Figure 4.2-11, DDT-AgNPs - Figure 4.2-7 and Table 4.2-4), the results obtained have demonstrated that both NPs have

similar attributes of collision behaviours but different nano-impact sizing characteristics overall. When comparing to the sizing by TEM; 2.8 ± 1.04 nm and 4.9 ± 1.2 nm for DDT-AuNPs and DDT-AgNPs respectively, nano-impact sizing of AgNPs detected clusters thus generating inflated sizing of NPs (527 ± 575 nm at 5 µL/min and 33 ± 8.50 nm at 100 µL/min) compared to individual NPs detected by TEM characterisation. However, nano-sizing of AuNPs detected sizes of that can be said to be comparable to that of TEM characterisation at both flow rates; 4.18 ± 1.57 nm and 5.16 ± 1.68 nm at 5 and 100 µL/min respectively.

We concluded that higher flow rates generated multiple individual NP collisions whereas singular NP collisions were generated at lower flow rates, seen by the detection of multiple spikes at higher flow rates compared to individual (sparse) spikes at lower flow rates.

4.2.3. Nano-impact collisions of FcHT-capped metal nanoparticles

4.2.3.1. Nano-impact collision experiments of FcHT-AgNPs

The Electrochemical deposition method was also used to immobilise the gold electrode surface in the same way as was outlined in the DDT-capped experiments. The electrochemical technique used to determine the redox characteristics of FcHT-AgNPs in a solution of 0.1 M KNO_3 was differential pulse voltammetry (DPV). The electrochemical responses recorded an oxidative peak at +0.35 V, which was identified as the ferrocenium ion (Fc+) peak (Figure 4.2-12); oxidised Fc sites on nanoparticle have been recorded to give peaks in the region of +0.2 to +0.30 V with the formal redox potential of Fc at +0.4 V.[31] The peak at +0.03V corresponds to the oxidation of silver to silver(I) ions.

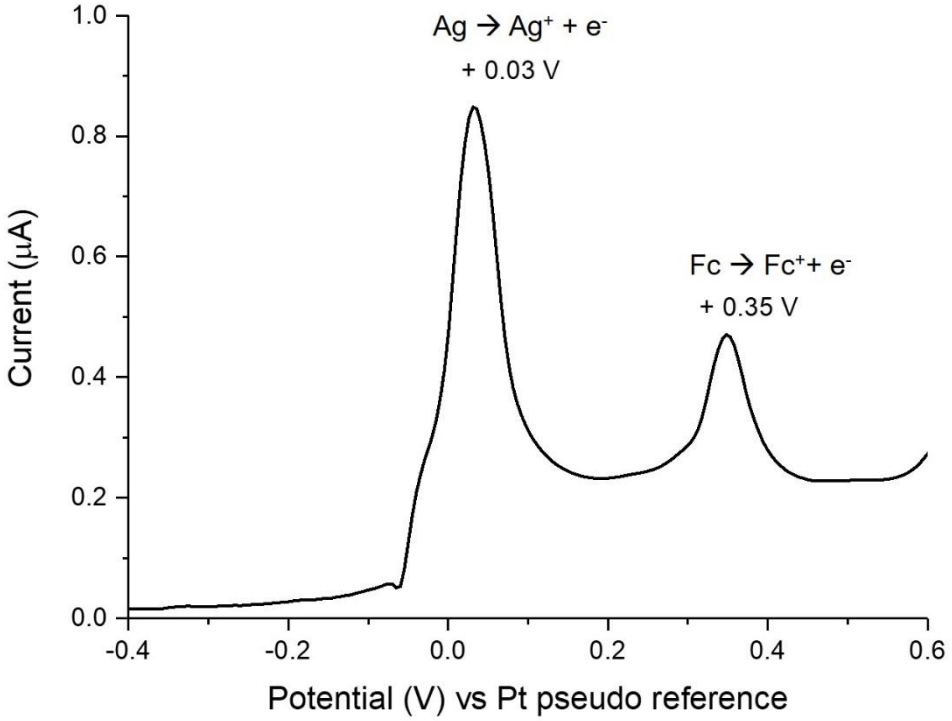

Figure 4.2-12: Voltammetry responses of FcHT-AgNPs modified gold electrode in 0.1 M KNO_3; DPV after modification of electrode. Sweep amplitude: 5 mV.

Both RESI and Chronoamperometry were then used to monitor the impact of the FcHT-AgNPs in a flow configuration (Figure 4.2-13).

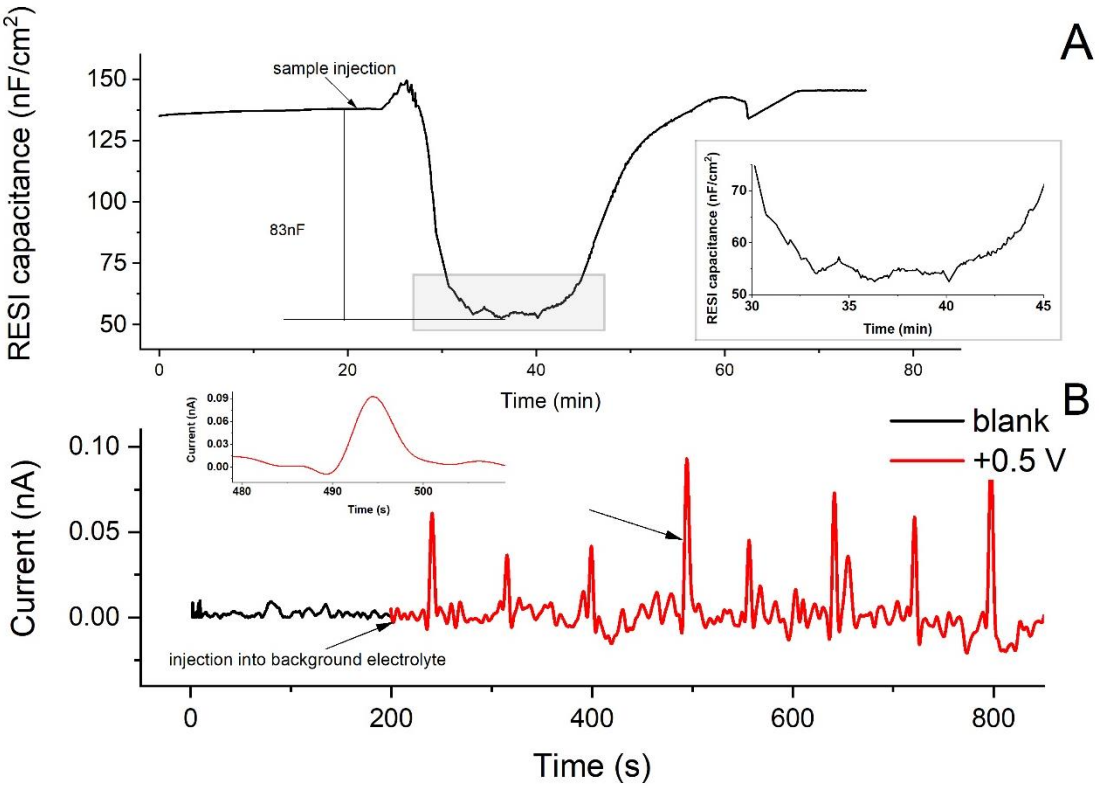

Figure 4.2-13: A) Change in RESI capacitance vs time for the collision behaviour of FcHT-AgNPs (dispersed in EtOH solvent) upon their introduction into a running electrolyte solution of 0.1 M KNO_3 at a set flow rate of 5 µL/min; insert showing of nano-impact events at electrode's surface. B) Current-time signals representing the redox events of FcHT-AgNPs (dispersed in EtOH solvent) at bare gold electrodes by applying potential at +0.5 V (inducing oxidation of FcHT ligands) at 5 µL/min as the set flow rate in 0.1 M KNO_3. 'Blank' is the background electrolyte. [FcHT-AgNPs] = 3.0 µM.

RESI analysis

The collision, adsorption and agglomeration behaviour in real time of using z-LAB was made in a background solution of 0.1 M KNO_3. 200 µL of FcHT-AgNPs dispersed in EtOH (3.0 µM) was injected after 15 min stabilisation of the system and the changes in RESI capacitance responses were recorded at 5 µL/min as set flow rate. The shape of the z-LAB traces for RESI capacitance, following injection of FcHT-AgNPs in EtOH, showed an instantaneous U-shaped decrease.

Reverting to the interpretation of the U-shape being significant to the indication of nano-impact events of agglomerated NPs colliding at electrode's surface seen with the presence of smaller changes in RESI capacitance observed at the bottom of the U-shaped well. The RESI capacitance for FcHT-AgNPs was lowered by 83 ± 1.8 nF (Figure 4.2-13A) compared to the background solution. This drop is approximately 16 nF lower compared to DDT-AgNPs and

the dwell time of the agglomerated FcHT-AgNPs was calculated at approximately 16 min compared to 14 min for the DDT-AgNPs, (insets; Figure 4.2-7A and Figure 4.2-13A). This interpretation is further supported by a study by Compton *et al.*[31] who reported that capacitive effects on impacted electrode surface can be due to the perturbation of the double layer electrode–electrolyte interface and from charging effects of the impacting NP. In view of this, it is likely that the smaller RESI capacitive changes at the trough of the well are due to perturbations of the bulky 6-(Ferrocenyl)hexanethiol groups upon impact as a sinusoidal voltage of 40 mV is applied to the electrodes.

Any electrochemical response from a nanoparticle bearing multiple electroactive ligands contains two contributions; one from the redox reactions of the ligand, and another from the charging of the metal core. This means these metallic NPs can store multiple charge equivalents which can be released over a narrow window of potential.

Chronoamperometric analysis

Chronoamperometric measurements were performed by poising the electrode potential at +0.5 V, based on the DPV results (Figure 4.2-12). No Faradaic features were recorded at 'blank' injection, under potentiated conditions. However, spikes were generated immediately following the injection of FcHT-AgNPs (Figure 4.2-13B). The collision of FcHT-AgNPs at the electrode's surface at positive potential must be, primarily, due to the oxidation at +0.5 V, of FcHT ligands attached to the NPs and secondarily, to the multiple redox events of AgNPs core and the ferrocene ligands as the stabilising monolayer (Figure 4.2-13B).

FcHT-AgNPs are neutral in the bulk electrolyte. The current spikes generated by direct oxidation of Fc ligand to Fc^+ cation via the collision of NP results in the repulsive NP-electrode interaction at the electrode poised at +0.5 V, thus the inhibition of the formation of agglomerates at electrode surface. Due to the complexity of the origination of cause of current peaks; the ligands' redox reactions or that of core metal charging, the estimation of NPs size

using the Eq.4-1, may not be applicable, thus the comparison of sizes between impacting NPs may be skewed.

4.2.3.2. Nano-impact collision experiments of FcHT-AuNPs

Differential pulse voltammetry (DPV) was used to determine the redox characteristics of FcHT-AuNPs in a solution of 0.1 M KNO_3 and, the deconvoluted curves revealed the peak for FcHT-AuNPs for the ferrocenium ion (Fc+) peak (Figure 4.2-14) was identified at +0.23 V and the oxidation of gold to gold(I) ions at 0.15 V; when compared the DDT-AuNPs peak at 0.05 V for the metal core oxidation, the anodic shift in voltage can be said to be influenced by the Fc ligands.

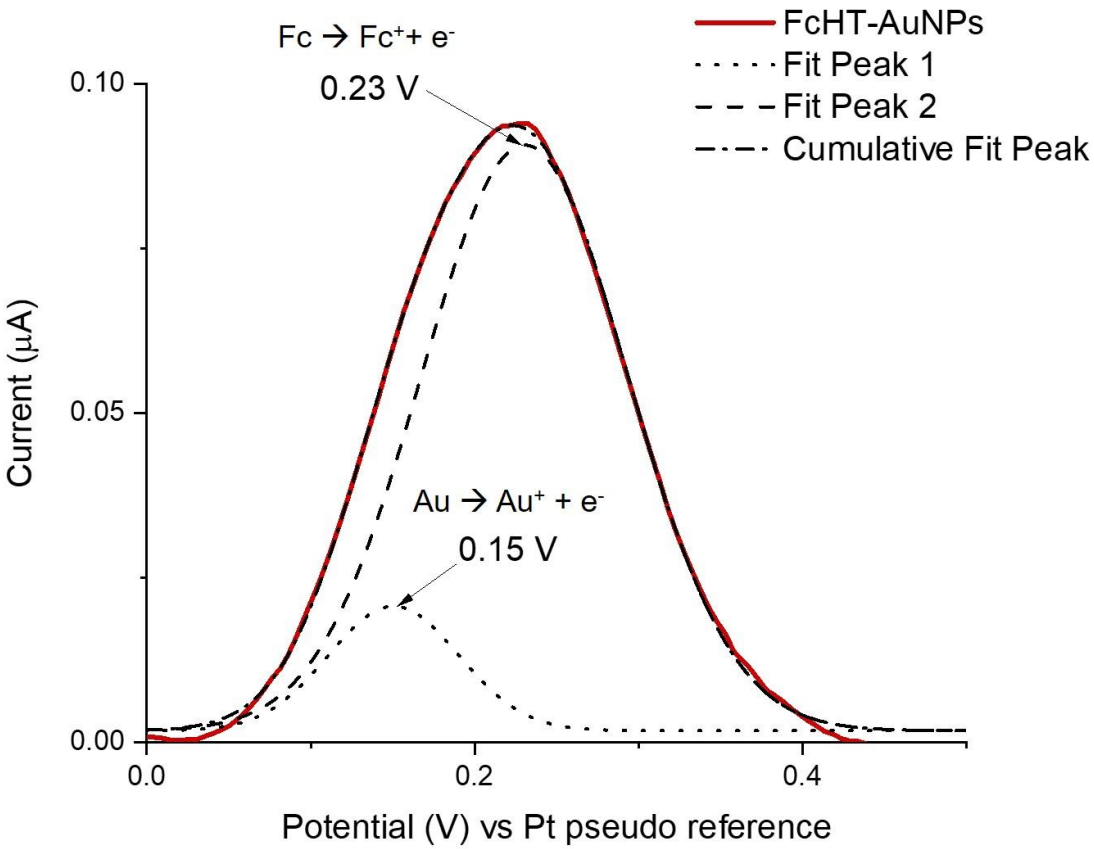

Figure 4.2-14: Voltammetry responses of FcHT-AuNPs modified gold electrode in 0.1 M KNO_3; DPV after modification of electrode. Sweep amplitude: 5 mV. Insertion of deconvoluted curves for the differentiation of metal core oxidation from Fc oxidation.

Applying +0.5 V potential at the working electrode for the oxidation of Fc ligands on the NPs enabled the quantitative characterisation of NPs via nano-impacts (Figure 4.2-15).

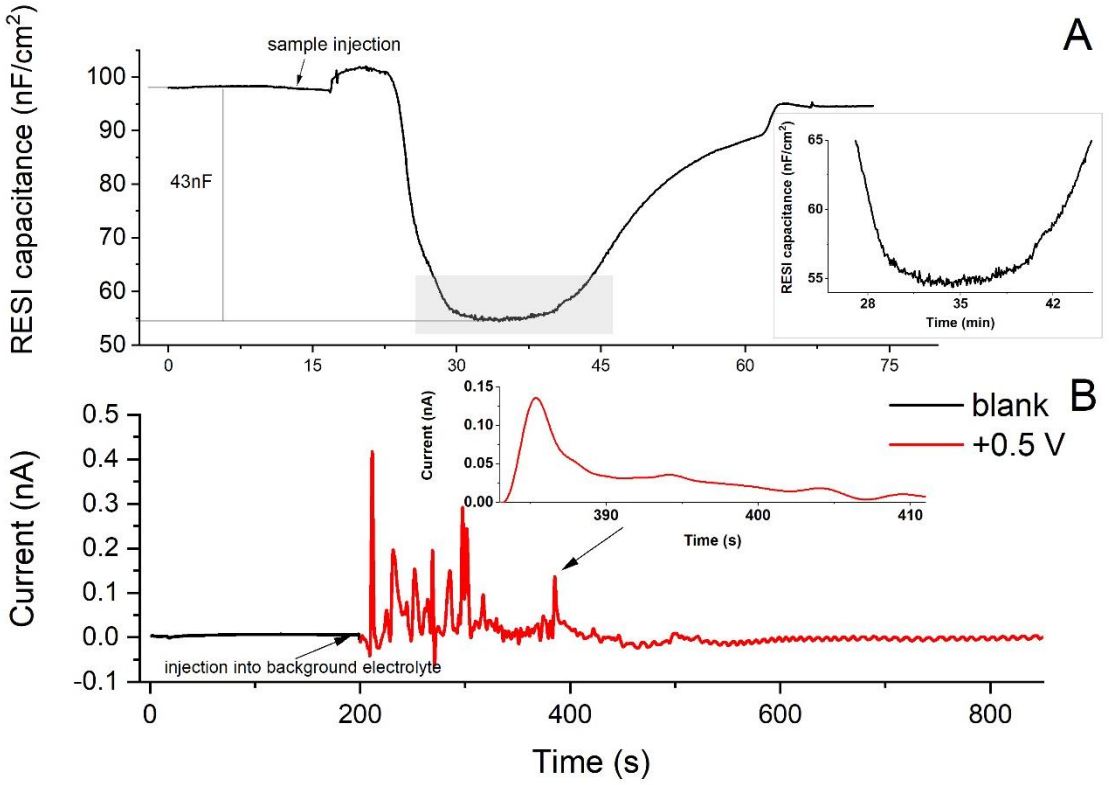

Figure 4.2-15: A) Change in RESI capacitance vs time for the collision behaviour of FcHT-AuNPs (dispersed in EtOH solvent) upon their introduction into a running electrolyte solution of 0.1 M KNO_3 at a set flow rate of 5 µL/min; insert showing of nano-impact events at electrode's surface. B) Current-time signals representing the redox events of FcHT-AuNPs (dispersed in EtOH solvent) at bare gold electrodes by applying potential at +0.5 V (inducing oxidation of FcHT ligands) at 5 µL/min as the set flow rate in 0.1 M KNO_3. 'Blank' is the background electrolyte. [FcHT-AuNPs] = 2.8 µM.

RESI analysis

The same parameters were applied for the nano-impact collision experiment for FcHT-AuNPs as was carried out for FcHT-AgNPs; 200 µL of the dispersed ethanoic solution of the colloid (2.8 µM) was injected into the system after 15 min system stabilisation at 5 µL/min as set flow rate in a background solution of 0.1 M KNO_3.

We reported for the FcHT-AgNPs, that the response of the RESI capacitance due to the nano-impact events at electrode surface showed an instantaneous U-shaped decrease, with a lowered RESI capacitance for FcHT-AgNPs of 83 ± 1.8 nF (Figure 4.2-13A) compared to the background solution. A decrease of RESI capacitance of 43 ± 0.92 nF was obtained for FcHT-AuNPs when compared to DDT-AuNPs, this RESI capacitance drop was approximately 27 nF higher that of the DDT-AuNPs with a dwell time of 12 min.

The calculations for the number of Fc ligands were adapted from Wolfe *et al*[32]; assuming 1.5 nm as the 'headprint' of Fc molecules arranged as a sphere with its radius equal to the average radius size of the metal core (Ag) plus the ligand chain length (-SC6Fe). The number of Fc ligands was calculated as 63 for AgNPs and 57 for AuNPs.

As the nano-sizing results for FcHT-metal NPs cannot be utilised for further analysis in determining the number of atoms at impacting events. Theoretical calculations were carried out to allow the comparison.

Theoretical calculation of number of ligands per nanoparticle

Assumed that all particles are completely spherical, the number of metal atoms per NP was determined using Eq.4-2 below from Liu *et al*[33].

$$N = \frac{\pi}{6}\frac{\rho D^3}{M} \qquad \textbf{(4-2)}$$

The TEM diameter (D), atomic molar mass of the metal (M, Ag = 108 g mol^{-1} and Au = 197 g mol^{-1}) and the density of face-centered cubic (fcc) of the metal (ρ, Ag = 10.5 g cm^{-3} and Au = 19.3 g cm^{-3}).

Table 4.2-5: Determination of the number of atoms and ligands per NP.

		TEM diameter (nm)	**Average number of metal atoms**	**The number of Fc ligands**
AuNPs	DDT	2.8 ± 1.04	6.57 x 10^2	**-**
	FcHT	5.5 ± 2.91	5.20 x 10^3	57
AgNPs	DDT	4.9 ± 1.2	3.60 x 10^3	-
	FcHT	8.0 ± 2.4	1.60 x 10^4	63

Comparing the number of atoms of FcHT-metal NPs to DDT-metal NPs, the former NPs have a higher number of atoms to add to the presence of Fc ligands, which can be said to be the reason for the shallower U-shaped dip of the RESI capacitance.

Chronoamperometric analysis

As was discussed in the results for FcHT-AgNPs, no Faradaic features were recorded at 'blank' injection, under potentiated conditions whilst current spikes appeared following the injection of FcHT-AuNPs (Figure 4.2-15B). As a particle collides with the electrode's surface, it generates an oxidation or reduction spike due to the electrochemical reaction taking place ($Fc \leftrightarrow Fc^{+} + e^{-}$). The redox spikes generated from FcHT-AuNPs have shown some characteristics of current-time decay behaviour illustrated by a sharp increase in current value followed by its slow decrease, which was found to be different from that of the FcHT-AgNPs (Figure 4.2-13B for AgNPs and Figure 4.2-15B for AuNPs).

The quantitative analyses of these current-time spikes are complicated due to the range of distributions and the multiple redox events involving the metallic core and electroactive ferrocene sphere. However, it is interesting to note that capping a nanoparticle with a redox active ligand can significantly affect the agglomeration behaviour of the particles, at the redox potential of the ligand.

4.3. Conclusion

Microfluidic cells with integrated electrodes are widely use in electrochemical analyses with modified metallic nanoparticles. To understand agglomeration, Resonance Enhanced Surface Impedance (RESI) and Chronoamperometry (CA) were used to analyse electrochemical behaviour. We were able to distinguish different nanoparticle-electrode collision behaviours using RESI technique, a qualitative technique that maps in real-time RESI capacitance on the surface of the electrode.

Electrochemical characterisation of thiol-capped silver and gold nanoparticles carried out using direct particle chronoamperometry via particle collisions at bare electrode surface revealed the effect of flow rates on agglomerate formation and dispersion of dodecanethiolate (DDT-) and *ω*-ferrocenylhexanethiolate (FcHT-) NPs at gold electrode surfaces. The results

show that factors such as flow rates and ligand electroactivity have significant impact on nanoparticle-electrode collision events.

The conclusion drawn from RESI results revealed that the shape of the RESI plot, U-shape decrease in RESI capacitance, was attributed to the solvent effect (EtOH) as well as NPs impacting at electrode's surface. We concluded that at slower flow rate (5 µL/min), the shape of the U-shaped dip was more pronounced to that at higher flow rate 100 µL/min, seen in both AuNPs and AgNPs nano-impact events. Thus, we associated these U-shaped dips to the state of reversible clustering and consequence disintegration of the clusters at surface electrode. Comparing AgNPs nano-impact events were found to generate shallower U-shaped dips compared to AuNPs; 67 ± 2.9 nF of DDT-AgNPs compared to16 nF of DDT-AuNPs, 83 ± 1.8 nF for FcHT-AgNPs compared to 43 ± 0.92 nF for FcHT-AuNPs. Both non- (DDT-stabilised) and electroactive (FcHT-stabilised) AuNPs showed depressed U-shaped dips compared to AgNPs suggestive of minimal signs of NPs aggregation due to nano-impacting events.

Quantitative results from direct particle chronoamperometry experiments emulated the RESI conclusion whereby the slow flow rate (5 µL/min) resulted in the detection of broad spikes, suggestive of large agglomerated particles compared to narrower spikes detected at higher flow rate (100 µL/min). The results obtained from the nano-impact events of thiolated metal NPs were assigned to the detection of multiple individual NP collisions which resulted to NPs sizing which can be said to be similar to TEM characterisation as seen in Table 4.3-1 for DDT-AuNPs at both flow rates. However, we assigned the detection of NPs agglomerates and/or clusters for DDT-AgNPs at both flow rates as their sizing were not comparable to the TEM characterisation (see Table 4.3-1). These results reiterated the instability of AgNPs in aqueous solvents, and their higher affinity to aggregate when compared to AuNPs.

Table 4.3-1: Particle size characterisation of the different techniques, TEM and nano-impact events, for thiolated metal NPs; DDT- and FcHT- Au and Ag NPs.

[a] nano-sizing via nano-impact events at 5 µL/min flow rate. [b] nano-sizing via nano-impact events at 100 µL/min flow rate.

	AuNPs		**ANPs**	
	TEM sizing (nm)	Nano-sizing (nm)	TEM sizing (nm)	Nano-sizing (nm)
DDT	2.8 ± 1.04	4.18 ± 1.57 [a]; 5.16 ± 1.68[b]	4.9 ± 1.2	527 ± 575[a]; 33 ± 8.50[b]
FcHT	5.5 ± 2.91	-	8.0 ± 2.4	-

FcHT-metal NPs, monitored at 5 µL/min, at the electrode held at an oxidising potential for ferrocene, similarly to the U-shaped dip observed with DDT-metal NPs, FcHT-metal NPs also generated this familiar pattern using RESI technique. However, we were not able to carry out quantitative analysis of FcHT-metal NPs to determine the nano-sizing of NPs by impacting events due to the inability to distinguish the redox reactions from Fc ligands or metal core charging. On the other hand, the techniques enabled the differentiation of individual singular collisions from agglomerated collisions of impacting NPs. The impacts of agglomeration can significantly influence analytical results with modified nanoparticles.

4.4. References

1 K. Tschulik, C. Batchelor-McAuley, H.-S. Toh, E. J. E. Stuart and R. G. Compton, *Phys. Chem. Chem. Phys.*, 2014, **16**, 616–623.

2 X. Xiao and A. J. Bard, *J. Am. Chem. Soc.*, 2007, **129**, 9610–9612.

3 N. V. Rees, *Electrochem. commun.*, 2014, **43**, 83–86.

4 J. M. Zook, R. I. MacCuspie, L. E. Locascio, M. D. Halter and J. T. Elliott, *Nanotoxicology*, 2011, **5**, 517–530.

5 S. V. Sokolov, K. Tschulik, C. Batchelor-McAuley, K. Jurkschat and R. G. Compton, *Anal. Chem.*, 2015, **87**, 10033–10039.

6 J. Ustarroz, M. Kang, E. Bullions and P. R. Unwin, *Chem. Sci.*, 2017, **8**, 1841–1853.

7 E. Katelhon and R. G. Compton, *Chem. Sci.*, 2014, **5**, 4592–4598.

8 A. Lundgren, J. Hedlund, O. Andersson, M. Brändén, A. Kunze, H. Elwing and F. Höök, *Anal. Chem.*, 2011, **83**, 7800–7806.

9 S. M. Oja, M. Wood and B. Zhang, *Anal. Chem.*, 2013, **85**, 473–486.

10 K. McKelvey, M. A. Edwards and H. S. White, *J. Phys. Chem. Lett.*, 2016, **7**, 3920–3924.

11 G. H. Woehrle, L. O. Brown and J. E. Hutchison, *J. Am. Chem. Soc.*, 2005, **127**, 2172–2183.

12 M. Brust, M. Walker, D. Bethell, D. J. Schiffrin and R. Whyman, *J. Chem. Soc. Chem. Commun.*, 1994, 801–802.

13 M. J. Hostetler, A. C. Templeton and R. W. Murray, *Langmuir*, 1999, **15**, 3782–3789.

14 M. J. Hostetler, S. J. Green, J. J. Stokes and R. W. Murray, *J. Am. Chem. Soc.*, 1996, **118**, 4212–4213.

15 M. Morita, M. Goto and Y. Matsuda, *J. Appl. Electrochem.*, 1992, **22**, 901–908.

16 E. Lust, A. Jänes and M. Arulepp, *J. Electroanal. Chem.*, 2004, **562**, 33–42.

17 Y. Hou, K. J. Aoki, J. Chen and T. Nishiumi, *J. Phys. Chem. C*, 2014, **118**, 10153–10158.

18 C. Brett, S. Kresak, T. Hianik and A. M. Oliveira Brett, *Electroanalysis*, 2003, **15**, 557–565.

19 K. Tschulik, B. Haddou, D. Omanović, N. V Rees and R. G. Compton, *Nano Res.*, 2013, **6**, 836–841.

20 N. K. Chaki, J. Sharma, A. B. Mandle, I. S. Mulla, R. Pasricha and K. Vijayamohanan, *Phys. Chem. Chem. Phys.*, 2004, **6**, 1304–1309.

21 J. Ellison, K. Tschulik, E. J. E. Stuart, K. Jurkschat, D. Omanović, M. Uhlemann, A. Crossley and R. G. Compton, *ChemistryOpen*, 2013, **2**, 69–75.

22 W. Cheng, X.-F. Zhou and R. G. Compton, *Angew. Chemie Int. Ed.*, 2013, **52**, 12980–12982.

23 S. V Sokolov, T. R. Bartlett, P. Fair, S. Fletcher and R. G. Compton, *Anal. Chem.*, 2016, **88**, 8908–8912.

24 J. Jiang, X. Huang and L. Wang, *J. Colloid Interface Sci.*, 2016, **467**, 158–164.

25 D. A. Robinson, J. J. Yoo, A. D. Castañeda, B. Gu, R. Dasari, R. M. Crooks and K. J. Stevenson, *ACS Nano*, 2015, **9**, 7583–7595.

26 S. J. Kwon, H. Zhou, F.-R. F. Fan, V. Vorobyev, B. Zhang and A. J. Bard, *Phys. Chem. Chem. Phys.*, 2011, **13**, 5394–5402.

27 B. Calderón-Jiménez, M. E. Johnson, A. R. Montoro Bustos, K. E. Murphy, M. R. Winchester and J. R. Vega Baudrit, *Front. Chem.*, 2017, **5**, 6.

28 A. K. San and Y.-S. Shon, *Nanomaterials*, 2018, **8**, 346.

29 A. P. Z. Stevenson, D. B. Bea, S. Civit, S. A. Contera, A. I. Cerveto and S. Trigueros, *Nanoscale Res. Lett.*, , DOI:10.1186/1556-276X-7-151.

30 R. Sardar, A. M. Funston, P. Mulvaney and R. W. Murray, *Langmuir*, 2009, **25**, 13840–

13851.

31 S. V Sokolov, S. Eloul, E. Katelhon, C. Batchelor-McAuley and R. G. Compton, *Phys. Chem. Chem. Phys.*, 2017, **19**, 28–43.

32 R. L. Wolfe, R. Balasubramanian, J. B. Tracy and R. W. Murray, *Langmuir*, 2007, **23**, 2247–2254.

33 X. Liu, M. Atwater, J. Wang and Q. Huo, *Colloids Surf. B. Biointerfaces*, 2007, **58**, 3–7.

5. Electroactive NPs and their interaction with lipid membranes

The use of nanomaterials such as Gold Nanoparticles (AuNPs) for biological and medical applications is on the rise. Consequently, it is vital to understand and control the interactions of nanoparticles (NPs) with biological components such as cell membranes which consist of a lipid bilayer. The research conducted in this chapter is to determine the penetration behaviour of metal NPs at lipid-modified electrode surfaces of various systems by using atomic force microscopy (AFM), electrochemical techniques and Resonance Enhanced Surface Impedance (RESI). This research will show resonance enhance impedance spectroscopy (RESI) as a highly sensitive method of studying the size effects of thiolated gold nanoparticle interaction with supported lipid bilayers in real time. Coupled with results from microscopic and electrochemical techniques, we were able to achieve parallel findings in the characterisation of NPs-membrane interactions for both electro and non-electro active ligands.

5.1. Introduction

In Chapter 2, section on the interaction of NPs with lipid membrane, we have already discussed the different ways that NPs interact with lipid membranes generally. Therefore, this introduction will focus on ferrocene (Fc) and its derivatives; a brief introduction on the compound, the applications using Fc and Fc derivatives and finally the electrochemistry of ferrocenyl alkanethiol on electrode surfaces (bare and immobilised).

5.1.1. Ferrocene

Iron (Fe) is one of the elements found in every living organism. It is essential to the human body as a complex bound to the protein (haemoglobin of the red blood cells) for the uptake of

the oxygen into living cells.[1] Iron can only enter the cell tissues if bound to the protein transferrin and when there is an iron overload, this can cause an excess of iron adsorption in the gut which may result in the formation of iron deposits in tissues that can lead to damages in the cells, and multiple organ dysfunction.[2] Years ago, inorganic iron compounds were synthesised for the treatment of diseases associated with iron deficiencies, it was found that these compounds were ineffective and they possessed side effects.[3] As a result, the use of ferrocene derivatives became alternatives due to their effectiveness as well as non-toxicity as medical substances.

Ferrocene ($Fe(C_5H_5)_2$), is an organometallic compound with iron as the central metal sandwiched between 2 cyclopentadiene rings (Figure 5.1-1A). This compound has exceptional properties which includes its ability to be soluble in organic solvents, to be stable at air as well as the ease at which ferrocene (Fc) derivatives and Fc containing compounds can be synthesised.[4]

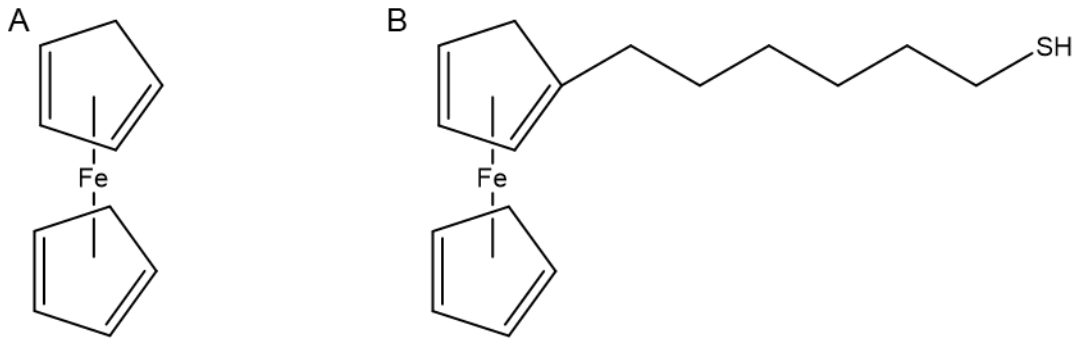

Figure 5.1-1: Illustration of the structures of A) ferrocene (Fc) and B) *ω*-ferrocenylhexanethiolate (FcHT).

In Electrochemistry, Fc is a favourable electron mediator due to the stable redox reversible state it can generate at low potential.[5] The oxidation of Fc into a stable blue ferrocenium salt (Fc^+) can be detected electrochemically giving a redox peak at 0.4 V using saturated calomel electrode (SCE) for a one-electron redox reaction, the redox potential varies with the nature of the solvent and its interaction with the central atom.[6]

5.2.1. Some applications of ferrocene and its derivatives

There are many applications that use Fc and its derivatives; one of which includes the attachment of Fc moieties to polymers, for the monitoring of an enzyme (xanthine, part of the polymer make-up) whose metabolic degradation relates to food's quality.[7] Other benefits of Fc include its use in pharmaceutical applications, thanks to the compound's ability to be compatible with biological environment as well as its lipophilicity. Fc's switch-able redox state coupled with its use as an amperometric sensor allows for the detection of glucose in blood.[8] Fc containing compounds with functionalised groups such as amide or amine, have been reported as an anti-tumour compound in the fight against lymphocytic leukemia P-388[9]. Besides their use in medicine and the food industry mentioned above, Fc and its derivatives have been used in fuel as additives in the removal of carbon deposits from fuel combustion thus promoting smokeless combustion of fuels.[10,11]

5.3.1. Ferrocene alkanethiol and its derivatives and their interaction with electrode surfaces

We are focusing specifically on the electrochemistry of ferrocene alkanethiolated ligands as this relates more to this research. We find that the electrochemistry of ferrocene alkanethiolated ligands on electrode surfaces has been studied and many journals published on the adsorption of these systems.[12–15] In a study by Auletta *et al.*[16] on the electroactivity of thiolated Fc monolayer on gold surfaces, the authors concluded that the increasing length of the alkane chain of the SAM components was found to enhance the adsorption process more so, the concentration of Fc molecules influenced the redox peak position on voltammograms. A study by Kasuya and Kurihara[17] investigating the effect of changing the potential at electrode surface with modified ferrocene alkanethiolated SAM on the interaction between Fc groups of the SAM and the electrolyte counteranions, revealed that ion adsorption at oxidised Fc sites was caused by ion pairing of Fc^+ cation with the counteranions; moreover, the authors demonstrated that the strength of the pairing was found to be due to their degree of dissociation.

Ferrocene alkanethiolated ligands have also been used as capping or stabilising ligands on nanomaterial.[18] The main advantage of such ligand stabilisers is their enhanced electrochemical charging capacities per nanomaterial over a relatively small potential range.[19] This was shown in a study by Schiffrin *et al.*[20] investigating the detection of multi-electron transfer reactions at bare electrode surface. They proposed 3 mechanisms for such reactions (Figure 5.1-2): the first (1) is via the electron-transfer reaction generated from the interactions between the electroactive centres in close proximity from each other; the second (2), the electron being conducted from the Fc groups through to the thiol linker chain down to the metal core; and finally (3) the successive oxidation and reduction of electroactive centres enabling electron-transfer reaction via fast rotational diffusion of the NP. This study not only demonstrated the advantageous use of Fc moieties as current signal enhancers but also their use coupled with NPs in the charging of redox sites within the ligand shell during oxidation reactions.

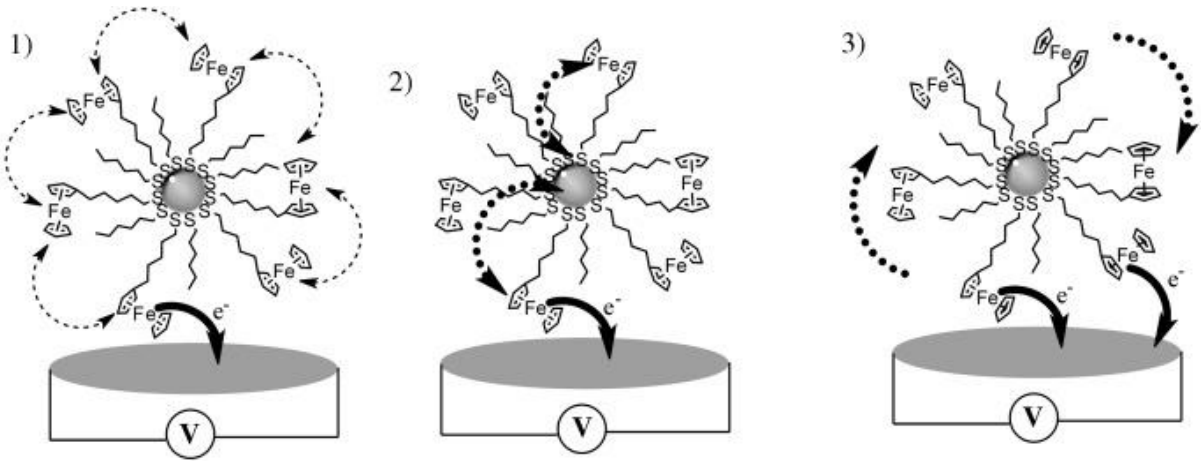

Figure 5.1-2: Schematic illustration of the detection of multi-electron transfer reactions at bare electrode surface; 1) self-exchange reaction between redox centres, 2) coupling between redox centres trough thiol linker chains and 3) fast rotational diffusion. Reprinted from Ref. 20 with permission from John Wiley and Sons (ChemPhysChem).

Well dispersed electroactive NPs have been found to react differently to immobilised electroactive NPs on electrode surface. Stiles *et al.*[21] investigated the interactions of electroactive NPs with bare electrode surfaces, they concluded that the adsorption of ferrocenyl alkanethiol capped AuNPs on bare Pt electrode was via anion-induced monolayer formation forming robust SAMs; ferrocenium cation from the NPs formed ion-bridging pairs

with the electrolyte anions. Whereas, a study by Sardar *et al.*[22] concluded that in the case of the adsorption of ferrocenyl alkanethiol capped AuNPs on negatively charged SAM electrode surface, there were many factors of the robust adsorption; the interaction between the charged SAM surface and the charged ferrocenium on the NPs, the interaction between ferrocenes on the same NP and the lateral interactions within the adsorbed NP layer.

This chapter addresses the gap in knowledge on the interaction of electroactive ligands with lipid membranes, most specifically the interaction of ferrocenyl alkanethiol stabilised metal NPs with lipid membrane immobilised on gold working electrodes. This chapter is generally devoted to the (semi)quantitative penetration behaviour of thiol-modified gold NPs to lipid immobilised gold electrodes using different techniques which includes atomic force microscopy (AFM), electrochemical techniques and the resonance enhanced surface impedance (RESI).

However, the chapter further discusses the observed effects on the (semi)quantitative penetration behaviour of thiol-modified gold NPs to lipid immobilised gold electrodes as follows:

i. the effect of increasing incubation time of modified electrodes in NPs solutions using AFM for non-electroactive (dodecanethiolated) AuNPs, and electrochemical techniques for electroactive (ferrocenylthiolated) AuNPs;

and

ii. the effect of NPs sizes for electroactive (ferrocenylthiolated) gold NPs while investigating their RESI and electrochemical responses of such particles.

5.2. Results and Discussion

NPs have been reported to interact with lipid membranes in 3 main ways namely: via NPs adhesion or adsorption at the electrolyte-lipid interface (Figure 5.2-1A); NPs embedment within the membrane architecture, which involves an interaction dominated by van der Waals forces (Figure 5.2-1B); and NPs translocation (Figure 5.2-1C) which occurs when the NPs penetrate through the membrane and are released on the other side, the latter interaction is usually observed in the NPs interaction with free-standing lipids or lipid vesicles.[23,24]

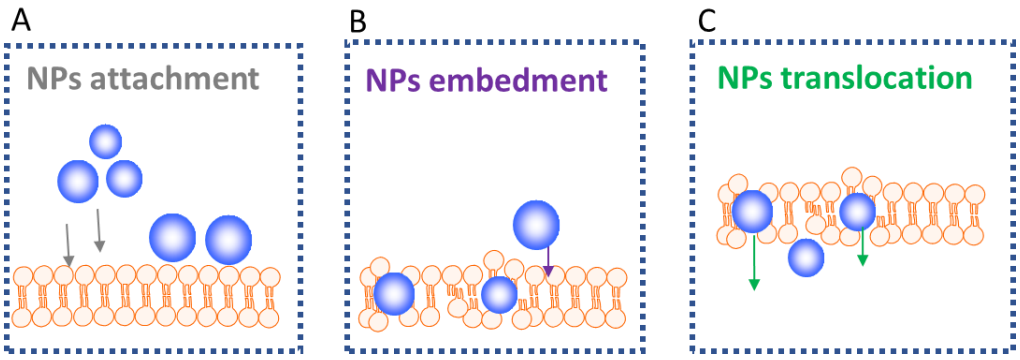

Figure 5.2-1: Schematic representation of NPs-membrane interactions.

The different studies in this chapter investigate the interactions between thiol-capped gold nanoparticles and lipid membranes immobilised on gold electrode surfaces, to determine the effect the immersion time has on the NPs-membrane interactions and, the effect that varying NP sizes have on the NPs-membrane interactions.

To carry out the first objective in this chapter, both non-electroactive and electroactive AuNPs were used and the second objective was carried out using only electroactive AuNPs; the commercial NPs were functionalised to introduce electroactivity. Particle size distribution from TEM analyses has demonstrated spherical shape for all samples with average core diameter sizes (Figure 5.2-2): 5.5 ± 2.9 nm (synthesised NPs), these will be referred to as 5 nm FcHT-AuNPs; 11 ± 0.69 nm (commercial NPs), these will be referred to as 10 nm FcHT-AuNPs; and 22 ± 2.9 nm (commercial NPs) these will be referred to as 20 nm FcHT-AuNPs.

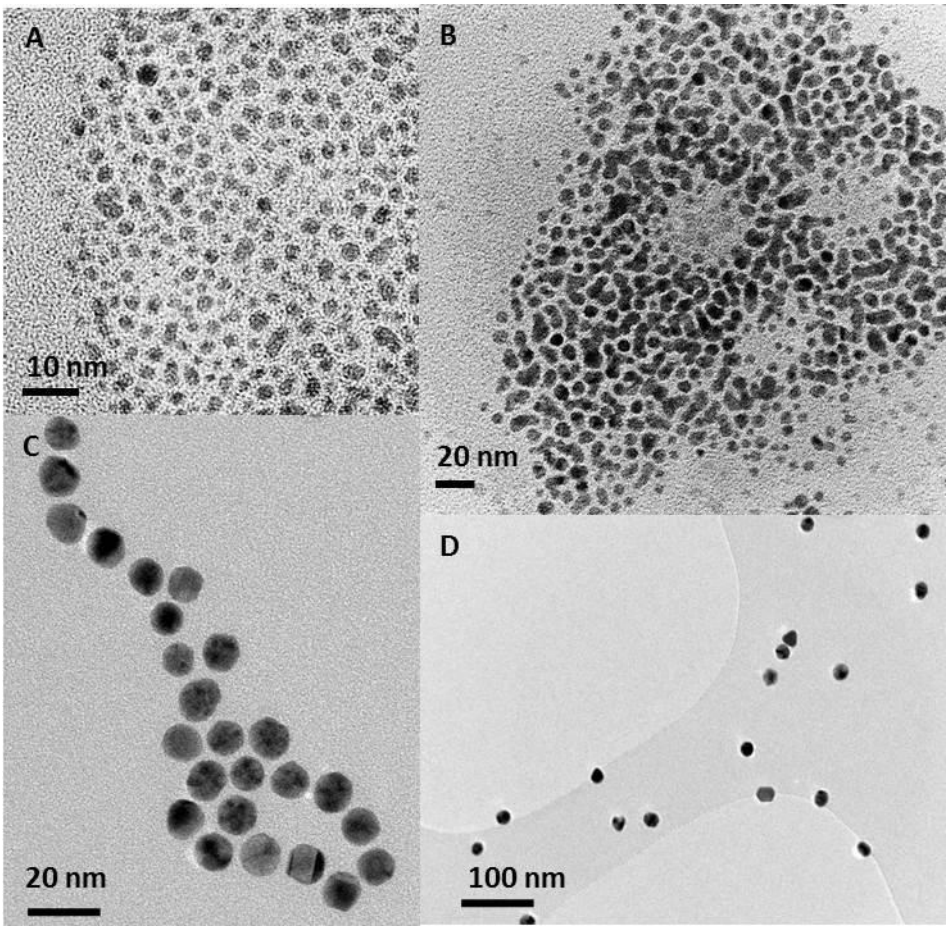

Figure 5.2-2: Transmission electron microscopy (TEM) images of thiolated gold nanoparticles; A) DDT-AuNPs, B) 5nm FcHT-AuNPs, C) 10 nm FcHT-AuNPs and D) 20 nm FcHT-AuNPs.

The synthesised nanoparticles used in this work (as well as the AgNPs included in the preliminary studies included) were from the same batch of NP synthesis/functionalisation as the ones used in the previous chapter (Chapter 4); the concentration for the DDT-AuNPs used throughout the experiments was 1.2 µM and 2.8 µM for FcHT-AuNPs.

5.2.1. Preliminary studies on the penetration of NPs through phospholipid membranes

In this study we have investigated the interaction of metallic NPs (gold, silver and copper) with lipid membranes immobilised on gold electrodes. Electrochemistry techniques used in this section were to investigate the electrochemical behaviour of FcHT-metal NPs penetrating through the lipid modified gold electrodes.

Clean gold macroelectrodes were modified with SAM and tBLM lipid membranes, the modified electrodes were tested for defect formations in redox rich electrolyte solution prior to the start of the studies.

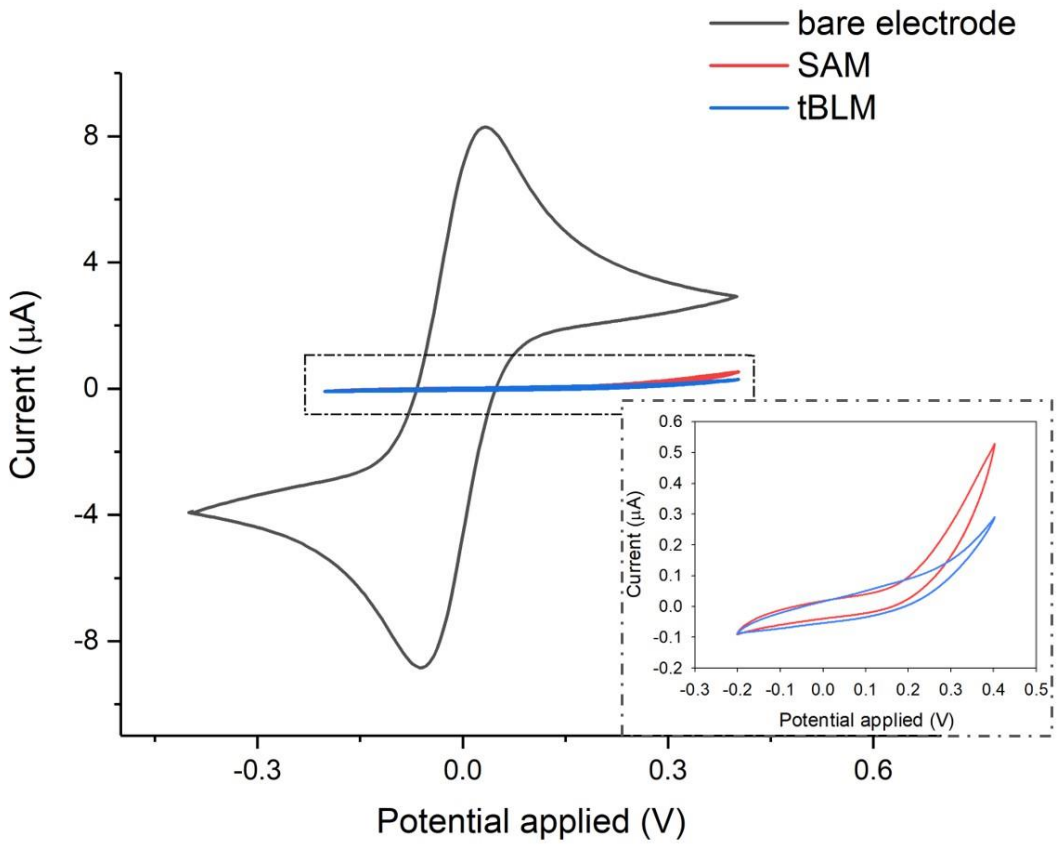

Figure 5.2-3**:** CV of bare vs lipid-modified gold electrodes in solution of 10 mM $Fe^{3+/4+}$ (5 mM $K_4[Fe(CN)_6]$ and 5 mM $K_3[Fe(CN)_6]$) in 0.1 M KNO_3 at 50 mV/s scan rate.

Well-insulated electrodes show no redox activities in a redox-rich solution (seen for SAM and tBLM models in Figure 5-2-3). Comparing bare gold electrode with SAM or tBLM modified electrodes, we can see the supressed redox peaks in both potential scans.

The penetration of non-electroactive (DDT-AgNPs) and electroactive NPs (FcHT-AgNPs) were compared for their electrochemical penetration behaviour (Figure 5.2-4). SAM-modified electrodes were immersed in the relevant NPs solutions for 60 min then CVs were carried out in the electrolyte solution, 0.1 M KNO_3. From these initial results, it was clear that non-electroactive, DDT-AgNPs showed no redox activity over the potential windows thus showed no oxidised particles were detected whereas FcHT-AgNPs curve had redox peaks.

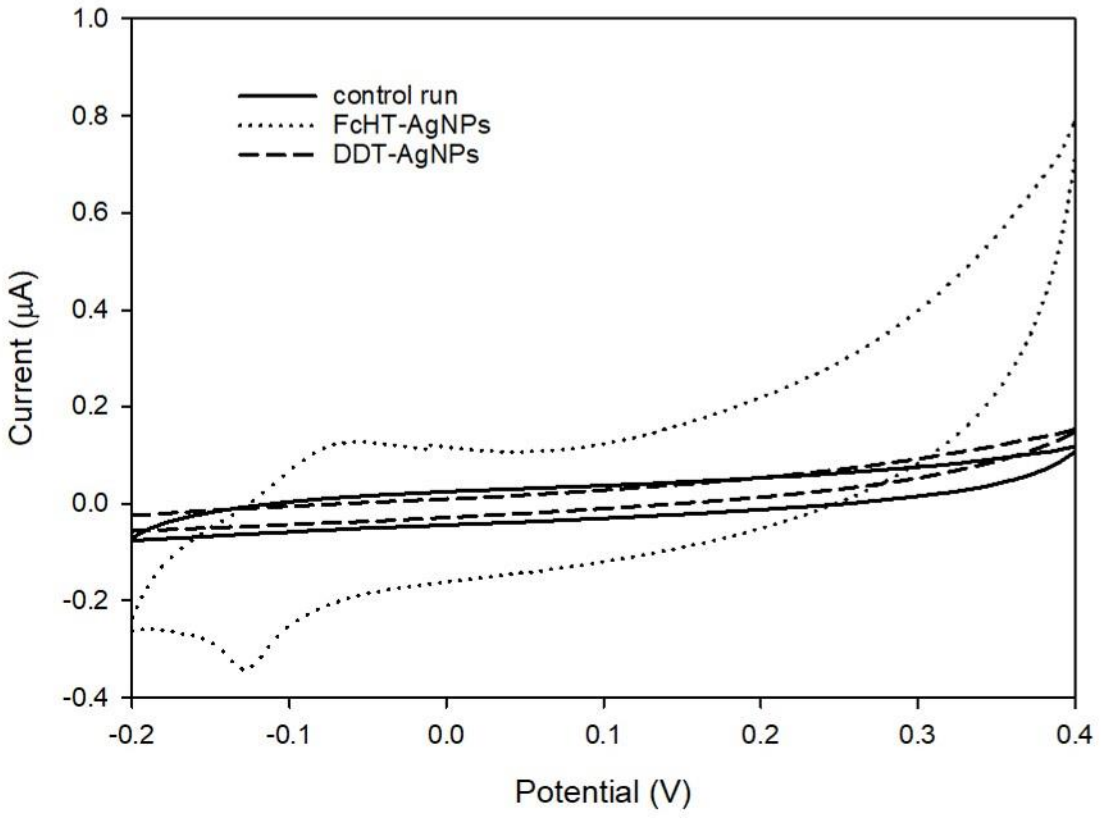

Figure 5.2-4: CVs showing the electrochemical behaviour of DDT-AgNPs, FcHT-AgNPs in 0.1 M KNO_3; 'control run' (SAM-modified electrode in electrolyte without immersion in NPs) and 'DDT-AgNPs, FcHT-AgNPs' were the incubation of SAM-modified electrode in the relevant colloid solution for 60 min. Scan rates: 50 mV/s. [DDT-AgNPs] = 2.1 µM and [FcHT-AgNPs] = 3.0 µM.

5.2.1.1. FcHT-metal NPs interaction with SAM

The insulated electrodes were immersed in solutions of FcHT-metal NPs, dispersed in EtOH solvent, at different intervals for up to 60 min (with 10 min increment between each run) and electrochemical measurements were carried out to determine the interactions of electroactive FcHT-metal NPs with the membrane immobilised on gold electrodes.

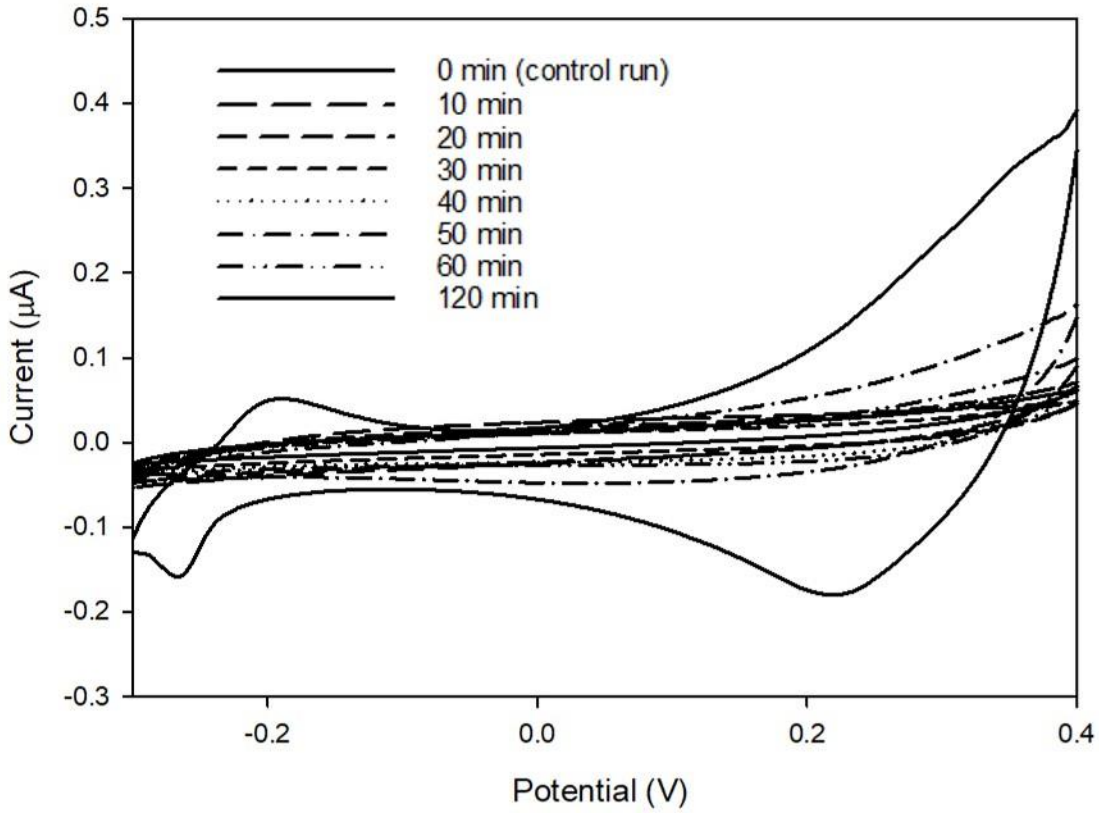

Figure 5.2-5: CVs of the SAM-modified gold electrode in 0.1 M KNO_3 at different immersion times in FcHT-AgNPs. Scan rate: 50 mV/s. [FcHT-AgNPs] = 3.0 µM.

From these results (Figure 5.2-5), no redox peaks were seen until after 60 min incubation time, thus we decided to use 60 min as our incubation starting point for 'after' incubation label.

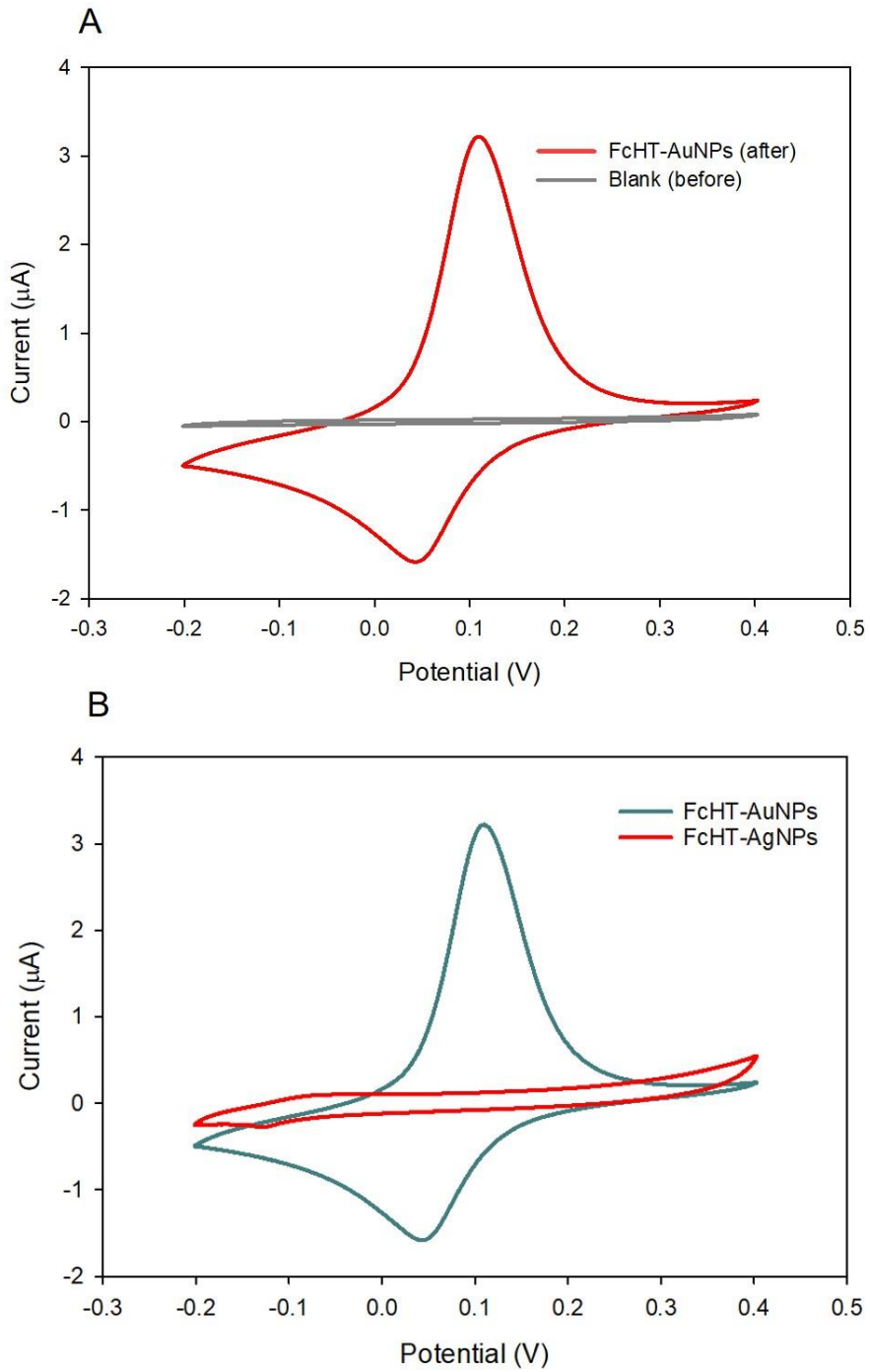

Figure 5.2-6: Cyclic voltammograms showing the electrochemical behaviour of FcHT-metal NPs in 0.1 M KNO_3; A) 'blank/before' (SAM-modified electrode in electrolyte without immersion in NPs, control run) and 'after' incubation of SAM-modified electrode in FcHT-AuNPs for 60 min, B) after incubations in FcHT-metal NPs (Au and Ag). Scan rates: 50 mV/s. [FcHT-AgNPs] = 3.0 μM and [FcHT-AuNPs] = 2.8 μM.

From Figure 5.2-6A, 'before' corresponding soaking (grey line), the current response showed no presence of redox peaks within the voltage window applied. The immersion of the modified electrodes in colloidal solutions after 60 min (red lines) caused changes to the lipid architecture; NPs perturbed the lipid's arrangement on the electrode by forming defects such

as pores enabling the NPs to penetrate through the lipid layer and for the redox activities to be detected at electrode's surface. Moreover, FcHT-metal NPs increased the electrochemical performance i.e. current density on the surface of the gold electrode as they penetrated through the lipid monolayer (Figure 5.2-6B); FcHT-AuNPs were found to penetrate further into the lipid membrane than FcHT-Ag thus having a larger current signal at 3.21 µA compared to 8.5 x 10^{-2} µA and 4.2 x 10^{-2} µA for AgNPs. Reports have shown that electroactive ligands stabilising the metal NPs increase the electrochemical performance on the surface of the gold electrode as the NPs penetrate through the lipid monolayer via electron transfer to the working electrode.[25]

As the stability of NPs in suspension is linked to their agglomeration behaviour therefore, the agglomeration behaviour of these NPs can be said to affect the NPs' penetration through the lipid membrane. Adding to that, the size and metal core of the NPs were found to have a significant effect on the penetration behaviour. Relating to the effect of NPs size, we concluded that the individual, isolated and smaller particles would readily penetrate deeper into the lipid membrane than clustered, agglomerated and bulky particles; FcHT-AuNPs were determined to have the smallest NPs size (5.5 ± 2.9 nm) compared to FcHT-AgNPs at 8.0 ± 2.4 nm. In terms of metal sore, AgNPs were found to agglomerate more readily than AuNPs; such susceptibility of the NPs to agglomerate and mechanical agitation of the colloidal solutions were seen to reverse their agglomeration to resuspended solutions.[26] As the nature of the metal core of NPs is closely related to their stability and size manipulation, as a result we identified the nature of the metal core the most significant factor.

5.2.1.2. Comparing the interaction of FcHT-metal NPs with SAM and tBLM

In this study, we compared the effect of FcHT-metal NPs penetration through SAM and tBLM modified electrodes.

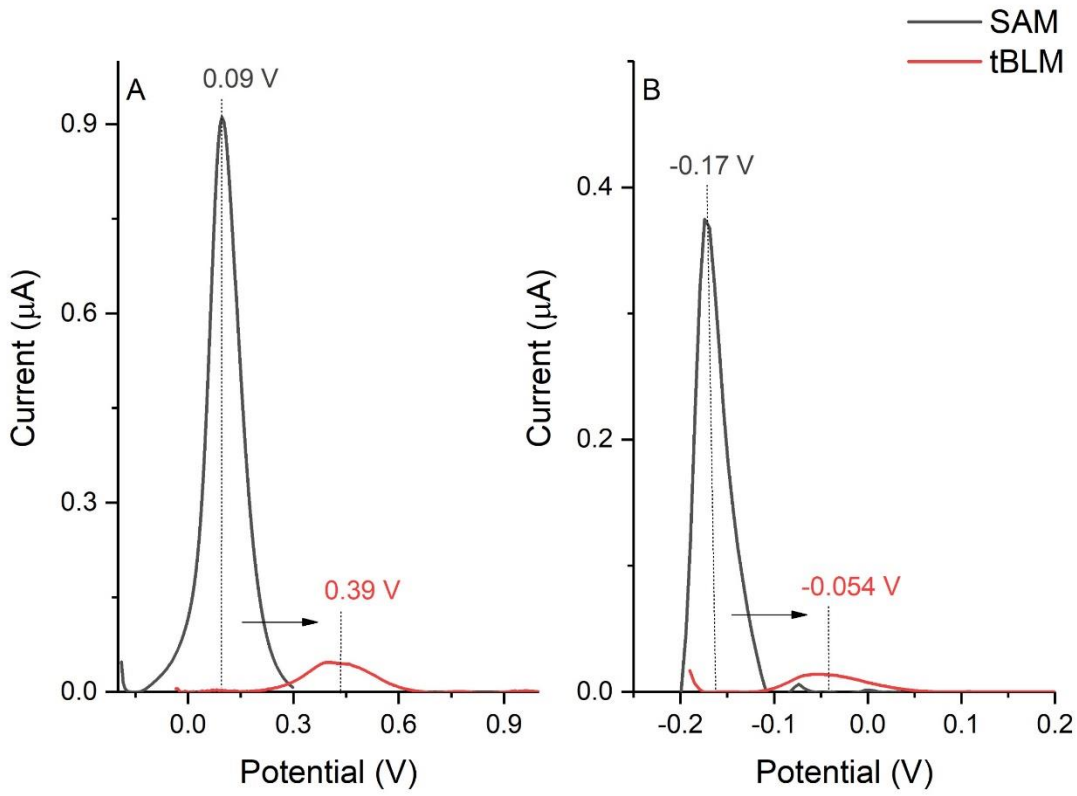

Figure 5.2-8: DPVs of penetration behaviour of the FcHT-metal NPs in 0.1 M KNO_3; comparing SAM and tBLM-modified after 60 min immersion time, A) FcHT-AuNPs penetration and B) FcHT-AgNPs penetration. Sweep amplitude: 5 mV. FcHT-AgNPs] = 3.0 µM and [FcHT-AuNPs] = 2.8 µM.

Redox activity was detected with the penetration of FcHT-metal NPs through both SAM and tBLM as seen in Figure 5.2-7. Further similarities were observed in the depletion in current density as well as the potential shift of AgNPs as was recorded for AuNPs.

From the obtained results, the amount of charge passed to oxidise the electroactive species (*Q*) was computed by the division of the area under the curve (obtained by integration of the oxidation peak curve, *A*) by the scan rate (υ, 50 mV/s) denoted by Eq. 5-1.

$$Q = \frac{A}{\upsilon} \qquad (5\text{-}1)$$

Eq. 5-2 was used to determine the adsorbed surface coverage of NPs (Γ_{NP}) at electrode surface; *n* is the average number of Fc ligands per NP, *A* is the area of the working electrode and *F* is the Faraday's constant.[22]

$$Q = nFA\Gamma_{NP} \qquad (5\text{-}2)$$

When comparing SAM to tBLM penetration behaviours as seen in Figure 5.2-8, we detected an anodic shift in potential, with more anodic potential required in the tBLM model for the electroactive FcHT ligands to be oxidised, than for the penetration and detection through SAM model. Also, a decrease in current density was recorded going from a monolayer to a bilayer (Table 5-1) hence a lowering of surface coverage which was indicative of the role of the lipid architecture in suppressing the electrochemical response of the FcHT ligands on the NPs as well as causing the formation of more lipids defects through the upper and lower leaflet of the lipid bilayer.

The depletion in current densities from SAM to tBLM models was much greater for AgNPs than AuNPs and so were the calculations of charge and NP surface coverage, we attributed this difference to be due to the NPs size, with larger sizes (AgNPs) causing more obstruction/crowdedness at lipid-electrolyte interface potentially caused by NPs agglomeration thus, these NPs were less able to penetrate through the membranes resulting in less charge being detected at electrode surface.

Table 5-1: Electrochemical parameters determined by using Eq. 5-1 and Eq. 5-2 for the penetration FcHT-metal NPs through SAM and tBLM lipid membrane immobilised electrodes.

	Membrane models	**I_{pa} /µA**	**Q /µC cm^{-2}**	**Γ_{NP} /mol cm^{-2}**
AuNPs	SAM	9.12×10^{-1}	1.09×10^{3}	1.13×10^{-8}
	tBLM	4.77×10^{-2}	1.10×10^{2}	1.14×10^{-9}
AgNPs	SAM	4.52×10^{-1}	2.37×10^{2}	2.45×10^{-9}
	tBLM	1.41×10^{-2}	1.32×10^{1}	1.36×10^{-10}

Following the results from the nano-impact chapter (Chapter 4) on the instability of AgNPs as colloidal solutions in suspension as well as their higher heterogeneity compared to AuNPs. Adding to the findings from the above preliminary results, we have decided to focus our research on AuNPs and their interactions with lipid membranes on gold surfaces.

5.2.2. Effect of incubation time on NPs-lipid membrane interactions

A study by Goreham *et al.*[28] on the interaction of citrate functionalised AgNPs on tBLM models (Dipalmitoylphosphatidylcholine monolayer with Diphytanyl Thiolipid making up the tBLM) concluded that longer exposure (24 h) of tBLM in the colloidal solution had irreversible changes to the architecture of the lipid membrane, such changes included formation of lipid holes as well as NPs embedment within membrane leaflets.

In view of this study, we wanted to investigate the effect of increasing the exposure time of tBLM modified gold electrodes in colloidal solutions of non-electroactive (DDT) and electroactive (FcHT) AuNPs, by having shorter time intervals. We used AFM technique to investigate the non-electroactive AuNPs and tBLM interactions whilst electrochemistry techniques (CV and DPV) investigated the interactions between electroactive AuNPs and tBLM.

5.2.2.1. AFM investigates the interaction of non-electroactive AuNPs with lipid membrane

Gold thin film microscope glass slides were used as gold substrates and immersed in the lipid DPPTE solution and a lipid monolayer was formed over 48 hrs at 4 °C. The immobilised gold substrates were immersed in 1 ml DDT-AuNPs in ethanol dispersion at different incubation times and analysed by atomic force microscopy (AFM), to allow the determination of changes to the morphology of the monolayer modified substrates resulting from their interaction with AuNPs in air.

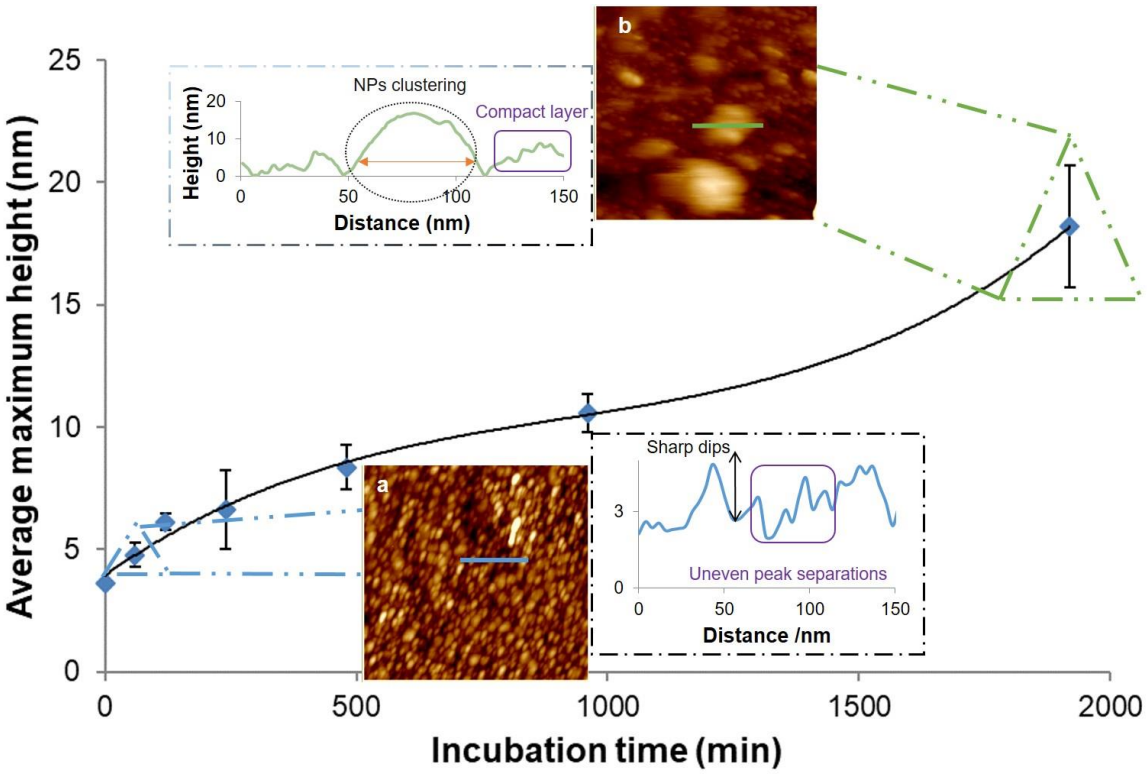

Figure 5.2-8: Time-lapsed study for the incubation of lipid immobilised substrates with DDT-AuNPs; average max. height of NPs on the lipid surface at different incubation times with the NPs including AFM images (a) after 60 min and (b) after 1920 min incubation in NPs solution. All images are 2 x 2 µm. [DDT-AuNPs] = 1.2 µM.

The analysis of results obtained from the time-lapsed study seen in Figure 5.2-8 have revealed the progressive increase in the recorded heights; after 60 min of incubation in 1 ml DDT-AuNPs, there was a slight increase in the recorded height from 3.62 ± 0.02 nm (t = 0) to 5.73 ± 0.51 nm (t = 60 min) shown as 'sharp dips' in Figure 5.2-8a, considering that the NPs are 2.77 ± 1.04 nm in diameter size, the results suggest that the NPs were embedded within the membrane and these created defects in the lipid membrane (4.78 ± 0.89 nm). Similar results were recorded by Abraham *et al.*[29] with their AFM study on the penetration of cysteine coated AuNPs (10 nm) through DPPC monolayer (avg. length at 2 nm) reported an increase in height to 7 nm. Adding to that, uneven peak separations were seen with presence of shoulder peaks as evidence of NPs adsorption at lipid layer and the formation of lipids defects i.e. pores.

When comparing t = 60 min with t = 1920 min (Figure 5.2-8b), it is clear to see the difference in peak separations from wider uneven peaks to more compact layer respectively showing reduced numbers, possible aggregation of NPs in order to smooth out the uneven separations

thus causing the appearance of the lack of pores at lipid surface for the latter time incubation; suggesting possible membrane collapse and/or the replacement of the lipid monolayer with NPs monolayer by NPs agglomeration forming big NP clusters (width of 64 nm and height of up to 20 nm) with the presence of small shoulder peaks. Our results and conclusion was supported by a study by Gordillo *et al.*[30] reporting that the main factor affecting the interaction of PEGylated AuNPs with phospholipid monolayer on mercury electrode was the NPs sizes; they observed that only small AuNPs (2-3 nm) were able to penetrate through the lipid monolayer compared to larger AuNPs (10 nm) that were adsorbed at the lipid's surface and, for longer immersion of the modified electrode in NPs solution, the smaller NPs formed a monolayer at the electrode's surface displacing the lipid membrane.[30]

5.2.2.2. Electrochemical techniques investigate the interaction of electroactive AuNPs with lipid membrane

The behaviour of electroactive alkanethiol on electrode surface has been investigated extensively and reported,[31–34] these reports focused on the redox activity of working electrodes modified with electroactive ligands as SAM. It was found that increasing the surface coverage by increasing Fc concentration as SAM on electrode surface altered the electrochemical signals/responses. Also, other reports have shown the detection of NPs at electrode surfaces as they penetrate through lipid monolayer and bilayer using electrochemistry.[35–37] Our study specifically focuses on the electroactive penetration behaviour of FcHT-AuNPs through tBLM models on gold working electrodes, an unique contribution using non-electroactive, neutral thiol lipid based tBLM models.

In our study, we investigated the effect of the incubation time of SAM-lipid modified electrodes in FcHT-AuNP solutions have on the NPs-phospholipid membrane interactions with the aid of electrochemical techniques such as cyclic voltammetry (CV) and differential pulse voltammetry (DPV).

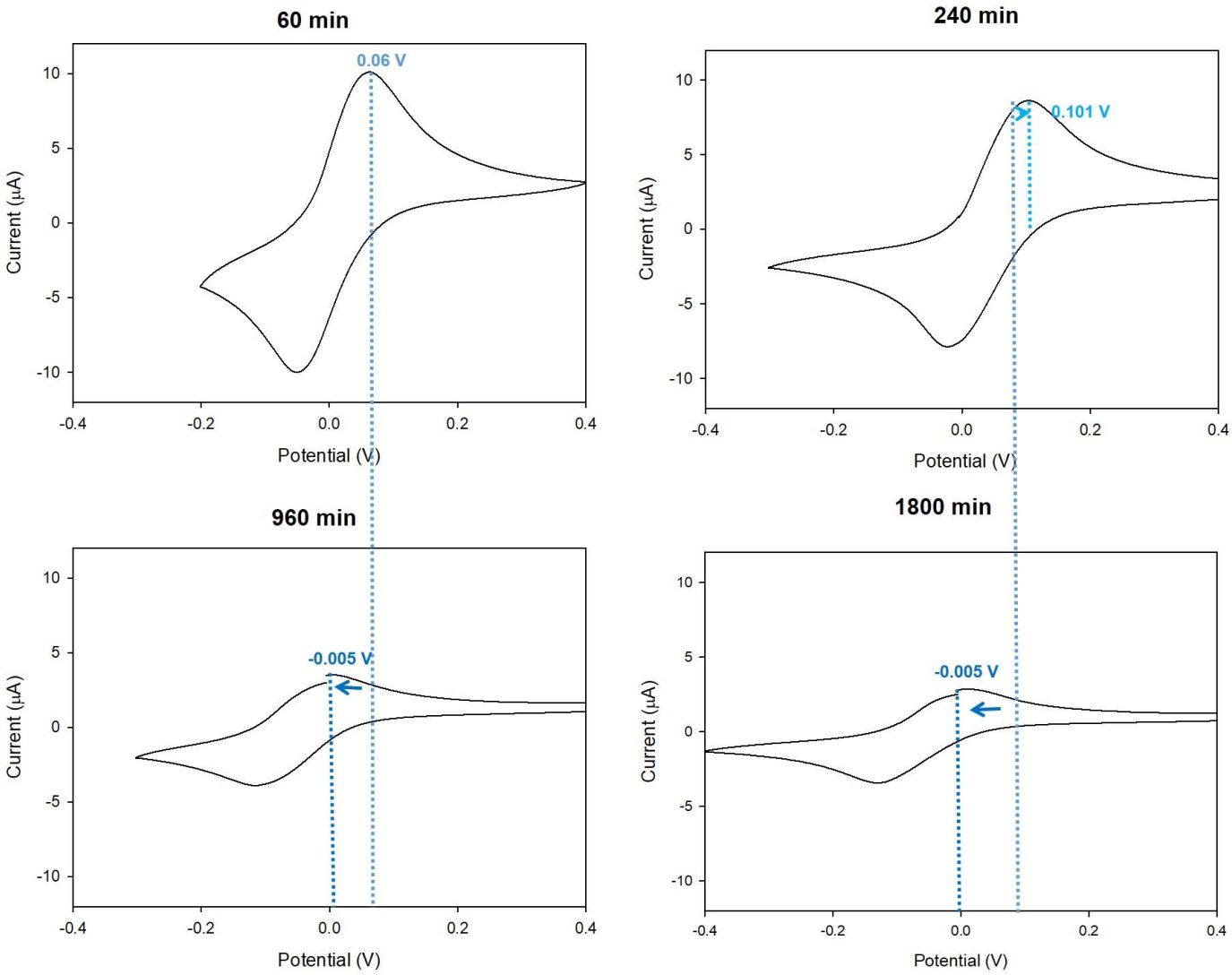

Figure 5.2-9: CVs of the SAM-modified gold electrode in 0.1 M KNO_3 at 60, 240, 960 and 1800 min immersion times in FcHT-AuNPs. Scan rate: 50 mV/s. [FcHT-AuNPs] = 2.8 µM.

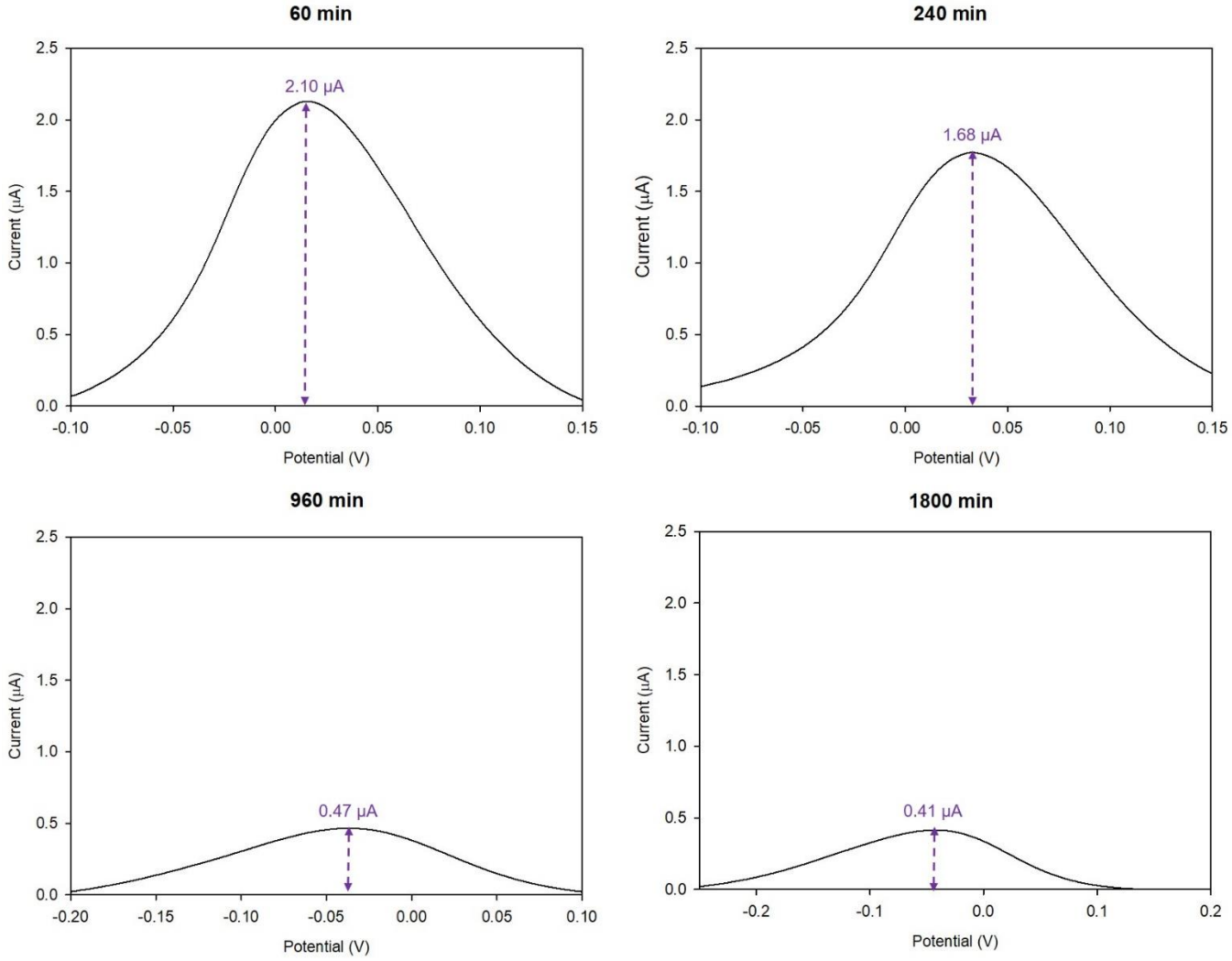

Figure 5.2-10: DPVs of the SAM-modified gold electrode in 0.1 M KNO_3 at 60, 240, 960 and 1800 min immersion times in FcHT-AuNPs. Sweep amplitude: 5 mV/s. [FcHT-AuNPs] = 2.8 µM.

Table 5-2: Electrochemical parameters determined by [a] CV (Figure 5.2-9) using Eq. 5-1 and [b] by DPV (Figure 5.2-10) using Eq. 5-2 for the penetration FcHT-AuNP through SAM lipid membrane immobilised electrodes at different incubation times.

Incubation time /min	**Q /µC cm^{-2}** [a]	**Γ_{NP} /mol cm^{-2}** [b]
60	32 ± 5.3	2.09 ± 1.10 x 10^{-9}
120	40 ± 13	2.10 ± 1.65 x 10^{-9}
240	28 ± 4.8	1.67 ± 0.76 x 10^{-9}
480	33 ± 11	3.55 ± 1.57 x 10^{-10}
960	14 ± 2.0	4.71 ± 2.04 x 10^{-10}
1800	11 ± 4.7	4.14 ± 1.49 x 10^{-10}

Shifts in potential were recorded from Figure 5.2-9; anodic shift from t = 60 to 480 min (0.06 V to 0.101 V) compared to cathodic shift to -0.005 V at higher increasing incubation times. These potential shifts where found to be synonymous to increasing $Fc(CH_2)_6SH$ concentration. Moreover, increasing the incubation time allowed more NPs to penetrate through the lipid monolayer and to be adsorbed onto the gold electrode surfaces, similarly seen with the results of non-electroactive AuNPs. This increase of NPs saturation at electrode's surface caused an increase in the electrochemical signals given by the increased *Q* values due to the increased redox activity with increasing surface coverage with FcHT-AuNPs. Table 5-2 but only for the first 120 min incubation duration. After 240 min, *Q* values decreased to 11 ± 4.7 μC cm^{-2} (t = 1800 min), this decrease in *Q* values was reflected in the negative shift of the peak potential from +0.101 V to -0.005 V (Figure 5.2-9) with increasing incubation times as well as the change in CV curves from peak-shaped to sigmoidal-shape (Figure 5.2-9). Such change in shape was found to be due to the more quasi-microelectrode behaviour seen in the cyclic voltammograms with increasing incubation time (see Figure 5.2-10), we attributed such changes to the formation of membrane defects or holes.

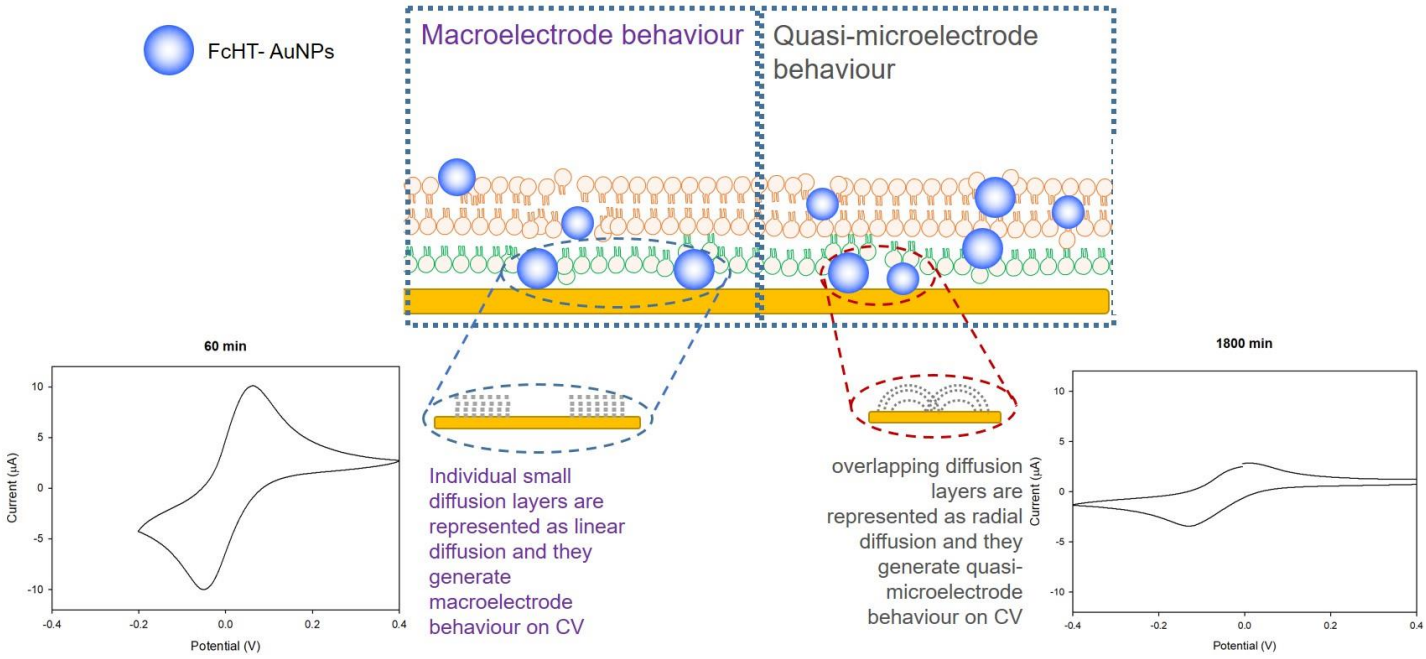

Figure 5.2-11: Illustration of the different penetration behaviour of FcHT-AuNPs and how they generate different CV shapes; peak-shaped and sigmoidal-shaped voltammograms.

The results from the non-electroactive (DDT-AuNPs, Figure 5.2-8) interactions with AFM technique have suggested the formation of agglomerates and NPs clusters with continuous

incubations, this was reflected in the decrease of electroactivity as well as the shift in redox potentials of the FcHT-AuNPs over time, seen in Figure 5.2-9; the decrease in height of the current peaks (Figure 5.2-8) and the shift of the peak potentials in more negative values after t = 240 min (Figure 5.2-9). A similar observation was recorded by Auletta *et al*.[16], their findings revealed that increasing the concentration of ferrocene moeity as part of SAM on gold electrode caused the ferrocene population to undergo intermolecular interactions shifting the redox potential peak to more negative anodic values. Shaowei Chen[38] also observed such anodic shift for the Fc redox potential peak with the formation of thin film n-octanethiolates (HSC_8Fc) capped AuNPs on solid substrates.

5.2.3. Real-time formation of tBLM

In this study, the RESI technique was used to monitor in real time the formation of lipid bilayer on SAM mobilised gold sensors. In these experiments, the gold electrode sensors were modified with phospholipid molecules (DPPTE) to form SAM by immersion in thiol solutions for 48 hrs; the thiol head-groups of the DPPTE SAM were covalently immobilized onto gold surfaces and the alkyl chains as the tail part of the phospholipids served as the hydrophobic template that was used as anchor for the deposition of lipid bilayer by vesicles fusion.[39] Then, the lipid vesicles in the prepared solution were injected in the z-LAB (at 5 µL/min flow rate) after 15 min system stabilization. The lipid bilayer formation was monitored in real time with the z-LAB, recording the changes in RESI capacitance values over time (Figure 5.2-12).

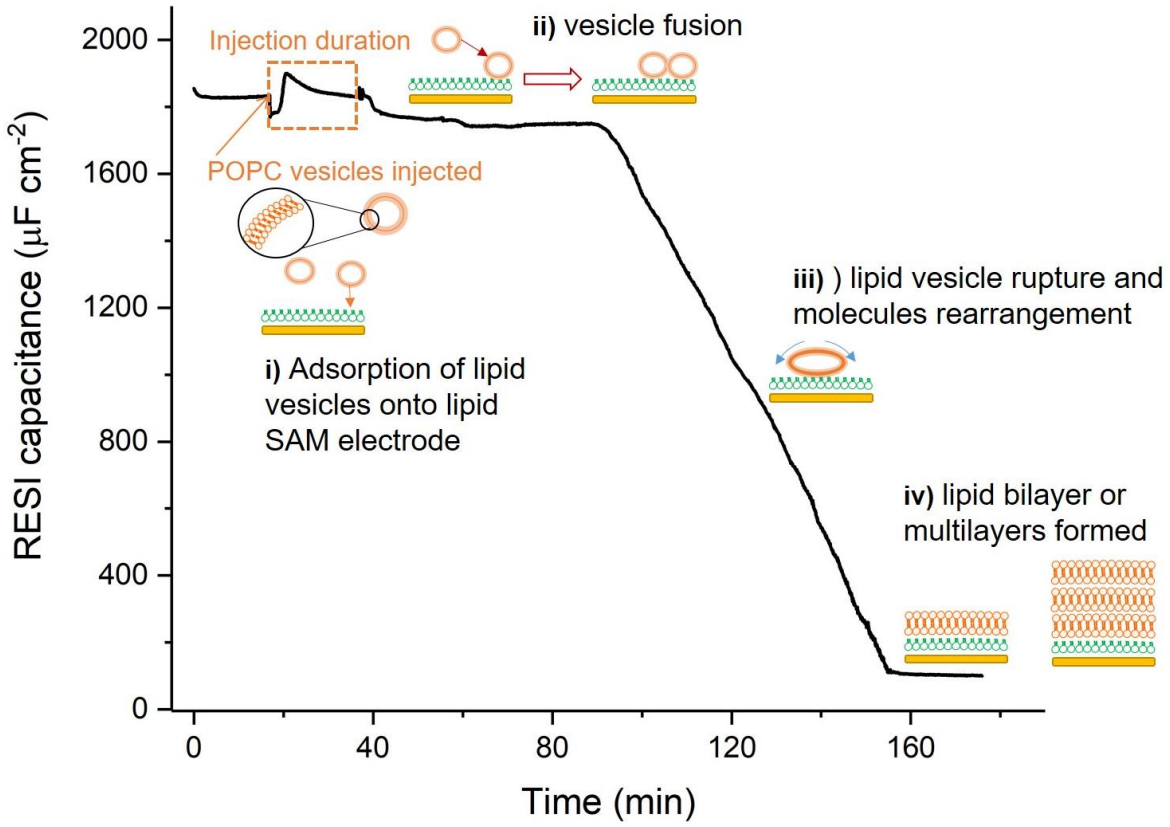

Figure 5.2-12: Real time formation of lipid bilayer on SAM electrode chip; i) adsorption of lipid vesicles onto DPPTE-Au sensors, ii) vesicle fusion, iii) lipid vesicle rupture and molecules rearrangement on modified sensor and iv) lipid bilayer or multilayers formed. POPC vesicle solution injected after 15 min system stabilisation with constant flow of 0.1 M PBS at fixed flow rate of 5 µL/min.

After 15 min equilibration time (Figure 5.2-12) with constant flow of phosphate buffer, the value for the RESI capacitance was around 1825 ± 200 nF, upon the injection of POPC lipid solution (20 min duration). There was an initial dip in capacitance due to the change in the environment of the running electrolyte solution with the injection of lipids into the system. The recorded changes in the capacitance values denoted the stages of lipid bilayer formation, possible formation of lipid multilayers;

i. Adsorption of lipid vesicles on DPPTE-modified gold sensors seen with the slight increase in capacitance values from its initial value at the start of the injection
ii. Vesicles fusion: small decrease in capacitance that was found to remain stable for up to 50 min

iii. Lipid vesicles rupture and molecules rearrangement on surface, seen by the dramatic decrease in RESI capacitance to 110 nF (ca 94% decrease from initial capacitance) due to the release of liquid from the interior of the vesicles

iv. Bilayer formation as upper leaflet seen as the RESI capacitance value remained steady for 20 min

After the bilayer was formed on the modified sensor, defects were checked by running a blank injection; only defects free sensors were used for this study to prevent penetration via pre-formed defects instead of penetration via NPs-membrane interactions. A further decrease in RESI capacitance values was recorded after the modified sensor was taken out of the system and flushed through with distilled water and re-fitted onto the zLAB, as the membrane stabilised any unerupted vesicles as well as any loosely bound lipid fragments were washed out of the system behind a rigid lipid bilayer membrane.

5.2.4. Effect of NPs sizes on NPs-lipid membrane interactions

Reports have shown that NPs sizes have great impact on the NPs interaction with lipid membrane, with bigger NPs causing the removal of lipid molecules from the lipid bilayer architecture.[41,42] RESI and electrochemical techniques were used in this section to investigate the penetration behaviour and the electrochemical responses of FcHT-AuNPs, of different sizes, as they interact with lipid membranes.

5.2.4.1. Real-time penetration of FcHT-AuNPs through tBLMs

We investigated the effect of NP sizes and their penetration behaviour through tBLM models using RESI technique. Real-time measurements denoting the NPs interaction with lipid membrane were monitored. This study was carried out by injecting 200 µl of FcHT-AuNPs (5, 10 and 20 nm) into the system fitted with tBLM-modified gold sensors, the electrolyte solution was flowing through the system for 15 min, stabilising the flow and, RESI capacitance measurements were recorded.

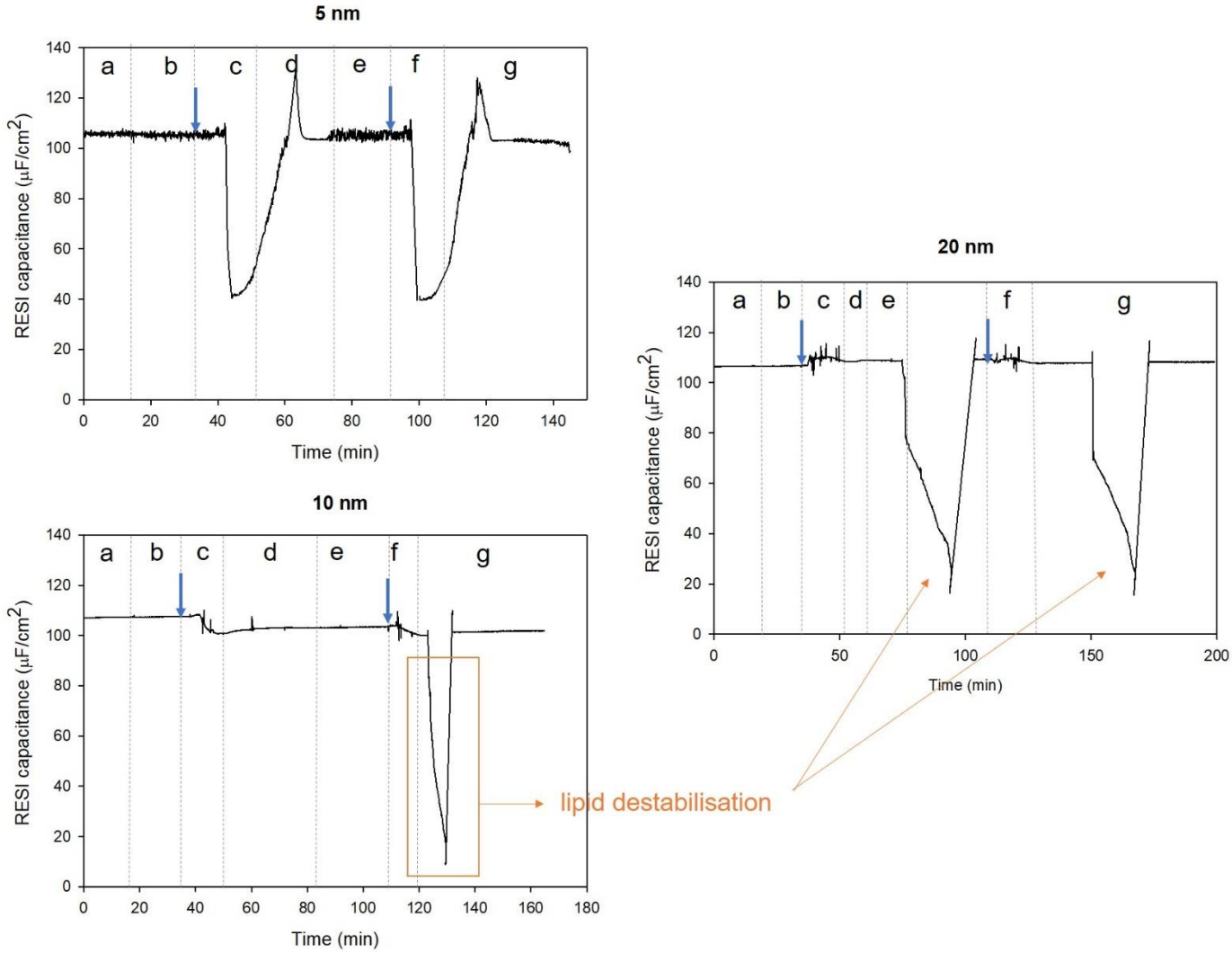

Figure 5.2-13: Change in RESI capacitance with FcHT-AuNPs injection over time as a function of NPs sizes; 5, 10 and 20 nm, a running electrolyte solution of 20 mM PBS at a set flow rate of 5 µL/min; the arrows representing the injection of NPs in the system. [5 nm FcHT-AuNPs] = 2.8 µM, [10 nm FcHT-AuNPs] = 3.0 µM and [20 nm FcHT-AuNPs] = 3.0 µM.

(a) = the stabilisation of the system for approximately 15 min at set flow rate of 5 µL/min with a constant flow of buffer (20 mM PBS). **(b)** = the injection of fresh solvent (deionised water) followed by 10 min of stabilisation. Stage **(c)** = the injection of 200 µl of AuNPs, dispersed in deionised water at a concentration of 200 nM into the system fitted with tBLM-modified gold sensors. Followed by a repeat of the earlier stages; buffer, solvent, NPs injection and buffer, for **(d)**, **(e)**, **(f)** and **(g)** respectively.

When comparing the penetration of FcHT-AuNPs of different sizes, the RESI capacitance dips caused by the injections of 5 nm NPs were attributed to the penetration of NPs through the lipid bilayer seen with a decrease of 63 % from initial RESI capacitance, RESI capacitance of the electrolyte solution flowing through the system (Figure 5.2-13– 5 nm). Although another interpretation of the results showing the sharp increases in RESI capacitance around 65 min for the first injection and around 120 min for the second injection would be of the penetration of NPs through the membrane and the U-shaped dips would be the solvent effect.

However, when comparing with the injection of 10 nm NPs, a change of 5.9 nF between the initial value and the recorded RESI capacitance after the first injection (Figure 5.2-13– 10 nm 'c'). Similarly to the RESI capacitance decrease for 5 nm, this was attributed to the adsorption of NPs at electrolyte-lipid interface. Moreover, after the 1st injection of 10 nm NPs, no lipid recovery was recorded, recovery back to the initial RESI capacitance value as seen for 5 nm injection, instead, spike responses were recorded instead. The conclusion deduced from this observation was of the adsorbed 10 nm particles, hence the capacitance value did not revert to its initial value after the injection. A study by Guo and co-workers[43] using a microfluidic device to monitor the translocation of hydrophobic AuNPs of different sizes, also detected that the penetration of larger NPs (>5 nm) through leaflets of the bilayer caused lipid rupture as well as the removal of lipids from the bilayer as these NPs are translocated. This similar behaviour was seen in the 2nd injection of 10 nm NPs that triggered the formation of holes and rearrangement of lipid molecules denoting the fluidity of lipid membrane, a phenomenon replicated with the injections of 20 nm NPs. However, where no drastic change to the capacitance values were recorded even after hole formation and lipid recovery, this type of phenomenon could suggest similarities with the non-destructive membrane destabilisation of smaller NPs, whereby the fluidic properties enabled the lipid membrane to recover thereafter, despite the increased NPs size.[37]

5.2.4.2. Electrochemical responses of the penetration of FcHT-AuNPs through tBLMs

Electrochemical studies were undertaken looking at the electrochemical responses of different sizes of FcHT-AuNPs and their penetration through tBLM modified gold macroelectrodes. In this study, the defects-free tBLM modified electrodes were immersed in solutions of FcHT-AuNPs (5, 10 and 20 nm) for 60 min and electrochemical measurements (DPV) were carried out.

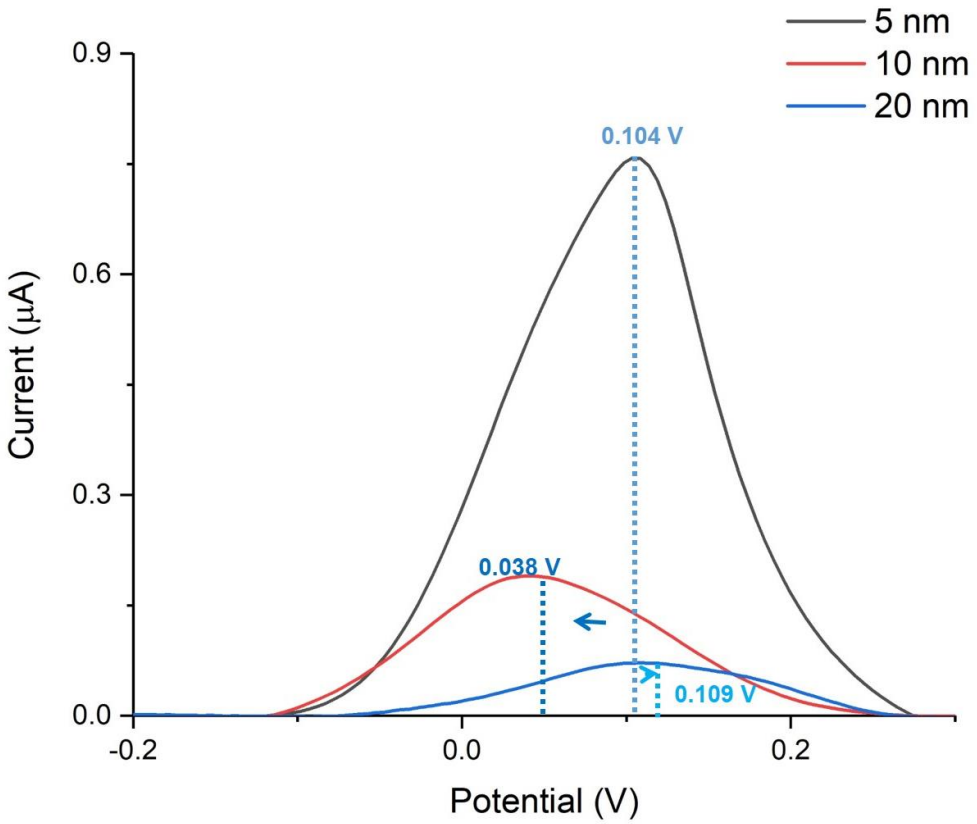

Figure 5.2-14: DPV responses of the penetration of FcHT-AuNPs (5, 10 and 20 nm) into tBLM-modified gold electrode in 20 mM PBS as a function of NP sizes. Sweep amplitude: 5 mV. [5 nm FcHT-AuNPs] = 2.8 µM, [10 nm FcHT-AuNPs] = 3.0 µM and [20 nm FcHT-AuNPs] = 3.0 µM.

Table 5-3: Electrochemical parameters determined by DPV (Figure 5.2-14) using Eq. 5-2 for the penetration FcHT-AuNP through tBLM lipid membrane immobilised electrodes for different NP sizes.

NPs size	***I* (µA)**	**Γ_{NP} (mol/cm^2)**
5 nm	0.76 ± 0.05	2.29 ± 0.90 x 10^{-05}
10 nm	0.19 ± 0.10	6.19 ± 1.05 x 10^{-06}
20 nm	0.07 ± 0.02	2.47 ± 1.03 x 10^{-06}

Small NPs (<5.5 nm AuNPs) easily penetrate cells and these NPs have been localised inside nucleus of cell compared to larger ones (>16 nm AuNPs), which were found to be unable to enter the cells.[44] Given that small NPs have an increased surface area compared to larger ones, this size advantage has been reported to ease the diffusion of NPs into the cell, this is especially seen *in vitro* studies.[45,46] Our results reflect such findings seen in the decrease of current magnitude for the detection of FcHT-AuNPs at electrode's surface (Figure 5.2-14 and Table 5-3); smaller FcHT-AuNPs (5 nm) penetrated further into the lipid, their small sizes

enabled more NPs to penetrate through the lipid membrane to be aggregated at the electrode's surface,[47] consequently increasing their detected redox activity at electrode's surface. 5 nm FcHT-AuNPs penetration was attributed to the NP adsorption and further NPs embedment within the bilayer.[37] Whereas larger NPs (10 and 20 nm) have been reported to cause membrane thinning as well as defects formations i.e. nanoscopic pores/holes within the bilayer architecture. A study by Leroueil *et.al.*[48] supports our results with NPs sizes on NPs-cell membrane interactions causing disruption of cell membrane; they suggested that small 2 nm NPs initially become adsorbed on the bilayer surface and eventually with more adsorptions, these formed aggregates resulting in their penetration into the lipid structure via existing defects. However, larger 50 nm NPs were reported to induce lipid defects such as holes, membrane thinning as these NPs interacted with the lipid membrane. From our results, we were able to map in real time the penetration and adsorption behaviour of electroactive FcHT-AuNPs through lipid membrane using RESI technique and electrochemistry technique enabled the quantification of these electroactive NPs via their redox activities and their comparison in terms of NP sizes.

5.3. Conclusion

In this chapter, we investigated the penetration behaviour as well as the NPs-membrane interactions of thiol-capped gold nanoparticles using atomic force microscopy (AFM), electrochemical techniques and resonance enhanced surface impedance (RESI) technique.

The investigation on the effect of incubation time on NPs-membrane interactions have shown that increasing the incubation time of lipid SAM modified gold substrates in DDT and FcHT-AuNPs resulted in different stages NPs-membrane interactions; the first being NPs adsorption at lipid surface followed by lipid defects formation for the penetration of NPs through the lipid membrane, eventually leading to lipid collapse and/or membrane displacement by NPs multilayers. Such was seen in both the AFM and voltammetry results, with the electrochemical responses being of suppressed redox activities with increased incubation time due to the increased intermolecular interactions of Fc moieties.

On the other hand, the investigation on the impact that NPs sizes has on NPs-membrane interactions have demonstrated that smaller electroactive AuNPs (5 nm) penetrated the lipid membrane, these could be said to be imbedded within the lipid's architecture if immersed longer in the NP solution as demonstrated in the DPV and ESI results. However, RESI results showed that the smaller NPs had overall no effect in the destabilising the integrity of the membrane i.e. the NPs penetration was found to be non-destructive, thus their eventual expulsion from the membrane did not change the RESI capacitance. Whereas, larger NPs (10 and 20 nm) were found to cause NPs adsorption at lipid-electrolyte interface, destabilisation of the membrane via the formation of lipid defects.

5.4. References

1 N. Abbaspour, R. Hurrell and R. Kelishadi, *J. Res. Med. Sci. Off. J. Isfahan Univ. Med. Sci.*, 2014, **19**, 164–174.

2 F. J. Lázaro, L. Gutiérrez, A. R. Abadía, M. S. Romero and A. López, *J. Magn. Magn. Mater.*, 2007, **316**, 126–131.

3 A. N. Nesmeyanov and N. S. Kochetkova, *Russ. Chem. Rev.*, 1974, **43**, 710–715.

4 D. Astruc, *Eur. J. Inorg. Chem.*, 2017, **2017**, 6–29.

5 X. Y. Ling, D. N. Reinhoudt and J. Huskens, *Langmuir ACS J. Surf. Colloids*, 2006, **22**, 8777–83.

6 I. Noviandri, K. N. Brown, D. S. Fleming, P. T. Gulyas, P. A. Lay, A. F. Masters and L. Phillips, *J. Phys. Chem. B*, 1999, **103**, 6713–6722.

7 R. Pietschnig, *Chem. Soc. Rev.*, 2016, **45**, 5216–5231.

8 A. E. G. Cass, G. Davis, G. D. Francis, H. A. O. Hill, W. J. Aston, I. J. Higgins, E. V. Plotkin, L. D. L. Scott and A. P. F. Turner, *Anal. Chem.*, 1984, **56**, 667–671.

9 C. Ornelas, *New J. Chem.*, 2011, **35**, 1973–1985.

10 V. E. Emel'yanov, L. S. Simonenko and V. N. Skvortsov, *Chem. Technol. Fuels Oils*, 2001, **37**, 224–228.

11 G. T. Linteris, M. D. Rumminger and V. Babushok, in *Proceedings. Halon Options Technical Working Conference, Albuquerque*, 2000, vol. 2, pp. 129–140.

12 D. J. Lavrich, S. M. Wetterer, S. L. Bernasek and G. Scoles, *J. Phys. Chem. B*, 1998, **102**, 3456–3465.

13 C. Vericat, M. E. Vela, G. Benitez, P. Carro and R. C. Salvarezza, *Chem. Soc. Rev.*, 2010, **39**, 1805–1834.

14 R. G. Nuzzo and D. L. Allara, *J. Am. Chem. Soc.*, 1983, 105, 4481–4483.

15 K. B. Rodenhausen, B. A. Duensing, T. Kasputis, A. K. Pannier, T. Hofmann, M. Schubert, T. E. Tiwald, M. Solinsky and M. Wagner, *Thin Solid Films*, 2011, **519**, 2817–2820.

16 T. Auletta, F. C. J. M. Van Veggel, D. N. Reinhoudt, F. C. J. M. van Veggel and D. N. Reinhoudt, *Langmuir*, 2002, **18**, 1288–1293.

17 M. Kasuya and K. Kurihara, *Langmuir*, 2014, **30**, 7093–7097.

18 S. Chen and R. W. Murray, *J. Phys. Chem. B*, 1999, **103**, 9996–10000.

19 R. L. Wolfe, R. Balasubramanian, J. B. Tracy and R. W. Murray, *Langmuir*, 2007, **23**, 2247–2254.

20 L. Cabo-Fernández, D. F. Bradley, S. Romani, S. J. Higgins and D. J. Schiffrin, *ChemPhysChem*, 2012, **13**, 2997–3007.

21 R. L. Stiles, R. Balasubramanian, S. W. Feldberg and R. W. Murray, *J. Am. Chem. Soc.*, 2008, **130**, 1856–1865.

22 R. Sardar, C. A. Beasley and R. W. Murray, *Anal. Chem.*, 2009, **81**, 6960–6965.

23 K. L. Chen and G. D. Bothun, *Environ. Sci. Technol.*, 2014, **48**, 873–880.

24 C. Contini, M. Schneemilch, S. Gaisford and N. Quirke, *J. Exp. Nanosci.*, 2018, **13**, 62–81.

25 W. Xia, Y. Li, Y. Wan, T. Chen, J. Wei, Y. Lin and S. Xu, *Biosens. Bioelectron.*, 2010, **25**, 2253–8.

26 J. Jiang, G. Oberdörster and P. Biswas, *J. Nanoparticle Res.*, 2009, **11**, 77–89.

27 A. Elsaesser and C. V. Howard, *Biol. Interact. Nanoparticles*, 2012, **64**, 129–137.

28 R. V. Goreham, V. C. Thompson, Y. Samura, C. T. Gibson, J. G. Shapter and I. Köper, *Langmuir*, 2015, **31**, 5868–5874.

29 N. Ábrahám, E. Csapó, G. Bohus and I. Dékány, *Colloid Polym. Sci.*, 2014, **292**, 2715–2725.

30 G. J. Gordillo, Ž. Krpetić and M. Brust, *ACS Nano*, 2014, **8**, 6074–6080.

31 G. K. Rowe and S. E. Creager, 1991, 2307–2312.

32 C. E. D. Chidsey, C. R. Bertozzi, T. M. Putvinski and A. M. Mujsce, 1990, 4301–4306.

33 A. V Rudnev, K. Yoshida and T. Wandlowski, *Electrochimica Acta*, 2013, **87**, 770–778.

34 A. V Rudnev, U. Zhumaev, T. Utsunomiya, C. Fan, Y. Yokota, K. Fukui and T. Wandlowski, *Electrochimica Acta*, 2013, **107**, 33–44.

35 S. Zhang, A. Nelson and P. A. Beales, *Langmuir*, 2012, **28**, 12831–12837.

36 M. Brust and G. J. Gordillo, *J. Am. Chem. Soc.*, 2012, **134**, 3318–3321.

37 R. P. Carney, Y. Astier, T. M. Carney, K. Voïtchovsky, P. H. Jacob Silva and F. Stellacci, *ACS Nano*, 2013, **7**, 932–942.

38 S. Chen, *Langmuir*, 2001, **17**, 6664–6668.

39 S. Lingler, I. Rubinstein, W. Knoll and A. Offenhäusser, *Langmuir*, 1997, **13**, 7085–7091.

40 C. Brett, S. Kresak, T. Hianik and A. M. Oliveira Brett, *Electroanalysis*, 2003, **15**, 557–565.

41 C. M. Bailey, E. Kamaloo, K. L. Waterman, K. F. Wang, R. Nagarajan and T. a. Camesano, *Biophys. Chem.*, 2015, **203**–**204**, 51–61.

42 S.-H. Park, S.-G. Oh, J.-Y. Mun and S.-S. Han, *Colloids Surf. B Biointerfaces*, 2006, **48**, 112–118.

43 Y. Guo, E. Terazzi, R. Seemann, J. B. Fleury and V. A. Baulin, *Sci. Adv.*

44 L. Shang, K. Nienhaus and G. U. Nienhaus, *J. Nanobiotechnology*, 2014, **12**, 5.

45 S. Salatin, S. Maleki Dizaj and A. Yari Khosroushahi, *Cell Biol. Int.*, 2015, **39**, 881–890.

46 A. E. Nel, L. Mädler, D. Velegol, T. Xia, E. M. V Hoek, P. Somasundaran, F. Klaessig, V. Castranova and M. Thompson, *Nat. Mater.*, 2009, **8**, 543.

47 Y. Liu and R. Mark Worden, *Biochim. Biophys. Acta*, 2015, **1848**, 67–75.

48 P. R. Leroueil, S. A. Berry, K. Duthie, G. Han, V. M. Rotello, D. Q. McNerny, Baker James R., B. G. Orr and M. M. Banaszak Holl, *Nano Lett.*, 2008, **8**, 420–424.

6. Complex polymeric AuNPs and their interactions with lipid membranes

Nanoparticles (NPs) are widely used in biomedical applications and they have become important tools in the design, synthesis and manufacturing of selective diagnostic systems, most especially in the combat against bacterial resistance. This chapter outlines the different studies undertaken with complex thiol-protected AuNPs, received form Dr Agasti's research group (Jawaharlal Nehru Centre for Advanced Scientific Research, Bangalore, India). The research conducted in this chapter explores the NP surface functionalities and their interactions with both artificial cell membranes and real bacterial cells. Quartz crystal microbalance (QCM), Resonance enhanced surface impedance (RESI) and electrochemical impedance spectroscopy (EIS) are used to investigate the penetration behaviours as well as the electrochemical responses of the complex NPs with tethered lipid membrane (tBLM) on gold electrodes. The minimum inhibitory concentration (MIC) technique is used to investigate of potency of these NPs against Gram-negative Escherichia coli bacterial cells.

6.1. Introduction

The use of nanoparticles (NPs) have seen a great increase in the field of bio-nanotechnology. This has been due to the unique physiochemical properties of NPs and the ease at which these particles can be synthesised and functionalised in a controlled manner thus they can be useful tool in biomedical applications such as sensing, delivery and imaging.[1] This chapter will consider the use of NPs as antibacterial agents; it will give background information on the bacterial cell walls and the toxicity mechanism of NPs against bacterial cells.

6.1.1. An Introduction to bacteria cell walls

The bacteria are prokaryotic cells; they do not possess a membrane bound nucleus thus the DNA is not surrounded by a membrane envelope but is hosted in the cytoplasm. The greatest difference is seen in the structural characteristics of the cell wall (Figure 6.1-1). Bacteria cell walls act as an outer envelope providing strength, rigidity and shape to the bacterial cell.[2] Hans Christian Gram developed a technique that allows the distinction of bacterial cell wall structures; this staining technique has been divided into two categories based on the response to the Gram stain procedure. In a Gram test, the bacteria is stained with violet crystal dye and a colour change is seen characteristic of the bacterial cell wall structure. A decolourisation is seen for Gram negative bacteria; this is due to the thin/single layer of cell wall (peptidoglycan) that cannot prevent the stain from leeching out, causing the outer membrane to dissolve and the peptidoglycan layer to break apart. However, Gram positive bacteria retain their colour (pink or red) due to the thick/several layer of peptidoglycan cross-linked in the matrices allowing the cell to retain its initial staining colour.[3]

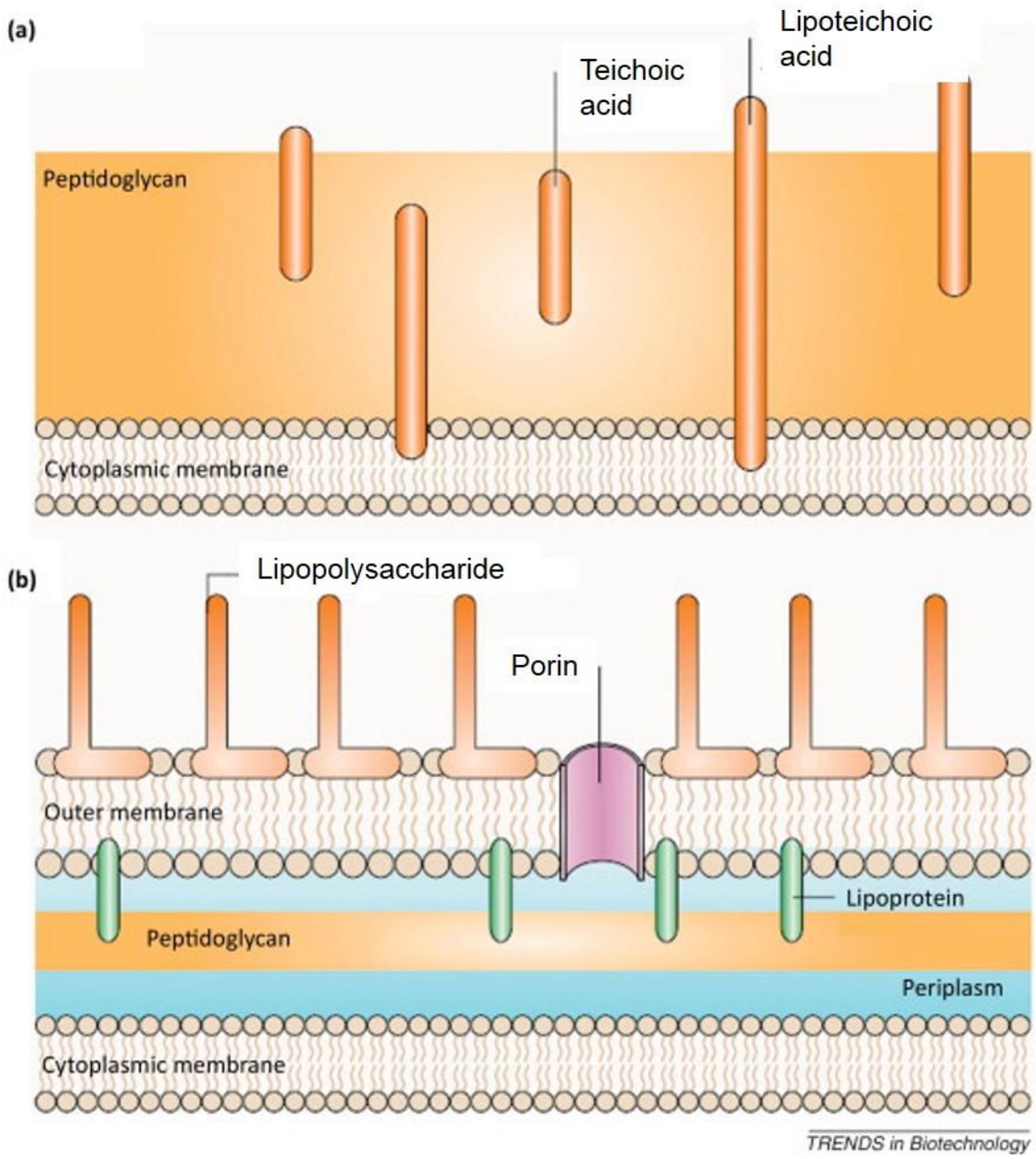

Figure 6.1-1: Illustration of the structure and composition of bacteria cell walls; A) Gram-positive and B) Gram-negative. Reprinted from Ref. 4 with permission from Elsevier (Trends in Biotechnology).

Table 6.1-1: Table showing different components of bacterial cell wall for both Gram positive and negative.[2,3]

Cell wall components	Gram positive	Gram negative
Peptidoglycan	15-80 nm in thickness, major component of cell wall (~50 %)	Thinner layer (2-3 nm)
Teichoic acid	Covalently bonded to peptidoglycan	None
Lipoteichoic acid	Lipid linked teichoic acid	None
Periplasmic space	Small or none	Contains enzymes
Outer membrane	None	Phospholipids with saturated fatty acids, embedded porins, lipoproteins
Lipopolysaccharide	None	Lipid A, core polysaccharide, O antigen

6.1.2. Mechanism of NPs against bacteria

There are bacteria that are useful to human life, such as bacteria that can convert nutrients in the soil into useful forms that can be taken up into plants, or bacteria that live in the gut in helping with food digestion. other bacteria are harmful to human lives and these are called pathogenic, disease causing. Such bacterial infections if not treated can cause serious illness even death. As a result, it is essential to find ways that will kill these harmful bacteria (bactericidal) or dramatically decrease their growth (bacteriostatic) without causing harm to the healthy surrounding human tissues. Scientists have developed antibacterial agents that can act in such ways, examples include β-lactams (penicillin), antibiotics (sulphonamides).[4] Due to the rise in bacterial resistance caused by the overuse of certain antibacterial drugs, antibiotics, there is a real need to manufacture antibacterial agents that can combat these multidrug-resistant bacteria while decreasing drug manufacturing costs as well as reducing side effects for patients as lower doses of the drugs would only be needed instead of multiple drugs. The formulation and use of NPs as antibacterial agents have been reported to be successful, whereas bacteria can develop resistance towards antibiotic drugs, the bacteria is unable to develop resistance against NPs as these react with multiple components of the cell.[5–7] The exact mechanism used by NPs to cause bacterial toxicity is still not well understood. However, antibacterial action of NPs have been reported to have two main

mechanisms; the first is the prevention of bacterial growth by inhibiting proteins in the cell that causes a decline in the bacterial metabolism and, the second is NPs inducing the formation of free radicals (reactive oxygen species) into the cell causing eventual cell lysis.[8–10]

It is also important to highlight that the toxicity of NPs are dependent on two main factors: the physicochemical properties of the NPs (NPs composition, size and surface functionalisation) and the bacteria species (Gram-positive or Gram-negative) and their rate of growth.[4,7,11]

In this chapter, the research focused on the (semi)quantitative interaction of complex thiol-modified gold NPs to lipid membranes; both artificial cell membrane models and real bacteria cells, using different techniques which includes quartz crystal microbalance (QCM), resonance enhanced surface impedance (RESI), electrochemical impedance spectroscopy (EIS) and minimum inhibitory concentration (MIC).

The chapter further discusses the observed effects for the studies of NPs with different surface composition on their (semi)quantitative penetration behaviour to both artificial cell membrane models i.e. tBLM model immobilised on gold electrodes and bacterial cells:

i. the effect of these complex NPs on tBLM immobilised on gold electrodes using QCM, RESI and EIS techniques;

and

ii. the effect of these complex NPs on Gram-negative Escherichia coli (*E. coli*) bacteria cells using MIC technique.

6.2. Results & Discussion

Surface composition of NPs have been reported to have an impact on NPs interaction with lipid membrane.[12] The results in this chapter investigates the effect of surface composition of NPs on both artificial and real lipid membranes.

6.2.1. Modified AuNPs

The complex functionalised AuNPs were from received from Dr Sarit S. Agasti (Jawaharlal Nehru Centre for Advanced Scientific Research, Bangalore, India), the size (3 nm) and structure characterisation were provided by the Agasti research group and, the NPs were used without purification, they were diluted to a concentration of 200 nM in deionised water. Unfortunately, since so little sample volumes were received, we were unable to do more characterisation of the NPs; however, the structures of the samples were assigned using the information received.

The functional groups incorporated in the makeup of the complex AuNPs consist of; alkanethiol group, TEG group, cationic ammonium group (primary, secondary and quaternary), alkyl group and aryl (aromatic hydrocarbon) group. Table 6.2-1 shows the samples that were used in the research as well as their chemical structures.

Table 6.2-1: Table showing the chemical structures of the modified AuNPs used in this research. The samples were dispersed in deionised water to a concentration of 200 nM.

Sample ID	Molecular weight /g mol^{-1}	Sample structure
$AuC_{11}TEGNHXyl$	653	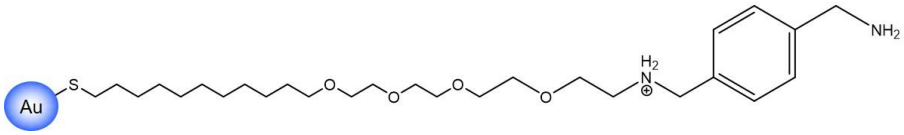
$AuC_{11}TEGNMe_2Bz$	651	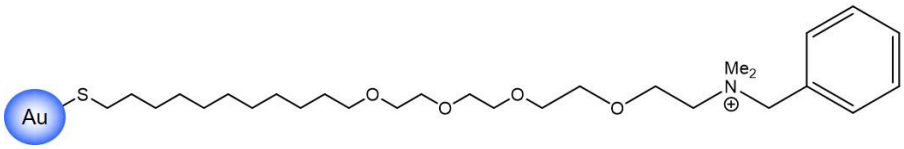
$AuC_{11}TEGNMe_2Hexyl$	645	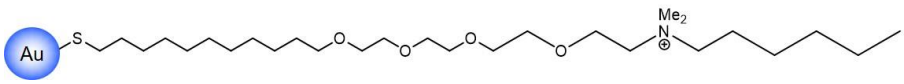
$AuC_{11}TEGNHC_6NH_2$	632	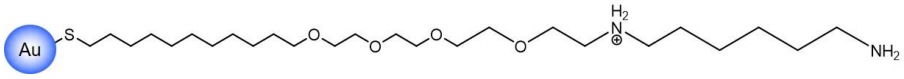

The advantage of having a strong thiolate bonding (R-S) covalently bonded to the gold metal core (R-S-Au group) enables the colloidal sample to have a great stability against aggregation as well as enabling the sample to have controlled NPs sizing; strong alkyl-thiol ligand binding on metal cores leads to small NP sizes, as well as improved/enhanced NPs stability.[13] Ordinarily thiol-modified NPs are synthesised in inorganic solvents such as toluene using the Brust-Schiffrin synthetic method[14] these NPs dispersed in inorganic

solvents are therefore immiscible with neutral aqueous solutions and biological media thus potentially limiting their uses in biomedical applications; the organic solvent can be said to be toxic to living organisms in other words, they are bio-incompatible. It has been reported that poly- or mono ethylene glycol units as part of the capping agent protecting the metal clusters adds the ability of the NPs to become soluble in water thus increasing their biocompatibility.[15,16] Adding to that, polyethylene glycol (PEG) acts as protecting layer on the surface of the NPs with functionality such as preventing the non-specific and unwanted interaction of pegylated NPs with proteins in biological samples.[17] The NP samples used in this research have triethylene glycol units (TEG, $C_6H_{14}O_4$) incorporated into the makeup of the NPs. As a low molecular compound of PEG, having TEG units would not only improve the water solubility and biocompatibility of the NPs, but also it would decrease the bulkiness that is associated with PEG units as well as maintain the stability of thiolated AuNPs.[18]

In this research, secondary and quaternary ammonium cations are part of the NP makeup. As charged groups, these would change the surface net charge of the NPs thus favouring oppositely charged ions, consequently affecting the interactions of the NPs with phospholipid membrane.[19] The addition of hydrophobic aryl (aromatic hydrocarbons) group as one of the functional groups on the AuNPs would enhance the NPs hydrophobicity. Generally hydrophobic NPs tend to aggregate, thus affecting the NPs physiochemical properties such as its large surface-to-volume ratio consequently its ability to cytotoxicity.[20] This can be overcome by having charged functionality as part of the NPs makeup, which eliminates the aggregation issue.

6.2.2. NPs interaction with artificial lipid membrane immobilised on gold substrates

Different techniques were employed to characterise the interactions of NPs with artificial lipid membranes (Figure 6.2-1); QCM focused on the change in mass density that the interaction of NPs with lipid membranes caused, RESI technique focused on the interaction of the NPs with tBLM models in terms of the changes in RESI capacitance and

electrochemical impedance spectroscopy (EIS) focused on the electrochemical responses induced by exposing lipid-insulated electrodes in AuNPs rich solutions.

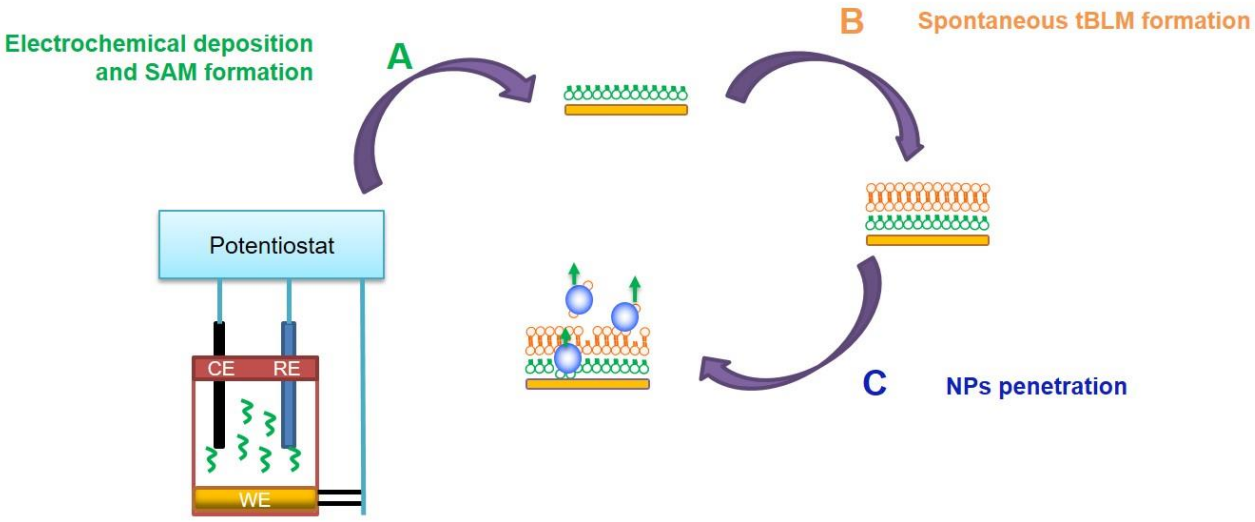

Figure 6.2-1: Illustration of the results aquired for the study of NPs intercation with artificial lipid membranes.

6.2.2.1. Spontaneous tBLM formation

In this study, QCM technique was used to monitor in real time the formation of lipid bilayer on SAM mobilised gold crystals. QCM crystals were modified with thiols to form SAM layer *in situ* by electrochemical deposition method; instead of the immersion of the gold substrates in thiol solutions for 48 hrs, this step was adjusted to enable the electrochemical deposition of thiol lipids on gold substrates, for a faster and effective technique for the formation of thiolated SAM on gold electrodes.[21] EQCM cells were set up with the working electrode (QCM gold crystal), counter electrode (Pt flag) and the pseudo reference electrode (Pt wire). The cells were filled with a mixture solution of thiol lipids in EtOH (1 mM) and 0.1 M KNO_3 and a potential of 0.6 V was held at the working electrode for 45 min. The quality of the monolayer formation was checked in a redox rich solution with the suppression of redox peaks for successfully formed SAM on gold substrates (Figure 6.2-2).

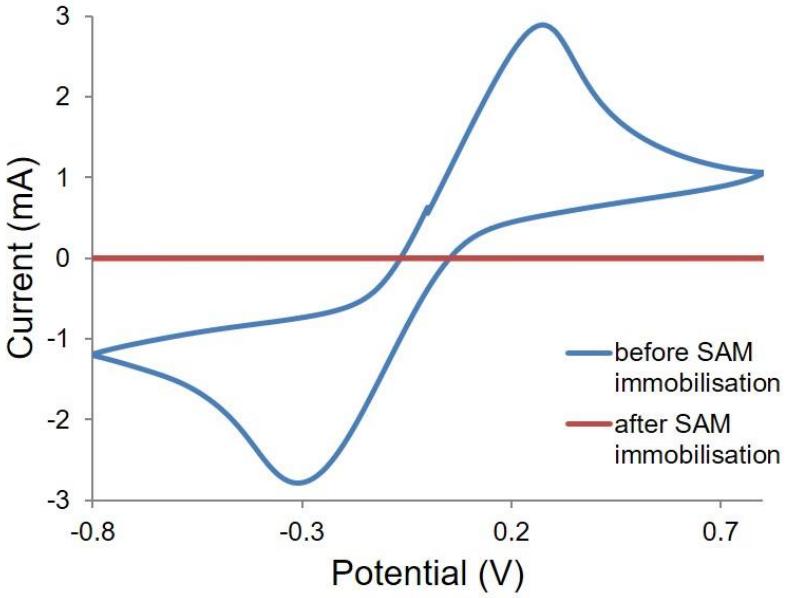

Figure 6.2-2: CV of SAM-modified gold crystals in solution of 10 mM $Fe^{3+/4+}$ (5 mM $K_4[Fe(CN)_6]$ and 5 mM $K_3[Fe(CN)_6]$) in 0.1 M KNO_3 at 50 mV/s scan rate.

Only the fully insulated SAM crystals without defects were used for the following stage, deposition of POPC lipid vesicles whist monitoring the formation of bilayer layer on the SAM modified gold crystals using QCM technique to record the change in frequency.

After a system stabilization time of 15 min was obtained which was similar to the studies used for RESI experiments (Chapter 5.3), the lipid vesicles in the prepared solution were dispersed in the QCM, the lipid bilayer formation was monitored as the changes in resonant frequency (Figure 6.2-3).

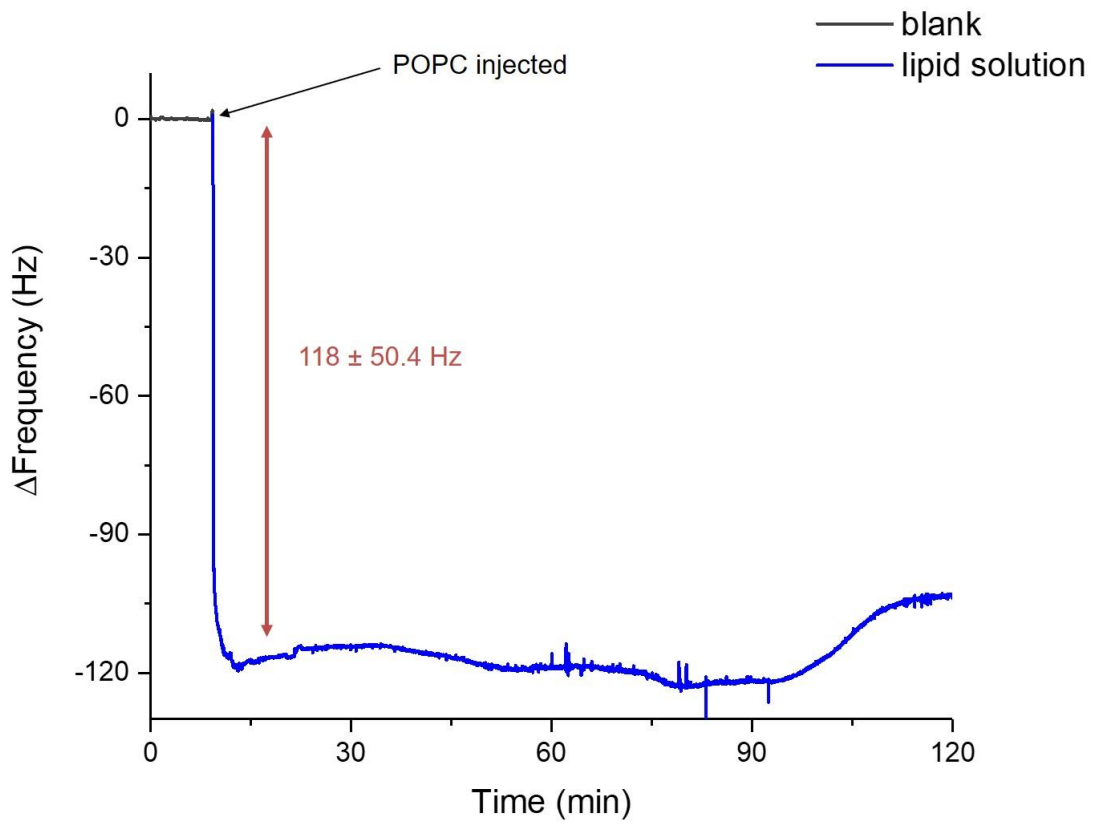

Figure 6.2-3: Measured QCM frequency shifts during the formation of lipid bilayer on SAM electrode.

Similarities of both systems is seen in the formation of the lipid bilayer causing decreases in RESI capacitance (Chapter 5.2.3, Figure 5.2-12) and resonant frequency (QCM, Figure 6.2-3). The decrease in frequency (negative Δf) has been reported on oxidised gold surface for the adsorption of intact lipid vesicles at 90 Hz resonant frequency shift[22] whilst on thiol monolayer on gold crystals, resonant frequency shifts generated from the lipid adsorption were from -26 to -350 Hz (depending on the nature of the thiol molecules).[23,24] From our results, Δf was recorded at -118 ± 50.4 Hz, within the range of reported resonant frequency shifts; this is evidence that our method is reliable for the formation of stable lipid bilayer on lipid monolayer immobilised on gold crystals. The injection of POPC vesicle solution generated the decrease in frequency (negative Δf) attributed to the addition of mass onto the crystal's surface due to the vesicles' deposition and adsorption and, the consequent formation of lipid film on the crystal surface. Using the Sauerbrey equation ($\Delta m = -C\Delta f$ with C = 56.6 Hz cm^2 μg^{-1}), the change in mass was determined to 1448 ± 134 ng/cm^2, equivalent

to 11 molecules/nm^2. The expected result was of direct fusion of POPC vesicles on SAM due to its hydrophilic interactions.[25] We also saw a slight increase of Δf, thus decrease in mass which can be interpreted as the release of water from the vesicles as these ruptured, this increase of Δf eventually reached stable values for the formation of intact lipid bilayer to form bilayer film.

6.2.2.2. NPs-bilayer interactions

We investigated the effect of NP surface charge and the penetration behaviour of these complex AuNPs through tBLM models using QCM, RESI techniques and impedance spectroscopy (EIS). QCM is a technique commonly used to monitor the interaction between NPs and lipid membrane in real time.[26] A study conducted by Bailey *et al*[27] investigated the NPs-membrane interaction using QCM coupled with dissipation monitoring. Their findings show that the ability of the technique distinguish between the different interaction mechanisms of NPs, whether it is through adsorption, as the calculated increase in mass corresponding to the changes in frequency values before and after exposure, and a subsequent NPs adsorption would be a calculated decrease in mass. EIS, on the other hand, is used to study of NPs-membrane interaction; giving information on the interaction mechanism after exposure of the model membrane to the NPs, in terms of electrical properties of the membrane before and after exposure. Lui *et al.*[28] reported on the influence of NPs surface chemistry on their interaction with lipid membrane tethered on gold electrode surfaces. The findings revealed that the changes in the component values of the fitted circuit related to the mechanism of NPs-membrane interaction; a decrease in the membrane resistance values after NPs exposure were due to the formation of membrane defects. Whereas changes in membrane capacitance has been reported to be due to the adsorption of NPs at lipid-electrolyte interface.[12]

Every experiment (RESI, EIS and QCM) was carried out at least three times.

As RESI is a relatively new technique, this will be used to give a qualitative interpretation of the penetration of NPs through lipid membranes; both techniques, QCM and RESI, gave real time measurements as to map the interactions of NPs with lipid membranes as illustrated in Figure 6.2-4.

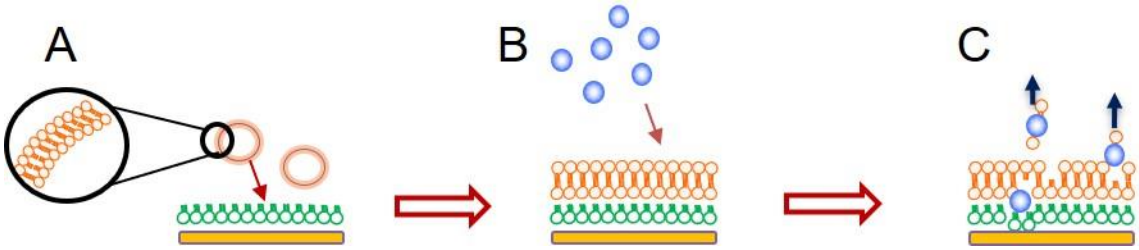

Figure 6.2-4: Schematic diagram to illustrate the interaction of complex AuNPs with planar lipid membranes; A) the formation of tethered lipid bilayer via the interaction of vesicles and hydrophobic SAM on gold electrode, B) the addition of NPs into the system leading to their interaction with the tBLM model and C) through NPs penetration and lipid desorption (lipid defects formation).

RESI results show the following stages Figure 6.2-5: **stage (a)** for the stabilisation of the system for approximately 15 min at set flow rate of 5 µL/min; as this was a continuous flow system, a constant flow of buffer (20 mM PBS) was maintained, following the injection of fresh solvent (deionised water) which was also left to run for another 10 min of stabilisation **stage (b)**. **Stage (c)** saw the injection of 200 µl of AuNPs, dispersed in deionised water at a concentration of 200 nM into the system fitted with tBLM-modified gold sensors. Followed by a repeat of the earlier stages; buffer, solvent, NPs injection and buffer, for the **stages (d)**, **(e)**, **(f)** and **(g)** respectively.

From the results obtained from QCM investigations, different stages were assigned: **stage (a')** showing the stabilisation of the system for approximately 15 min; static system where the cell is filled with 2 mL of buffer 20 mM PBS, after system stabilisation, the cell was emptied and re-filled with fresh solvent (deionised water) for another 10 min of stabilisation **stage (b')**. This treatment was applied to all four samples prior to the addition of NPs into the system; **stage (c')** saw the flush and refill of the cell with AuNPs making up the concentration of 200 nM, the dispersion of NPs into the system allowed the NPs to interact with the lipid membrane for approximately 40 min followed by the final flush and re-fill of the cell with fresh buffer as indicated in **stage (d')**.

Concerning EIS investigations, the tBLM electrodes were checked for lipid defects in redox rich solutions before they were used for the study; only well insulated electrodes were used. These tBLM electrodes were used as working electrodes in electrochemical cells as part of the 3-electrode set up: Pt flag as counter electrode and Pt wire as pseudo-reference electrode, the electrolyte solution used was 20 mM PBS. EIS experiments were run before and after one-hour incubation of the immobilised electrodes in the specified NPs solutions to determine the effect of NPs interaction with lipid membrane. The EIS data obtained were fitted to the equivalent circuits, included in the graphs for each NP. The circuits were composed of different parameters; the common parameters were solution resistance (R_s), membrane CPE (Q_m) and membrane resistance (R_m). The constant phase element (CPE) was used instead of a capacitor (C) to compensate for the non-homogeneity in the system which can be caused by imperfections of the lipid membrane on the surface of the electrode.

6.2.2.3. $AuC_{11}TEGNHXyl$

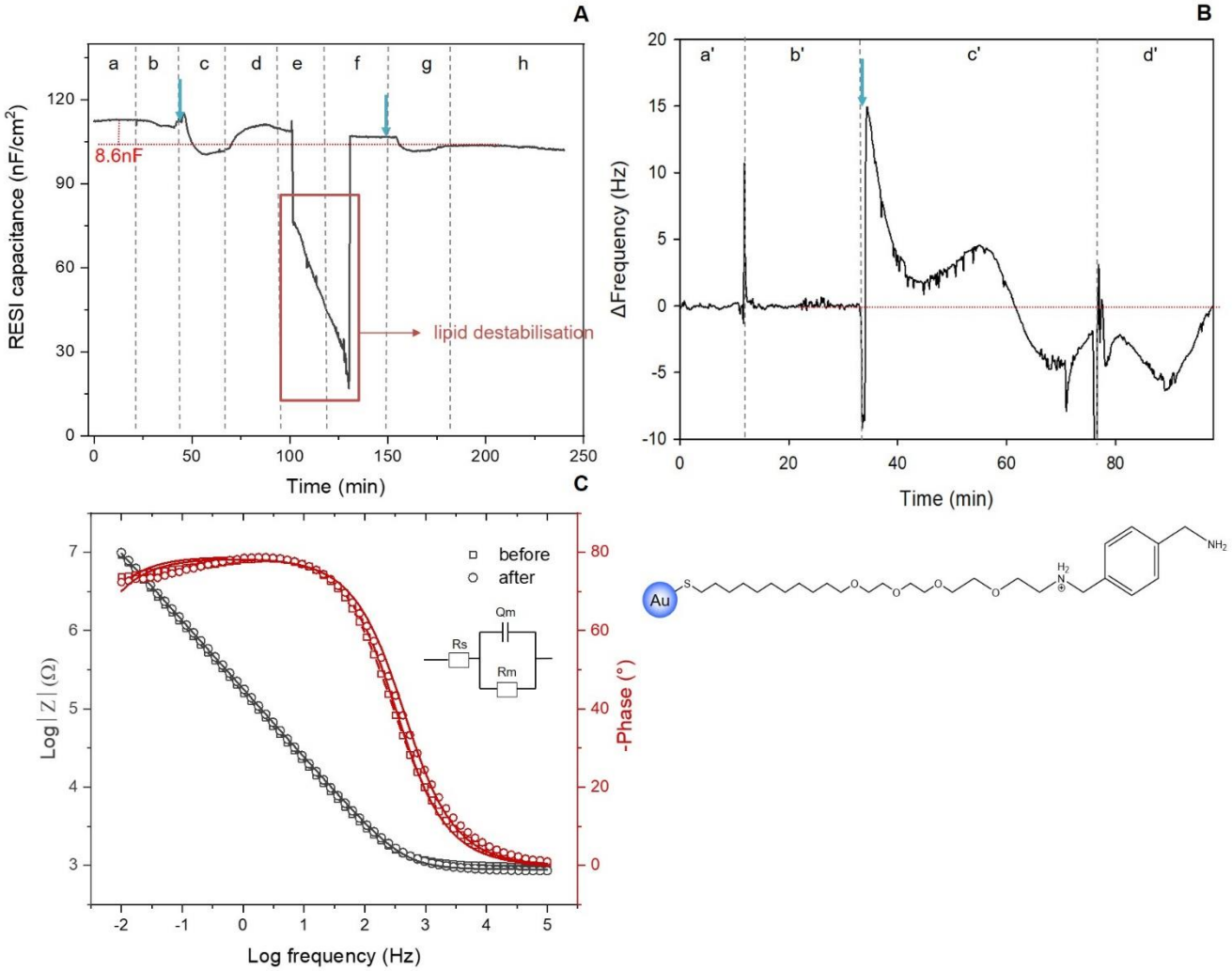

Figure 6.2-5: A) Change in RESI capacitance for the interaction of -NHXyl functionalised AuNPs with tBLM sensor over time in a running electrolyte solution of 20 mM PBS at a set flow rate of 5 µL/min, B) measured QCM frequency shifts during the interaction of NPs with tBLM electrode (blue arrows indicate the injection of NPs into the system) and C) experimental EIS spectra for the interaction of NPs with tBLM electrode, before and after 60 min incubation in NP solution. Left vertical axis: log of impedance (Z) magnitude (grey). Right vertical axis: minus phase angle (dark red). Solid lines are impedance curves simulated from an electric equivalent circuit model of R(QR) – see insert; R_s: solution resistance, Q_m & R_m: membrane CPE and membrane resistance respectively.

QCM & RESI results

The injection of –NHXyl functionalized NPs into the system saw unstable frequency shifts Figure 6.2-5B, this could be evidence of membrane perturbation by the addition of NPs. However, at the end of the NPs interaction time (stage **c'**), the frequency difference recorded was only -1.9 ± 1.46 Hz, synonymous of a calculated mass gain of 23.0 ± 18.3 ng/cm^2, this can be assumed to be caused by NPs adsorption at lipid's surface. However, at the end of the final flush and buffer stage, the Δf was recorded as +0.23 ± 1.49 Hz, which we assigned

as the desorption of NPs from the lipid-electrolyte interface due to the mass loss of 2.83 ± 0.71 ng/cm^2 (stage **d'**); implying the interaction between the NPs and the lipid surface membrane was of non-specific NPs adsorption of onto the lipid membrane.

The RESI results recorded a U-shaped well, created from the addition of NPs into the system (Figure 6.2-5A - stage **d**). We attributed this feature to the adsorption of NPs at electrolyte-lipid interface followed by the desorption of the NPs from the lipid's surface, which reflected the QCM results of the non-specific NPs adsorption. After the addition of the deionised water (solvent) into the system, a sharp RESI capacitance decrease was recorded (stages **e-f**) and this was referred to as lipid destabilisation which lasted 33 min. We attributed such lipid perturbation event to the rearrangement of lipid molecules, evidence of the bilayer self-healing property seen in the recovery of the RESI capacitance to near initial value, even the 2nd injection of the NPs only caused an overall RESI capacitance decrease of 8.6 ± 4.46 nF (stage **h**).

EIS results

The EIS fitting using the NOVA software gives values for R_0 and Q which are the terms defined in Eq. 6-1; where R_o is the low frequency real-axis intercept, T is the mean time constant, and n is related to the depression angle.

$\boldsymbol{Z = \frac{R_0}{(1+R_0Q(j\omega)^n)}}$ this can also be expressed as $\boldsymbol{Z = \frac{R_0}{(1+R_0Q(j\omega T)^n)}}$ **(6-1)**

The pseudo value of the capacitance was calculated from Eq. 6-1 using values from the CPE in parallel with the resistor, the value, expressed in Eq. 6-2, can be derived from the above equations knowing that T = RC.[29]

$$C = \frac{(Q_0 R)^{(1/n)}}{R} \quad (\textbf{6-2})$$

Eq. 6-2 was used for the CPE used in the calculation for the impedance; where Y_0 = capacitance, ω = frequency and n = coefficient (value between 0 and 1, where 1 is for an ideal capacitor).

$$Z = \frac{1}{Y_0(j\omega)^n} \quad (\textbf{6-3})$$

Table 6.2-2: Resistance and capacitance values of tBLM before and after incubation in -NHXyl functionalised AuNPs. [a] Capacitance values calculated from Eq. 6-2.

	Membrane resistance (R_m) /MΩ	**Membrane CPE (Q_m) /μMho**	**Membrane capacitance [a](C_m) /nF**
Before	69.0 ± 1.04	1.23 ± 0.07 (0.878)	49.0
After	64.0 ± 1.03	1.12 ± 0.09 (0.873)	37.4

From the impedance results and experimental data fit (Figure 6.2-5C and Table 6.2-2), we saw the lack of change in the electrical properties of the membrane when comparing before and after incubation of lipid-modified electrode in NP solution for 60 min; following very small changes in their components with fitting of R(QR) equivalent circuit. The changes observed in Table 6.2-2 was of small decreases in R_m and Q_m values and consequently to the membrane capacitance (C_m). These results suggest that the exposure of the lipid membrane in a solution of -NHXyl functionalised AuNPs after 60 min did not favour penetration of the NPs into the lipid membrane, NPs adsorption at electrolyte-lipid interface was of weak interactions as was identified with the other techniques (QCM and RESI).

A study by Lin and Alexander-Katz[30] on the effect of cationic NPs uptake through model cell membranes have revealed that the presence of terminal primary ammonium groups (R-$^+NH_3$) in an alkanethiol-functionalised AuNPs induce spontaneous translocation of NPs under transmembrane potential of -1.5 V using simulation studies. But before the translocation can occur, both NPs and cell membrane were constrained, and this caused membrane defects to form. Consequently, the NPs passed through the lipid holes, thus translocation took place. Adding to that, the authors also observed the self-healing property of the membrane model after NPs translocation occurred. Although the membrane model for our study was un-potentiated, it can be argued that similarities in our results and theirs can be drawn; in our study, NPs adsorption was the initial interaction process followed by

NPs desorption which caused membrane destabilisation then lipid rearrangement. As a result, the drawn similarities can be highlighted in the induced lipid destabilisation which caused non-destructive membrane defects seen by the membrane self-healing properties. Self-healing membrane properties in the RESI results referred to the ability to recover to near initial RESI capacitance values prior to NPs injection into the system and NPs interaction with lipid membrane.

6.2.2.4. $AuC_{11}TEGNMe_2Bz$

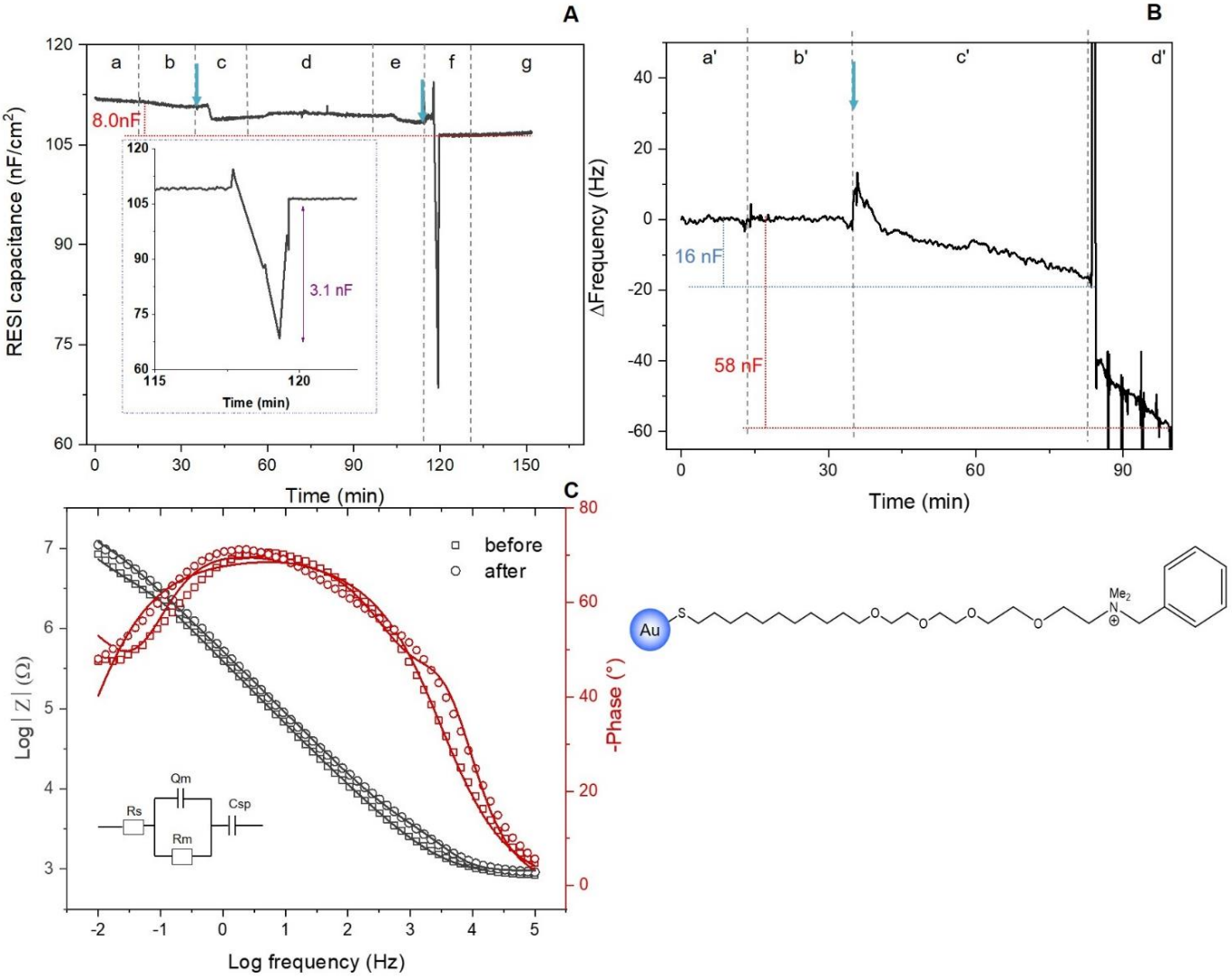

Figure 6.2-6: A) Change in RESI capacitance for the interaction of -NMe_2Bz functionalised AuNPs with tBLM sensor over time in a running electrolyte solution of 20 mM PBS at a set flow rate of 5 µL/min, B) measured QCM frequency shifts during the interaction of NPs with tBLM electrode and C) experimental EIS spectra for the interaction of NPs with tBLM electrode, before and after incubation in NP solution. Left vertical axis: log of impedance (Z) magnitude (grey). Right vertical axis: minus phase angle (dark red). Solid lines are impedance curves simulated from an electric equivalent circuit model of R(QR)C – see insert; R_s: solution resistance, Q_m: membrane CPE, R_m: membrane resistance and C_{sp}: spacer capacitance.

QCM & RESI results

From Figure 6.2-6B, the injection of sample (–NMe_2Bz) into the cell caused an initial decrease in frequency (Δf = -16 ± 2.96 Hz) for the NPs from QCM results, denoting the adsorption of NPs on electrolyte-lipid interface, following the flush of cell content and the addition of buffer solution, a further decrease in frequency of (Δf = -56 ± 19.27 Hz), equivalent to a mass gain of 712 ± 33.4 ng/cm^2 was detected. On the other hand, the RESI results for this sample (Figure 6.2-6A) saw the initial injection of NPs causing adsorption of NPs at electrolyte-lipid interface, a later NPs injection caused brief NP penetration and NP expulsion events which only lasted 1.9 min (Figure 6.2-6A insert).

Considering the structure and surface chemistry of these NPs, the presence of the hydrophobic benzyl group together with the quaternary ammonium salt made the polymer-based NPs hydrophilic.[31] It is probable that the hydrophilic nature of the NPs contributed to the brief penetration of the NPs into the membrane, seen in RESI results. This conclusion was supported in a simulation study by Pogodin *et al*[32] though our membrane model was not of a free-standing membrane model used in the simulation study. The study reported that the penetration of hydrophilic cylindrical peptides into bilayer membrane was energetically unfavourable, thus supporting our conclusion on the brief NPs penetration which followed the NPs ejection from the lipid membrane. As a result, the penetration of the hydrophilic NPs could not cause NPs translocation.[12] In view of this finding, the brief penetration of the –NMe_2Bz functionalised hydrophilic AuNPs can also be said to be energetically unfavourable owing to the subsequent repulsion of the NPs from the membrane environment after 1.9 min, we believe that the brief penetration could have been due to NPs accumulation at electrolyte-lipid membrane interface.

EIS results

Figure 6.2-6C, the fitting of experimental data with equivalent circuit (insert) revealed R(RQ)C circuit to represent our system; RQ in series with a capacitor and solution resistance. The capacitor was referred as a spacer capacitor as it combines the spacer

region of the membrane and the electrode interface.[24] The analysis of these results revealed that the equivalent circuit was the same, suggesting that the incubation of the tBLM in sample solution did not affect the electrical properties of the membrane. Implying that the exposure of tBLM in –NMe_2Bz functionalised AuNP solution did not result in membrane defects formation. However, changes to the values of the components of the circuitry seen in Figure 6.2-6C suggest interactions of the NPs at electrolyte-lipid interface. The circuit expected for this sample penetration would have been a simple Randles, R(QR), as this also reflect the results from the RESI and QCM experiments of the perturbation of the lipid's architecture by the interaction of lipid membrane with the NPs, thus causing lipid defects, seen with the decrease in RESI capacitance and frequency change values.

Table 6.2-3: Resistance and capacitance values of tBLM before and after incubation in -NMe_2Bz functionalised AuNPs. [a] Capacitance values calculated from Eq. 6-2.

	Membrane resistance (R_m) /MΩ	**Membrane CPE (Q_m) /nMho**	**Membrane capacitance [a](C_m) /nF**	**Spacer capacitance (C_{sp}) /μF**
Before	6.65 ± 0.63	682 ± 12.5 (0.759)	1.71×10^{-1}	4.68 ± 0.62
After	13.0 ± 2.4	521 ± 13.0 (0.744)	7.48×10^{-2}	3.24 ± 0.90

It has been reported that polymer containing quaternary ammonium group are found to be weakly bound to POPC vesicles without inducing pores.[33] Comparing the structure of –NHXyl with –Me_2Bz functionalised AuNPs, the differences arise in the additional primary ammonium end group to the aryl group as well as a secondary ammonium group instead of the quaternary ammonium group present in the –Me_2Bz functionalised AuNPs. Though the interaction mechanism of both NPs promoted NPs adsorption with lipid membrane, the differences in structure and surface chemistry of the NPs were found to have played a role in the penetration of NPs though the lipid membrane.

6.2.2.5. $AuC_{11}TEGNMe_2Hexyl$

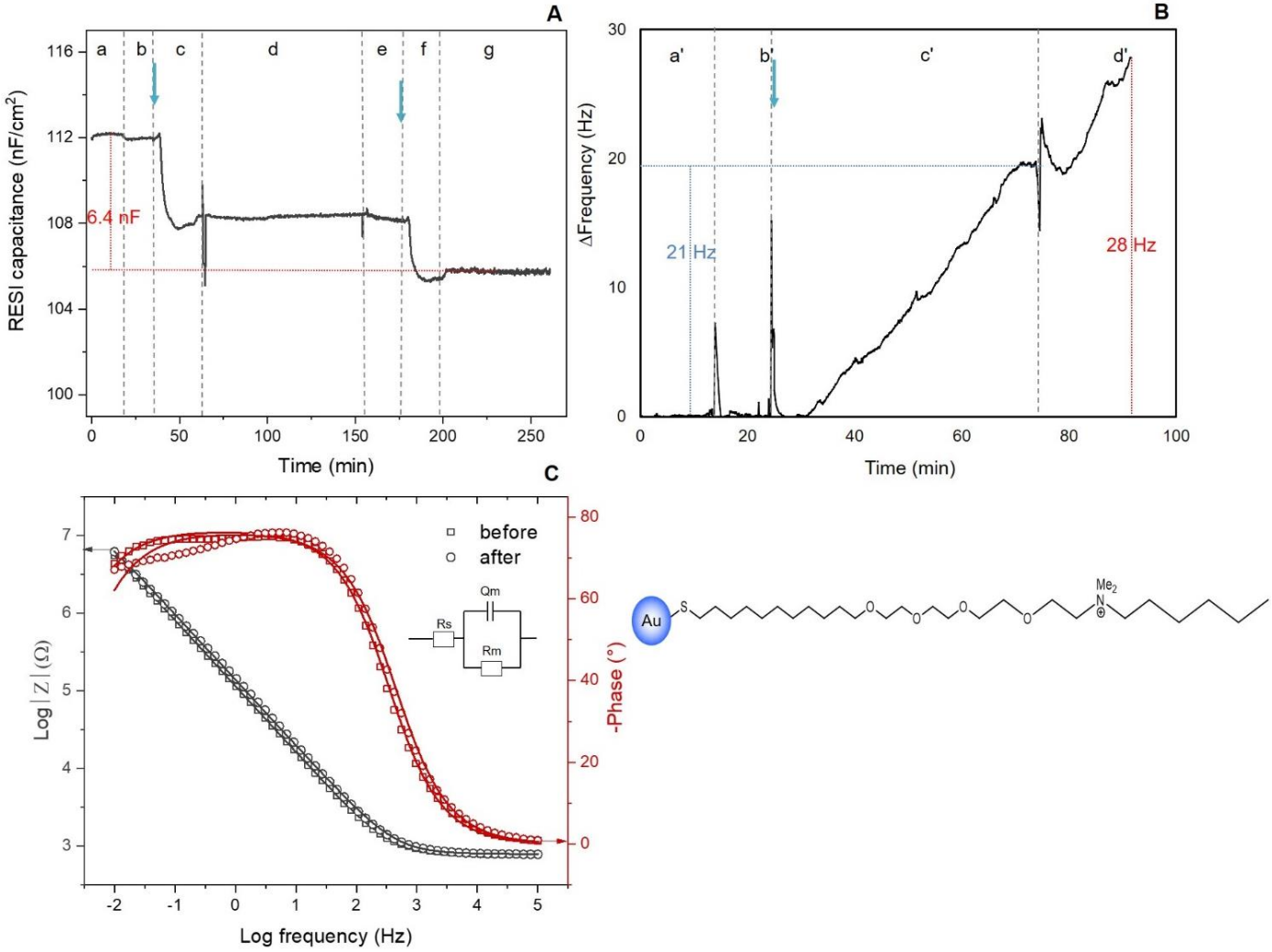

Figure 6.2-7: A) Change in RESI capacitance for the interaction of -NMe_2Hexyl functionalised AuNPs (dispersed in deionised water) with tBLM sensor over time in a running electrolyte solution of 20 mM PBS at a set flow rate of 5 µL/min, B) measured QCM frequency shifts during the interaction of NPs with tBLM electrode (blue arrows indicate the injection of NPs into the system) and C) experimental EIS spectra for the interaction of NPs with tBLM electrode, before and after incubation in NP solution. Left vertical axis: log of impedance (Z) magnitude (grey). Right vertical axis: minus phase angle (dark red). Solid lines are impedance curves simulated from an electric equivalent circuit model of R(QR) – see insert; R_s: solution resistance, Q_m & R_m: membrane CPE and membrane resistance respectively.

QCM & RESI results

The addition of NPs into the system caused an initial NPs adsorption on the surface of the lipid membrane which was seen in the unchanging frequency values following the addition of the NPs for the first 5-6 min (Figure 6.2-7B, stage **c'**), enabling the clustering of NPs at electrolyte-lipid interface. Further interaction time of the NPs with the membrane caused a gradual increase in frequency, calculated as a total mass loss of 266 ± 52.7 ng.

The RESI results have shown parallel results to the QCM, the injections of samples into the system caused decreases in RESI capacitance (Figure 6.2-7A), seen for both injection stages **c** and **f**. These RESI capacitance decreases were found unable to recover back to their initial values from the buffer and solvent runs, synonymous to the permanent change to the electrolyte-lipid interface caused by the NPs-membrane interaction. The RESI capacitance U-shaped well as seen with the –NHXyl sample, for the temporary adsorption of NPs at electrolyte-lipid interface, was not recorded for this sample (–NMe_2Hexyl). Instead, the decrease in RESI capacitance saw a repeated pattern of L-shaped wells, we attributed these to the permanent adsorption of NPs at electrolyte-lipid interface.

EIS results

The experimental results for the penetration of the –NMe_2Hexyl NPs (Figure 6.2-7C) was fitted using R(RQ) equivalent circuit, although no circuitry changes was observed before and after 1hr exposure of tBLM modified electrode in NPs solution, denoting that there was no changes to the overall architecture of the lipid membrane during the interaction with NPs. However, the EIS data recorded small decreases for R_m , Q_m and C_m values were recorded in Table 6.2-4. Although the change in shapes of the EIS curves, before and after immersion in colloidal solution could suggest possible accumulation at electrolyte-lipid membrane without disruption of the lipid membrane via defects' formation or possibly NPs penetration.

Table 6.2-4: Resistance and capacitance values of tBLM before and after incubation in -NMe_2Hexyl functionalised AuNPs. [a] Capacitance value calculated from Eq. 6-2.

	Membrane or pore resistance (R_m) /MΩ	**Membrane CPE (Q_m) /µMho**	**Membrane capacitance [a](C_m) /nF**
Before	36.0 ± 3.01	1.82 ± 0.08 (0.852)	31.0
After	24.8 ± 2.75	1.52 ± 14.5 (0.847)	19.9

Comparing the makeup of the NPs, –NMe_2Bz with –NMe_2Hexyl, the difference is with the presence of aryl group in –NMe_2Bz, whilst the –NMe_2Hexyl NPs only contained alkyl terminal chain. From our results, we can conclude that –NMe_2Hexyl functionalised AuNPs were found to permanent adsorption of NPs at the electrolyte-lipid interface (RESI and EIS results), with the possibility of NPs clustering at electrolyte-lipid interface (QCM results). Compared to the interaction mechanism of the –NMe_2Bz functionalised AuNPs with lipid membrane that was of a non-destructive nature, the results obtained from the different techniques agree that the exposure of the tBLM in the colloidal solution (–NMe_2Hexyl functionalised NPs) caused irreversible changes to the lipid membrane via electrostatic interaction between the negatively charged phosphate group of the membrane and the positively charged units of the NPs; whereby the structure and surface charge of the NPs were found to play a role in the interaction mechanism of the NPs with lipid membrane.

A study by Mensch *et al.*[34] agreeing with our conclusion on the effect of the electrostatic attraction between positively charged nanomaterials with the negative surface potential of the bilayer induced membrane perturbation. In their study, the authors reported the interaction of quaternarly ammonium (poly-diallyldimethylammonium chloride, PDDA) stabilised quantum dots with lipid membrane (DOPC bilayers) using QCM with dissipation monitoring and AFM, they suggested that the interaction of quantum dots with the lipid membrane caused structural changes to the membrane upon interaction, these were seen as large aggregates or ‘microdomains’.

6.2.2.6. $AuC_{11}TEGNHC_6NH_2$

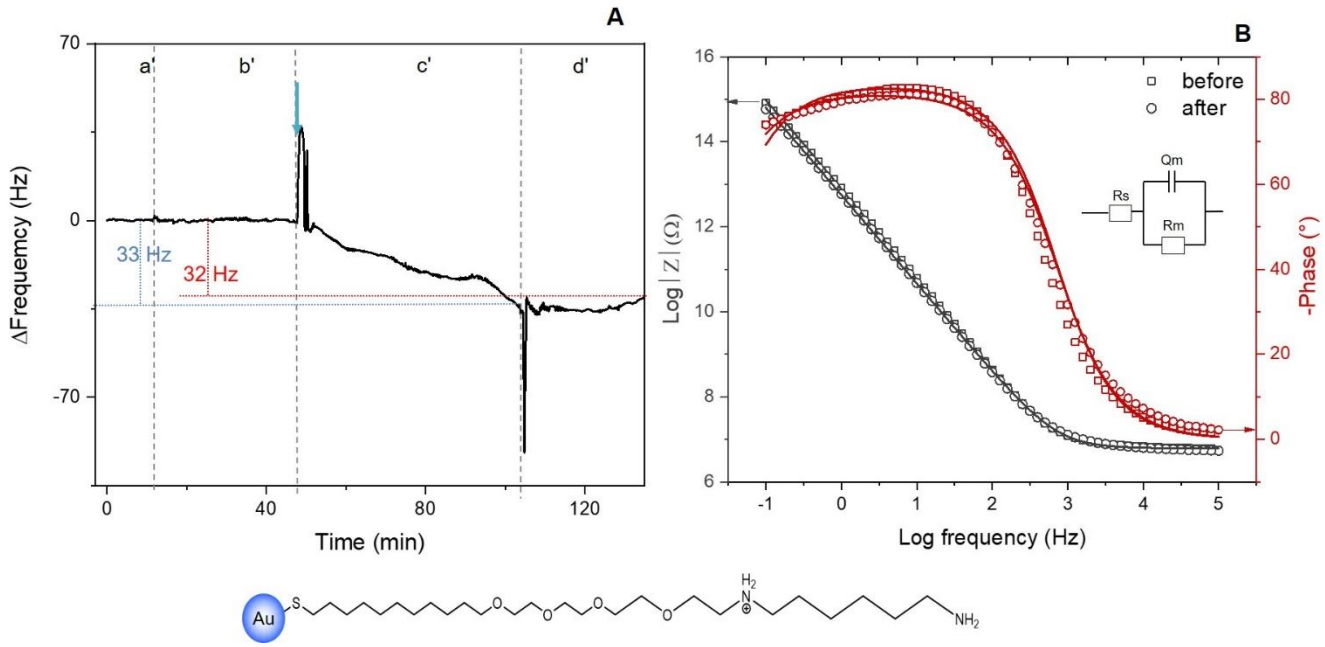

Figure 6.2-8: A) Change in RESI capacitance for the interaction of -NHC_6NH_2 functionalised AuNPs with tBLM sensor over time in a running electrolyte solution of 20 mM PBS at a set flow rate of 5 µL/min, B) measured QCM frequency shifts during the interaction of NPs with tBLM electrode (blue arrow indicates the injection of NPs into the system) and C) experimental EIS spectra for the interaction of NPs with tBLM electrode, before and after incubation in NP solution. Left vertical axis: log of impedance (Z) magnitude (grey). Right vertical axis: minus phase angle (dark red). Solid lines are impedance curves simulated from an electric equivalent circuit model of R(QR) – see insert; R_s: solution resistance, Q_m & R_m: membrane CPE and membrane resistance respectively.

QCM results

It has been reported that terminal cationic ammonium groups on AuNPs are strongly attracted to the phosphate groups of the neutral zwitterionic lipid bilayer which caused membrane defects on supported lipid bilayers.[35] However, our results did not show such trend Figure 6.2-8A; the calculated mass increase (observed frequency decrease) was found to be synonymous to the adsorption of NPs onto the electrolyte-membrane interface and/or the embedment of NPs into the lipid membrane.

EIS results

No change to the circuit model was observed for before and after the incubation period, which suggest that no change electrical property occurred to the systems after –NHC_6NH_2 functionalised AuNPs exposure (Figure 6.2-8B).

However, the increase in electrical conductance has been reposted to be due to the perturbation of the lipid membrane by the NPs exposure.[36] Though our results did not express the circuitry components in terms of conductance, we associated the increase in R_m and Q_m values after NPs exposure to the embedment of NPs into the lipid membrane, which did not lead to an overall membrane destabilisation.

Table 6.2-5: Resistance and capacitance values of tBLM before and after incubation in -NHC_6NH_2 functionalised AuNPs. [a] Capacitance values calculated from Eq. 6-2.

	Membrane resistance (R_m) /MΩ	**Membrane CPE (Q_m) /μMho**	**Membrane capacitance [a](C_m) /μF**
Before	13.0 ± 1.13	457 ± 4.61 (0.927)	59.7
After	15.7 ± 2.10	547 ± 5.82 (0.907)	40.1

Unlike the interaction mechanism of –NMe_2Hexyl functionalised AuNPs that promoted NPs penetration and induced lipid defects, the interaction of –NHC_6NH_2 functionalised AuNPs however, was not found to disrupt the lipid membrane. We concluded that the binding interaction between the surface functionality of the NPs i.e. the cationic ammonium functional groups (primary and secondary ammonium groups) on the monolayer protecting the NPs and, the phosphate group on the zwitterionic lipid membrane promoted the clustering of the NPs at lipid's surface without inducing membrane disruption.[36]

The overall conclusion to this study gave emphasis to the impact of surface charge of the NPs on NP-membrane interactions. NPs containing aromatic substituents were found to weakly bind to the cell membrane's surface without causing permanent membrane disruptions, whereas the aliphatic containing NPs were found to cause permanent destabilisation of the membrane structure either by defects formation via or due to NPs penetration or by NPs embedment into the cell membrane.

6.2.3. NPs interaction with bacteria cell membrane

It has been reported that positively charged (cationic) NPs adhere to the surface of the Gram-negative bacteria, due to electrostatic attraction between the positively charged NPs and the negatively charged (anionic) lipopolysaccharides found in the outer cell wall of Gram-negative bacteria.[37]

Quaternary ammonium groups have been reported to have “bacteria-killing capability”[38] so we wanted to investigate the potency of complex functionalised AuNPs (containing quaternary ammonium groups) using the minimum inhibitory concentration (MIC) by serial dilution method of the NPs, the technique is also referred to as the broth micro-dilution method. MIC is “the lowest concentration of an antimicrobial that will inhibit the visible growth of a microorganism after overnight incubation”.[39] This method was based on the protocol reported by Jennifer M. Andrews[39], a preparation of two-fold dilution of NPs in different agar plates treatments; these treatments included environment with only the Lysogeny Broth (LB) and NPs (control), others with both the LB, NPs and the Gram-negative Escherichia coli (*E. coli*) bacteria.

The interaction between the NPs and the bacteria causes a change to the NPs optical properties thus a variation in the absorbance would be observed. From our results, the treatment of the bacteria, *E. coli*, with NPs at various concentration saw the formation of precipitates at higher concentrations, we attributed the formation of precipitates to the growth of bacteria and the inability of the NPs to function as bacterial inhibitors. The determination of the MIC was for the concentrations with the least amount of precipitates, which correlated to the absence of bacterial growth.

Table 6.2-6: Minimum inhibitory concentration (MIC) of AuNPs against *E. coli*.

Nanoparticles	**MIC (nM)**
$AuC_{11}TEGNHXyl$	1.25 ± 0.25
$AuC_{11}TEGNMe_2Bz$	0.63 ± 0.45
$AuC_{11}TEGNMe_2Hexyl$	0.16 ± 0.06
$AuC_{11}TEGNHC_6NH_2$	0.16 ± 0.03

In terms of bacterial growth inhibition, the NPs with the lowest MIC value against *E. coli* would suggest that it was able to prevent visible bacterial growth at a low concentration, this would be beneficial to use as antibacterial agent as it is required to have a low dosage of drug concentration yet be effective in preventing bacterial growth.

The observed results revealed the NPs with bulky, aromatic side chains (-NMe_2Bz and -NHXyl) to have higher MIC values than the aliphatic side chains (-NMe_2Hexyl and -NHC_6NH_2), as seen in Table 6.2-6, we can ascertain that the presence of aromatic substituents which introduced steric hindrance, affected the NPs' ability to inhibit bacterial growth at lower concentrations, whereby these bulky, aromatic side chains NPs were least efficient at preventing bacterial growth at low concentrations.

It has been reported that linear quaternary ammonium containing polymers are bactericidal because of the electrostatic attractions between the polymer's positively charged cationic groups and the negatively charged bacterial membranes, such interactions allows for the straight alkyl chain to be integrated into the hydrophobic portion of the bacterial membrane and cause subsequent bacterial cell death due to the denaturisation of the structural proteins and enzymes.[40,41] In view of this, our results can be said to agree of such findings as we

have demonstrated the potency of aliphatic quaternary ammonium containing NPs to be bactericidal at lower MIC values compared to their bulkier counterparts.

6.3. Conclusion

This chapter investigated the effects of NPs with different surface composition on both artificial cell membrane models immobilised on gold electrodes i.e. tBLM models and Gram-negative Escherichia coli (*E. coli*) bacteria cells.

The investigation focusing on the (semi)quantitative penetration behaviour of complex NPs on tBLM immobilised on gold electrodes using QCM, RESI and EIS techniques, have shown that the surface functionality of some NPs (bulky, aromatic containing cationic AuNPs; -NMe_2Bz and -NHXyl) did not favour a penetration into artificial lipid membranes. Whereas, aliphatic containing cationic AuNPs (-NMe_2Hexyl and -NHC_6NH_2) were found to penetrate the lipid membrane and affect its overall structure.

Our results (RESI and EIS) revealed that although the interaction of -NHXyl functionalised NPs with lipid membrane induced lipid destabilisation, however this did not cause any permanent damage to the lipid membrane as the latter showed signs of membrane self-healing properties. In comparison, –Me_2Bz functionalised AuNPs showed signs of NPs penetration into the lipid membrane upon prolonged interaction. These initial studies using artificial lipid membranes of neutral overall membrane charge have shown that the surface chemistry of the NPs can affect the type of interactions with lipid membranes. Following this, the results obtained using real bacterial cells have revealed that these bulky, aromatic containing cationic AuNPs generated the highest MIC values thus were least effective at inhibiting bacterial growth compared to aliphatic containing cationic AuNPs.

Further work would be needed to determine the extent of the bactericidal properties of these NPs, in terms of any morphological changes induced by their interactions as well as the ability to be effective against various bacteria, fungi and yeast, thus increasing their potential uses within the biomedical field as antimicrobial agents.

6.4. References

1 Y.-C. Yeh, B. Creran and V. M. Rotello, *Nanoscale*, 2012, **4**, 1871–1880.

2 J. C. Pommerville, *Fundamentals of microbiology*, Jones & Bartlett Publishers, 2013.

3 G. Seltmann and O. Holst, in *The Bacterial Cell Wall*, Springer, 2002, pp. 219–265.

4 M. J. Hajipour, K. M. Fromm, A. Akbar Ashkarran, D. Jimenez de Aberasturi, I. R. de Larramendi, T. Rojo, V. Serpooshan, W. J. Parak and M. Mahmoudi, *Trends Biotechnol.*, 2012, **30**, 499–511.

5 I. Sondi and B. Salopek-Sondi, *J. Colloid Interface Sci.*, 2004, **275**, 177–182.

6 A. Simon-Deckers, S. Loo, M. Mayne-L'hermite, N. Herlin-Boime, N. Menguy, C. Reynaud, B. Gouget and M. Carriere, *Environ. Sci. Technol.*, 2009, **43**, 8423–8429.

7 Y. Zhou, Y. Kong, S. Kundu, J. D. Cirillo and H. Liang, *J. Nanobiotechnology*, 2012, **10**, 19.

8 S. M. Dizaj, F. Lotfipour, M. Barzegar-Jalali, M. H. Zarrintan and K. Adibkia, *Mater. Sci. Eng. C*, 2014, **44**, 278–284.

9 Y. N. Slavin, J. Asnis, U. O. Häfeli and H. Bach, *J. Nanobiotechnology*, 2017, **15**, 65.

10 A. E. Nel, L. Mädler, D. Velegol, T. Xia, E. M. V Hoek, P. Somasundaran, F. Klaessig, V. Castranova and M. Thompson, *Nat. Mater.*, 2009, **8**, 543.

11 J. P. Ruparelia, A. K. Chatterjee, S. P. Duttagupta and S. Mukherji, *Acta Biomater.*, 2008, **4**, 707–716.

12 E. Rascol, J.-M. Devoisselle and J. Chopineau, *Nanoscale*, 2016, **8**, 4780–4798.

13 R. A. Sperling and W. J. Parak, *Philos. Trans. R. Soc. A Math. Phys. Eng. Sci.*, 2010, **368**, 1333–1383.

14 M. Brust, M. Walker, D. Bethell, D. J. Schiffrin and R. Whyman, *J. Chem. Soc. Chem.*

Commun., 1994, 801–802.

15 P. Pengo, S. Polizzi, M. Battagliarin, L. Pasquato and P. Scrimin, *J. Mater. Chem.*, 2003, **13**, 2471–2478.

16 W. P. Wuelfing, S. M. Gross, D. T. Miles and R. W. Murray, *J. Am. Chem. Soc.*, 1998, **120**, 12696–12697.

17 L. Guerrini, A. R. Alvarez-Puebla and N. Pazos-Perez, *Materials (Basel).*, , DOI:10.3390/ma11071154.

18 A. G. Kanaras, F. S. Kamounah, K. Schaumburg, C. J. Kiely and M. Brust, *Chem. Commun.*, 2002, 2294–2295.

19 C. M. Goodman, C. D. McCusker, T. Yilmaz and V. M. Rotello, *Bioconjug. Chem.*, 2004, **15**, 897–900.

20 G. Rossi and L. Monticelli, *Adv. Phys. X*, 2016, **1**, 276–296.

21 C. Brett, S. Kresak, T. Hianik and A. M. Oliveira Brett, *Electroanalysis*, 2003, **15**, 557–565.

22 C. A. Keller and B. Kasemo, *Biophys. J.*, 1998, **75**, 1397–1402.

23 J. Ekeroth, P. Konradsson and F. Höök, *Langmuir*, 2002, **18**, 7923–7929.

24 I. K. Vockenroth, C. Rossi, M. R. Shah and I. Köper, *Biointerphases*, 2009, **4**, 19–26.

25 E. Kalb, S. Frey and L. K. Tamm, *Biochim. Biophys. Acta - Biomembr.*, 1992, **1103**, 307–316.

26 N. Yousefi and N. Tufenkji, *Front. Chem.*, 2016, **4**, 46.

27 C. M. Bailey, E. Kamaloo, K. L. Waterman, K. F. Wang, R. Nagarajan and T. A. Camesano, *Biophys. Chem.*, 2015, **203**, 51–61.

28 Y. Liu and R. Mark Worden, *Biochim. Biophys. Acta*, 2015, **1848**, 67–75.

29 M. E. Orazem, P. Shukla and M. A. Membrino, *Electrochim. Acta*, 2002, **47**, 2027–2034.

30 J. Lin and A. Alexander-Katz, *ACS Nano*, 2013, **7**, 10799–10808.

31 Y. Chen, G. Shan and P. Pan, *Colloid Polym. Sci.*, 2017, **295**, 2207–2215.

32 S. Pogodin, N. K. H. Slater and V. A. Baulin, *ACS Nano*, 2012, **6**, 1308–1313.

33 E. F. Palermo, D.-K. Lee, A. Ramamoorthy and K. Kuroda, *J. Phys. Chem. B*, 2011, **115**, 366–375.

34 A. C. Mensch, J. T. Buchman, C. L. Haynes, J. A. Pedersen and R. J. Hamers, *Langmuir*, 2018, **34**, 12369–12378.

35 J. Lin, H. Zhang, Z. Chen and Y. Zheng, *ACS Nano*, 2010, **4**, 5421–5429.

36 K. L. Chen and G. D. Bothun, *Environ. Sci. Technol.*, 2014, **48**, 873–880.

37 H. Su, Q. Ma, K. Shang, T. Liu, H. Yin and S. Ai, *Sensors Actuators B Chem.*, 2012, **161**, 298–303.

38 J. Song, H. Kong and J. Jang, *Colloids Surfaces B Biointerfaces*, 2011, **82**, 651–656.

39 J. M. Andrews, *J. Antimicrob. Chemother.*, 2001, **48**, 5–16.

40 A. Jain, L. S. Duvvuri, S. Farah, N. Beyth, A. J. Domb and W. Khan, *Adv. Healthc. Mater.*, 2014, **3**, 1969–1985.

41 C. J. Ioannou, G. W. Hanlon and S. P. Denyer, *Antimicrob. Agents Chemother.*, 2007, **51**, 296 LP – 306.

7. Conclusions and Future Work

The work carried out in this thesis outlined the investigations of thiol-capped metal nanoparticles (NPs) and their interactions with lipid membranes. These NPs have found extensive biomedical applications which include usage as sensing tools in gene therapy, and delivery of therapeutics to name a few. The thesis specifically investigated the interactions between thiolated metal NPs (electroactive and non-electroactive ligands), and complex thiolated polymeric gold nanoparticles (AuNPs) with lipid membranes (artificial lipid models and biological bacterial cells). The thesis considered how the thiolated metal NPs and complex thiolated AuNPs interacted with artificial lipid models on the one hand, and how the complex thiolated AuNPs interacted with biological bacteria cells.

Chapter 4 investigated NP-electrode collision behaviours of thiol-capped metal NPs on gold electrodes using Resonance Enhanced Surface Impedance (RESI) and Chronoamperometry (CA) in microfluidic cells setup with integrated electrodes. Factors such as flow rates and ligand electroactivity were found to have a significant impact on the NP-electrode collision events.

At low flow rate (5 µL/min), the non-electroactive dodecanethiol (DDT) NPs were found to agglomerate at the gold electrode surfaces, both techniques detected specific patterns that were interpreted as either agglomerates or individual particle collision events depending on the nano-impact sizing characteristics. From the RESI results, we were able to compare the U-shaped dips generated at slower flow rate (5 µL/min) from NPs colliding at potentiated electrode surfaces; DDT-AgNPs's RESI capacitance was at 67 ± 2.9 nF of compared to16 nF for DDT-AuNPs, we concluded that the presence of these U-shaped dips were suggestive of the detection of clusters of NPs at surface electrode, these clusters consequently disintegrated following the nano-impact collision events, hence generating U-shaped dips on RESI graphs. Chronoamperometry (CA) results echoed the RESI results with the detection of broad spikes, suggestive of large agglomerated particles compared to narrower spikes detected at higher

flow rate (100 µL/min) which were assigned as the detection of multiple individual NPs as these impacted on the potentiated electrode surface.

While altering the ligand electroactivity, introducing electroactive ligands *ω*-ferrocenylhexanethiolate (FcHT) revealed that NP-electrode collision events were generated under potentiated electrode conditions (oxidising potential for ferrocene). However, due to the complexity of the electroactive response generated from the modified NPs, nano-impact sizing could not be derived. Although the RESI capacitance values were of similar to that obtained for DDT-metal NPs whereby FcHT-AgNPs generated deeper U-shaped dips than FcHT-AuNPs; 83 ± 1.8 nF and 43 ± 0.92 nF respectively. We concluded from these results that both non- (DDT-stabilised) and electroactive (FcHT-stabilised) AuNPs showed depressed U-shaped dips compared to AgNPs, we concluded that AuNPs generated minimal signs of NPs aggregation, possibly due to the AgNPs' higher propensity to aggregate in compared to AuNPs. .

Chapter 5 reported the investigation of the penetration behaviour of thiol-capped AuNPs (electroactive and non-electroactive) through artificial lipid membranes (tethered lipid membranes on gold working electrodes). We reported the NPs-membrane interactions using AFM, RESI and electrochemical techniques. The incubation intervals of tethered bilayer lipid membrane (tBLM) models in NPs solutions resulted in initial NPs adsorption followed by lipid defects formation for the penetration of NPs through the lipid membrane, eventually leading to lipid collapse and/or membrane displacement by NPs monolayer. We observed that increasing the incubation times of tBLM electrodes in FcHT-AuNPs solution was found to change the curves of the cyclic voltammograms from peak-shaped to sigmoidal-shape, this also affected the NPs redox activities by supressing the current generated. Such behaviour was attributed to the changes of the lipid membrane via the formation of membrane defects or holes due to the increasing incubation time in colloidal solutions.

The other investigation of the effect of NPs size (FcHT-AuNPs) on NPs-membrane interactions revealed that small NPs (5 nm) have non-destructive penetration behaviours, though they were able to penetrate further into the lipid membrane whereas larger NPs (10 and 20 nm) caused irreversible changes to the lipid membrane, membrane thinning or lipid defect formation.

Further work from this study could investigate the interactions between electroactive AuNPs encapsulated in a lipid shell, with bare electrode surface and the NPs interaction with lipid membranes as tBLM models. Preliminary work on potential controlled penetration of FcHT-AuNPs was carried out showing great potential (see Appendix 2d-2f). This new approach using electroactive AuNPs encapsulated in lipid shell would increase the biocompatibility of the NPs thus they can be used in biological media such as studies involving biological bacterial cells, and this would enable the investigation of the NPs potency against bacterial cells. This potential-controlled release system can be useful in many applications that requires biocompatible conditions.

Chapter 6 investigated the effect of NPs surface charge on NPs-membrane interactions for different systems (artificial and biological membranes), the NPs under investigations were the complex thiolated polymeric AuNPs. The investigations revealed that bulky, aromatic cationic AuNPs were not able to penetrate through artificial tBLM models whilst aliphatic cationic AuNPs penetrated the lipid membrane and were found to alter the membrane's architecture.

The study using biological bacterial cells (*E. coli*) and the MIC technique, concluded that the bulky, aromatic cationic AuNPs generated the highest MIC values compared to aliphatic cationic AuNPs; the former NPs contained higher positive charge density and the presence of aromatic substituents play a role in inhibiting bacterial growth.

Following the work on complex polymeric AuNPs and their interaction with lipid membranes, future studies could include studies on the immobilisation of bacterial cell membrane on gold electrode surfaces and the interactions and penetration behaviours of such NPs with bacterial

lipid membranes. This will enable us to expand our knowledge and understanding of such interactions.

Appendix

Appendix 1

Additional data to supplement the characterization of metal NPs (Au and Ag NPs).

Appendix 1a. Size distribution of thiolated metal NPs.

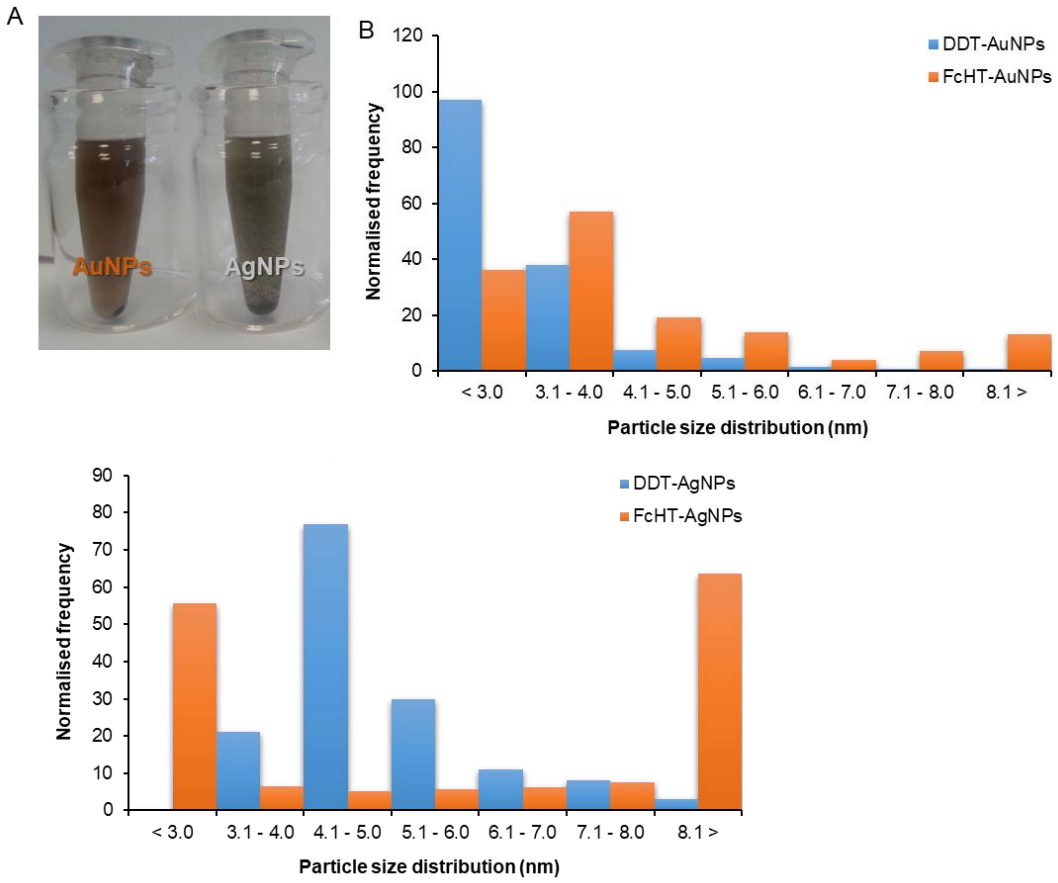

A) Optical image of thiolated DDT-metal NPs, B) size distribution of thiolated metal NPs (DDT and FcHT).

Table A1a. Particle size distribution of metal NPs from TEM sizing.

	AuNPs	**AgNPs**
DDT	2.8 ± 0.9	4.9 ± 1.2
FcHT	5.5 ± 2.9	8.0 ± 2.4

Appendix 1b. Theoretical calculation of number of ligands per nanoparticle.

Assuming that all particles are completely spherical and using the determined TEM diameter (*D*) from Table A1a. The number of metal atoms per NP (*N*) was determined using the equation below from Liu *et al.*[1].

$$N = \frac{\pi}{6}\frac{\rho D^3}{M} \quad \textbf{(A1)}$$

The atomic molar mass of the metal (*M*, Ag = 108 g mol^{-1} and Au = 197 g mol^{-1}) and the density of face-centered cubic (fcc) of the metal (*ρ*, Ag = 10.5 g cm^{-3} and Au = 19.3 g cm^{-3}).

Table A1b. Determination of the number of atoms and ligands per NP.

	Average number of Au atoms	**Average number of Ag atoms**
DDT	6.57 x 10^2	3.6 x 10^3
FcHT	5.20 x 10^3	1.6 x 10^4

Appendix 1c. Theoretical calculation of the molar concentration of NPs in the solution

The calculations for the molar concentration of the NPs (*C*) were adapted from Kalishwaralal *et al.*[2] using the equation below, assuming that 100% reduction of salt ($AgNO_3$ for AgNPs and $HAuCl_4$ for AuNPs) to Ag or Au atoms respectively.

$$C = \frac{N_{Total}}{NVN_A} \quad \textbf{(A2)}$$

The total number of metal atoms added i.e. the initial amount of salt ($AgNO_3$ for AgNPs and $HAuCl_4$ for AuNPs) added to the reaction (N_T, M), the number of metal atoms per NP determined from Eq. 3 (*N*) and the volume of the reaction solution (*V*, L).

Table A1c. Determination of the molar concentration of NPs.

	Molar concentration of AuNPs /μM	**Molar concentration of AgNPs /μM**
DDT	3.38 x 10^2	1.03 x 10^2
FcHT	4.11	3.27

Further required concentrations were made out from the initial concentration determined above.

References

1 X. Liu, M. Atwater, J. Wang and Q. Huo, *Colloids Surf. B Biointerfaces*, 2007, **58**, 3–7.
2 K. Kalishwaralal, S. BarathManiKanth, S. R. K. Pandian, V. Deepak and S. Gurunathan, *Colloids Surf. B Biointerfaces*, 2010, **79**, 340–344.

Appendix 2

Additional data to supplement the chapter on electroactive NPs and their interaction with lipid membranes (chapter 5).

Appendix 2a. AFM results for the time dependent study of non-electroactive (DDT) AgNPs. The conclusion from this study revealed a uniform coverage of the membrane on the gold substrate at t=0 min and after 60 min incubation, uneven peak separations were detected suggestive of the presence of adsorbed NPs at lipid surface as well as the presence of holes in the lipid membrane. At t=480 min, clusters of NPs were evident as well as a more compacted layer with no hole separations suggesting the filling of holes on the lipid membrane by NPs, this can be interpreted as the replacement of the lipid layer with NPs forming a monolayer on the gold substrate. Beyond 480 min of incubation, larger clusters of NPs i.e. agglomerates were detected, we speculate that the replacement of the lipid membrane layer by NPs monolayer will be more prevalent with increase time of incubation in the NPs solution.

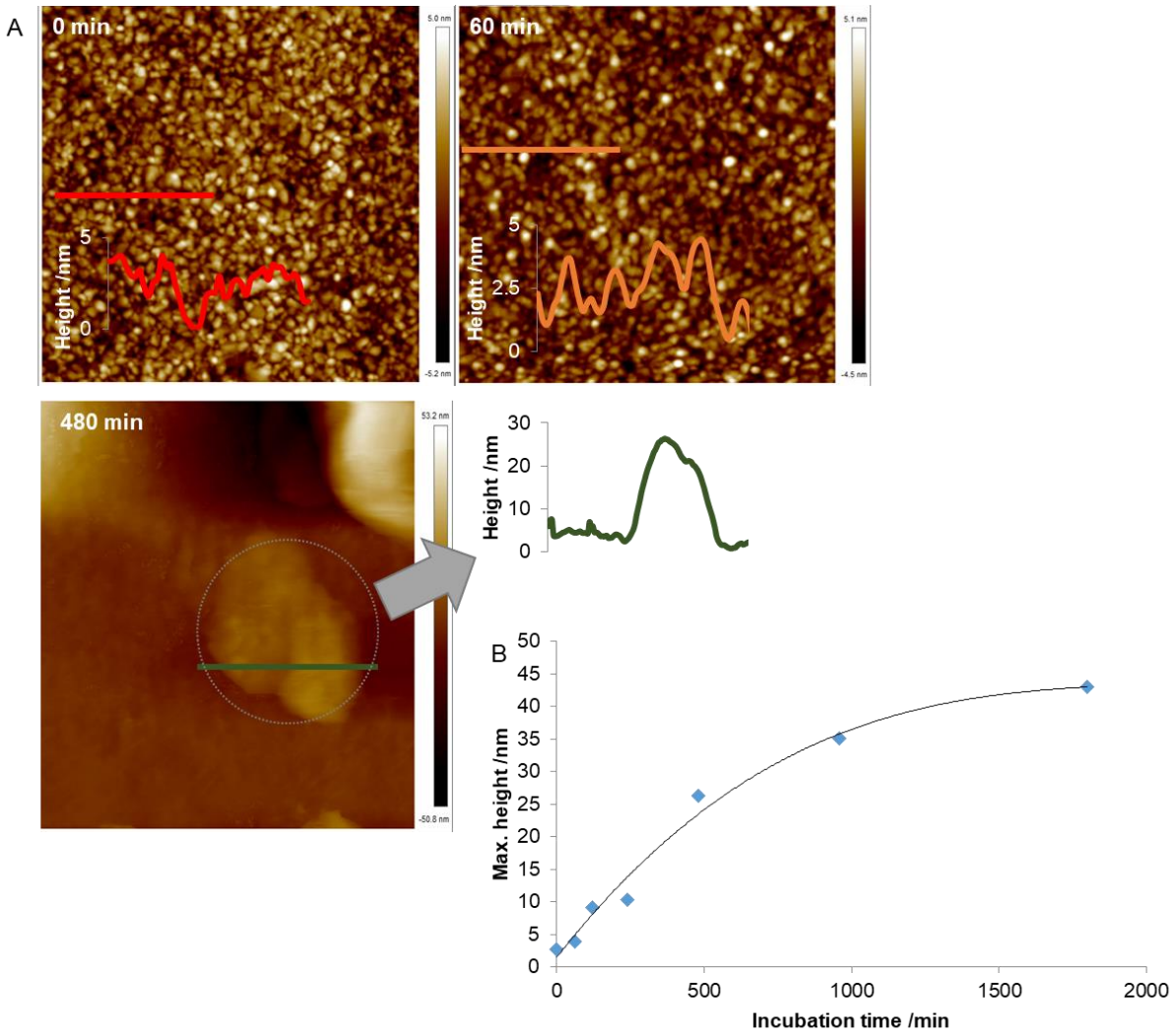

Time-lapsed study for the incubation of lipid immobilised substrates with DDT-AgNPs; including AFM images at 0 min, after 60 min and after 480 min incubation in NPs solution. All images are 2 x 2 µm. B) A graph showing the average max. height of NPs on the lipid surface at different incubation times with the NPs

Appendix 3b. Electrochemical results for the time dependent study of electroactive (FcHT) AgNPs.

The conclusion from this study revealed that increasing the incubation time increases the magnitude of the current peak as well as the charge, seen for bo9th Ag and Fc redox peaks. The attributed the presence of the ferrocene/ferrocinium couple to be due to membrane defects (holes) caused by over saturation of the lipid membrane with NPs, thus enabling the electroactive response of Fc moieties to be recorded. This broadening of redox couple peak and current magnitudes over time were found to be due to the increase in interactions between

the electroactive centres with each other which also caused the shifts of the peak potentials to more negative values.

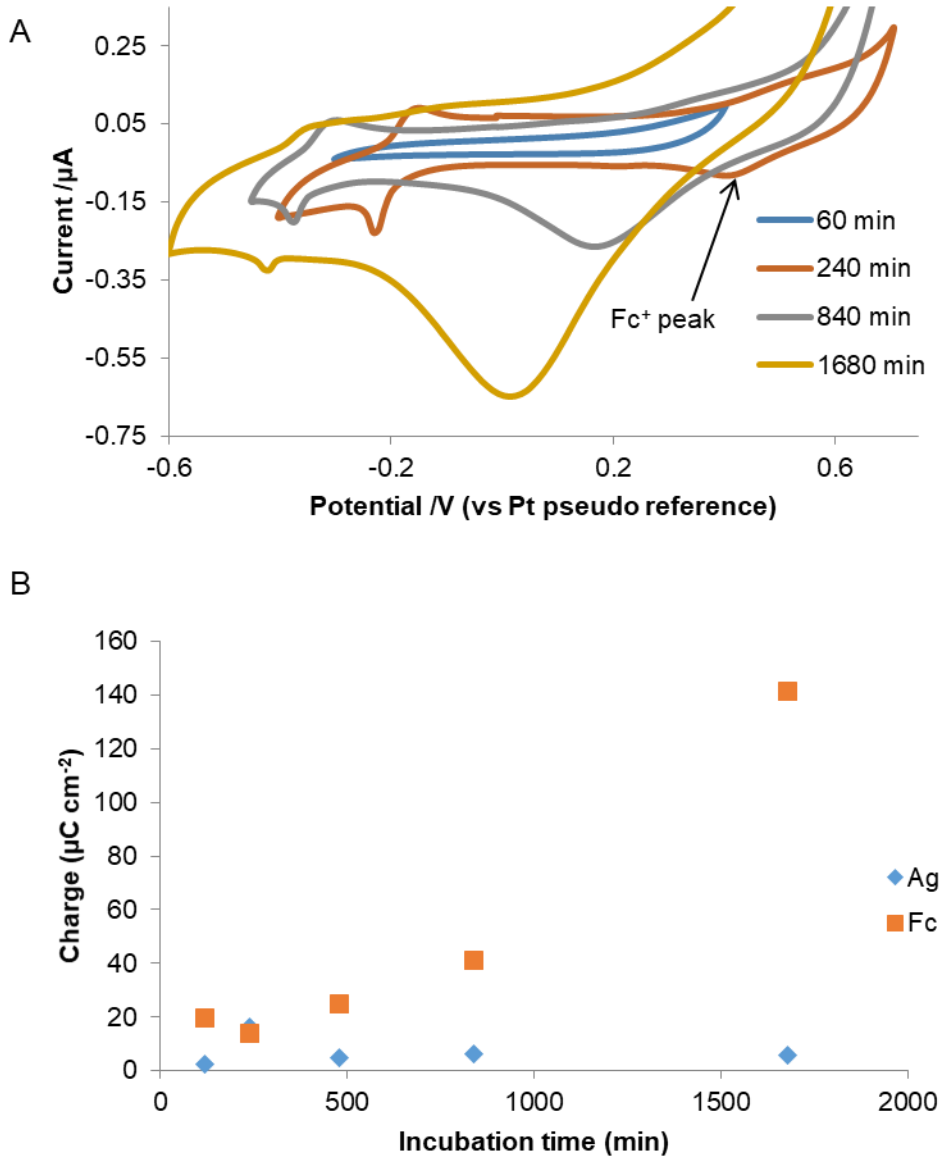

A) CVs of the SAM-modified gold electrode in 0.1 M KNO_3 at 60, 240, 840 and 1680 min immersion times in FHT-AuNPs. Scan rates: 100 mV/s. B) plot of charge per unit electrode (*Q*) over increased incubation time period; charge generated by Ag and Fc redox peaks using $Q = A/v$ where area under the curve (obtained by integration of the oxidation peak curve, *A*) by the scan rate (*v*, 100 mV/s).

Appendix 3c. RESI results for penetration behaviour of thiolated AgNPs through lipid membrane models as a function of NP concentrations.

Penetration of DDT-AgNPs through SAM models at different concentrations revealed different penetration behaviour whereby lower NPs concentration generated deeper NP penetration wells and for longer time and higher NPs concentration generated fewer NP penetration wells.

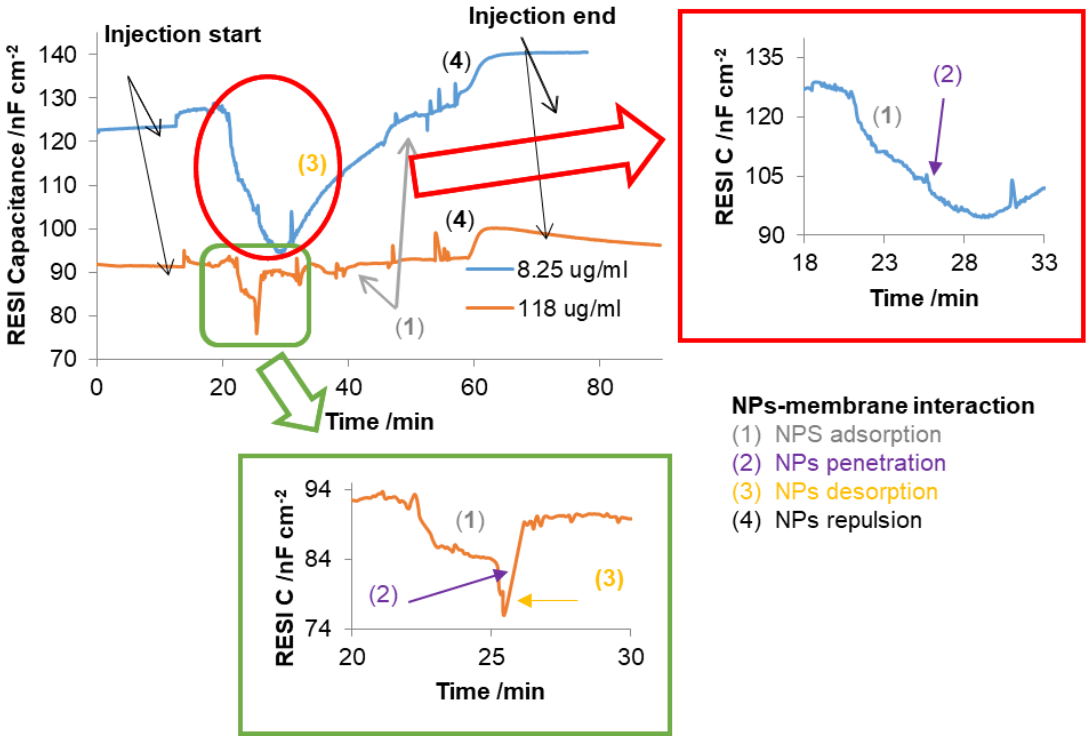

Change in RESI capacitance with DDT-AgNPs injection over time as a function of NPs concentrations in 0.1 M KNO_3 at 5 µL/min flow rate; NPs penetration through SAM-modified gold sensors and the penetration mechanisms over the experiment duration.

Appendix 2d. RESI results for penetration behaviour of FcHT-AuNPs through tBLM models during potential controlled experiments.

The conclusion from this study revealed that back to back changes of the potential of the lipid membrane; +0.4 V to induce oxidation and -0.1 V reduction of the Fc ligands on the AuNPs. The results generated suggested that at positive potential hold, Fc oxidation was promoted thus the change in surface charge of the NPs enabled NPs penetration into the lipid membrane but for a brief period due to the same positive charges acting on the NPs and the lipid membrane. Through at open circuit potential, NPs penetration was also evident however this was far penetration lasted longer compared to that at potentiated lipid membrane.

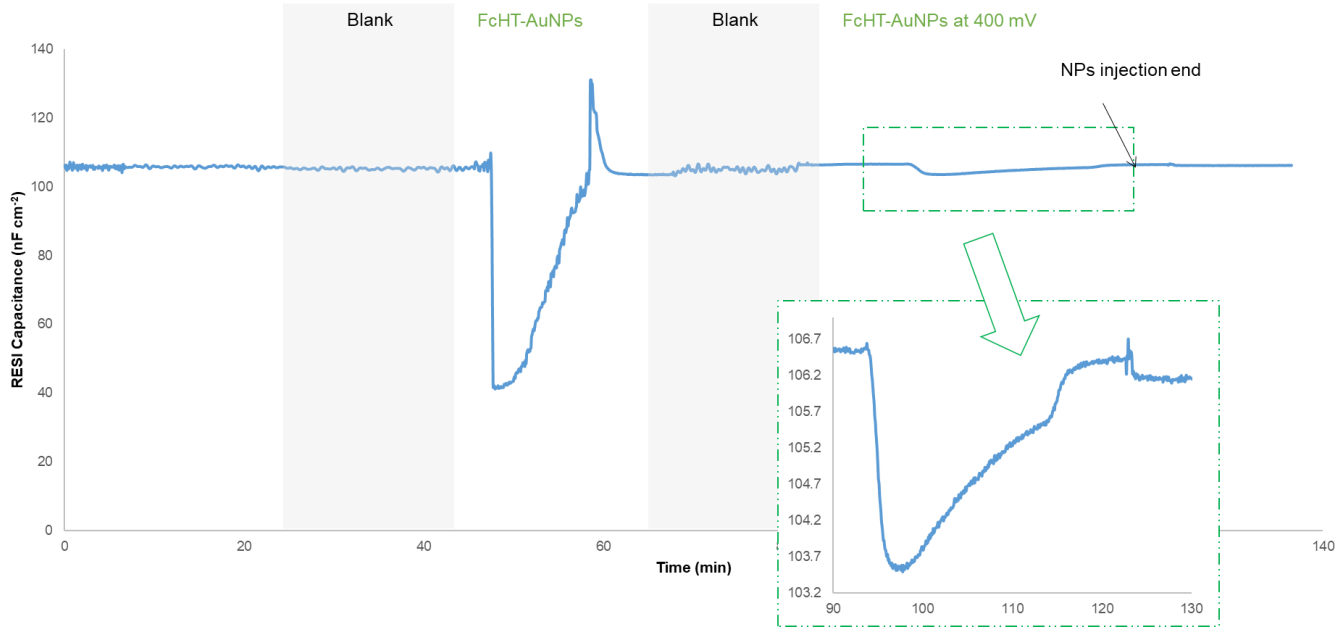

Change in RESI capacitance with FcHT-AuNPs injection over time as a function of potential controlled penetration through tBLM models on gold sensors; a running electrolyte solution of 20 mM PBS at a set flow rate of 5 µL/min.

Appendix 2e. Electrochemical results for penetration behavior of FcHT-AuNPs through SAM and tBLM models.

Oxidation peaks are seen for SAM penetration, but these were suppressed for tBLM at -0.1 V applied potential, such peaks were evidence of electron transfer at electrode surface as the NPs penetrate through the lipid membrane; the 2 peaks observed were suggested to be from the Au metal core (-0.076 V) and Fc couple (+0.362 V). The immersion of the lipid models in FcHT-AuNPs at potentiated electrodes suggested possible penetration of the NPs through the membrane but the neutral state of the ligand at negative potential hold enabled the NPs to remain in the lipid membrane thus producing redox peaks. Similarly to the RESI results at positive potential, brief penetration was recorded seen in DPVs as suppressed peaks near the potentials for the SAM redox peaks.

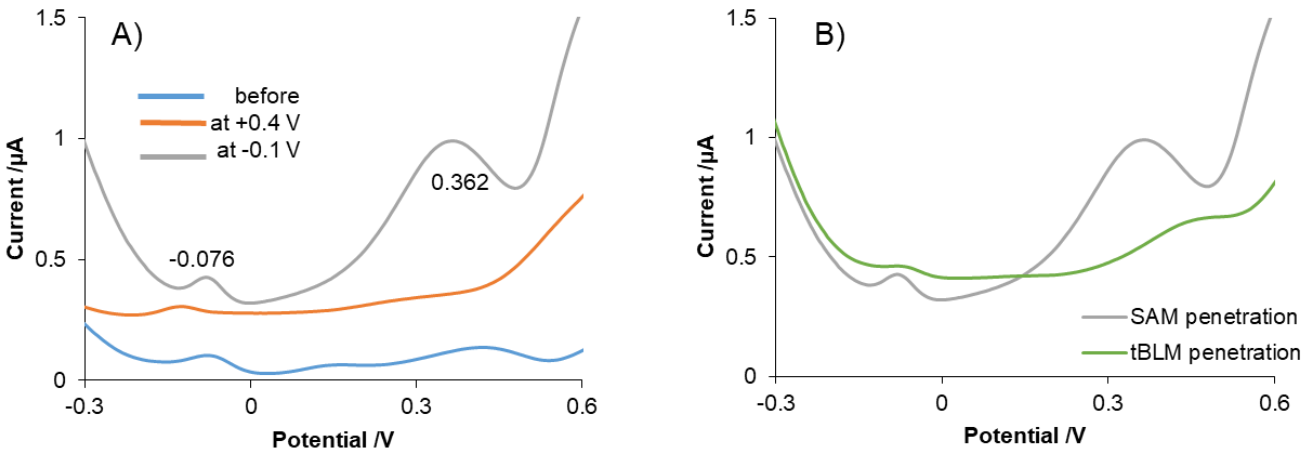

DPVs of the electrochemical response of lipid modified gold electrodes after incubation in FcHT-AuNPs after 60 min in 0.1 M KNO_3 at 100 mV/s scan rate; A) SAM-modified gold electrodes in electrolyte solution before incubation and at potentiated electrodes (+0.4 V and -0.1V). Scan rates: 100 mV/s. B) penetration of NPs through SAM and tBLM.

Appendix 2f. RESI results for penetration behavior of thiolated AuNPs through tBLM models. FcHT ligands are more hydrophobic than DDT ligands therefore FcHT responses revealed penetration well that was deeper than that for the DDT. Similarities in the penetration behavior was identified in the non-disruptive penetration behavior of both systems as the lipid membrane recovered to its initial RESI capacitance values after NPs repulsion.

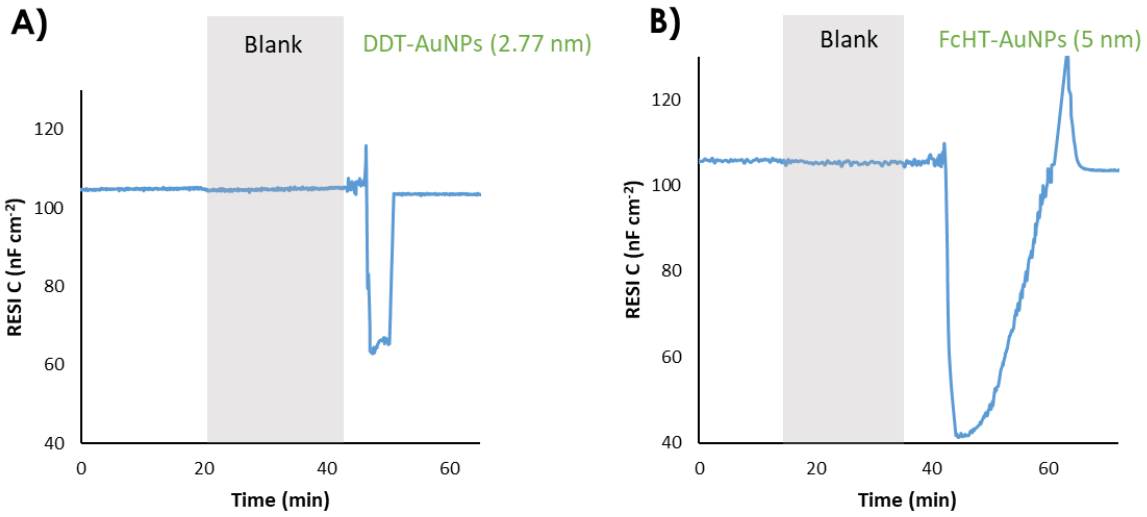

Change in RESI capacitance with FcHT-AuNPs injection over time as a function of NP stabilising ligands through tBLM models on gold sensors; a running electrolyte solution of 20 mM PBS at a set flow rate of 5 µL/min; A) DDT-AuNPs and B) FcHT-AuNPs.

Appendix 3

Additional data to the complex polymeric AuNPs and their interactions with lipid membranes chapter (chapter 6).

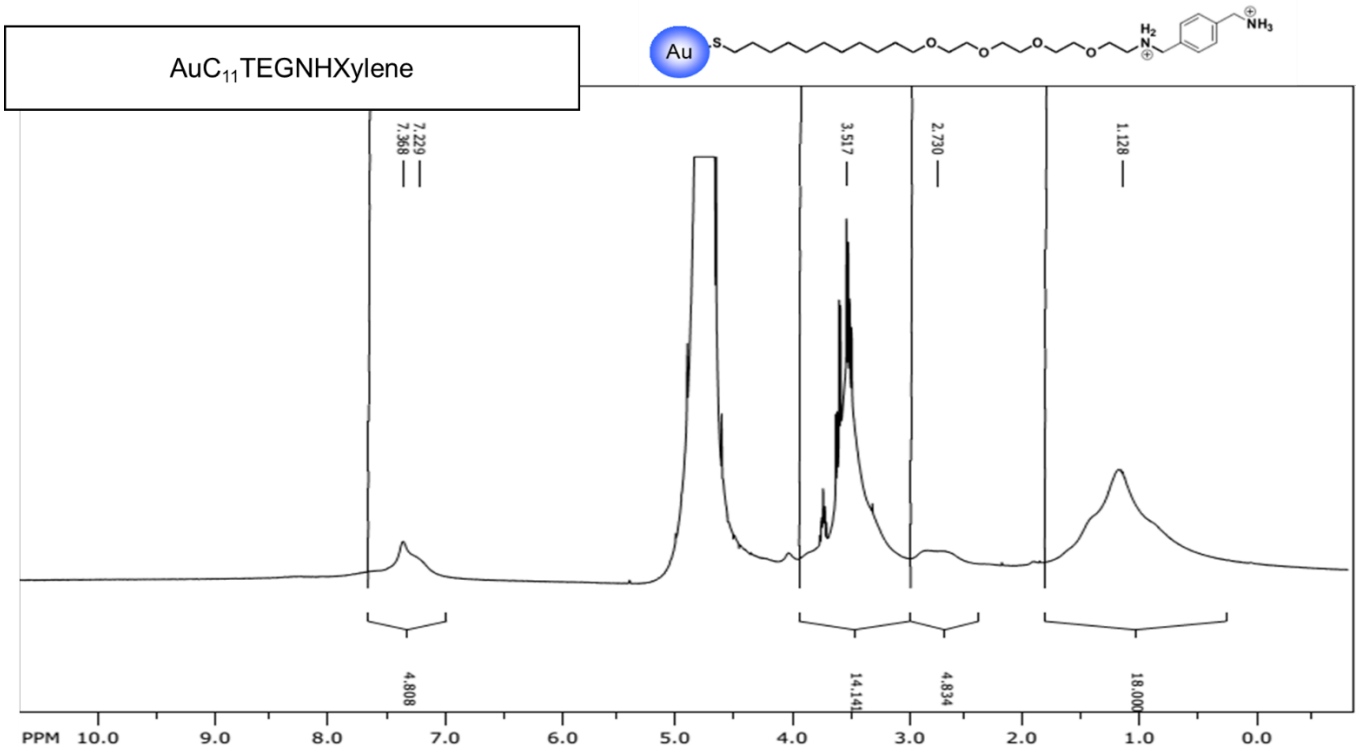

^{1}H NMR of $AuC_{11}TEGNHXylene$ with chemical structure.

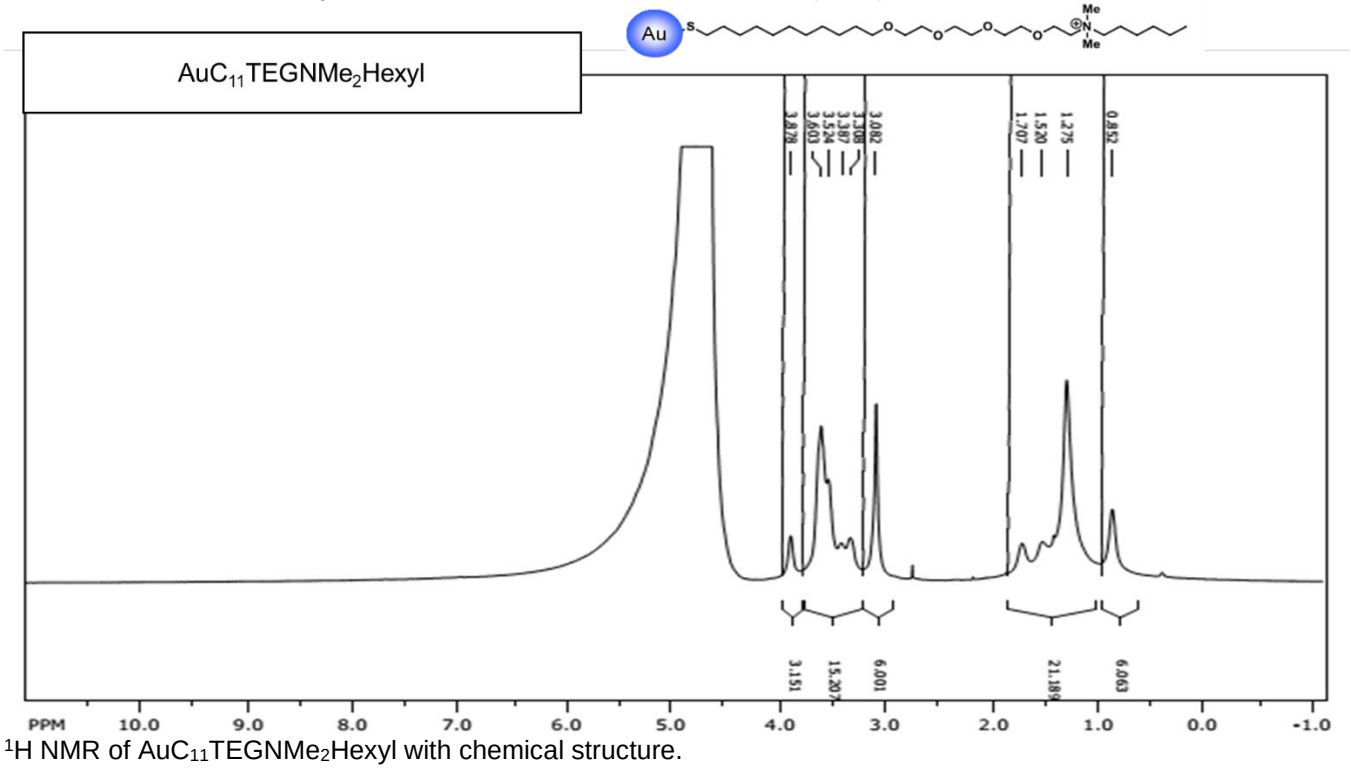

^{1}H NMR of $AuC_{11}TEGNMe_2Hexyl$ with chemical structure.

Chemical shift (ppm)	**Multiplicity**	**Assignments**
3.878	singlet	Au-S-C**H$_2$**-(CH$_2$)$_9$-CH$_2$-(O-CH$_2$-CH$_2$)$_4$-N$^+$-[(CH$_3$)$_2$]-(CH$_2$)$_5$-CH$_3$
1.275	singlet	Au-S-CH$_2$-(C**H$_2$**)$_9$-CH$_2$-(O-CH$_2$-CH$_2$)$_4$-N$^+$-[(CH$_3$)$_2$]-(CH$_2$)$_5$-CH$_3$
3.308; 3.387; 3.524; 3.603	multiplet	Au-S-CH$_2$-(CH$_2$)$_9$-C**H$_2$**-(O-C**H$_2$**-C**H$_2$**)$_4$-N$^+$-[(CH$_3$)$_2$]-(CH$_2$)$_5$-CH$_3$
3.082	singlet	Au-S-CH$_2$-(CH$_2$)$_9$-CH$_2$-(O-CH$_2$-CH$_2$)$_4$-N$^+$-[(C**H$_3$**)$_2$]-(CH$_2$)$_5$-CH$_3$
1.707	singlet	Au-S-CH$_2$-(CH$_2$)$_9$-CH$_2$-(O-CH$_2$-CH$_2$)$_4$-N$^+$-[(CH$_3$)$_2$]-(C**H$_2$**)$_5$-CH$_3$
0.852	doublet	Au-S-CH$_2$-(CH$_2$)$_9$-CH$_2$-(O-CH$_2$-CH$_2$)$_4$-N$^+$-[(CH$_3$)$_2$]-(CH$_2$)$_5$-C**H$_3$**

Proton Chemical Shift Assignments for AuC$_{11}$TEGNMe$_2$Hexyl

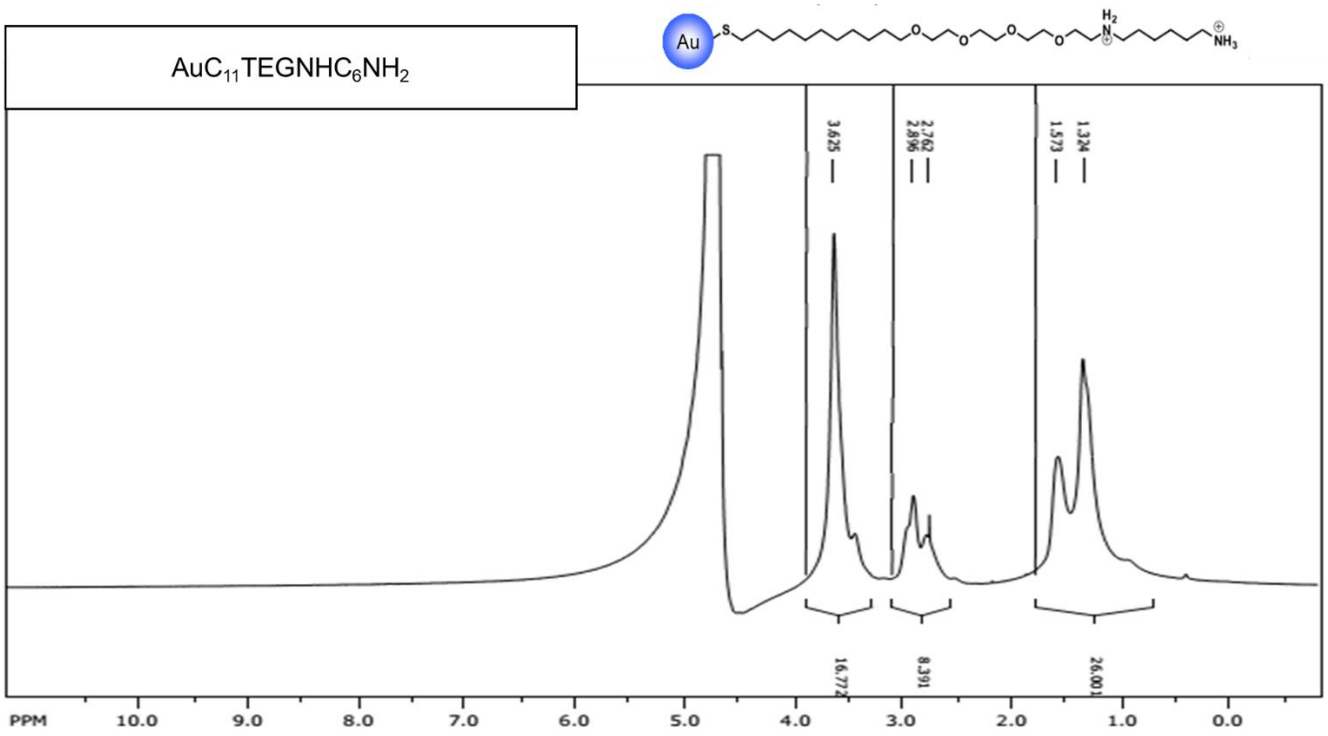

^{1}H NMR of AuC$_{11}$TEGNHC$_6$NH$_2$ with chemical structure.

Chemical shift (ppm)	**Multiplicity**	**Assignments**
3.625	doublet	Au-S-C**H$_2$**-(CH$_2$)$_9$-CH$_2$-(O-CH$_2$-CH$_2$)$_4$-N$^+$[H$_2$]-CH$_2$-(CH$_2$)$_4$-CH$_2$-NH$_2$

1.573	singlet	Au-S-CH_2-(CH_2)$_9$-CH_2-(O-CH_2-CH_2)$_4$-N^+[H_2]-CH_2-(CH_2)$_4$-CH_2-NH_2
2.896	singlet	Au-S-CH_2-(CH_2)$_9$-CH_2-(O-CH_2-CH_2)$_4$-N^+[H_2]-CH_2-(CH_2)$_4$-CH_2-NH_2
1.324	singlet	Au-S-CH_2-(CH_2)$_9$-CH_2-(O-CH_2-CH_2)$_4$-N^+[H_2]-CH_2-(CH_2)$_4$-CH_2-NH_2
2.762	singlet	Au-S-CH_2-(CH_2)$_9$-CH_2-(O-CH_2-CH_2)$_4$-N^+[H_2]-CH_2-(CH_2)$_4$-CH_2-NH_2

Proton Chemical Shift Assignments for $AuC_{11}TEGNHC_6NH_2$

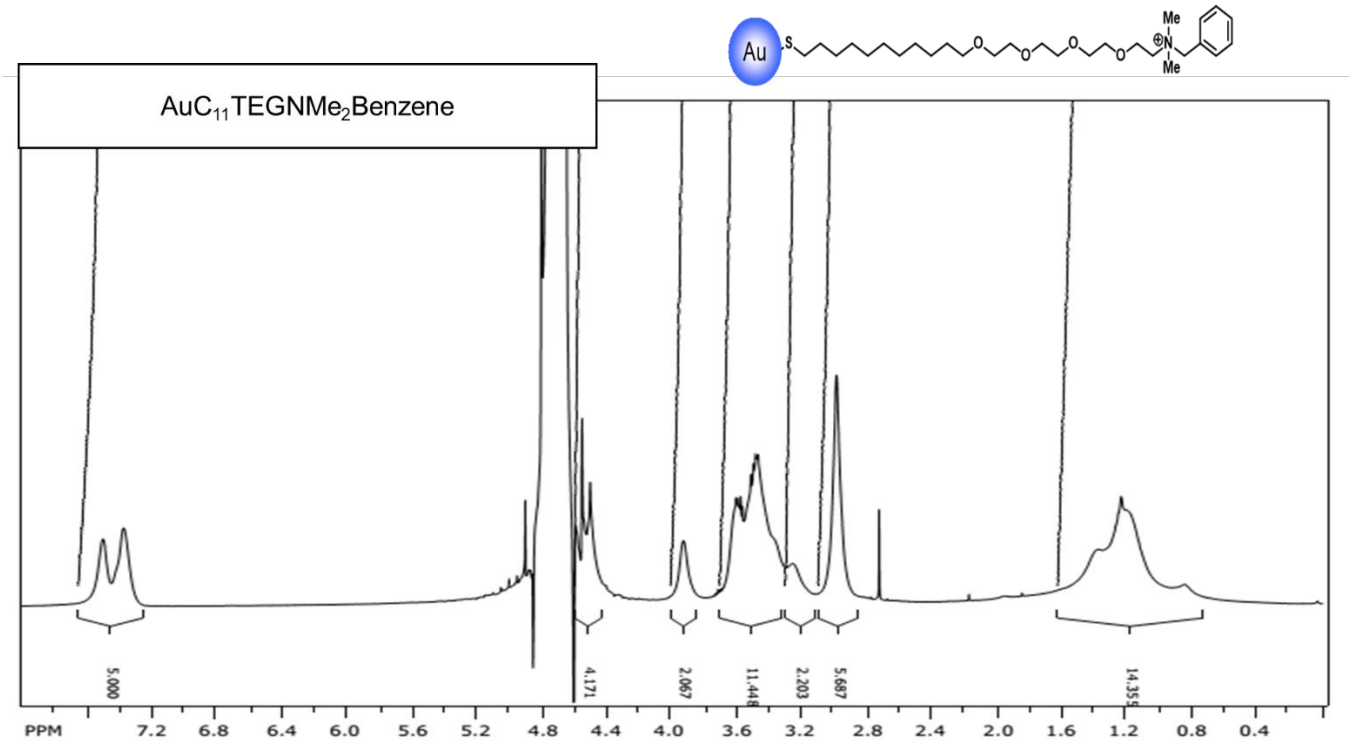

^{1}H NMR of $AuC_{11}TEGNMe_2Benzene$ with chemical structure.

Appendix 4

Additional studies on microgripper that were carried out throughout the research period. The objectives of this work stream were to fabricate microgrippers that can be used as microelectrode. On one gripper arm, a gold microelectrode was incorporated onto the design thus can be used for electrochemical studies as the working electrode. These gold electrode arms were to be immobilised with ferrocene moieties; simple self-assembled monolayers made up of ferrocene thiol molecules and more complex monolayer of ferrocene-capped nanoparticles adsorbed on the surface of the gold electrode.

Appendix 4a. The fabrication of microgrippers on silicon wafers was carried out by photolithography in clean room facilities and their characterisation using CV.

Near sigmoidal shapes of the CV responses for all scan rates were rescored as evidence of hemispherical (radial) diffusion layer as the amount of ferrocene moieties diffusing at the electrode surface being defined by the expanding hemisphere. The results show that the scan rate does not affect the current value; the steady-state current is independent of the scan rate thus suggesting good microelectrode behaviour of the device.

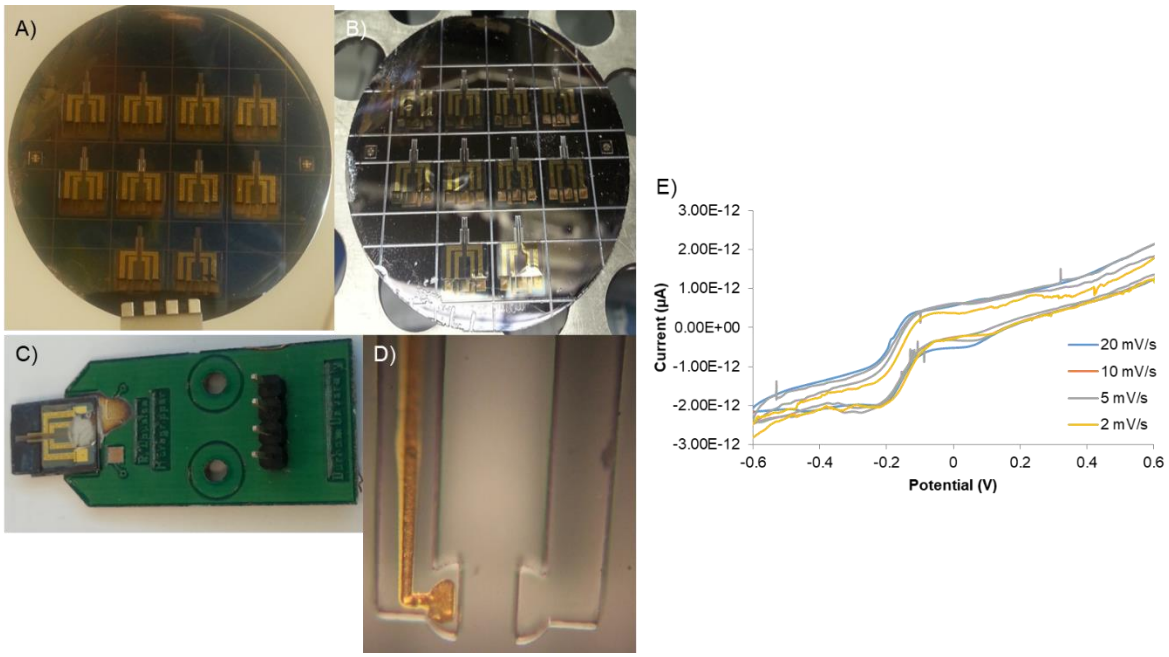

Images of silicon wafer A) before XeF_2 etching, B) after XeF_2 etching, C) image of microgripper after mounting on a PBC, D) microgripper arms after the release from silicon wafer and E) CV responses of microgripper immersed in electrolyte solution mixture of 0.05 M $K_3Fe(CN)_6$ and 0.25 M PBS at different scan rates.

Appendix 4b. Issues encountered during the fabrication of microgrippers and new approach undertaken to overcome the problems.

The electroplating step of the fabrication of the microgrippers was identified to be the cause of poor-quality devices, the gold electroplating solution was sent to be analysed to the manufacturer company and it was reported that the solution was contaminated. Alternative option was to bypass the electroplating step yet retain the electrode arm on the grippers. Some samples showed that the evaporated metal film was unable to be fully removed even after 24 hr immersion in acetone and other samples even after successful lift-off of the gold layer, the electrode arm did not survive. After reviewing the progress of this work-stream, it was advised to discontinue the microgripper study as these did not produce positive results and use instead commercially available electrodes.

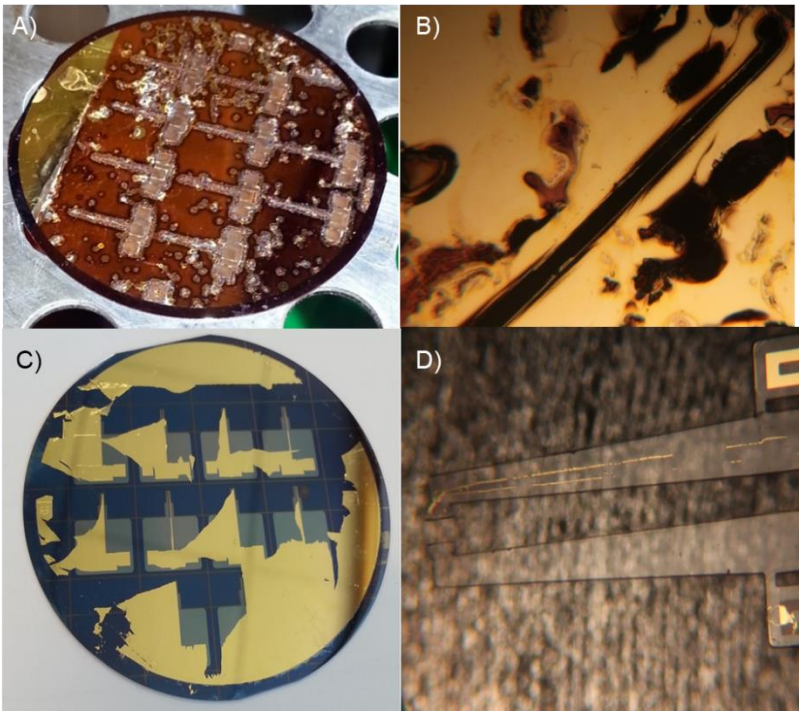

Images showing the wafers after electroplating steps A) whole wafer, B) zoomed image of an electrode arm, images of substrates after lift-off processes; C) after immersion in acetone and D) after gripper tip release.